

# Experimental and Modelling Studies of Pit-to-Crack Transition under Corrosion Fatigue Conditions

by  
Xuejun Huang

B.S., Physics (2012), Peking University

SUBMITTED TO THE  
DEPARTMENT OF NUCLEAR SCIENCE AND ENGINEERING

IN PARTIAL FULFILLMENT OF THE REQUIREMENTS FOR THE DEGREE OF  
DOCTOR OF PHILOSOPHY IN NUCLEAR SCIENCE AND ENGINEERING

AT THE  
MASSACHUSETTS INSTITUTE OF TECHNOLOGY  
September 2017

© 2017 Massachusetts Institute of Technology  
All rights reserved.

Signature of Author: \_\_\_\_\_

Xuejun Huang  
Department of Nuclear Science and Engineering  
September 1, 2017

Certified by \_\_\_\_\_

Ronald G. Ballinger  
Professor of Nuclear Science and Engineering  
Professor of Materials Science and Engineering  
Thesis Supervisor

Certified by \_\_\_\_\_

Lallit Anand  
Warren and Towneley Rohsenow Professor of Mechanical Engineering  
Thesis Reader

Accepted by \_\_\_\_\_

Ju Li  
Battelle Energy Alliance Professor of Nuclear Science and Engineering  
Professor of Materials Science and Engineering  
Chair, Department Committee on Graduate Students



# **Experimental and Modelling Studies of Pit-to-Crack Transition under Corrosion Fatigue Conditions**

by

Xuejun Huang

Submitted to the Department of Nuclear Science and Engineering  
on September 1, 2017 in partial fulfillment of the requirements for the degree of  
Doctor of Philosophy in Nuclear Science and Engineering

## **Abstract**

Corrosion fatigue cracking is a material degradation mechanism which occurs when materials are under cyclic loading and in a corrosive environment. The joint effect of both mechanical and environmental factors makes it one of the most challenging topics in the study of material degradation. The corrosion fatigue cracking process can be separated into four phases, namely development of crack initiation sites (e.g. film breakdown, compositional inhomogeneity, processing variables), development of crack precursors (e.g. pit initiation/growth, grain boundary or localized corrosion), short crack growth and long crack growth. While the mechanism in the long crack growth regime is relatively well understood, the other three regimes are still the subject of much research. The primary goal of this project is to study the transition from the phase 2 to 3, specifically, initiation of cracks from a pit.

The material under current investigation is X65 pipeline steel. A galvanostatic method was applied to artificially generate pits on a smooth surface of the material to produce a pitted specimen. The specimen was then cyclically loaded in four-point bending in air, NaCl solution and CO<sub>2</sub>-saturated NaCl solution at room temperature and 120°C. An alternating current potential drop (ACPD) system was developed and used to detect crack initiation from an existing pit and thus the incubation time to pit-to-crack transition was experimentally obtained. An autoclave system was built in order to apply the desired corrosive environment. Pit-to-crack transition has been successfully captured under fatigue loading and in the environments identified above. Results of experiments in different environments show that the pit-to-crack transition is dominated by a combination of mechanical factors and corrosion processes that facilitate subsequent crack initiation and growth by promoting microstructural barrier removal.

A finite element isotropic model with kinematic hardening has been developed to simulate local fatigue ratcheting around the pit up to large strain levels. An approximate value for the plastic strain level at crack initiation was experimentally determined using electron backscatter diffraction (EBSD) techniques. Given the critical strain level, the model can be used to predict the number of cycles of pit-to-crack transition.

Based on the experimental and modelling results, the underlying mechanism of pit-to-crack transition under current test conditions is proposed to be local ratcheting around the pit that provides sufficient strain accumulation when coupled to an appropriate corrosive environment. This combination provides the necessary crack “precursors”. Environmental effects on crack propagation are also identified and discussed.

Thesis Advisor: Ronald G. Ballinger

Title: Professor of Nuclear Science and Engineering, and Materials Science and Engineering



## Acknowledgements

I am very grateful for my advisor, Professor Ballinger, for his advice throughout my doctoral research. I was new to corrosion and fatigue when I started this project, and learned everything from scratch. I could not have finished this thesis without Professor Ballinger's continued support.

I would like to thank my committee members: Professor Anand, Professor Short, and Professor Yildiz, for their guidance with this thesis. I want to specially thank Professor Anand, for his tremendous help on the mechanical simulation in this thesis. Without his help, this thesis would not have been possible.

The nano-strain (EBSD) measurements were performed by Dr. Michelle Othon, under the supervision of Dr. Martin Morra, at the GE-Global Research Center in Niskayuna, NY. These results, along with their technical input in interpreting the results, were critical to the success of the research. The pipeline steel measurements were the first ever attempted in a ferritic steel which required breaking new ground in this area.

Many thanks to Pete Stahle for his help with designing and constructing the autoclave and ACPD system. My experimental skills were very limited until Pete's tutelage. He helped me to become more like a qualified engineer compared to when I first started the project. Many thanks to my lab mate, Lun Yu, for his help with my experiments. I could not have completed the many experiments without his help. Many thanks to Yusaku and Ehsan, for giving advice to my research and making these years more enjoyable.

Many thanks to my girlfriend for her support. Without her, I could not have survived my PhD study.

Many thanks to my family for their encouragement throughout my PhD study.

Many thanks to Professor Robert Akid and Dr. Olusegun Fatoba from University of Manchester, UK, for their help and comments on my research.

This research has been funded by BP-Global. Thanks to Dr. Roberto Morana, the BP technical lead, for his input and comments. There were several other BP-Global scientists, too many to name, who also contributed.



# Table of Contents

Chapter 1 Introduction .....	20
1.1 Motivation .....	20
1.2 Aims and Objectives.....	21
1.3 Thesis Outline.....	21
Chapter 2 Literature Review.....	23
2.1 Corrosion of Carbon Steel .....	23
2.1.1 General Corrosion of Carbon Steel in Seawater.....	23
2.1.2 Corrosion of Carbon Steel in CO <sub>2</sub> Environment.....	26
2.2 Corrosion Fatigue of Carbon Steel .....	40
2.2.1 Fatigue of Metals .....	40
2.2.2 Fatigue Crack Initiation in Carbon Steel .....	44
2.2.3 Corrosion Fatigue.....	49
2.2.4 Pit-to-Crack Transition .....	56
2.2.5 Ratcheting .....	62
2.3 Crack Detection Techniques.....	66
2.3.1 DCPD Technique .....	66
2.3.2 ACPD Technique .....	67
2.3.3 Resolution of DCPD and ACPD for Small Surface Cracks .....	68
2.3.4 ACPD vs. DCPD for This Research .....	71
Chapter 3 Experimental Methods .....	73
3.1 Material.....	73
3.2 Metallography.....	74
3.3 Pit Generation.....	74
3.4 Four-point Bending.....	77
3.5 Specimen Preparation.....	78
3.6 ACPD System.....	79
3.7 Integrated System for Fatigue Tests in Air and in Aerated NaCl Solution .....	80
3.8 Integrated System for Fatigue Tests in CO <sub>2</sub> -saturated NaCl at RT and 120 °C.....	82
3.8.1 Circulation System.....	82

3.8.2 Temperature and Pressure Control System.....	85
3.8.3 Data Acquisition and Loading Control System .....	86
3.8.4 Autoclave Setup .....	88
Chapter 4 Experimental Results.....	90
4.1 Material Characterization .....	90
4.1.1 Microstructure and Vickers Hardness.....	90
4.1.2 Tensile Behavior .....	96
4.2 Alternate Pit Generation Methods .....	97
4.2.1 Jiang et al. Method [193] .....	97
4.2.2 Anodic Polarization .....	101
4.3 Fatigue Tests.....	104
4.3.1 Introduction of the Fatigue Tests .....	104
4.3.2 Fatigue Tests in Air at Room Temperature (RT).....	105
4.3.3 Fatigue Tests in Aerated NaCl Solution at Room Temperature (RT) .....	108
4.3.4 Fatigue Tests in CO <sub>2</sub> -saturated NaCl Solution at RT .....	110
4.3.5 Fatigue Tests in CO <sub>2</sub> -saturated NaCl Solution at 120 °C .....	116
4.3.6 Summary of the fatigue tests in different environments.....	117
4.4 Conversion of ACPD Data to Crack Growth Rate .....	118
Chapter 5 Simulation of Strain Accumulation around Pit during Fatigue Cycles .....	128
5.1 Introduction .....	128
5.2 Model Description .....	128
5.3 Summary of the constitutive equations .....	136
5.4 Calibration of the Material Parameters of the Model.....	140
5.4.1 Material parameters used in the model .....	140
5.4.2 Benchmark Simulation Results.....	141
5.4.3 Discussion.....	148
5.5 Application to Strain Accumulation around a Pit.....	150
Chapter 6 Plastic Strain Estimation using Electron Backscatter Diffraction (EBSD).....	156
6.1 Introduction .....	156
6.2 Calibration Procedure and Results .....	158
6.3 Estimation of plastic strain level of the actual pit .....	163
Chapter 7 Discussions, Conclusions and Future Work.....	168

7.1	Discussions .....	168
7.1.1	Pit-to-crack Transition Mechanism.....	168
7.1.2	Role of Corrosion in Pit-to-crack Transition .....	171
7.1.3	Resolution of the ACPD System.....	179
7.2	Conclusions .....	180
7.3	Major Contributions .....	181
7.4	Future Work.....	182
	References.....	184
	Appendix A: Stress Intensity Factor of an Elliptical Crack.....	206
	Appendix B: Time Integration Procedure of the Finite Element Model .....	209

## List of Figures

Figure 2-1: A schematic of corrosion loss as a function of exposure time in seawater [25].....	24
Figure 2-2: Morphologies of cross-sections of carbon steel samples immersed in seawater. (a) after 6 weeks. (b) after 11 weeks. (c) after 18 weeks. (d) after 48 weeks [35].....	26
Figure 2-3: A photo of a corroded pipe showing the specific morphology of CO <sub>2</sub> corrosion [37]. .....	28
Figure 2-4: Calculated concentrations of carbonic species as functions of pH for a CO <sub>2</sub> -saturated aqueous solution at $pCO_2=1\text{bar}$ , 1 wt.% NaCl and (a) at 25 °C, (b) at 120°C.....	30
Figure 2-5: Calculated solubility constant $K_{sp}$ as a function of temperature. ....	32
Figure 2-6: In a CO <sub>2</sub> -saturated aqueous solution at $pCO_2=1\text{bar}$ , 1 wt.% NaCl, $cFe^{2+}=0.01\text{ mol/l}$ , calculated supersaturation factor as a function of (a) Temperature, at equilibrium pH, (b) pH, at 25°C.....	32
Figure 2-7: Pourbaix diagrams for Fe-CO <sub>2</sub> -H <sub>2</sub> O systems, $cFe^{2+}=10\text{ ppm}$ , $cFe^{3+}=10\text{ ppm}$ , $pH_2=1\text{bar}$ , $pO_2=1\text{bar}$ . Left: at T=25 °C, Right: at T=120 °C [42]. ....	33
Figure 2-8: CO <sub>2</sub> corrosion rate of a carbon steel at different pH at 20°C ( $pCO_2=1\text{ bar}$ ) and 80°C ( $pCO_2=0.5\text{ bar}$ ), in a 3 wt.% NaCl solution [38].....	34
Figure 2-9: CO <sub>2</sub> corrosion rate of a carbon steel at different temperatures at pH=4 and pH=6.6, in 1 wt.% NaCl solution, at equilibrium $pCO_2$ with pH and temperature [38]. ....	35
Figure 2-10: Corrosion rate as a function of time at different temperatures, at pH=6, $[CO_2]_{aq}=0.030\text{M}$ [43]. ....	36
Figure 2-11: SEM image of the surface of a steel sample after 20 hours test at T=120°C, pH=6. $[CO_2]_{aq}=0.030\text{M}$ [43]. The FeCO <sub>3</sub> scales thoroughly covered the steel surface. ....	36
Figure 2-12: Partial removal of the FeCO <sub>3</sub> corrosion layer and observed localized corrosion. Left: SEM image. Right: Infinite focus microscopy tomography, red cycles highlight spots of localized corrosion [44].....	38
Figure 2-13: Different morphologies observed for protective and nonprotective corrosion layers (after Crolet, et al. [49]) .....	39
Figure 2-14: A schematic of typical S-N curve showing the stress amplitude versus cycles to failure [58]. ....	41

Figure 2-15: Schematic representation of the three fatigue crack growth stages [63].....	43
Figure 2-16: (a) A SEM micrograph of appearance of PSBs on the surface of a fatigued polycrystalline copper. (b) A TEM image of dislocation distribution in PSBs and matrix of fatigued copper single crystal [68]. .....	44
Figure 2-17: Schematics of dislocation structures in the matrix and the PSBs [55]. .....	45
Figure 2-18: Left: A schematic showing the relations between PSBs, matrix and PSMs [67]; Right: Crack initiation from the interface of PSBs and matrix in a copper single crystal [76].....	46
Figure 2-19: Intergranular crack initiation in pure iron at 220K, (a) high intergranular density, (b) intergranular crack caused by shape changes of grains, (c) intergranular crack initiation caused by intrusion of slip against grain boundaries, (d) intergranular crack initiation follow by transgranular crack growth [90] .....	47
Figure 2-20: (a) Surface rumpling of pure iron, (b) crack initiation from the valley of surface rumpling, at 400K, $\Delta\epsilon_{pl} = 4 \times 10^{-3}$ , $N_f = 1.3 \times 10^4$ . The existence of a grain boundary is not needed for crack initiation in this case [90]. .....	48
Figure 2-21: Transgranular crack initiation at PSBs in carburized iron, 74 wt. ppm C, at 343K, $\Delta\epsilon_{pl} = 2 \times 10^{-3}$ , $N_f = 8.3 \times 10^4$ [90].....	48
Figure 2-22: Current transients observed in strain-controlled tension–compression tests ( $\Delta\epsilon = 0.03$ ) on a low carbon steel cycled at 0.1 Hz. Left: Schematic of strain wave and corresponding current transient; Right: Typical current transients recorded in different media at a common pH of 8 [92]. .....	50
Figure 2-23: S-N curves of turbine blade steel samples with different pre-pit sizes. The fatigue limit is lower with a larger pre-pit size. Tests carried out in air at 50 Hz [96]. .....	52
Figure 2-24: Dependence of fatigue limit of turbine blade steel on pre-pit size for tests carried out in air at 50 Hz, highlighting the representation of a pit, of depth $a$ , as a short crack but with effective size [96]......	52
Figure 2-25: Left: Ratio of fatigue crack growth rate in 3.5 % NaCl to fatigue crack growth rate in air as a function of surface crack length. Right: Fatigue crack growth in an intermittent air/corrosion fatigue test, the air fatigue limit is 910 MPa. Both figures show the effect of corrosion at microstructural barriers [103]. .....	54

Figure 2-26: Predicted variation of crack-tip pH with crack length at different external potentials of -600mV SCE and -690mV SCE, cyclic loading frequency=0.1 Hz, R=0.5, and $\Delta K = 20 \text{ MPam}$ . Crack tip pH varies little in the C-Mn steel case but change significantly in the 1% Cr steel case [91].	55
Figure 2-27: Schematic of defect development stages in air and aggressive environment, $\sigma_1 > \sigma_2 > \sigma_3$ [135].	56
Figure 2-28: Corrosion fatigue of high strength steel ( $\sigma_y = 1400 \text{ MPa}$ ) in 3.5% NaCl at different torsional loads with fully reversed cycles, $f=5 \text{ Hz}$ . $a$ and $N$ are the defect size and number of load cycles and $af$ and $Nf$ are crack length and number of load cycles at failure. A significant portion of the lifetime is consumed before cracking occurs [94].	57
Figure 2-29: A schematic of Kondo's model for pit-to-crack transition. The transition occurs when the crack growth rate exceeds the pit growth rate at a critical stress intensity factor range [18].	59
Figure 2-30: Change in pit current density as a function of number of fatigue cycles [94][140]	60
Figure 2-31: (a) Maximum principal stress distribution and (b) maximum principal strain distribution of a hemi-spherical pit in cylindrical specimen viewed in cross section [19].	61
Figure 2-32: Ratcheting behavior of Type 304 stainless steel [143].	62
Figure 2-33: Ratcheting behavior of carbon steel 1020 [143].	63
Figure 2-34: Evolution of macroscopic true strains for various peak stresses of 490, 500, 510, 550 MPa. The stress ratio is the same for all cases with R=0.1 [144].	63
Figure 2-35: Fractograph of an interstitial free steel ratcheted for a loading condition of mean stress of 10 MPa and stress amplitude of 140MPa [152].	65
Figure 2-36: A Schematic of a DCPD system [160].	66
Figure 2-37: A Schematic of an ACPD system [160].	68
Figure 2-38: Relative change of potential versus crack depth for DCPD and ACPD.	70
Figure 2-39: AC/DC ratio of relative change versus crack depth, showing that AC is more sensitive than DC for small cracks.	71
Figure 3-1: As-received X65 pipeline steel	73
Figure 3-2: A schematic of the Pit Generation System.	76
Figure 3-3: The actual pit generation system setup.	76

Figure 3-4: Geometry of the artificial pit. Left side looking down into the pit. Right side looking from the side after polishing. ....	77
Figure 3-5: A schematic of four-point bending fixture [185]. ....	78
Figure 3-6: A schematic of cutting the specimen out of the original pipe section (unit: inch). ...	79
Figure 3-7: Actual pre-pit sample. ....	79
Figure 3-8: A schematic of the ACPD system circuit. ....	80
Figure 3-9: The spot-welded wires and the pit. ....	81
Figure 3-10: Plastic cell on top of the pit for addition of NaCl solution (top view). ....	82
Figure 3-11: System configuration for test in air and aerated NaCl solution at RT. ....	82
Figure 3-12: A schematic of the water board. ....	84
Figure 3-13: A photo of the actual setup of the water board. ....	85
Figure 3-14: Circuit design of the temperature and pressure control system. ....	86
Figure 3-15: A screen shot of user interface of the data requisition and control program. ....	88
Figure 3-16: Flow chart showing how the ACPD system and the fatigue machine work together. ....	88
Figure 3-17: Inside of the autoclave ....	89
Figure 3-18: The cap of the autoclave. ....	89
Figure 4-1: Diagram of sample sectioning for microstructural observation and Vickers hardness measurement. ....	91
Figure 4-2: Microstructures of the base metal of the X65 pipe at different locations. ....	92
Figure 4-3: Microstructures of the base metal of the X65 pipe at higher magnification. ....	93
Figure 4-4: Microstructures of areas around the weld of the X65 pipe. ....	94
Figure 4-5: Schematic of Vickers hardness measurement map ....	95
Figure 4-6: Hardness distribution around the weld (0.25 inch far from the outer surface) ....	95
Figure 4-7: Hardness distribution around the weld (middle of the thickness). ....	96
Figure 4-8: Hardness distribution around the weld (inner surface) ....	96
Figure 4-9: Tensile stress-strain curve for X65 steel at room temperature. ....	97
Figure 4-10: Setup of electrochemical cells. ....	99
Figure 4-11: Surface morphology after stage 1. ....	99
Figure 4-12: Some bare metal spots found after stage 2. ....	100
Figure 4-13: Pit found after stage 3. ....	100

Figure 4-14: Photos of optical microscope showing the morphology of the naturally formed corrosion layer in CO <sub>2</sub> -saturated 1 wt.% NaCl solution at 80°C.....	102
Figure 4-15: Change of LPR and CR versus immersion time. The corrosion rate decreased as the corrosion product layer formed.....	102
Figure 4-16: Potentiostat curves at different applied anodic potential levels. Increase of corrosion current was observed with a +200 mV applied anodic potential.....	103
Figure 4-17: Surface condition after anodic polarization. Left: after +180 mV; Right: after +200 mV. A pit form at the bare metal surface was observed in the +200 mV case.....	104
Figure 4-18: A schematic of sectioning the specimen.....	105
Figure 4-19: Photos of optical microscope showing small crack initiated in an air fatigue test. Left: 200x magnification; Right 500x magnification.....	106
Figure 4-20: SEM images of pit cross section showing small crack initiated in an air fatigue test.....	106
Figure 4-21: SEM images of top view of a pit showing small cracks initiated in an air fatigue test. (a) Locations of cracks with respect to the pit, the surface stress is along the vertical direction; (b) a small crack found at the bottom of the pit; (c) a small crack found at the near-mouth of the pit.....	107
Figure 4-22: ACPD signals of two fatigue tests in aerated NaCl solution using two detection thresholds. (a) 1%; (b) 0.25%.....	109
Figure 4-23: Crack initiation from pits. Left: 550 μm crack corresponding to 1% detection threshold; Right: 250 μm crack corresponding to 0.025% detection threshold.....	110
Figure 4-24: ACPD signals of a fatigue test in CO <sub>2</sub> -saturated NaCl solution at RT.....	111
Figure 4-25: SEM image of a pit in CO <sub>2</sub> -saturated NaCl after 2.34 x 10 <sup>5</sup> cycles (top view). The surface stress is along the vertical direction.....	112
Figure 4-26: Microscopic photos of three pit cross sections. The schematic shows the locations of the three cross sections.....	112
Figure 4-27: ACPD signals of a fatigue test in CO <sub>2</sub> -saturated NaCl solution at RT.....	114
Figure 4-28: Optical microscope photo of the fracture surface of a sample tested test in CO <sub>2</sub> -saturated NaCl solution at RT. The brighter area at the bottom of the photo is fracture surface of fatigue in air.....	115
Figure 4-29: SEM image of the fracture surface of the same sample.....	115

Figure 4-30: SEM images of the fracture surface at higher magnification.....	116
Figure 4-31: Optical microscope photos of the pit cross section after $1.7 \times 10^5$ cycles in CO <sub>2</sub> -saturated NaCl solution at 120 °C. The figure on the right is a zoom-in view of the green box area on the left.....	117
Figure 4-32: SEM image of the pit cross section after $1.7 \times 10^5$ cycles in CO <sub>2</sub> -saturated NaCl solution at 120 °C. ....	117
Figure 4-33: Model setup in COMSOL.....	119
Figure 4-34: Change of ACPD signals with different sizes of pits.....	120
Figure 4-35: Change of ACPD signals with different sizes of 1D cracks. ....	121
Figure 4-36: Calculated Potential drop versus crack depth for different frequencies. Quadratic functions are used to fit the curves. ....	123
Figure 4-37: Converted crack length using the ACPD data shown in Figure 4-22 (a).....	123
Figure 4-38: Calculated Crack growth rate using 4000 Hz data from Figure 4-37. ....	125
Figure 4-39: A schematic showing the geometric parameters used in (Eq. 4-5).....	126
Figure 4-40: Converted crack growth data compared with data from Vosikovsky [201]. ....	127
Figure 5-1: Model setup for benchmark tests. ....	142
Figure 5-2: Results of experiment and simulation of uniaxial tensile test.....	142
Figure 5-3: First 1 ¼ cycle of 1% systemic strain cyclic test. ....	143
Figure 5-4: First 1 ¼ cycle of 0.5% systemic strain cyclic test. ....	144
Figure 5-5: Engineering stress-strain curves of asymmetric stress cyclic test with mean stress = 100 MPa, stress amplitude = 450 MPa. Left: Experimental data; Right: Simulation.....	145
Figure 5-6: Comparison between experiment and simulation for selected cycles (1 <sup>st</sup> , 50 <sup>th</sup> , 100 <sup>th</sup> , 200 <sup>th</sup> cycles). ....	146
Figure 5-7: Strain versus number of cycles curve of experiment and simulation. ....	146
Figure 5-8: Simulation results and experimental data of various loading conditions.....	147
Figure 5-9: Instability of strain accumulation at the first cycle causing by the yield point phenomenon. Left: Mean stress of 130 MPa, stress amplitude of 430 MPa; Right: Mean stress of 140 MPa, stress amplitude of 430 MPa. ....	147
Figure 5-10: Comparison between the current model, AF model and Ohno-Wang model using the experimental data of mean stress of 100 MPa, stress amplitude of 450 MPa.....	149
Figure 5-11: Model setup for the pit geometry. ....	150

Figure 5-12: Comparison between true plastic train, equivalent tensile plastic strain and $E33p$ in a uniaxial tensile test. ....	152
Figure 5-13: Comparison between true plastic train, equivalent tensile plastic strain and $E33p$ in an asymmetric stress cyclic test with mean stress = 100 MPa, stress amplitude = 450 MPa. ....	153
Figure 5-14: Magnitude of plastic strain around the pit after $10^4$ cycles. ....	154
Figure 5-15: Plastic strain magnitude versus number of cycles curve of the element at the bottom of the pit. ....	155
Figure 5-16: Linear fit of the plastic strain accumulation. ....	155
Figure 6-1: Left: Schematic of sub-grains generated by a dislocation wall [237]. Right: Schematic of change in orientation as the electron beam scan across the sample surface. Notice that the orientation only change when the beam crosses an array of dislocations with a net non-zero Burgers vector [227]. ....	156
Figure 6-2: A schematic of the EBSD scan across grains. ....	157
Figure 6-3: A schematic of EBSD sample preparation. ....	158
Figure 6-4: BSE images of transverse and longitudinal samples at different plastic strain levels. ....	160
Figure 6-5: Boundary maps of transverse and longitudinal samples at different plastic strain levels (black line at bottom left corner in each figure is a scale bar of 20 $\mu\text{m}$ ). The density of low angle boundaries (red lines) increases with higher plastic strain levels. ....	162
Figure 6-6: Calibration curves for both transverse and longitudinal directions. ....	162
Figure 6-7: Averaged calibration curve for X65 steel. ....	163
Figure 6-8: BSE image of the pit after $1.7 \times 10^5$ cycles in $\text{CO}_2$ -saturated NaCl solution at 120 $^\circ\text{C}$ . ....	164
Figure 6-9: (a) A BSE image of the scanned area at the bottom of the pit; (b) AMIS line values measured in the scanned area. ....	165
Figure 6-10: AMIS area values derived from Figure 6-9. ....	166
Figure 6-11: Converted plastic strain at the bottom of the pit. ....	167
Figure 7-1: True stress- strain curve of a monotonic tensile test of the X65 steel. ....	170
Figure 7-2: Comparison of crack initiaiton in air (left) and in $\text{CO}_2$ -saturated NaCl at 120 $^\circ\text{C}$ (right). ....	172

Figure 7-3: Specimen used in [251], the red line shows the scanning path for corrosion current measurement. ....	173
Figure 7-4: Left: Distribution of von Mises stress and plastic strain along the scanning path; Right: Measured corrosion current density [251]. A positive correlation between the plastic strain and the corrosion rate can be observed.....	173
Figure 7-5: Left: Optical microscopic photo of crack initiation in aerated 1 wt.% NaCl solution; Right: SEM image of crack initiation site at higher magnification. ....	174
Figure 7-6: EDS analysis of the surface of a specimen test in CO <sub>2</sub> -saturated NaCl solution at RT after 14 hours. Left: SEM image of the surface, red rectangle highlights the analysis area; Right: EDS analysis result. The blue box highlights the atomic ratio of different elements. The result shows that the surface is mainly Fe. ....	177
Figure 7-7: EDS analysis of specimen surface after test in CO <sub>2</sub> -saturated NaCl solution at 120 °C after one weeks. Left: SEM image of the surface, red rectangle highlights the analysis area; Right: EDS analysis result. The blue box highlights the atomic ratio of different elements. The result suggests that the surface is mainly covered by FeCO <sub>3</sub> and iron oxide. ....	177
Figure 7-8: SEM images of specimens tested in at CO <sub>2</sub> -saturated NaCl solution at different temperatures. Left: specimen tested at RT, the surface is mainly corroded bare metal; Right: specimen tested at 120 °C, the surface is covered by FeCO <sub>3</sub> scales.....	178
Figure 7-9: Possible crack arrestment at grain boundary observed from the specimen fatigued in CO <sub>2</sub> -saturated NaCl solution at 120 °C. ....	179
Figure 7-10: Change of potential drop versus crack length with different probe spacings. ....	180

## Lists of Tables

Table 2-1: Key chemical reactions occurring in aqueous CO <sub>2</sub> solution and corresponding equilibrium expressions [38].....	28
Table 2-2: Equilibrium constants for homogeneous reactions listed in Literature Review as a function of temperature, pressure and ionic strength ( $T_f$ is temperature in degrees Fahrenheit, $T_k$ is absolute temperature in Kelvin, $I$ is ionic strength in molar, and $p$ is pressure in psi.) [38] .....	29
Table 3-1: Chemical composition of received X65 pipeline steel. Data provided by BP. ....	74
Table 4-1: Values of $p/q$ for different frequencies .....	122
Table 5-1: Values of material parameters used in the model.....	141

## Nomenclature

The frequently used abbreviations and symbols are listed below.

$a$  : Pit depth

ACPD: Alternating current potential drop

AMIS: Average intragrain misorientation

$c$  : Half pit width

CR: Corrosion rate

DCPD: Direct current potential drop

EBS: Electron backscatter diffraction

$f$ : Frequency of the fatigue loading or the alternating current

HSLA: High strength low alloy

HV: Vickers hardness number

$\Delta K$ : Stress intensity factor range

$K_{sp}$  : Solubility product constant

LEFM: Linear elastic fracture mechanics

R: Stress ratio

RT: room temperature

SS: Supersaturation

$\Delta\varepsilon$ : Strain range

$\Delta\sigma$ : Stress range

# Chapter 1 Introduction

## 1.1 Motivation

The lifetime prediction of a component under corrosion fatigue conditions is challenging because of the need to address the statistics of pit growth, the transition from pit to crack, and subsequent growth in the short and long crack regimes [1]. For example, in the oil and gas industry, pipelines or other critical structures may be subjected to the simultaneous actions of corrosion and fatigue during operations, which limits their lifetime [2]. In CO<sub>2</sub>-saturated brine-like solutions, pits can occur on the internal surface of the pipe due to the partial breakdown of the iron carbonate and/or iron sulfide scales that are formed on the internal surface in these environments [3][4]. These pits can become preferential sites for crack initiation due to the increased stress/strain intensification owing to the pit geometry and the aggressiveness of the local chemistry (e.g. acidic pH, high concentration of aggressive anions) [5]. Further “precursors” can then develop due to localized corrosion within the pit in response to both accumulated strain and corrosion. Cracks then propagate to the final failure of the component.

The pit-to-crack transition is considered to be a critical stage in the corrosion fatigue process, and might be regarded as a damage mechanism transition point, i.e. from a corrosion dominated process to a mechanics dominated process [6]. Depending on the stress level and the environment, a substantial fraction of the corrosion fatigue lifetime can be consumed in the pit-to-crack transition stage [6][7]. However, the underlying mechanism of the pit-to-crack transition is still unclear.

Some investigators [8]–[12] have used statistical methods to study the probability of crack initiation from pits with different test conditions and pit geometries. Specimens are loaded and immersed in an environment in which pitting corrosion occurs. After some time, specimens are removed from the environment for characterization. An estimated probability of crack initiation can then be calculated statistically and the effect of various factors such as the geometry of the pit and the environment can be assessed.

Several deterministic models [13]–[17] have been developed based on the concept proposed by Kondo [18]. Kondo [18] attempted to predict the pit-to-crack transition in corrosion fatigue by

introducing a critical stress intensity factor range due to the presence of the pit  $(\Delta K)_p$  above which cracks would initiate. Kondo's model provides some insights into the pit-to-crack transition process. However, adopting a linear elastic fracture mechanics (LEFM) parameter, such as  $\Delta K$ , to characterize the point where the pit-crack transition occurs is not considered appropriate because this parameter is derived from long crack studies [1]. Also,  $\Delta K$  is an elastic parameter, which fails to account for the microplasticity generated by the pit.

In summary, an understanding of the underlying physical mechanism of pit-to-crack transition is still lacking. Turnbull et al. [5][19] based on their experimental observation of different crack initiation sites from pits, suggested that the localized plastic strain was the key of pit-to-crack transition. This study attempts to develop a mechanistic understanding of the pit-to-crack transition phenomenon with special focus of plasticity around the pit in combination with environmental effects.

## 1.2 Aims and Objectives

This thesis investigates the pit-to-crack transition behavior of API 5L X-65 steel under corrosion fatigue conditions in environments containing NaCl and CO<sub>2</sub>. The aims of the present work are to develop a mechanistic understanding of the underlying driving force for crack initiation from pits, and to develop a model which can be used to predict the number of cycles to crack initiation under fatigue loading conditions. In order to achieve these aims, the main objectives of this thesis are as follows:

1. To build an integrated system which can be used to detect pit-to-crack transition in the material in different environments and under different loading conditions.
2. To develop a finite element model which simulates the strain evolution around the pit under fatigue loading.
3. To access the strain level for pit-to-crack transition in the X65 steel.

## 1.3 Thesis Outline

This thesis consists of seven chapters. A literature review on corrosion, fatigue and corrosion fatigue mechanisms with special focus on steels is presented in Chapter 2. In Chapter 3, details of

the experimental methods and the setup of the experimental system is described. Chapter 4 presents the experimental results obtained in this study, along with some discussion of these results. In Chapter 5, details of the finite element model are presented, including the constitutive equations used in the model, the calibration of the material parameters, and the application of the model to pit-to-crack transition. In Chapter 6, the test procedure of assessing plastic strain level around the actual pit using EBSD technique is presented. The measured plastic strain levels are used to compare with the simulation results. Conclusions drawn from the present work and suggestions for future work are presented in Chapter 7.

## Chapter 2 Literature Review

### 2.1 Corrosion of Carbon Steel

Corrosion can be generally described as the destructive chemical reaction between a material and its environment which causes the degradation of the material [20]. In this definition we limit our discussion to corrosion of metallic materials. The cost of corrosion damage has increased over the years and has significantly impacted the economies of nations. The global cost of corrosion in has been estimated to be 3.4% of the global Gross National Product (GNP) in 2013 [21]. Carbon steels are alloys of iron, with about 0.05 to 1% carbon. Carbon steels are widely used as structural materials in the oil and gas, marine and nuclear industries where they are subject to both general and localized corrosion (e.g. see review articles on oil and gas [22], marine [23], and nuclear [24]). For the purpose of this thesis, corrosion of carbon steel in seawater and in aqueous environments also containing CO<sub>2</sub> will be reviewed in the following sections.

#### 2.1.1 General Corrosion of Carbon Steel in Seawater

Carbon steel is widely used in coastal infrastructure such as bridges, pipelines and ships. Because of the aggressiveness of salt water to carbon steel, in practice many of these infrastructures are protected by coatings, sacrificial anodes or impressed cathodic current. However, this is not always the case. In some cases these measures are not fully protective [25]. For this reason, it is a common practice to estimate degradation rates and make some allowance for future corrosion related material loss. This is especially true for infrastructure exposed to marine environments.

The general corrosion of carbon steel in marine environments has been intensively studied by R. Melchers [25]–[30]. An illustrative figure for the different stages of corrosion is shown in Figure 2-1.

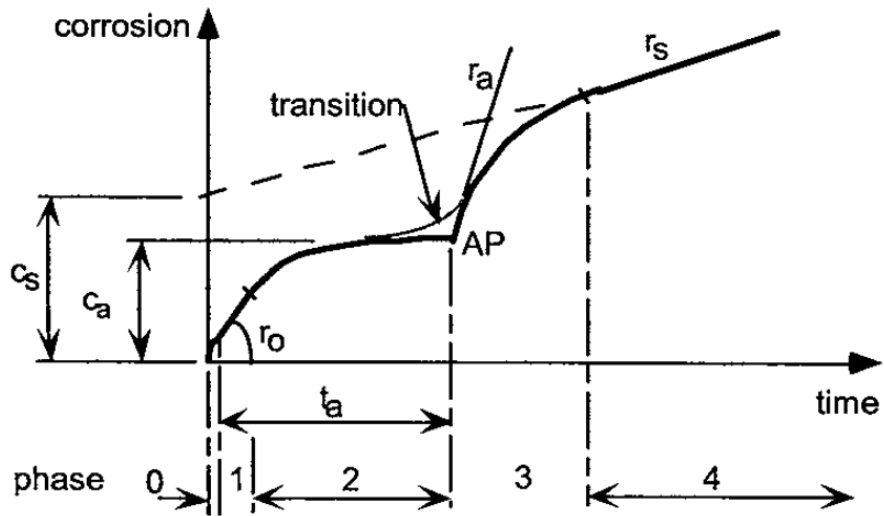


Figure 2-1: A schematic of corrosion loss as a function of exposure time in seawater [25]

Depending on the exposure time, the phases of this model can be summarized as follows:

Phase 0: This phase is a very short time period when the seawater initially accesses the fresh metal surface. The corrosion is under kinetic control and its rate is determined by local chemical reaction without limitations due to external diffusion or oxygen concentration.

Phase 1: This phase is the period during which the process is under oxygen concentration control, in which the corrosion rate is governed by the rate of arrival of oxygen through the water and the corrosion product layer to the corroding surface. While the entire diffusion process is not perfectly linear, in practical application the corrosion process can be considered as quasi-linear with a constant corrosion rate,  $r_0$ .

Phase 2: The corrosion rate in this phase is controlled by the oxygen diffusion through the increasing barrier of corrosion product. As a result, the corrosion process is non-linear. With the buildup of corrosion product, the amount of oxygen that get to the corroding surface will decline and eventually an anaerobic condition will exist between the corrosion product layer and the metal surface. The transition point is AP in Figure 2-1, which can be characterized using a time  $t_a$  and a total corrosion loss  $c_a$ .

Phase 3: During Phase 3 (anaerobic conditions), sulfate-reducing bacteria (SRB) begin to grow rapidly under the corrosion product layer. The corrosion process after the transition point is governed by the SRB and the high initial corrosion rate is due to their rapid growth.

Phase 4: Due to limited data available and the lack of understanding of microbiology of the SRB, this phase has been assumed to be linear in time.

A detail mathematical and theoretical model has been established by R. Melchers and R. Jeffrey [30]. They calibrated their model with existing long time corrosion data of carbon steel in marine environments. They showed that most of the parameters of the model depended on the temperature of the seawater. For example, at 20 °C, the corrosion rate during phase 1,  $r_0 \sim 0.22$  mm/yr, and the transition time  $t_{\alpha} \sim 1$  yr. Specific to the experiments performed in this research in NaCl solution, the typical experiment time is less than 12 hours, so the corrosion process is within phase 0 and phase 1.

The composition and protectiveness of the corrosion product layer formed during the corrosion process is critical to the overall corrosion rate. The corrosion layer formed in chloride containing environments is composed of  $\alpha$ -FeOOH (goethite),  $\beta$ -FeOOH (akaganeite),  $\gamma$ -FeOOH (lepidocrocite) and Fe<sub>3</sub>O<sub>4</sub> (magnetite) [12][13]. Among all compositions, researchers found that  $\beta$ -FeOOH is the key corrosion product that determined the corrosion rate of the metal surface [33]–[35].

Y. Ma et al. [33] studied the atmospheric corrosion of carbon steel in high chloride environment. The carbon steel samples were exposed at 25 m from the sea line in Wanning area, China, and subjected to a natural wet-dry cycle caused by the sea tides. The wetness time at the site was on average 6736 hour/year. In their two-year study, they found that the corrosion rate sharply increased in the first six months and then gradually reduced for longer exposure times. They concluded the  $\beta$ -FeOOH layer, which was porous and transformed from initially-formed  $\gamma$ -FeOOH within the first six months, was accounted for the acceleration of the corrosion rate. And as the  $\beta$ -FeOOH transformed into  $\gamma$ -Fe<sub>2</sub>O<sub>3</sub> in the dry process and formed a more protective layer at longer exposure times, the corrosion rate decreased.

Nishimura et al. [34] investigated the effect of chloride ion on the transformation of rust formed on carbon steel during wet/dry exposure. They observed that the content of  $\beta$ -FeOOH increased with concentration of chloride.  $\beta$ -FeOOH formed after the intermediate formation of green rust I (GRI), a type of rust consisting of layered Fe<sup>2+</sup> and Fe<sup>3+</sup> hydroxides [36], in the dry process as Cl was released into the environment. And in the wet process, due to the reduction of  $\beta$ -FeOOH to Fe<sub>3</sub>O<sub>4</sub>, the corrosion of the steel was accelerated.

Y. Zou et al. [35] studied the corrosion of mild steel for long-term immersion in seawater [35].

Figure 2-2 shows the morphology of the corrosion product layer at different times during the immersion in seawater. The rust was loose during the initial immersion period and a double-layer structure of the corrosion layer started to form after six weeks. By IR spectra, Y. Zou et al. confirmed that, compared to the outer layer, the inner layer contained more of the  $\beta$ -FeOOH phase.  $\beta$ -FeOOH has higher electrochemical activity and its reduction to  $\text{Fe}_3\text{O}_4$  in the wet process can accelerate corrosion. Y. Zou et al. also pointed out that the reduction of  $\beta$ -FeOOH could be accelerated when using electrochemical method to measure corrosion rate, which could cause erroneous results.

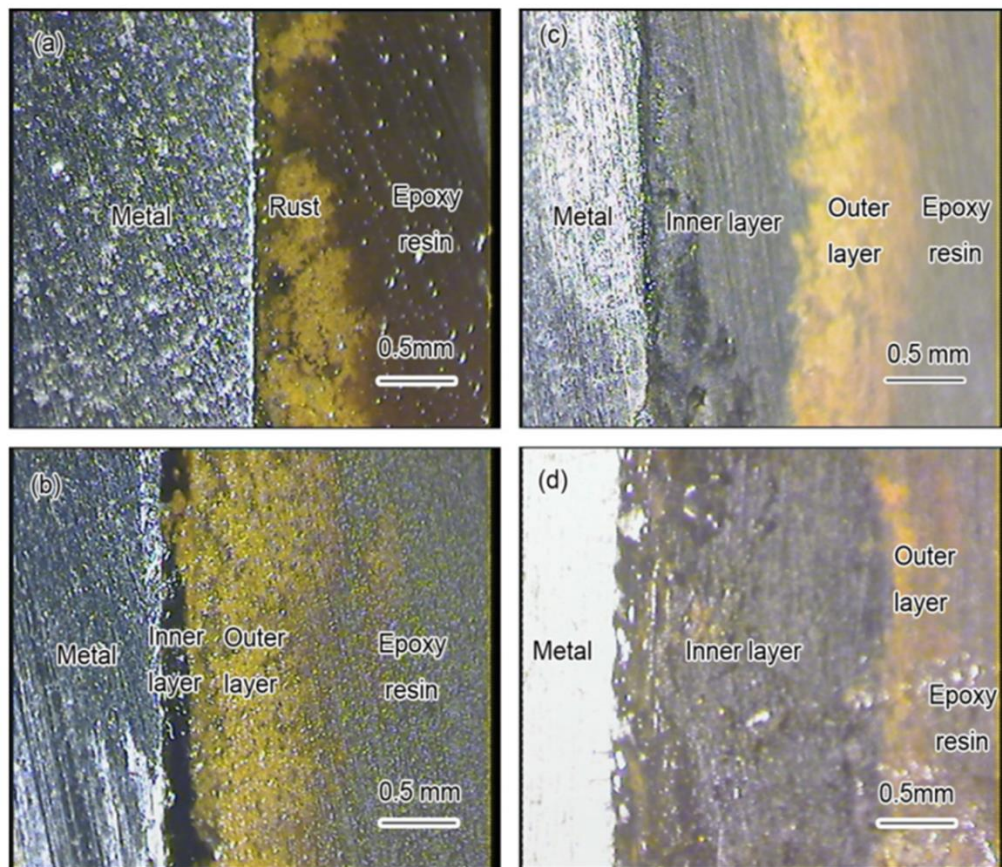


Figure 2-2: Morphologies of cross-sections of carbon steel samples immersed in seawater. (a) after 6 weeks. (b) after 11 weeks. (c) after 18 weeks. (d) after 48 weeks [35].

### 2.1.2 Corrosion of Carbon Steel in $\text{CO}_2$ Environment

$\text{CO}_2$ -accelerated corrosion is by far the most prevalent form of attack encountered in upstream operations in oil and gas industry, which includes the exploration and production of crude oil and

natural gas. Corrosion failures, the majority of which are related to carbon dioxide (CO<sub>2</sub>) corrosion, have been reported to account for approximately 25% of all safety incidents in the oil and gas industry [22].

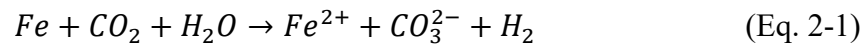
Recent studies clearly have demonstrated that, despite extensive research over the past four decades, a mechanistic understanding of CO<sub>2</sub> corrosion remains incomplete.

#### 2.1.2.1 Thermodynamics of CO<sub>2</sub> Corrosion

Dry CO<sub>2</sub> gas by itself is not corrosive at the temperatures encountered within oil and gas production. However, its presence in contact with an aqueous phase can result in very high corrosion rates where the mode of attack is often localized. An example of CO<sub>2</sub> corrosion of pipeline is shown in Figure 2-3 [37].

S. Netic has provided a thorough review of uniform CO<sub>2</sub> corrosion in aqueous solutions in a chapter of the Uhlig's corrosion handbook [38]. The discussion below is based on this review, augmented by results from more current literature.

In general, the aqueous corrosion of carbon steel containing CO<sub>2</sub> proceeds in accordance with the overall reaction:



To give a detailed analysis of the overall reaction, one must first consider the homogenous aqueous chemistry (bulk chemistry) which provides the concentration of CO<sub>2</sub> and related ions in bulk the solution, and then examine the reduction/oxidation processes occurring at the steel surface which determines the corrosion rate.



Figure 2-3: A photo of a corroded pipe showing the specific morphology of CO<sub>2</sub> corrosion [37].

The homogenous reactions in CO<sub>2</sub>-saturated aqueous solutions and related equilibrium equations are summarized in [38], and is given in Table 2-1 and Table 2-2.

Table 2-1: Key chemical reactions occurring in aqueous CO<sub>2</sub> solution and corresponding equilibrium expressions [38]

Name	Reaction	Equilibrium Expression
Dissolution of carbon dioxide	$CO_2(g) \xrightleftharpoons{K_{sol}} CO_2$	$K_{sol} = \frac{c_{CO_2}}{p_{CO_2}}$
Carbon dioxide hydration	$CO_2 + H_2O \xrightleftharpoons{K_{hyd}} H_2CO_3$	$K_{hyd} = \frac{c_{H_2CO_3}}{c_{H_2O}c_{CO_2}}$
Carbon acid dissociation	$H_2CO_3 \xrightleftharpoons{K_{ca}} H^+ + HCO_3^-$	$K_{ca} = \frac{c_{H^+}c_{HCO_3^-}}{c_{H_2CO_3}}$
Bicarbonate anion dissociation	$HCO_3^- \xrightleftharpoons{K_{bi}} H^+ + CO_3^{2-}$	$K_{bi} = \frac{c_{H^+}c_{CO_3^{2-}}}{c_{HCO_3^-}}$
Water dissociation	$H_2O \xrightleftharpoons{K_{wa}} H^+ + OH^-$	$K_{wa} = \frac{c_{H^+}c_{OH^-}}{c_{H_2O}}$

Table 2-2: Equilibrium constants for homogeneous reactions listed in Literature Review as a function of temperature, pressure and ionic strength ( $T_f$  is temperature in degrees Fahrenheit,  $T_k$  is absolute temperature in Kelvin,  $I$  is ionic strength in molar, and  $p$  is pressure in psi.) [38]

Name	Equilibrium Constant
Dissolution of carbon dioxide	$K_{sol} = 14.463 \times 10^{-(2.27+5.65 \times 10^{-3} \times T_f - 8.06 \times 10^{-6} \times T_f^2 + 0.075 \times I)}$
Carbon dioxide hydration	$K_{hyd} = 2.58 \times 10^{-3}$
Carbon acid dissociation	$K_{ca} = 387.6 \times 10^{-(6.41-1.594 \times 10^{-3} \times T_f + 8.52 \times 10^{-6} \times T_f^2 - 3.07 \times 10^{-5} \times p - 0.4772 \times I^{0.5} + 0.118 \times I)}$
Bicarbonate anion dissociation	$K_{bi} = 10^{-(10.61-4.97 \times 10^{-3} \times T_f + 1.331 \times 10^{-5} \times T_f^2 - 2.624 \times 10^{-5} \times p - 1.166 \times I^{0.5} + 0.3466 \times I)}$
Water dissociation	$K_{wa} = 10^{-(29.3868-0.0737549 \times T_k + 7.47881 \times 10^{-5} \times T_k^2)}$

One can calculate the carbonic species concentrations dissolved in a CO<sub>2</sub>-saturated aqueous solution using the equations listed in Table 2-1 and Table 2-2. Figure 2-4 shows the species concentrations at 25 °C and 120 °C, respectively, as a function of pH.

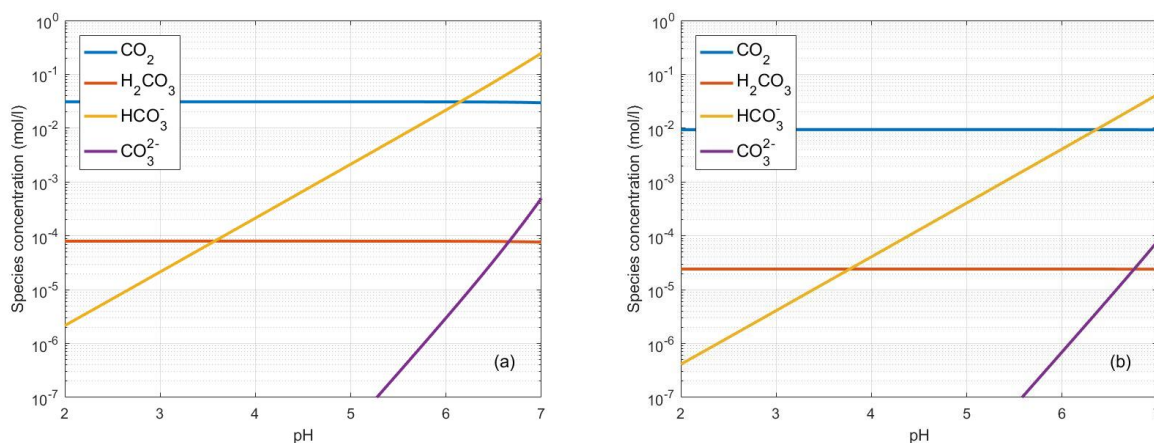
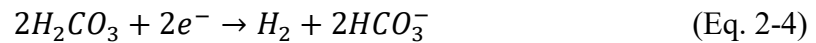


Figure 2-4: Calculated concentrations of carbonic species as functions of pH for a CO<sub>2</sub>-saturated aqueous solution at  $p_{CO_2}=1\text{bar}$ , 1 wt.% NaCl and (a) at 25 °C, (b) at 120°C.

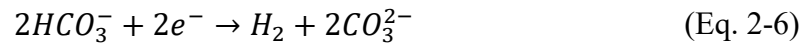
Heterogeneous reactions, anodic and cathodic, at the steel surface are the most important reactions which directly control the corrosion rate of the steel. The anodic reaction on low-carbon steel in CO<sub>2</sub>-saturated aqueous solution is:



The cathodic reactions in near-neutral solution ( $4 < \text{pH} < 6$ ) are the reduction of dissociated hydrogen ions and hydrogen evolution by reduction of carbonic acid:



There are two other possible cathodic reactions in this case, which are the cathodic hydrogen evolution by reduction of water and cathodic hydrogen evolution by reduction of bicarbonate ion:



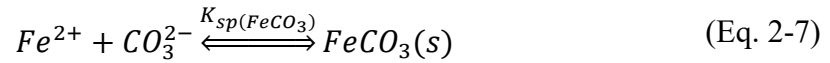
However, Nesic et al. [39] by analyzing the experimental data showed that the direct reduction water pathway for hydrogen evolution is comparatively small compared to the reduction of carbonic acid and thus can be neglected. Also, Nesic [38] concluded that the kinetics of reduction of bicarbonate ion is slower than the reduction of carbonic acid, and in the pH range of 4 to 6, the concentrations of bicarbonate ion and carbonic ion are comparable which makes the reduction of carbonic ion dominate.

It is worth noting that for the two main cathodic reactions in near-neutral pH conditions, the reduction of hydrogen ion is strongly pH dependent, while the reduction of carbonic acid is pH

independent and is a function of  $H_2CO_3$  concentration. The concentration of  $H_2CO_3$  is a linear function of  $CO_2$  partial pressure. Nesic [38] pointed out that the reduction of carbonic acid provides an additional pathway for hydrogen reduction which significantly increased the corrosion rate of steel compare to steel in strong acid at the same pH value.

### 2.1.2.2 Ferrous Carbonate Precipitation

Under certain conditions, a ferrous carbonate ( $Fe_2CO_3$ ) layer can form at the surface and reduce the corrosion rate of the steel. The reaction for formation of ferrous carbonate is [40]:



$K_{sp}$  is the solubility product constant and is a function of temperature and ionic strength:

$$K_{sp(FeCO_3)} = 10^{(-59.35 - 0.04138 \times T_k - 2.1963/T_k + 24.5724 \times \log_{10} T_k + 2.518 \times I^{0.5} - 0.657 \times I)} \quad (\text{Eq. 2-8})$$

Due to corrosion, the ferrous ion concentration is usually high, especially at the steel surface. When the product of concentration of  $Fe^{2+}$  and  $CO_3^{2-}$  exceed the solubility limit, ferrous carbonate will precipitate from the solution onto the steel surface. The non-equilibrium situation is termed supersaturation, defined as [38]:

$$SS_{(FeCO_3)} = \frac{C_{Fe^{2+}} C_{CO_3^{2-}}}{K_{sp(FeCO_3)}} \quad (\text{Eq. 2-9})$$

Figure 2-5 shows the  $K_{sp}$  as a function of temperature. As temperature increases,  $K_{sp}$  decreases steadily which favors the precipitation process at higher temperatures. Figure 2-6 shows supersaturation factor as a function of temperature and pH given other factors fixed. From Figure 2-6 (a) we can see that the supersaturation factor increases as the temperature increases. What may be surprising is the dramatic effect of pH on supersaturation as shown in Figure 2-6 (b) (notice that the y axis is on a log scale). This is because the concentration of carbonic anion is a strong function of pH (see Figure 2-4 for reference). From Figure 2-6 we can directly see that the iron carbonate scale formation is favored at near neutral or high pH but not likely at low pH.

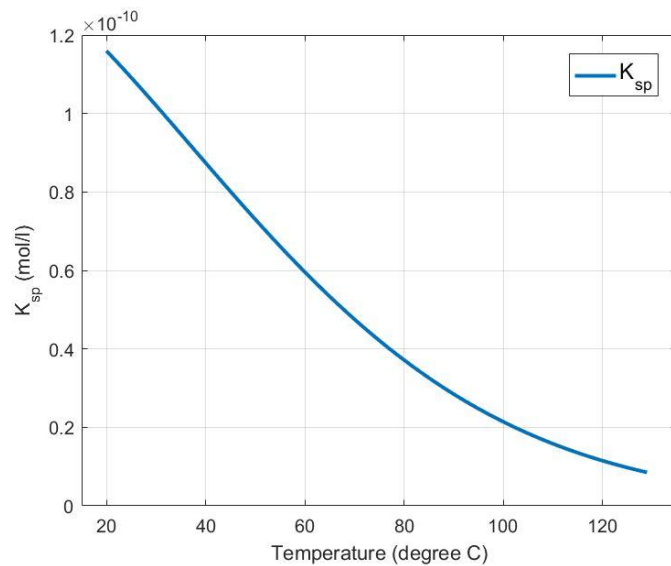


Figure 2-5: Calculated solubility constant  $K_{sp}$  as a function of temperature.

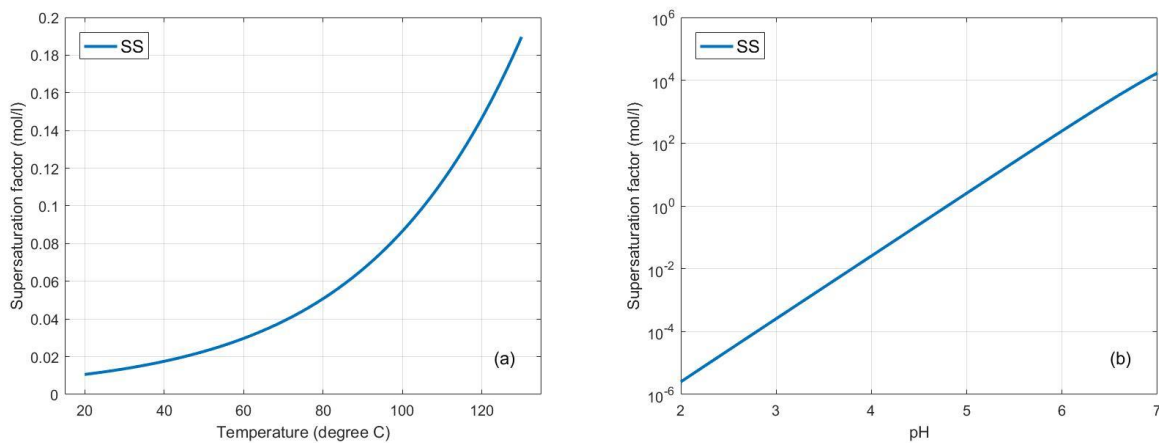


Figure 2-6: In a  $\text{CO}_2$ -saturated aqueous solution at  $p_{\text{CO}_2}=1\text{bar}$ , 1 wt.% NaCl,  $c_{\text{Fe}^{2+}}=0.01\text{ mol/l}$ , calculated supersaturation factor as a function of (a) Temperature, at equilibrium pH, (b) pH, at  $25^\circ\text{C}$ .

The rate of precipitation on the steel surface can be written as a function of supersaturation [41]:

$$R_{\text{FeCO}_3} = k_r \frac{A}{V} K_{sp} (SS_{(\text{FeCO}_3)} - 1) \quad (\text{Eq. 2-10})$$

where  $k_r$  is the kinetic constant,  $A/V$  is the ratio of exposed sample surface area to bulk solution volume. Nesic [38] concluded that rapid formation of  $\text{FeCO}_3$  layers only occurs at higher temperatures ( $T > 50^\circ\text{C}$ ) and at high pH ( $\text{pH} > 5$ ).

Nesic et al. [42] has also constructed the full thermodynamic Pourbaix diagram for  $\text{Fe-CO}_2\text{-H}_2\text{O}$  at different temperatures. Two of the Pourbaix diagrams (at  $25^\circ\text{C}$  and  $120^\circ\text{C}$ ) are shown in Figure 2-7. From the constructed Pourbaix diagrams and actual experimental results, they concluded that  $\text{FeCO}_3$  was the dominant corrosion product from  $80\text{-}150^\circ\text{C}$  at near-neutral pH while  $\text{Fe}_3\text{O}_4$  became primary corrosion product at temperature higher than  $200^\circ\text{C}$ .

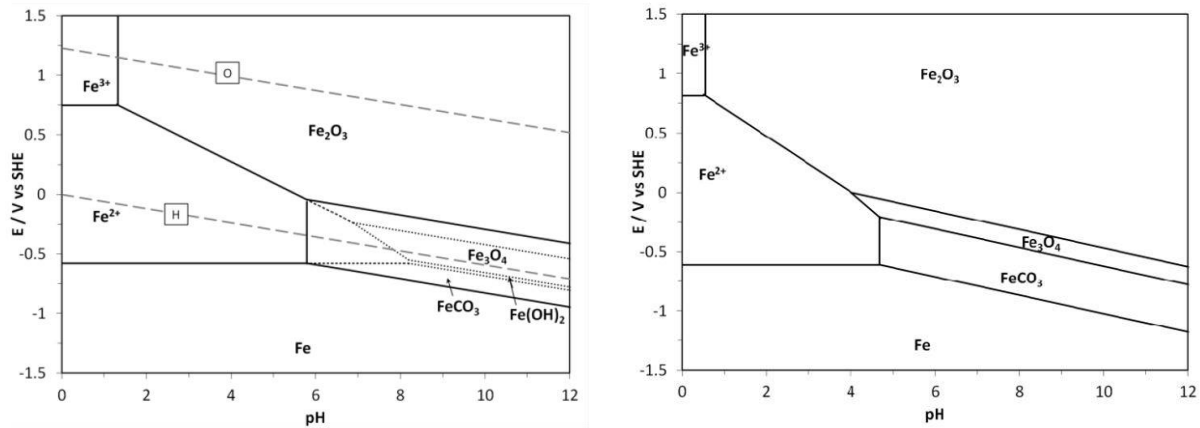


Figure 2-7: Pourbaix diagrams for  $\text{Fe-CO}_2\text{-H}_2\text{O}$  systems,  $c_{\text{Fe}^{2+}}=10$  ppm,  $c_{\text{Fe}^{3+}}=10$  ppm,  $p_{\text{H}_2}=1\text{bar}$ ,  $p_{\text{O}_2}=1\text{bar}$ . Left: at  $T=25^\circ\text{C}$ , Right: at  $T=120^\circ\text{C}$  [42].

### 2.1.2.3 $\text{CO}_2$ Corrosion Rate

The corrosion rate of mild steel in an aqueous  $\text{CO}_2$ -containing environment is affected by many factors, e.g. pH, temperature,  $\text{CO}_2$  pressure [38].

The pH is probably the most influential factor affecting acidic corrosion of steel in a  $\text{CO}_2$ -containing aqueous environment. At lower pH, there are more free  $\text{H}^+$  ions in the solution, thus facilitating the cathodic reaction of hydrogen ion reduction (Eq. 2-3). Figure 2-8 shows the corrosion rates as a function of pH at  $20^\circ\text{C}$  and  $80^\circ\text{C}$ . The effect of pH is amplified at higher temperature because high pH promotes the formation of  $\text{FeCO}_3$  scale (see Figure 2-6), and the kinetics of this process is temperature dependent [38].

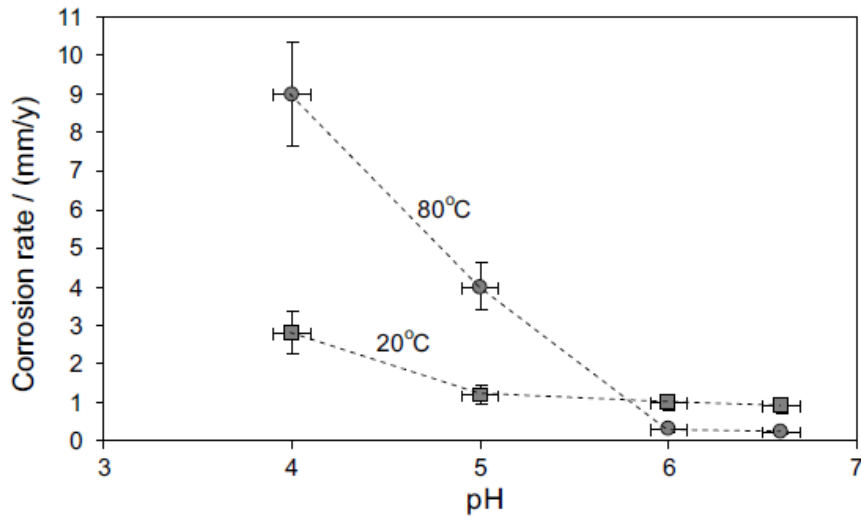


Figure 2-8: CO<sub>2</sub> corrosion rate of a carbon steel at different pH at 20°C ( $p_{CO_2}=1$  bar) and 80°C ( $p_{CO_2}=0.5$  bar), in a 3 wt.% NaCl solution [38].

The effect of CO<sub>2</sub> partial pressure is mainly through the cathodic reaction (Eq. 2-4). Higher  $p_{CO_2}$  increases the concentration of H<sub>2</sub>CO<sub>3</sub> in the solution and accelerates the cathodic reaction and the corrosion rate.

Increased temperature accelerates all the electrochemical processes in corrosion. At low pH, when the FeCO<sub>3</sub> layers do not form, the corrosion rate steadily increases with temperature. At higher pH, however, the corrosion rate first increases with temperature to a point when the protective corrosion layer begins to form and then the corrosion rate decreases with temperature, as shown in Figure 2-9.

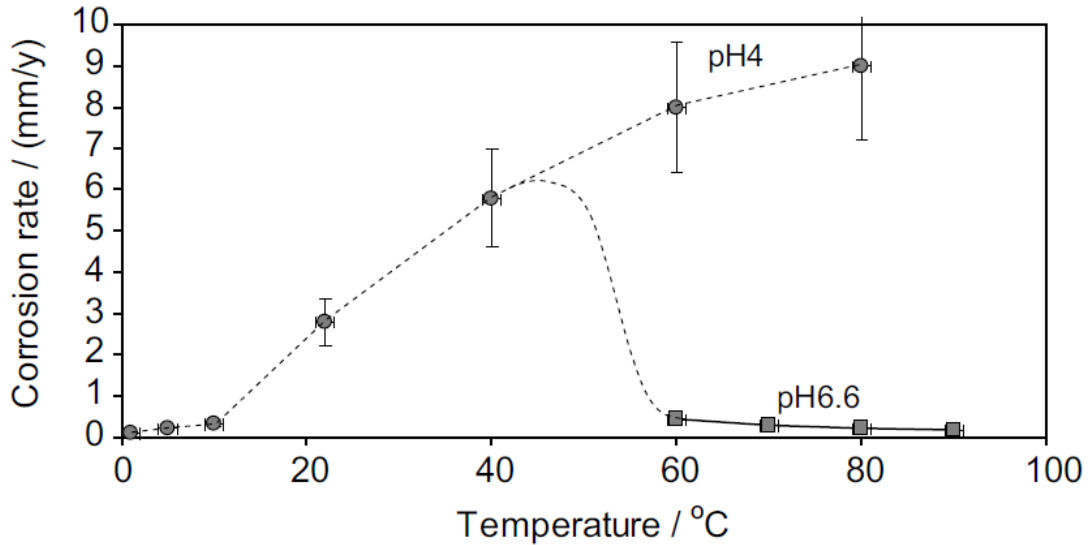


Figure 2-9: CO<sub>2</sub> corrosion rate of a carbon steel at different temperatures at pH=4 and pH=6.6, in 1 wt.% NaCl solution, at equilibrium  $p_{CO_2}$  with pH and temperature [38].

The CO<sub>2</sub> corrosion of carbon steel at elevated temperature (above 100°C) was also studied by Netic et al. [43]. In this paper, Netic et al. discussed the corrosion scale formation and corrosion rate in under different temperatures and pH. The condition of our test environment (pH=6.0, T=120°C), to be discussed further later, was also discussed in this paper. From Figure 2-10, we can see that at high temperature, although the corrosion rate is high initially, it drops dramatically within the first few hours of exposure as the corrosion layer forms. Figure 2-11 shows the morphology of corrosion layer on the corroded surface. Netic et al. concluded that the corrosion layer is composed of FeCO<sub>3</sub> by XRD analysis, while trace amounts of Fe<sub>3</sub>O<sub>4</sub> were also found at higher temperature (150°C and 200°C).

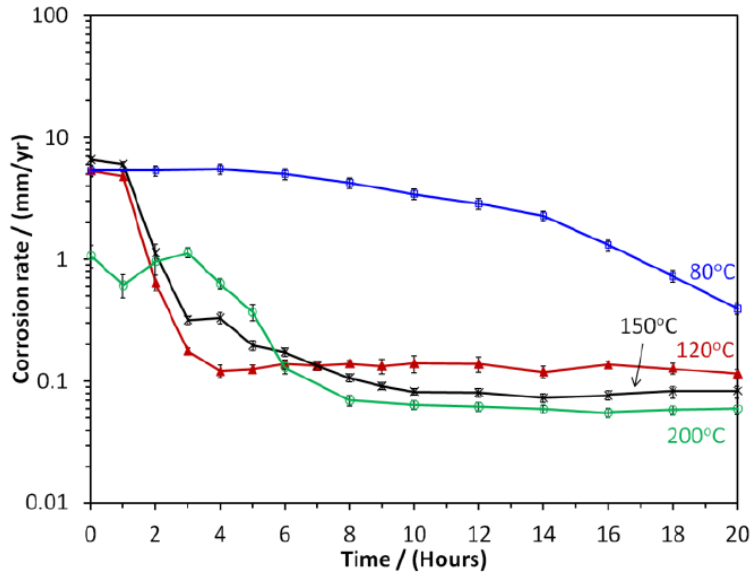


Figure 2-10: Corrosion rate as a function of time at different temperatures, at pH=6,  $[\text{CO}_2]_{\text{aq}}=0.030\text{M}$  [43].

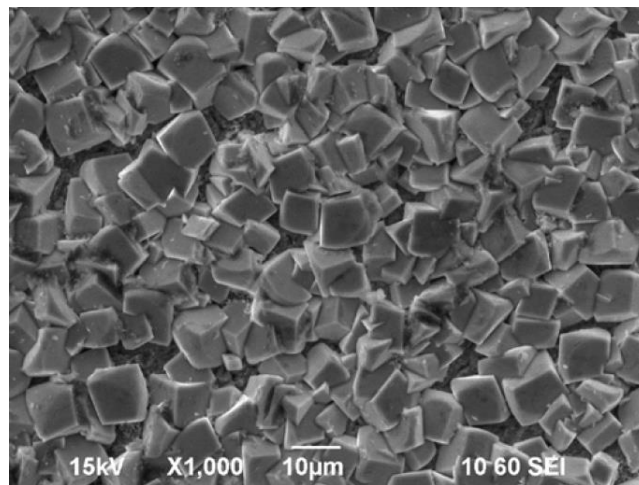


Figure 2-11: SEM image of the surface of a steel sample after 20 hours test at  $T=120^\circ\text{C}$ , pH=6,  $[\text{CO}_2]_{\text{aq}}=0.030\text{M}$  [43]. The  $\text{FeCO}_3$  scales thoroughly covered the steel surface.

#### 2.1.2.4 Localized Corrosion in $\text{CO}_2$ Environment

Compared to uniform corrosion, knowledge about localized corrosion in  $\text{CO}_2$ -containing aqueous environments is more limited. The term localized corrosion is broadly defined for carbon steel in  $\text{CO}_2$ -containing aqueous environments because it only identifies that corrosion occurs in certain locations but not everywhere. It can occur on a rather large scale, on the order of centimeters

or more, as shown in Figure 2-3. This specific morphology with large, flat, receded areas compared to surrounding surface is termed as “mesa attack”. The other type, which occurs on much smaller scale, on the order of microns or millimeters, is termed pitting. Pitting may also be the incipient sites for mesa attack [22].

Whether localized corrosion or general corrosion will take place in CO<sub>2</sub>-containing aqueous environments is determined by the sensitive balance between the formation and destruction of a protective film on the metal surface [22]. In CO<sub>2</sub> aqueous corrosion, FeCO<sub>3</sub> is the most important film that can grow on the carbon steel surface. Instability and partial breakdown of the FeCO<sub>3</sub> layer can induced pitting in the base metal. As discussed in the last section, the FeCO<sub>3</sub> layer formation is dependent on the thermodynamics and kinetics of FeCO<sub>3</sub> precipitation. Supersaturation is the key to FeCO<sub>3</sub> precipitation and growth, which is a function of a set of environmental parameters, e.g. temperature, pH, etc.

Nesic [44][45] attempted to initiate localized corrosion by controlling the supersaturation of the bulk solution. The procedure included three steps. The first step was to form a compact FeCO<sub>3</sub> corrosion layer by adding ferrous chloride to the solution and achieving a supersaturation factor of 200 for FeCO<sub>3</sub>. After the corrosion layer was formed, the second step was to partially remove the corrosion layer. The supersaturation factor was adjusted to 0.04 by lowering the pH. The last step was called localized corrosion when the pH was adjusted again in order to make the supersaturation fall into the “grey zone” of 0.5 to 2.0 [44]. Localized corrosion was observed after the three-step process and is shown in Figure 2-12.

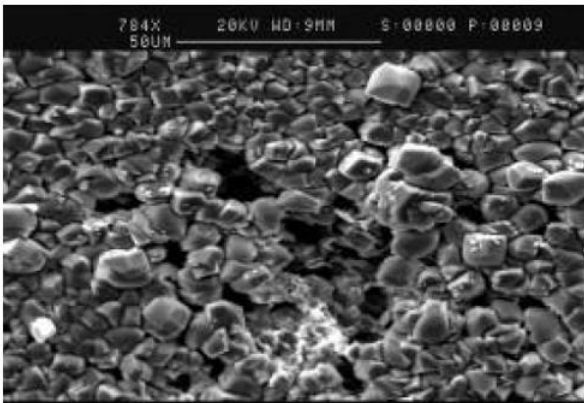


Figure 2-12: Partial removal of the  $\text{FeCO}_3$  corrosion layer and observed localized corrosion. Left: SEM image. Right: Infinite focus microscopy tomography, red cycles highlight spots of localized corrosion [44].

While a change of the bulk solution chemistry can destabilize the  $\text{FeCO}_3$  layer and generate localized corrosion, the flow of the fluid also has a significant impact on localized corrosion, through either mechanical breakdown of the corrosion layer, or removal of the reactant on the surface to achieve low supersaturation [46]–[48]. Nyborg [46] observed initiation of pitting and mesa type attack in a flow loop test with flow velocity of 7m/s by video recording the sample surface during  $\text{CO}_2$  corrosion. He concluded that the initiation of localized corrosion was facilitated by the partial removal of the corrosion layer by mechanical forces of the turbulent flow. Dugstad [47] in his experiments observed mesa type attack occurred at  $80^\circ\text{C}$  with a flow velocity of 4.1 and 6.8 m/s but not 2.5 m/s. He also found that when given a stagnant condition of a few days, the steel formed a protective layer and the corrosion rate decreased significantly. Schmitt [48] estimated the scale adherent strengths to be on the order of 1 MPa to 30 MPa, and concluded that the wall shear stress under general flow condition, which was at most on the order of 0.1 MPa, was small compared to the critical adherent strengths of the iron carbonate film. He suggested that the intrinsic stresses from scale growth must be considered for scale rupture. However, wall shear stresses could contribute to exceedance of the critical stresses. To summarize, while the mechanical stresses caused by the fluid flow are a consideration, the more important effect of flow velocity is likely its influence on the local chemistry. High flow velocity prevents the growth of the  $\text{FeCO}_3$  corrosion layer and if that happens in a restricted area, facilitates localized corrosion.

In addition to the iron carbonate film, an iron carbide layer may also play an important role in forming a protective film for some conditions [49]. For carbon steels with relatively high carbon content (e.g. above 0.1% [50]), an iron carbide (cementite) network is left behind on the metal surface during the corrosion process because of the preferential dissolution of iron/ferrite. Iron carbide which is conductive and electrochemically more noble than ferrite, serves as a cathode in the corrosion process. It may form a galvanic cell with the ferrite phase and further accelerate the corrosion process and even pitting [49][51]. However, in an environment where iron carbonate reaches saturation, the iron carbide network can anchor the iron carbonate precipitate and help

form a more protective film [52]–[54]. Crolet, et al. [49] summarized the different morphologies for protective and nonprotective corrosion layers, which are shown in Figure 2-13. Crolet, et al. concluded that when a porous  $\text{Fe}_3\text{C}$  layer was in contact with the metal surface, the corrosion layer was not protective no matter how thick of the  $\text{Fe}_3\text{C}$  layer was. Conversely, when the mixed layer of  $\text{Fe}_3\text{C}$  and  $\text{FeCO}_3$  was in contact with the metal surface, the corrosion layer was protective.

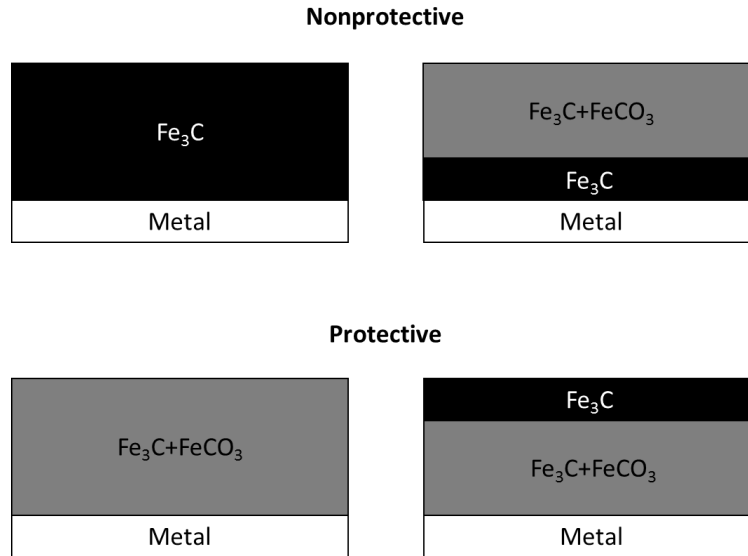


Figure 2-13: Different morphologies observed for protective and nonprotective corrosion layers (after Crolet, et al. [49])

In summary, the mechanism of pitting corrosion of carbon steel in  $\text{CO}_2$  environment can be described by the following steps:

- (1) Formation of an iron carbonate corrosion scale (protectiveness depend on environment and characteristics of steel)
- (2) Breakdown of corrosion scale by local chemistry change or mechanical stresses induced by fluid flow.
- (3) Galvanic corrosion between the protective  $\text{FeCO}_3$  scale/the  $\text{Fe}_3\text{C}$  layer and the exposed metal surface. Pits form.
- (4) Mesa type corrosion can result from coalescence of small local attacks.

## 2.2 Corrosion Fatigue of Carbon Steel

### 2.2.1 Fatigue of Metals

Fatigue is a term used to describe degradation of materials due to initiation and propagation of cracks under cyclic loading. The study of fatigue has been one of the most important topics of materials science for approximately the last 150 years [55].

In the 1860s, Wöhler first introduced the stress-life approach to fatigue [56]. In this approach, fully reversed cyclic loading with mean zero stress is applied to a smooth test specimen and the number of cycles to final fracture is measured. Figure 2-14 shows a graphic description of the test and its parameters. The stress amplitude  $\sigma_a$  is then plotted against the number of fatigue cycle to failure,  $N_f$ . This type of curve is called an S-N curve or Wöhler diagram. In general, an S-N curve can be divided into three regions. In region I, from 1/4 cycle to about  $10^4$ - $10^5$  cycles, the material is stressed in the vicinity or beyond the yield stress. The material deforms plastically and the plastic strain dominates the fatigue life. Region I is often referred to low cycle fatigue. In region II, the material behaves elastically, at least at the macroscopic level. The stress amplitude is lower than the yield stress of the material. However, some degree of irreversible microstructure changes or local microplasticity occurs within the material and this results in crack initiation, as will be discussed later in this section. This region is often referred to as the high cycle fatigue. Region II goes up to  $10^6$  or  $10^7$  cycles where the S-N region begins to flatten at a stress amplitude termed the “fatigue limit”. Region III is loosely defined as the region for which failure does not occur either for a specified number of cycles or at all. For some materials, steels and titanium in air as examples, failure does not occur at all [55]. In this case the “fatigue limit” is termed the endurance limit. For other materials, such as aluminum alloys, there is no endurance limit in air and the fatigue limit is defined as no failure for a fixed number of cycles. When a corrosive exists there is essentially no practical endurance limit so the fatigue limit is defined as above. The S-N curve is usually fitted using the Basquin relation [57],

$$\sigma_a = \frac{\Delta\sigma}{2} = \sigma_f'(2N_f)^b \quad (\text{Eq. 2-11})$$

where  $\sigma_f'$  is the fatigue strength coefficient, and b is called fatigue strength exponent or Basquin exponent.

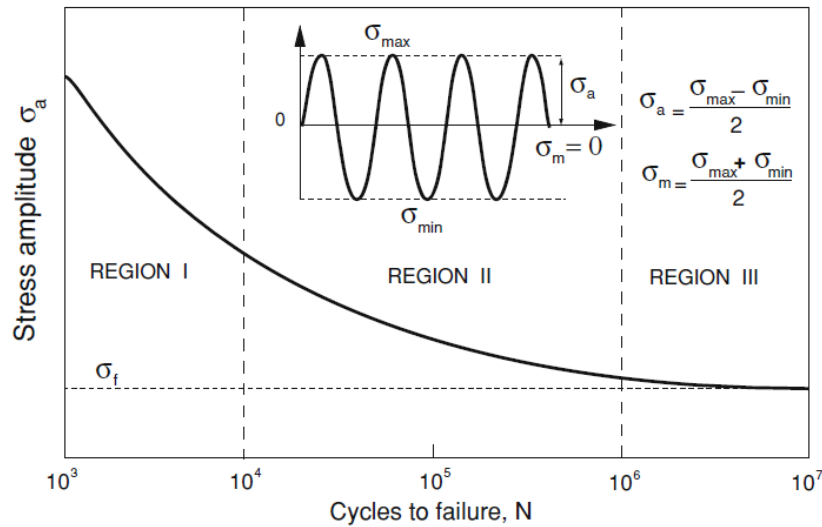


Figure 2-14: A schematic of typical S-N curve showing the stress amplitude versus cycles to failure [58].

The S-N curve pertains to the total fatigue life of a nominally smooth-surfaced, 'defect-free' material [55], which can be divided into two main stages. The first stage is the initiation stage, where micro cracks nucleate from the defect free material. The second stage is the propagation stage, where the crack propagates and leads to the final failure. The percentage of life occupied by the initiation stage over the total fatigue life may vary from small number approaching 0%, for specimens containing sharp stress concentrations or with rough surfaces, to as high as 80% for very carefully polished, high purity materials [55].

The S-N curve is a powerful tool for engineering design of structural components against fatigue loading. As the study of fatigue advances, researchers have focused more on the underlying mechanism of fatigue. The first insight into the mechanism of metal fatigue was obtained by Sir Ewing and Hemfrey in 1903 [59], when they found that slip bands appeared on the surface of steel under cyclic loading with stresses that were below elastic limit. Their discovery implied that fatigue damage originated from accumulation of irreversible microplasticity during cyclic loading. In 1953, Manson [60] and Coffin [61] showed that the fatigue life depended on the plastic strain amplitude. Their work gave birth to the famous Manson-Coffin relation:

$$\frac{\Delta\epsilon_p}{2} = \epsilon'_f (2N_f)^c \quad (\text{Eq. 2-12})$$

where  $\epsilon'_f$  is the fatigue ductility coefficient, and  $c$  is called fatigue ductility exponent.

One can combine Basquin relation (Eq. 2-11) and Manson-Coffin relation (Eq. 2-12) to take into account both elastic stress and plastic strain:

$$\frac{\Delta\epsilon}{2} = \frac{\Delta\epsilon_e}{2} + \frac{\Delta\epsilon_p}{2} = \frac{\Delta\sigma}{2E} + \frac{\Delta\epsilon_p}{2} \quad (\text{Eq. 2-13})$$

$$\frac{\Delta\epsilon}{2} = \frac{\sigma'_f}{E} (2N_f)^b + \epsilon'_f (2N_f)^c \quad (\text{Eq. 2-14})$$

The first and second terms on the right hand side of (Eq. 2-14) account for the elastic and plastic contributions to the total fatigue life, respectively. The transition life, the number of cycles that divides the total life into elastic and plastic dominant regions, can be calculated by equating the two terms:

$$\frac{\sigma'_f}{E} (2N_f^*)^b = \epsilon'_f (2N_f^*)^c \quad (\text{Eq. 2-15})$$

which gives the transition life:

$$N_f^* = \frac{1}{2} \left( \frac{\epsilon'_f E}{\sigma'_f} \right)^{1/(b-c)} \quad (\text{Eq. 2-16})$$

At short fatigue lives, i.e. when  $N_f \ll N_f^*$ , plastic strain amplitude is more dominant than the elastic strain amplitude at each cycle, and the fatigue life of the material is controlled by ductility. At long fatigue life, i.e. when  $N_f \gg N_f^*$ , elastic strain amplitude is more significant than the plastic strain amplitude at each cycle, and the fatigue life is dominated by the rupture strength [55].

Fatigue is a damage accumulation process which can be divided into two stages: crack initiation and crack propagation [62]. Crack propagation can be further subdivided into three stages:

(1) Stage I crack; (2) Stage II crack and (3) stage III crack (final fracture). A schematic of the three stages of fatigue crack propagation is shown in Figure 2-15.

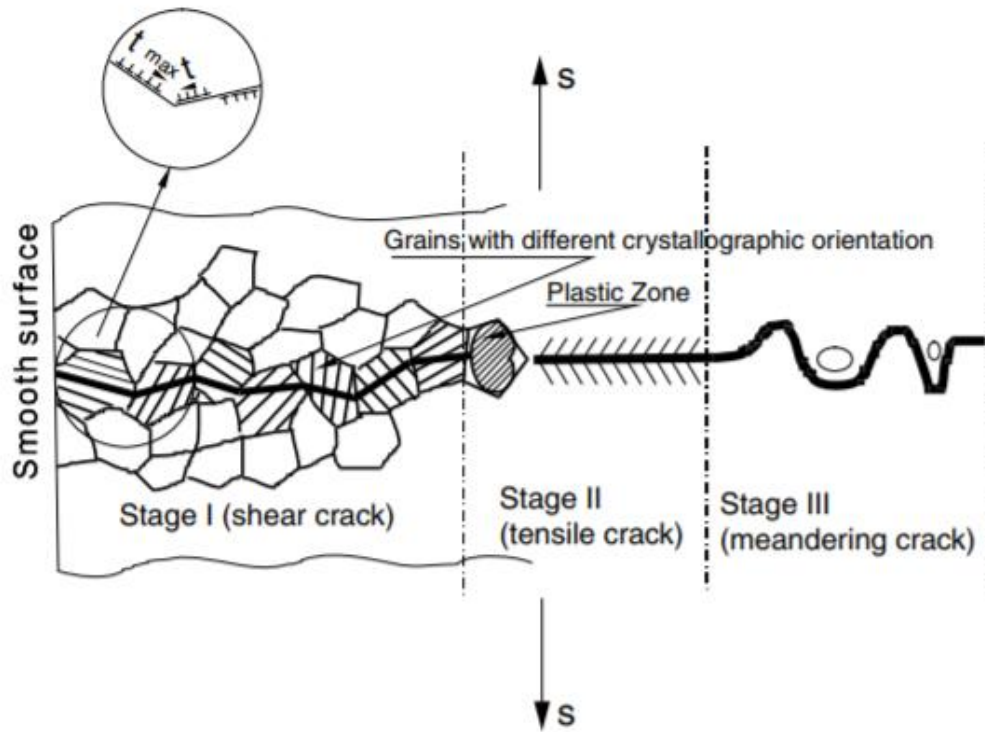


Figure 2-15: Schematic representation of the three fatigue crack growth stages [63].

Stage I crack propagation is driven by microscopic shear stresses. Single slip failure along the primary slip planes with maximum shear stresses induces a serrated fracture morphology [55][63]. A stage I crack may reach a few grains in length and has a zig-zag crack path [63]. As the crack grows longer, the attendant crack growth process involves simultaneous or alternating flow along two slip systems [55]. The duplex slip mechanism results in a planar crack path normal to the far field stresses. When the crack continues and the stress intensity range reaches the unstable crack propagate value, stage III begins. At this stage, crack growth is driven by a tearing mechanism, the crack advances through coalescence of small cracks initiated at inclusions ahead of the crack tip [64]. Cracks grow rapidly in stage III and lead to the final fracture.

Fatigue crack initiation and crack propagation will be discussed in the following sections, with special focus on the crack initiation stage.

## 2.2.2 Fatigue Crack Initiation in Carbon Steel

### 2.2.2.1 Fatigue Crack Initiation in FCC Metals

For pure FCC metals, cracks are often observed to initiate at the interface between persistent slip bands (PSB) and the matrix. Some recent review articles of crack initiation in FCC materials along with other materials can be found in [65]–[67]. For low and medium amplitude of strain cycles, PSBs formed after the saturation of cyclic hardening/softening phase [55]. High resolution TEM analysis shows a ladder structure that is embedded in the matrix containing of vein structure of dislocations (Figure 2-16). A schematic dislocation arrangement of the PSBs and the matrix is shown in Figure 2-17. The matrix contains about 50%, by volume, of vein-like structure which consists dense edge dislocations. On the other hand, the walls with PSBs consists of dislocation dipoles. Dislocation density in veins and walls are estimated to be at the order of  $10^{11}$ - $10^{12}$   $\text{cm}^{-2}$ , which is two to three orders of magnitude higher than the area between the veins and walls [55].

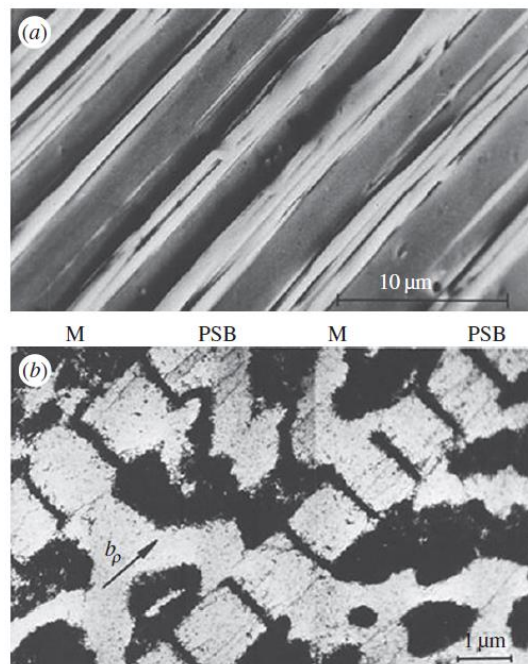


Figure 2-16: (a) A SEM micrograph of appearance of PSBs on the surface of a fatigued polycrystalline copper. (b) A TEM image of dislocation distribution in PSBs and matrix of fatigued copper single crystal [68].

A PSB consists of a large number of slip planes ( $\sim 5000$  in Cu at  $20^\circ\text{C}$ ) which form a flat lamellar structure and span the entire cross section of a grain [55]. A periodic array of dislocation walls divides the PSB lamellae into channels (See Figure 2-17). Under the applied shear stress, edge dislocation loops are proposed to bow out of the walls until the loop intersects the adjacent walls. The bowing-out edge dislocations generate screw dislocation segments across the channels, which are then glide along the channels and deposit new edge dislocation in the walls (Figure 2-17) [69]. Repetition of this process will lead to increase of edge dislocations density and the growth of the wall. Because of the dislocation multiplication mechanism, the walls in PSBs accommodate much higher strain levels than the matrix. The matrix veins accommodate plastic strains only of the order of  $10^{-4}$ , and hence these regions undergo only microyielding. On the other hand, PSBs support high plastic shear strains of the order of 0.01 and support macroyielding [55].

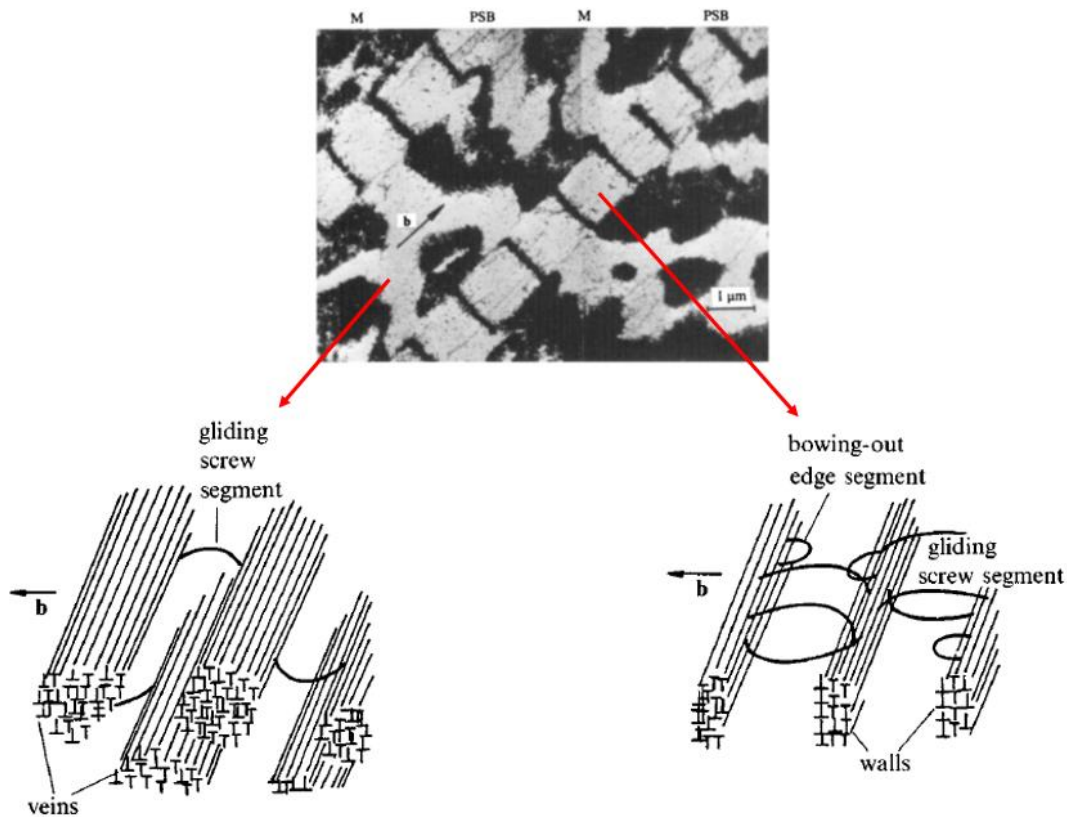


Figure 2-17: Schematics of dislocation structures in the matrix and the PSBs [55].

When PSBs intersect with the surface of the material undergoing fatigue loading, persistent slip markings (PSMs) or persistent bands are observed. PSMs consists of intrusions and extrusions,



The addition of carbon to iron significantly changes the dislocation dynamics of the material. Carbon atoms can lower the thermal activation energy for screw dislocation to overcome the Peierls potential [88][89] and thus reduces the mobility gap between the edge and screw dislocations.

Sommer et al. [90] have studied fatigue crack initiation in both pure iron and carburized iron (up to 74 wt. ppm). They found that at low temperatures in decarburized iron, crack initiation was dominantly intergranular (Figure 2-19). The cracks initiated either from localized glide zones on grain boundaries or grain boundaries between two adjacent grains with incompatible shape changes. At the surface, the cracks grew mainly intergranularly but can transform to transgranular cracks when propagated into the bulk. At higher temperature, surface rumpling developed and cracks initiated from the valley of surface rumpling as shown in Figure 2-20. The crack initiation can be either transgranular or intergranular. The existence of a grain boundary is not necessary in this case (See Figure 2-20).

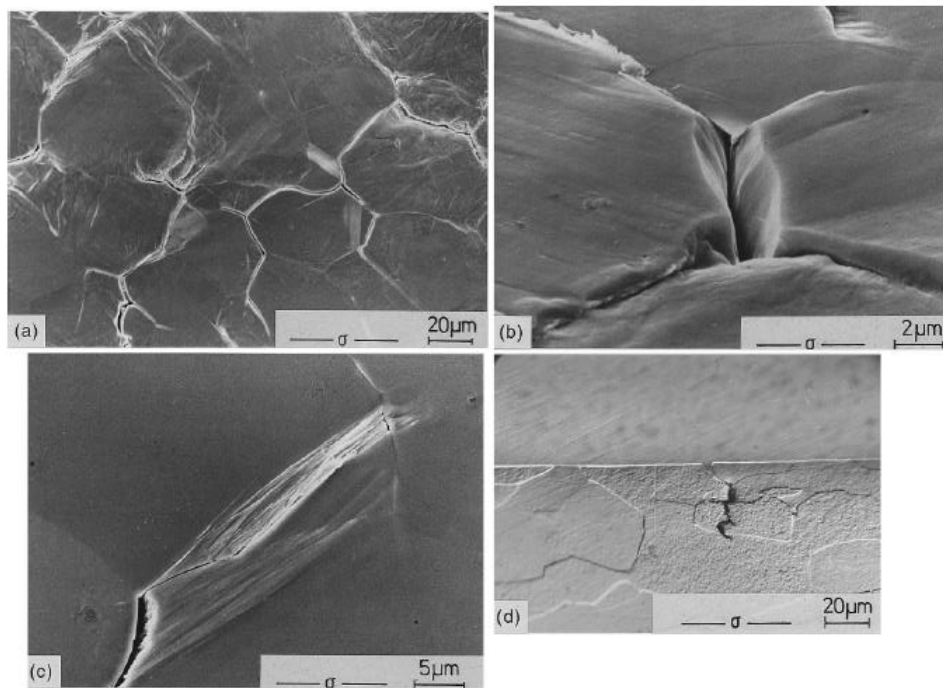


Figure 2-19: Intergranular crack initiation in pure iron at 220K, (a) high intergranular density, (b) intergranular crack caused by shape changes of grains, (c) intergranular crack initiation caused by intrusion of slip against grain boundaries, (d) intergranular crack initiation follow by transgranular crack growth [90]

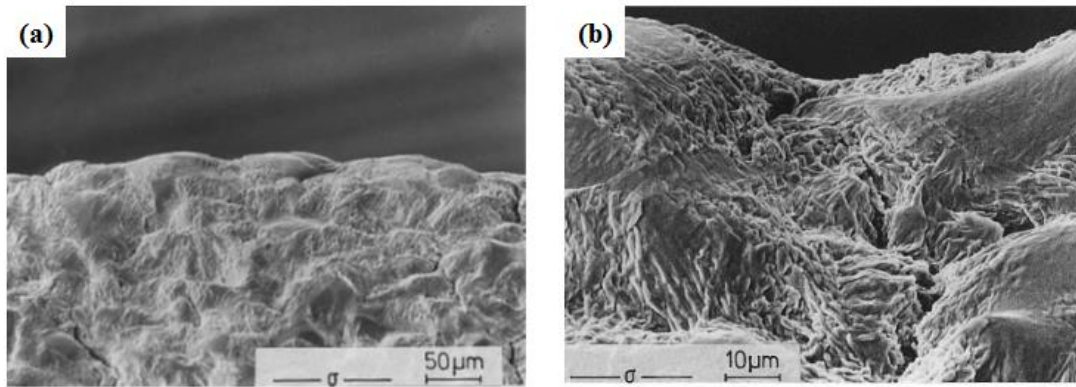


Figure 2-20: (a) Surface rumpling of pure iron, (b) crack initiation from the valley of surface rumpling, at 400K,  $\Delta\epsilon_{pl} = 4 \times 10^{-3}$ ,  $N_f = 1.3 \times 10^4$ . The existence of a grain boundary is not needed for crack initiation in this case [90].

For carburized iron, there was no change of the crack initiation mechanism at low temperature and intergranular cracking initiation was dominant. At high temperature, however, a fundamental change of the crack initiation mechanism was observed. Crack initiated transgranularly from the root of surface intrusions caused by PSBs structure (Figure 2-21). The occurrence of PSBs structure was above 300-350K for carbon content of 13 or 74 wt. ppm.

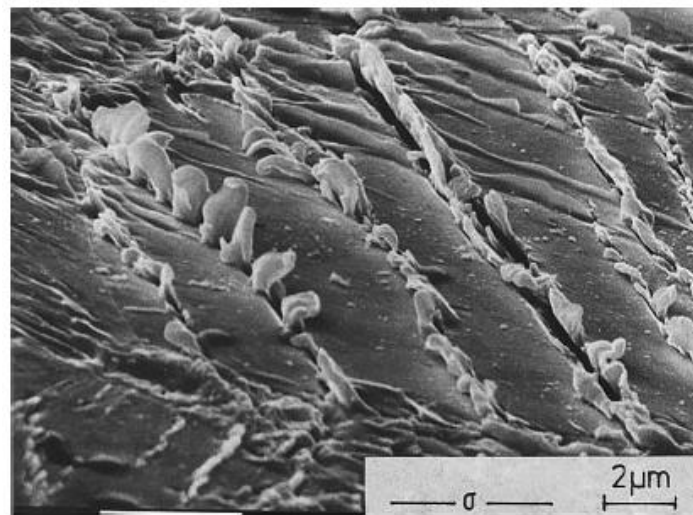


Figure 2-21: Transgranular crack initiation at PSBs in carburized iron, 74 wt. ppm C, at 343K,  $\Delta\epsilon_{pl} = 2 \times 10^{-3}$ ,  $N_f = 8.3 \times 10^4$  [90].

### 2.2.3 Corrosion Fatigue

Corrosion fatigue is a degradation mechanism of materials subject to the combined actions of cyclic loading and corrosion. An aqueous corrosive environment can affect the fatigue process in both the crack initiation and propagation stages in a number of ways [91].

#### 2.2.3.1 Corrosion Effect on Crack Initiation

During fatigue cycles, PSMs form and emerge at the surface. For metals that form a passive film or corrosion layer formed in the aqueous environment, the PSMs may break this layer and expose fresh metal surface to the electrolyte. The transient current or enhancement of surface activity induced by the cyclic strained surface has been observed by Patel [92], Akid [93], Dmytrakh et al. [94]. Localized corrosion at the point where the film rupture occurs thus can become the embryo of a crack. Further corrosion at the same area will result in the growth of the crack.

For example, Patel [92] in his experiments, observed the current transients of low carbon steel samples under tension-compression strain cycles with a strain amplitude of 3%. Current peaks were observed when the strain changed from compression to tension or vice versa. The author concluded that the surface films were destabilized by the emerging slip steps during the strain change, and results in the observed current peaks. By comparing the current transients observed in different environments, he further concluded sulfate ions were more disruptive than chloride and nitrate regarding to the cyclic plastic strain-enhanced dissolution effects (See Figure 2-22).

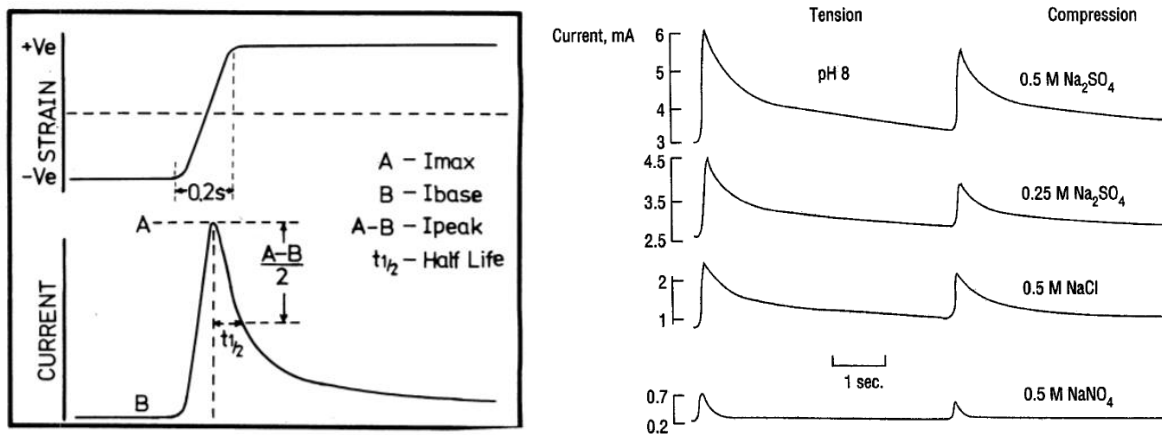


Figure 2-22: Current transients observed in strain-controlled tension–compression tests ( $\Delta\epsilon = 0.03$ ) on a low carbon steel cycled at 0.1 Hz. Left: Schematic of strain wave and corresponding current transient; Right: Typical current transients recorded in different media at a common pH of 8 [92].

In addition to corrosion-PSB interaction, the corrosive environment may induce pits on the surface of the material. Pits can serve as a stress concentrator and provide an aggressive local environment within the pit, which facilitates crack initiation. Cerkit et al. [95] calculated the elastic stress concentration factor for semi-elliptical corrosion pits with different aspect ratios (the ratio of pit depth to the diameter of the pit opening). According to their simulation, the elastic stress concentration factor of a pit under uniaxial tension can be approximately expressed as:

$$K_t = \frac{1 + 6.6(a/2c)}{1 + 2(a/2c)} \quad (\text{Eq. 2-17})$$

where  $a$  is the depth of the pit and  $2c$  is the diameter of the pit opening. For a hemispherical pit, the stress concentration factor is predicted to be 2.15. The location of maximum principle stress moves from the bottom of the pit toward the mouth as the aspect ratio  $a/2c$  increases. The authors also considered the effect of a secondary pit, one that forms within an existing pit, and concluded that the stress enhancement was significant if the aspect ratio of the secondary pit was small.

Zhou and Turnbull [96] have investigated the effect of pits on the fatigue lifetime of turbine blade steel. Fatigue tests in air showed a reduction in fatigue limit with increasing pit depth. The fatigue strength (defined at  $10^7$  cycles) of the specimens with 35, 110 and 250  $\mu\text{m}$  deep pits was 87%, 70% and 52% of the fatigue strength of the smooth specimens (See Figure 2-23). The aspect ratios of 35, 110 and 250  $\mu\text{m}$  deep pits were 0.5, 0.72, and 0.73. From the viewpoint of fatigue limit, and following El Haddad et al. [97], they proposed that the reduction of fatigue strength due to the pit can be estimated by assuming the pit was a small pre-crack, with an additional constant  $a_0$  for small crack correction for the linear elastic fracture mechanics stress intensity (LEFM), i.e.

$$\Delta K = \alpha \Delta \sigma \sqrt{\pi(a + a_0)} \quad (\text{Eq. 2-18})$$

Here  $\Delta K$  is range of the stress intensity factor,  $\Delta\sigma$  is the stress range,  $\alpha$  is a geometrical factor,  $a$  is the depth of the pit.  $a + a_0$  is considered as the effective size of the pit. And at the fatigue limit,

$$\Delta K_{th} = \alpha \Delta\sigma_{th} \sqrt{\pi(a + a_0)} \quad (\text{Eq. 2-19})$$

We can see that as the pit depth  $a$  increases, given  $\Delta K_{th}$ , the threshold stress intensity factor, as a material constant, the fatigue limit  $\Delta\sigma_{th}$  decreases. And from (Eq. 2-19), we can get:

$$a = \frac{(\Delta K_{th})^2}{\alpha^2 \pi (\Delta\sigma_{th})^2} - a_0 \quad (\text{Eq. 2-20})$$

A plot of  $a$  versus  $(\Delta\sigma_{th})^2$  will yield fitting values of  $\Delta K_{th}$  and  $a_0$ , which are both material constants. By using this method, Zhou and Turnbull obtained a Kitagawa-Takahashi [98] type of plot for the pit, as shown in Figure 2-24. The parameters used in this figure are  $\Delta K_{th} = 8.0 \text{ MPa}\sqrt{\text{m}}$ ,  $\alpha = 0.67$ ,  $a_0 = 82 \mu\text{m}$ . The authors arrived to the conclusion that the dependence of the fatigue limit on pit depth was consistent with pits acting as an effective cracks using the small crack model [97] When the pit grew larger, the small crack correction  $a_0$  is negligible, and a stress intensity factor for long cracks can be used for the large pit, as also indicted in Figure 2-24.

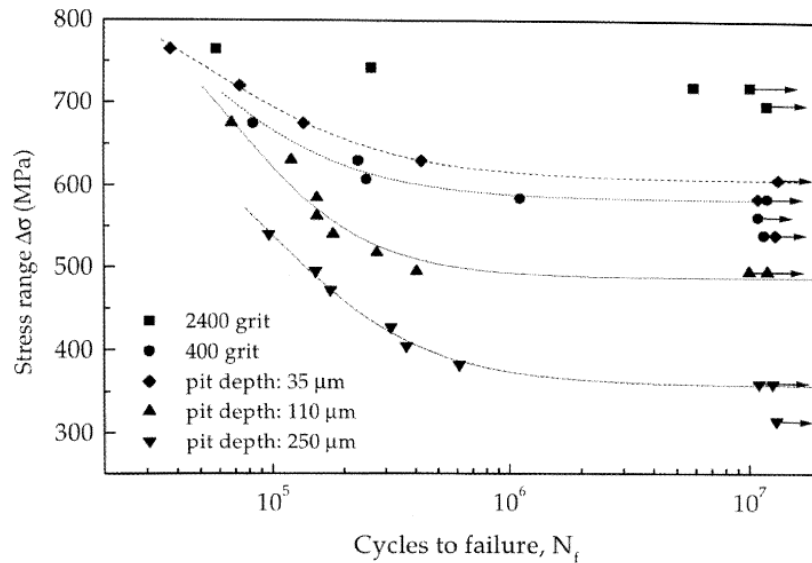


Figure 2-23: S-N curves of turbine blade steel samples with different pre-pit sizes. The fatigue limit is lower with a larger pre-pit size. Tests carried out in air at 50 Hz [96].

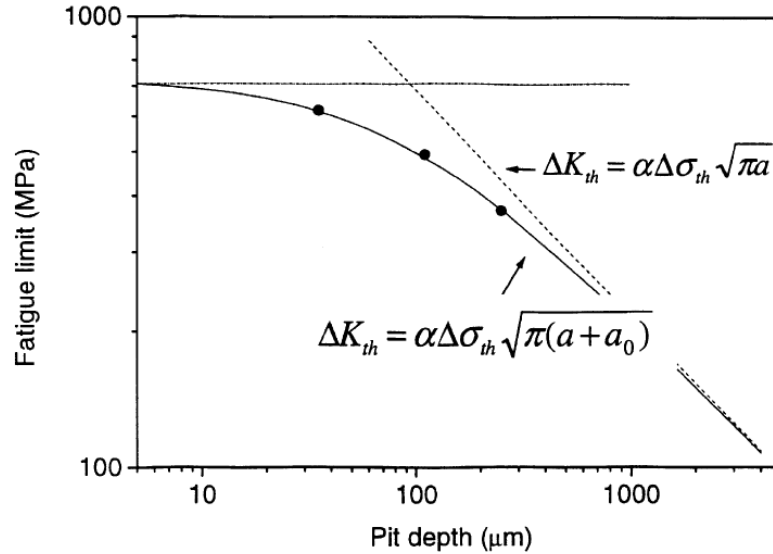


Figure 2-24: Dependence of fatigue limit of turbine blade steel on pre-pit size for tests carried out in air at 50 Hz, highlighting the representation of a pit, of depth  $a$ , as a short crack but with effective size [96].

While from the viewpoint of the fatigue limit, the pit can be regarded as an effective crack, this does not indicate that a pit acts like a crack from the perspective of growth in the very early stages. There may be a number of cycles required to initiate a crack from a pit [99]. This specific transition, pit-to-crack transition, will be discussed in the next section.

Whether the crack will initiate from slip bands or pits depends on the specific combination of the loading and environment. For example, Duquette and Uhlig [100] observed crack initiation in low carbon steel from slip bands at high stress level at a low pH of 2-4. In their case, slip bands formed early and there was insufficient time for pits to develop. Conversely, Akid [101] observed crack initiation from pits using a similar steel at near-neutral pH environment. Nevertheless, pitting is one of the principle mechanism for corrosion fatigue crack initiation [62].

### 2.2.3.2 Corrosion Effect of Crack Growth

In addition to the initiation stage, corrosion also plays an important role in short crack growth.

There are different ways to defined short cracks. Suresh and Ritchie [102] suggested that cracks can be considered short cracks in following cases:

1. Microstructurally short cracks: cracks which are of a length comparable to the microstructure of the material (e.g. grain size).
2. Mechanically short cracks: cracks which are embedded within the local plasticity zone of a notch or within their own crack tip plastic zone.
3. Physically or chemically short cracks: cracks are physically small (e.g. <0.5-1 mm) or cracks which their growth rate are dominated by the environmental effects.

Corrosion tends to weaken the microstructural barriers such as grain boundaries and helps the crack to grow into the adjacent grains. Akid [103] discussed the retardation effect of microstructural barriers and the effect of the environment. He compared the fatigue crack growth of a high-strength steel in air and in 3.5 wt.% NaCl. On the left of Figure 2-25,  $d_1, d_2, d_3, d_4$ , represent individual microstructural barriers and equate to a total surface crack length of 120  $\mu\text{m}$ . The data shows crack growth drops at the microstructural barriers and yet there is an increase of crack growth rate in the NaCl environment compared to in an air environment at these barriers. Akid also applied intermittent air/corrosion fatigue test to further illustrate the environment effect. The data is shown on the right of Figure 2-25. For the test with applied stress of 854 MPa (below fatigue limit), the crack did not grow initially without the introduction of the environment (marked as  $E_1, E_2, E_3$ , the environment was removed shortly after introduction). Interestingly, after the first two times of  $E_1$  and  $E_2$ , the crack grew to a larger length and then ceased to grow. However, after  $E_3$ , the crack continued to grow in the absence of the environment. These results imply that the fatigue limit should be referred to non-propagating microstructurally short cracks and represents the strength of microstructural barriers against cracking [102][104]. An introduction of a corrosion environment, even for a short period of time, may eliminate the fatigue limit (which is determined in air fatigue tests). As the crack grows longer, i.e. much larger than the size of a particular microstructural barrier, the significance of the environment may be minimized, and the crack growth is dominated by the mechanical driving force.

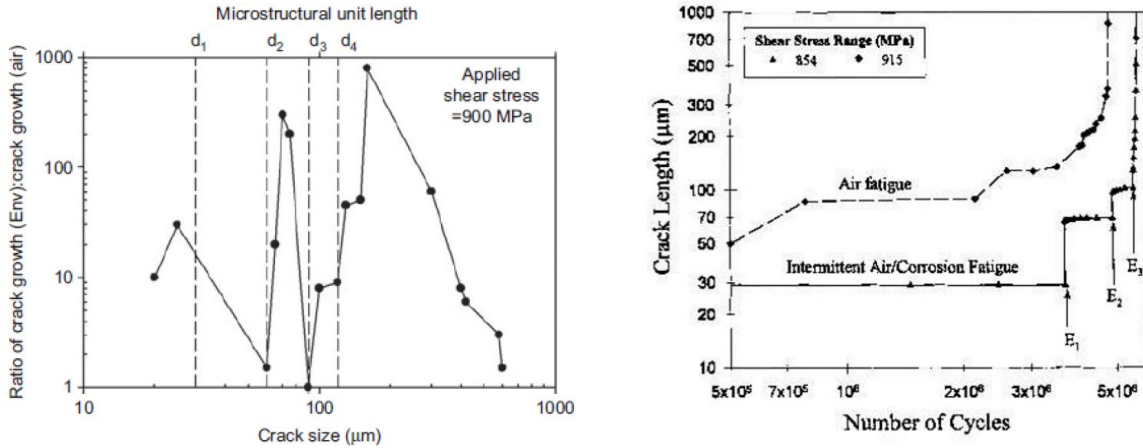


Figure 2-25: Left: Ratio of fatigue crack growth rate in 3.5 % NaCl to fatigue crack growth rate in air as a function of surface crack length. Right: Fatigue crack growth in an intermittent air/corrosion fatigue test, the air fatigue limit is 910 MPa. Both figures show the effect of corrosion at microstructural barriers [103].

Beyond the microstructurally small crack regime, corrosion also affect the crack growth rates in chemically short crack growth regime [105]. Gangloff [106] reported accelerated short crack growth compared to long crack growth with the same  $\Delta K$  based on LEFM in high strength low alloy steel. He concluded that increased hydrolytic acidification to form  $H^+$  and the decreased oxygen inhibition to consume  $H^+$  within small cracks were responsible for the observed enhanced short crack growth rate. Turnbull and Ferriss [107][108] through their mathematically modelling of the crack tip environment, confirmed the lower pH at the crack tip of a short crack compared to a long crack for low alloy steel with 1% Cr. They concluded that the low pH could lead to enhanced generation of hydrogen at the crack tip and accelerated the short crack growth. Turnbull and Ferriss also modelled the chemical environment within the crack tip of C-Mn steel. Their results suggested no pH change in either a short or long crack. Their results for both 1% Cr steel and C-Mn steel is shown in Figure 2-26. They concluded no enhanced short crack growth predicted by the model. Berechid et al. [109] reported no short crack growth enhancement in C-Mn steel under free corrosion or cathodic protection conditions, which supported the results by Turnbull and Ferriss. Enhanced short crack growth in steel was also reported by Dowling [110], Tanaka et al. [111][112], Nakashima et al. [113].

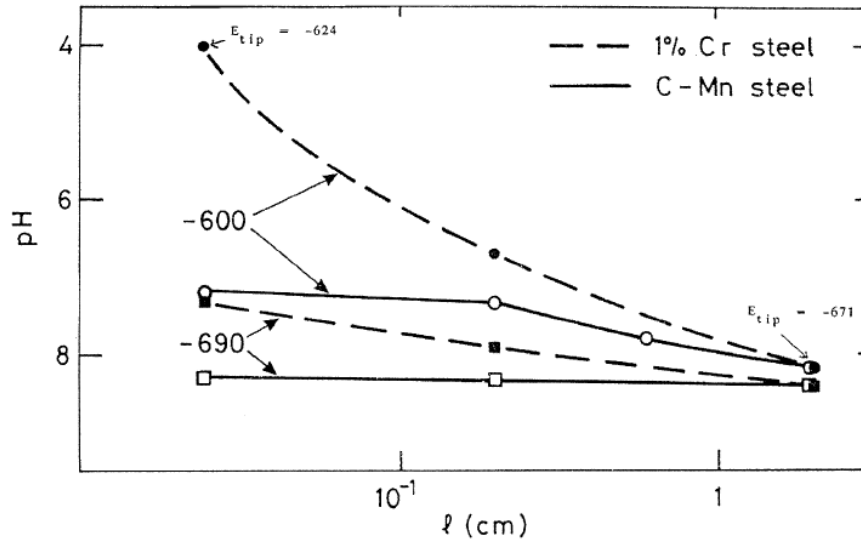


Figure 2-26: Predicted variation of crack-tip pH with crack length at different external potentials of -600mV SCE and -690mV SCE, cyclic loading frequency=0.1 Hz, R=0.5, and  $\Delta K = 20 \text{ MPa}\sqrt{\text{m}}$ . Crack tip pH varies little in the C-Mn steel case but change significantly in the 1% Cr steel case [91].

The opposite scenario, slower short crack growth rate for small cracks, has also been observed by James [114]. In his tests of high sulfur steel in aqueous environment at 243 °C, James observed lower crack growth for short cracks. He concluded that for high sulfur steel at high temperature, there was a high concentration of the aggressive species (i.e.  $\text{S}^{2-}$  or  $\text{HS}^-$ ) originating at the crack tip. As cracks grew longer, it became more difficult for these aggressive species to be transported out to the bulk environment from the crack tip, thus the crack growth rate increased. Turnbull [91] concluded that the short crack growth acceleration compared to long crack may develop because of the reduced closure (plastic wake has not fully developed) and declined aggressive species from the external environment to the crack tip. However, if the aggressive species are dissolved from the alloy, then growth rate for the short crack may be less than those for the long crack. Because when the crack is small, the aggressive species generated at the crack tip may be removed by the external flow.

Corrosion can also affect long crack growth relative to the inert environment, by enhancing the crack closure because of the corrosion product deposition on crack surfaces [115]–[118], and by enhancing anodic reactions [119][120] or hydrogen absorption [121][122].

## 2.2.4 Pit-to-Crack Transition

As mentioned in Section 2.2.3.1, corrosion pits are generally the preferred sites for crack nucleation where pits are precursors to cracking [8], [18], [123]–[133]. Pitting may encourage crack nucleation due to the increased stress/strain intensification owing to the pit size and geometry and the aggressiveness of the local chemistry (e.g., acidic pH, high concentration of aggressive anions). In the latter case this could lead to dissolution of surface films, increased rate of anodic dissolution, de-alloying, and increased rate of hydrogen generation and also absorption through removal of the oxide-film barrier to hydrogen uptake [134].

Akid [62] summarized four different stages of the fatigue lifetime of a component (Figure 2-27):

- (1) Stage 1: Surface film breakdown;
- (2) Stage 2: Pit growth;
- (3) Stage 3: Pit-to-crack transition;
- (4) Stage 4: Cracking (includes short and long crack growth).

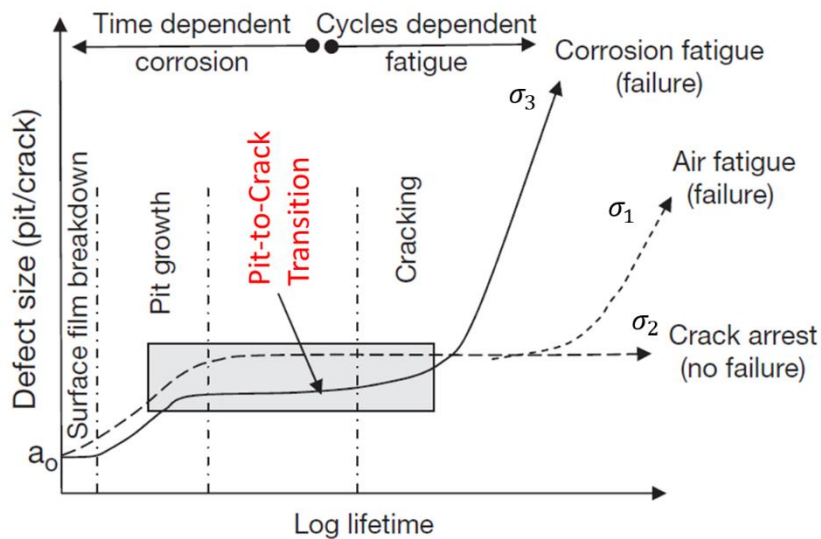


Figure 2-27: Schematic of defect development stages in air and aggressive environment,  $\sigma_1 > \sigma_2 > \sigma_3$  [135].

As can be seen from Figure 2-27, before the pit-to-crack transition, the process (including

surface film breakdown and pit growth) is dominated by the corrosion environment. After the pit-to-crack transition, the process (including small crack growth and long crack growth) is dominated by fatigue or mechanical factors. The transition from a pit to a crack is considered to be an important life controlling stage and may be regarded as a damage mechanism transition point [94].

The pit-to-crack transition stage can consume a significant portion of the lifetime of a component, especially when the nominal applied stress is relatively low and the stress concentration of the pit is more important. Akid et al. [6][94] performed fatigue tests on a high strength steel in NaCl solution, and showed that the fraction of pit-to-crack transition period to the total lifetime increased as the applied stress amplitude decreased. At the lowest stress amplitude ( $\Delta\tau = 414 \text{ MPa}$ ), this fraction was about 60% (See Figure 2-28).

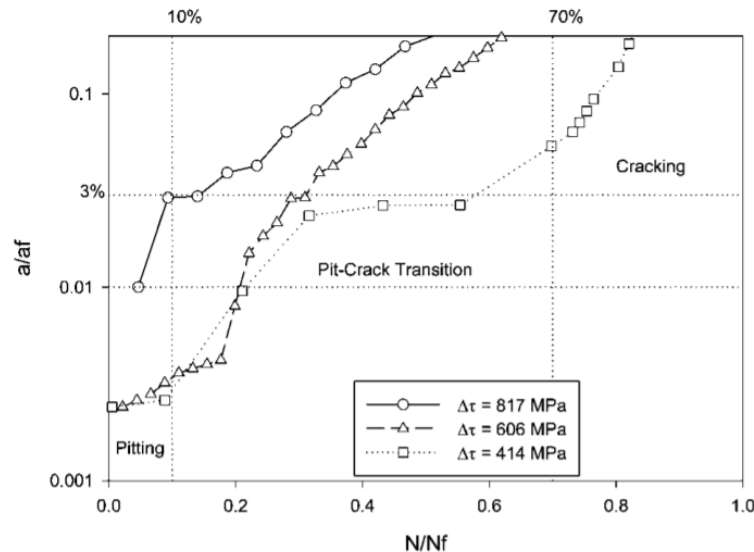


Figure 2-28: Corrosion fatigue of high strength steel ( $\sigma_y = 1400 \text{ MPa}$ ) in 3.5% NaCl at different torsional loads with fully reversed cycles,  $f=5 \text{ Hz}$ .  $a$  and  $N$  are the defect size and number of load cycles and  $a_f$  and  $N_f$  are crack length and number of load cycles at failure. A significant portion of the lifetime is consumed before cracking occurs [94].

Kondo [18] attempted to predict the pit-to-crack transition in corrosion fatigue by introducing a critical stress intensity factor range due to the presence of the pit  $(\Delta K)_p$  above which cracks would initiate. In his model, the stress intensity factor for a critical pit was calculated using fracture mechanics by assuming that the pit is a sharp crack. Based on his experimental results, Kondo

proposed that, the opening radius ( $c$ ) of a corrosion pit can be described by the equation:

$$c = C_p t^{1/3} = C_p (N/f)^{1/3} \quad (\text{Eq. 2-21})$$

where  $C_p$  is a coefficient,  $t$  is the time,  $N$  is the number of stress cycles,  $f$  is the frequency, and  $c$  is the radius of the pit opening.

Thus the pit growth rate  $dc/dN$  is given by:

$$dc/dN = (1/3)C_p f^{-1/3} N^{-2/3} = (1/3)C_p^3 f^{-1} c^{-2} \quad (\text{Eq. 2-22})$$

Meanwhile, the range of stress intensity factor ( $\Delta K$ ) is given by:

$$\Delta K = 2.24\sigma_a \sqrt{\pi c \alpha / Q} \quad (\text{Eq. 2-23})$$

where  $\sigma_a$  is the stress amplitude,  $\alpha$  is the aspect ratio ( $a/c$ ), and  $Q$  is a shape factor. Combining, we can get

$$dc/dN = (1/3)C_p^3 f^{-1} \alpha^2 \pi^2 Q^{-2} (2.24\sigma_a)^4 \Delta K^{-4} \quad (\text{Eq. 2-24})$$

The conclusion of his analysis indicates that the pit growth rate decreases as the pit grows, while it is well known that the crack growth rate increases as the crack grows. At the critical stress intensity factor range, the fatigue crack growth rate, shown by the solid line in Figure 2-29, exceeds the pit growth rate (the dash line) and a crack initiates from the pit. The point of intersection of these two lines gives the critical pit-to-crack transition condition  $(\Delta K)_p$ .

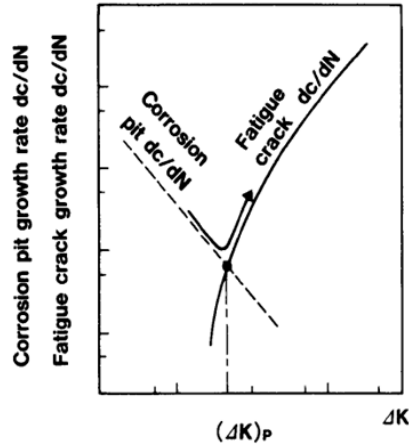


Figure 2-29: A schematic of Kondo’s model for pit-to-crack transition. The transition occurs when the crack growth rate exceeds the pit growth rate at a critical stress intensity factor range [18].

Kondo’s model provides insights into the pit-to-crack transition process and was adopted by several studies to predict pit-to-crack transition [136]–[138]. However, adopting an LEFM parameter, such as  $\Delta K$ , as the point where the pit-crack transition occurs has been criticized as not considered appropriate because this parameter is derived from long crack studies [1]. Also,  $\Delta K$  is an elastic parameter, which may be inappropriate considering the microplasticity generated by the pit. Furthermore, the Kondo’s model seems to imply that if the pit does not grow (e.g. in air fatigue), there will be not crack initiation or that a crack will initiate immediately under a given loading and  $\Delta K$  (i.e. no incubation time for crack initiation). His analysis cannot explain the crack initiation of pre-pitted samples in air fatigue observed by Fatoba [139].

Akid et al. [94][140] suggested that the pit-to-crack transition can be monitored using electrochemical measurements such as scanning reference electrode techniques (SRET). In their fatigue tests of 316L stainless steel in  $\text{FeCl}_3$  solution, they used SRET to measure the local current density of the pit. They found that the current density initially increased with the number of cycles until the pit-to-crack transition occurred, which is associated with a drop in local current density. They suggested that when pit-to-crack transition occurred, there would be a peak of measured current density around the pit area because of the change of local electrochemistry (Figure 2-30).

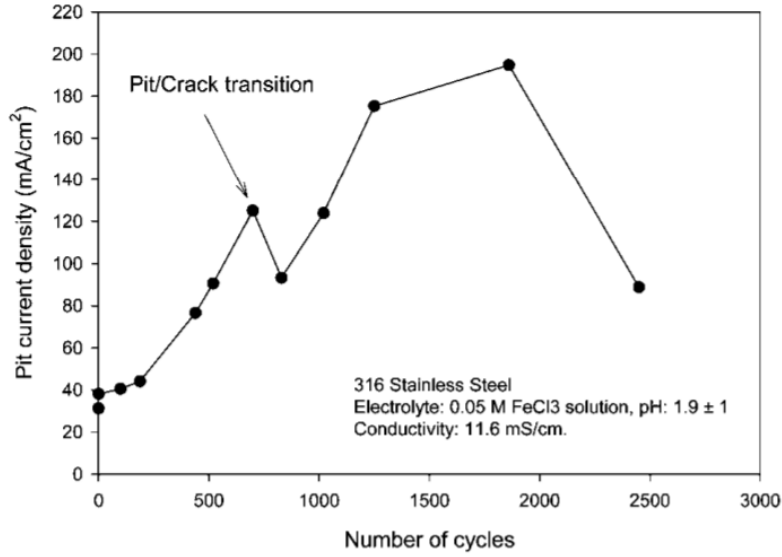


Figure 2-30: Change in pit current density as a function of number of fatigue cycles [94][140]

In their analysis, the pit depth for critical pit-to-crack transition can be calculated using an equation proposed by Harlow and Wei [141]:

$$a = \left[ \left( \frac{3MI_{po}}{2\pi nF\rho} \right) \exp\left(-\frac{\Delta H}{RT}\right) t + a_0^3 \right]^{1/3} \quad (\text{Eq. 2-25})$$

where  $a$  is the pit depth at the pit to crack transition;  $M$  is the atomic weight of material,  $n$  is the number of electrons transferred,  $\rho$  is the density,  $\Delta H$  is the activation enthalpy,  $F$  is the Faraday constant,  $T$  is the absolute temperature,  $R$  is the universal gas constant,  $I_{po}$  is the pit current,  $t$  is time for a pit to reach a threshold size and  $a_0$  is the initial pit depth. By recording the pit current, the critical pit depth at pit-to-crack transition can be estimated and the critical stress intensity factor can be calculated as well [94].

While Akid et al. proposed a way to detect pit-to-crack transition, he did not explain the underlying mechanism and thus the scenario cannot be modeled or predicted. Turnbull et al. [1][19][15] in their studies, ascribed the driving force of pit-to-crack transition to the plastic strain built up around the pit. In their experiments, Turnbull et al. observed that cracks initiated from either the mouth of the pit or the bottom of the pit, and they argued that the location of initiation depended the location of the maximum plastic strain, which was related to the geometry of the pit

and loading condition. They also found that the location of maximum (elastic) stress and the location of maximum strain could be different. Figure 2-31 shows the results of their stress/strain calculations for a hemispherical pit which would indicate that for this geometry cracking could initiate from the pit side (where the strain is maximum) instead of the base of the pit (where the elastic stress is maximum).

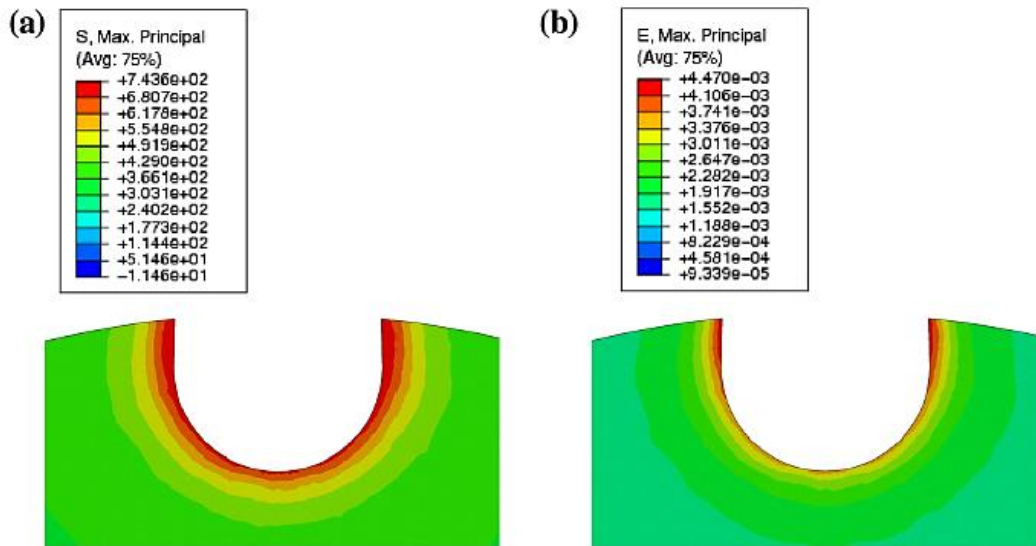


Figure 2-31: (a) Maximum principal stress distribution and (b) maximum principal strain distribution of a hemi-spherical pit in cylindrical specimen viewed in cross section [19].

As a transition point between pitting and cracking, corrosion and fatigue will both affect the timing of pit-to-crack transition. Thus the pit-to-crack transition process is not solely governed by stress intensity associated with the pit and applied stress, but is also determined by the local electrochemistry which controls pit growth rate, and induces the degradation of the strength of any microstructural barrier (e.g. grain boundary) or other feature which is exposed to the environment [94]. Ratcheting effects, to be further discussed below, during fatigue loading, where the local plastic strains continue to accumulate, provide the strain that is needed for cracks to initiate after a certain number of cycles [142]. On the other hand, grain boundaries or grains that are exposed to the corrosive environment may be corroded and weakened, which then may lower the crack initiation barrier.

In summary, the driving force for pit-to-crack transition is still unclear, as well as the

qualitative effects of mechanical and environmental factors on the incubation time before a crack initiates. These are the fundamental issues that this thesis addresses.

### 2.2.5 Ratcheting

Ratcheting is a phenomenon that occurs under asymmetric stress loading cycles where net plastic strain accumulates in the direction of the mean stress [143]. In a ratcheting scenario, the hysteresis of the stress-strain loop is not closed, and keeps translating to the direction of the mean stress. An example of ratcheting of Type 304 stainless steel is given in Figure 2-32 and an example of ratcheting of carbon steel 1020 is given in Figure 2-33. Large strain accumulation leads to ductile failure of the material by void formation and coalescence. Specimens failed when the accumulated strain reached a critical strain level comparable to the fracture strain in monotonic tension [144]. Ratcheting behavior of various steels has been studied intensively in the past two decades [145]–[157].

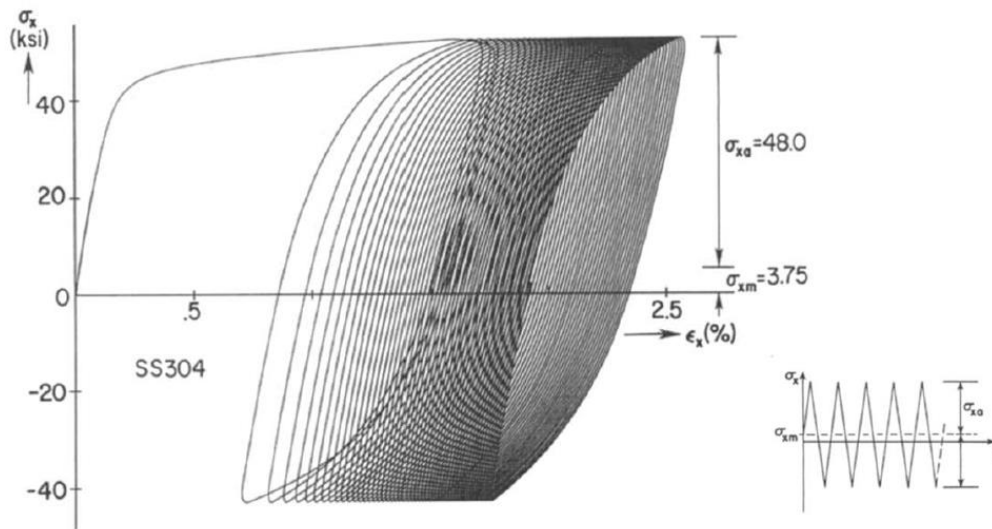


Figure 2-32: Ratcheting behavior of Type 304 stainless steel [143].

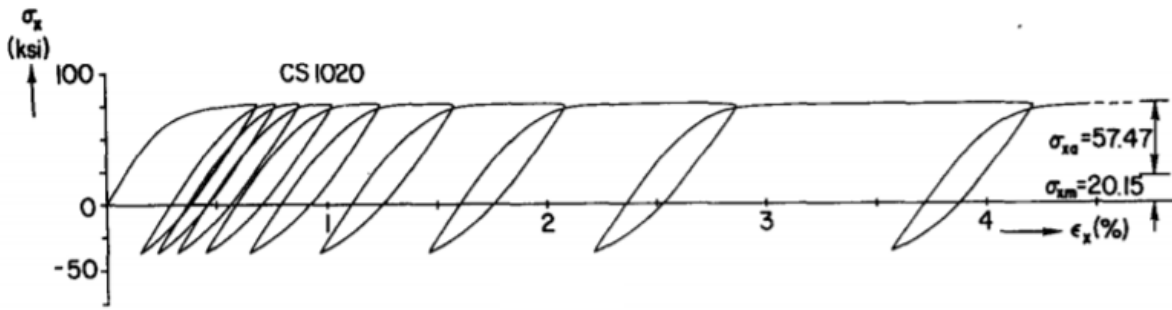


Figure 2-33: Ratcheting behavior of carbon steel 1020 [143].

Sinha and Ghosh [144] studied the ratcheting life of high strength low alloy (HSLA) steel under various applied stresses. Their results are shown in Figure 2-34. They found that the ratcheting strain accumulation can be divided into three stages: (1) a primary stage for the first few cycles where the ratcheting rate is large but decreases rapidly; (2) a secondary stage where the ratcheting rate is stable and is nearly a constant; (3) a tertiary stage of large strain accumulation with rapidly increasing ratcheting rate, preceding the final rupture of the specimen.

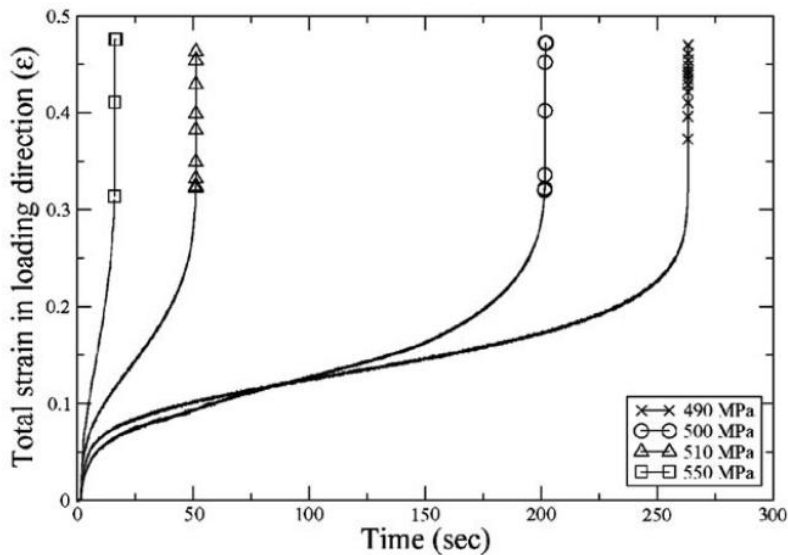


Figure 2-34: Evolution of macroscopic true strains for various peak stresses of 490, 500, 510, 550 MPa. The stress ratio is the same for all cases with  $R=0.1$  [144].

Kang et al. [155][156] and Kang and Liu [153] observed similar ratcheting behavior in

25CDV4.11 steel and tempered 42CrMo steel, but not in Type 304 stainless steel or annealed 42CrMo steel where a constant non-zero ratchetting strain rate was reached after the first stage and the ratchetting strain keeps on increasing at this constant rate. They identified that materials like 25CDV4.11 steel and tempered 42CrMo which exhibit cyclic softening in symmetric cyclic strain tests will show a three-stage ratcheting behavior, while materials like Type 304 and annealed 42 CrMo steel which exhibit cyclic hardening in symmetric cyclic strain tests will reach a stable ratcheting rate in a ratcheting test.

For material subject to cyclic loading with high stress amplitude, low cycle fatigue and ratcheting can occur simultaneously. Failure occurs according to which mechanism corresponds to a shorter life. [144]. If low cycle fatigue does not intervene and the failure occurs by ratcheting, the number of cycles to failure can be calculated by [144]:

$$N_{f,r} = \epsilon_c / \Delta\epsilon_r \quad (\text{Eq. 2-26})$$

where  $\epsilon_c$  is a critical strain level, and  $\Delta\epsilon_r$  is the ratcheting rate which is found to be increased with stress amplitude and mean stress [145][151]. Similarly, if ratcheting does not intervene and the failure occurs by low cycle fatigue, the number of cycles to failure can be calculated by the Coffin-Manson relation:

$$N_{f,LCF} = \frac{1}{2} \left( \frac{\Delta\epsilon_p}{2\epsilon_f'} \right)^{1/c} \quad (\text{Eq. 2-27})$$

where  $\Delta\epsilon_p$  is the plastic strain amplitude,  $\epsilon_f'$  is the fatigue ductility coefficient, and  $c$  is the fatigue ductility exponent. If  $N_{f,r} < N_{f,LCF}$ , the failure is dominated by the ratcheting mechanism. If  $N_{f,LCF} < N_{f,r}$ , the failure is dominated by the low cycle fatigue mechanism.

In the case of cyclic softening/hardening materials, the ratcheting rate  $\Delta\epsilon_r$  may not be a constant. Kang et al. [155] pointed out that for a cyclic hardening material such as Type 304 stainless steel, the ratcheting strain rate decreased as the cycles increased. If the load level was relatively small, the ratcheting strain rate became very small after certain cycles. Kang pointed out that this could be considered as a quasi-plastic shakedown scenario [158], as the stress-strain hysteresis loop stopped to translate and the specimen was subjected to symmetric cyclic strain. In

this case, the failure of the specimen is controlled by the low-cycle fatigue with almost constant strain amplitude [156]. For a cyclic softening material such as 25CDV4.11, ratcheting strain increased with the number of cycles, no shakedown took place and the material failed due to the increasing ratcheting strain. In the study of the ratcheting behavior of tempered and anneal 42CrMo steel, Kang and Liu [153] concluded that when the applied nominal stress level was low, the strain amplitude remained small and almost unchanged. The final ratchetting strain resulting from the cyclic stressing was small, and the failure of the material was mainly controlled by low-cycle fatigue with constant strain amplitude. However, when the applied nominal stress was relatively high, the material failed due to large ratchetting strain. They also found that the final ratchetting strain increased apparently with nominal stress amplitude and mean nominal stress if they were small; however, if the nominal stress amplitude and mean nominal stress were larger than certain values, their further increasing did not result in apparent increased final ratchetting strain.

Dutta and Ray [152] examined the fracture surface, shown in Figure 2-34, of an interstitial free steel after ratcheting failure. Microvoids were observed on the fracture surface which indicates that the ratcheting failure is caused by void formation and coalescence, similar to ductile fracture in a monotonic tensile test [144].

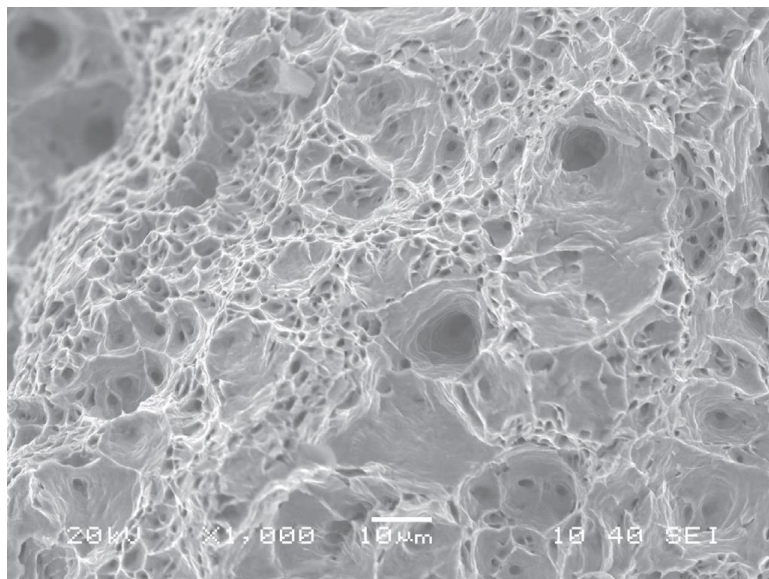


Figure 2-35: Fractograph of an interstitial free steel ratcheted for a loading condition of mean stress of 10 MPa and stress amplitude of 140MPa [152].

## 2.3 Crack Detection Techniques

Non-destructive testing (NDT) techniques are widely used in industry to measure material properties and to detect defects within the material. Among these, potential drop techniques are often used to determine crack initiation, growth and growth rate [159]. Potential drop techniques are of two types: the direct current potential drop (DCPD) method and the alternating current potential drop (ACPD) method.

### 2.3.1 DCPD Technique

The DCPD technique is based on the principle that the potential drop through a material increases as its cross-sectional area is reduced for a fixed current. The technique is widely used in laboratory tests using specimens with a fixed geometry such as compact tension specimens. A simple schematic of a typical DCPD system, with a compact tension geometry is shown in Figure 2-36.

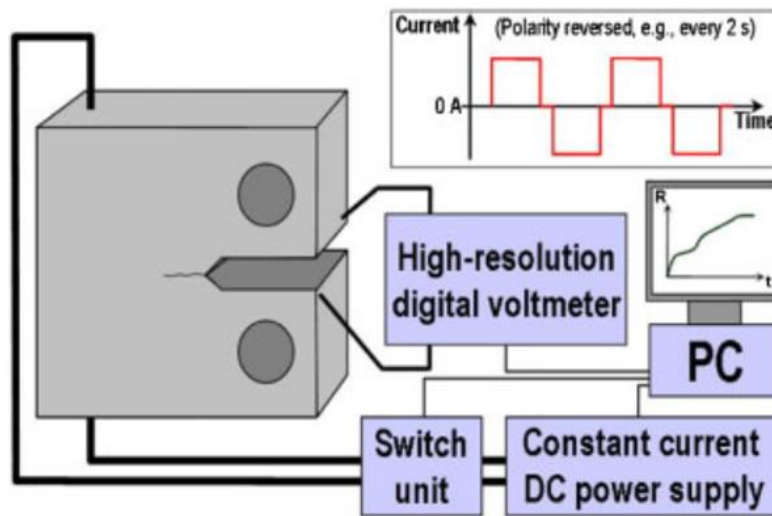


Figure 2-36: A Schematic of a DCPD system [160]

A modern DCPD system includes a constant current power supply, a switching unit, a high precision voltmeter and an associated data acquisition system. The DCPD method usually uses a direct current at the range of 5-50 A, and the voltage drop is usually the order of 100  $\mu\text{V}$  between two probes across the crack surface [159]. The current probes are usually far from the crack in

order to provide a uniform current field at the crack site, but they can be adjusted to get better results for specific geometries [161]. As the crack advances, the potential drop increases. Crack length or crack growth data can then be obtained by applying proper calibrations [162]. A switching unit is used to alternate the polarity of the current during a measuring cycle to eliminate the thermal electromotive forces (EMF) due to the interface resistance and thermocouple effect of the bimetallic connections (i.e., specimen-probe and probe-wire) [163]. By differentiating the consecutive voltage signals with reversed current, the EMF effect can be reduced [164]. Many researchers have applied DCPD technique to detect crack initiation and growth [165]–[167].

### 2.3.2 ACPD Technique

In principle, the ACPD technique is similar to DCPD technique. The main difference is that ACPD uses an alternating current as input instead of direct current. Because of the physical phenomenon termed the “skin effect”, alternating current in conductive materials can be confined and forced to flow only at (or near) the surface [168]. The intensity of the current decays exponentially with depth into the material from the surface. A measure of the depth that the current can penetrate is called the skin depth, and is given by:

$$\delta = \frac{1}{\sqrt{\pi f \sigma \mu}} \quad (\text{Eq. 2-28})$$

where  $f$  is the frequency of the alternating current,  $\sigma$  is the electric conductivity of the material and  $\mu$  is its absolute magnetic permeability. A simple schematic of a typical ACPD system is shown in Figure 2-37.

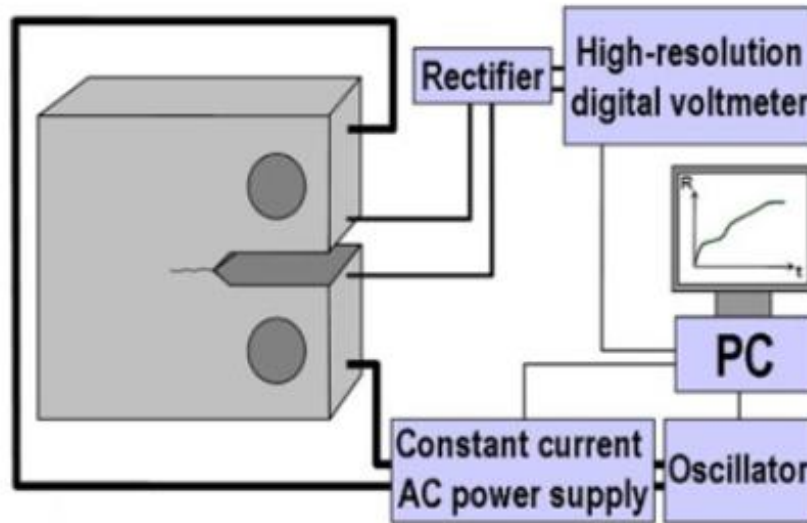


Figure 2-37: A Schematic of an ACPD system [160]

A typical ACPD system includes an AC power supply (or power amplifier), an oscillator, a special rectifier and a high precision voltmeter. Usually the oscillator, the rectifier and the voltmeter are lumped into a lock-in amplifier [159]. The oscillator generates a signal with a certain frequency and drives the power supply or power amplifier to supply the alternating current through the sample. The voltage drop between the voltage probes is recorded by the lock-in amplifier which is designed to reject the noise and only read the signal that has the same frequency as the oscillator.

Several researchers have applied ACPD to detect crack initiation and growth [169]–[172]. Hwang and Ballinger developed a multi-frequency ACPD system (17 to 203 kHz) to detect crack initiation in nickel alloys at 350 °C in aqueous environments [171]. They reported a sensitivity of 50  $\mu\text{m}$  for crack initiation from the surface of round bar specimens. Dai et al. detected crack initiation from single-notched specimens using ACPD at 30kHz and reported a similar sensitivity of 50  $\mu\text{m}$  from a through-thickness notch [172].

### 2.3.3 Resolution of DCPD and ACPD for Small Surface Cracks

The theoretical DC potential drop for a small crack with a depth  $a$  and a surface length of  $2c$  was reported by Gangloff et al. [173]:

$$V = V_0 \frac{\frac{\sqrt{1 - k^2 \sin^2 \theta}}{\tan \theta} + E(k, \theta) - Q}{E(k, \pi/2) - Q} \quad (\text{Eq. 2-29})$$

where  $V_0$  is the potential drop without the crack and  $V$  is the potential drop with the crack. For simplicity, we consider  $a = c$ . In this case, according to [173], the other terms in (Eq. 2-29) are:

$$E(\delta_1, \delta_2) = \int_0^{\delta_2} (1 - \delta_1^2 \sin^2 x)^{1/2} dx \quad (\text{Eq. 2-30})$$

$$k = 1 - \frac{a^2}{c^2} = 0 \quad (\text{Eq. 2-31})$$

$$\theta = \tan^{-1}(\sqrt{\alpha}) \quad (\text{Eq. 2-32})$$

$$Q = E(k, 0) = 0 \quad (\text{Eq. 2-33})$$

where

$$\alpha = \frac{1}{2} \left[ \frac{L^2 - c^2}{a^2} + \sqrt{\left( \frac{L^2 - c^2}{a^2} \right)^2 + \frac{4L^2 c^2}{a^4}} \right] \quad (\text{Eq. 2-34})$$

And  $2L$  is the spacing between the two voltage probes.

The theoretical AC potential drop for a semicircular small crack with a depth  $a$  was reported by Dover et al. [168]:

$$V/V_0 = \frac{2a}{3L} \cot\left(\frac{\xi}{3}\right) \quad (\text{Eq. 2-35})$$

where  $V_0$  is the potential drop without the crack and  $V$  is the potential drop with the crack.  $2L$  is the spacing between the two voltage probes, and  $\xi = 2\cot^{-1}(L/a)$ .

Figure 2-38 shows the relative change of potential for DCPD and ACPD versus crack depth according to (Eq. 2-29) and (Eq. 2-35). The probe spacing used in the calculation was 4 mm and the crack was assumed to be semicircular in shape. It can be seen that ACPD is more sensitive to DCPD for all crack depths. Figure 2-39 shows the ratio of relative change of ACPD over DCPD. The ratio starts from a very high number when the crack is small and approaches one when the crack is large. Based on the theoretical calculation, it is concluded that ACPD is more sensitive than DCPD, especially when the surface crack is small.

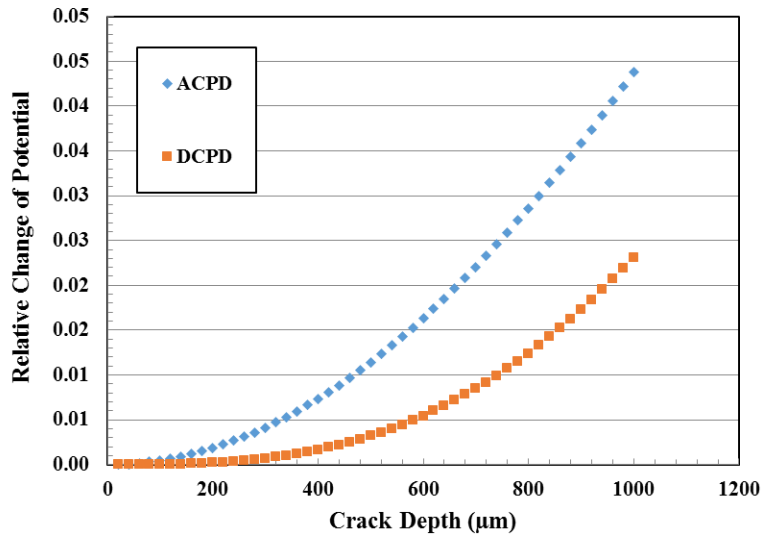


Figure 2-38: Relative change of potential versus crack depth for DCPD and ACPD.

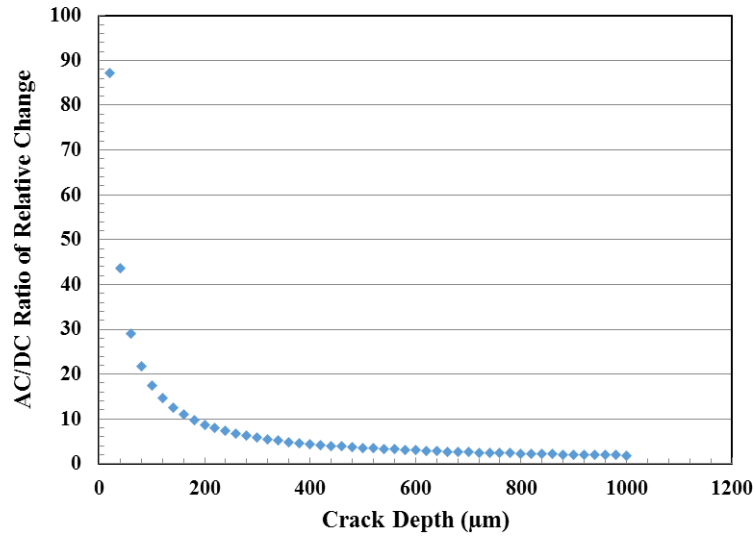


Figure 2-39: AC/DC ratio of relative change versus crack depth, showing that AC is more sensitive than DC for small cracks.

#### 2.3.4 ACPD vs. DCPD for This Research

In general, both DCPD and ACPD techniques have been accepted as reliable and precise crack measurement techniques. The main advantage of DC over AC is its ability to detect and measure subsurface cracks that occur under high stress or strain situations [159]. This is because DC current flows through the whole cross section of the material. Yet one can argue that it is also possible to use ACPD to achieve the same goal by lowering its frequency and allowing the skin depth be comparable to the thickness of the material [174]. Other advantages of DCPD include easier noise control and simpler instrument setup. However, ACPD does have advantages.

Compared to DCPD, the main advantages of ACPD include:

- (1) Due to the skin effect and the increased potential drop due to the increased surface current density, ACPD requires less total current than DCPD to achieve the same potential drop level for surface cracks. This also helps to avoid potential heating issues which may influence the DCPD measurement.
- (2) The DCPD technique effectively measures the reduction of cross sectional area during the cracking process, thus its sensitivity depends on the cross sectional area compared to the cracked area of the specimen. In the AC case, because the current only flows at surface (at least when the skin depth is much less than the thickness of the specimen), its resolution

will not be affected by the thickness. Thus to achieve good resolution, DCPD specimens may need to have a very small cross section [167]. For ACPD, there is no such requirement. For the same reason, ACPD is considered as a better NDT method in the field [175].

- (3) According to the results of R. Collins [40][41], the ACPD signal will stay unchanged for an axis-symmetric defect between two voltage probes compared to a completely flat surface. This means that the ACPD method cannot detect pit initiation and growth for an axisymmetric pit geometry. At the same time, the ACPD method can detect crack growth. This property makes ACPD a unique technique in the context of detecting pit-to-crack transition.
- (4) Most importantly, based on the discussion in last section, ACPD is more sensitive than DCPD, especially when the crack is small. Thus ACPD will be a better choice for detection of crack initiation.

## Chapter 3 Experimental Methods

The objective of this chapter is to describe the material and the experimental techniques that were used in this research. It will also describe the techniques that were applied to collect the data that were obtained from the experiments.

### 3.1 Material

The material used in this research was APL 5L X65 grade steel, which is a high strength low alloy steel used for line pipe in the oil and gas industry. The material was provided by British Petroleum (BP) in the form of as welded seamless pipe sections with an inner and outer diameter of 273 mm and 313 mm respectively. Figure 3-1 shows sections from the as-received pipe. The specimens used for all the fatigue testing carried out in this work were cut from the base metal or the area away from the weld by at least 50 mm to avoid the heat affect zone. The microstructure and micro hardness of both weld and base metal parts were examined. The material was tested in the ‘as-received’ (quenched and tempered) condition with no further treatment.

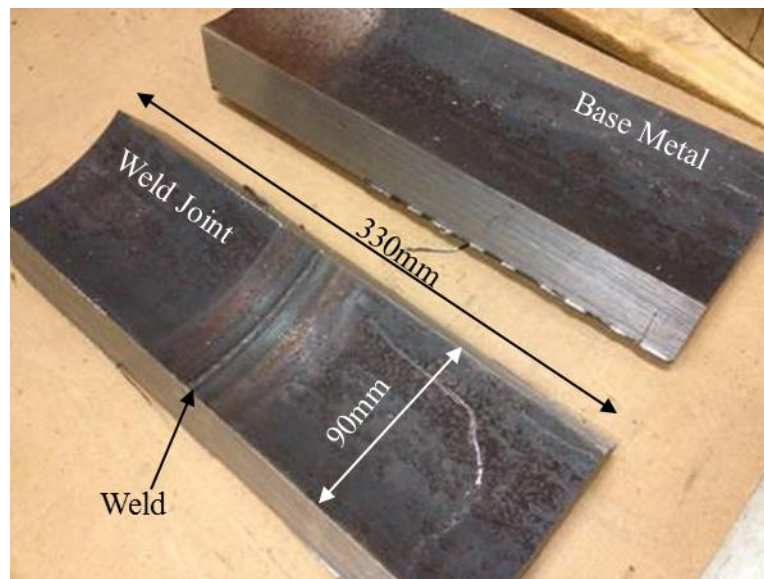


Figure 3-1: As-received X65 pipeline steel

The chemical composition of the material (wt. %) is given in Table 3-1.

C	Si	Mn	P	Mo	V	Cr	Ni	Cu	Nb	Ti	Al	S	Fe
0.05	0.28	1.08	0.01	0.13	0.06	0.07	0.37	0.16	0.027	0.03	0.037	0.001	Bal.

Table 3-1: Chemical composition of received X65 pipeline steel. Data provided by BP.

### 3.2 Metallography

Metallographic examination and micro hardness testing was carried out on both weld and base metal to obtain information about the microstructure of the material. Metallographic specimens were cut perpendicular to the weld and in such a way that it contained the weld, the heat affect zone and the base metal. For optical microscope observation, samples were ground and polished using 120, 240, 600, 800 grit sand papers and then 9, 6, 3, 1  $\mu\text{m}$  diamond suspension. For scanning electron microscopy (SEM), samples were further polished using 0.25 and 0.05  $\mu\text{m}$  diamond suspension. For microstructure observation, samples were etched using 2% Nital solution for 15-45 seconds. The metallographic photos were taken using a Zeiss microscope. Vickers hardness measurements were obtained using a LECO LM 247AT microhardness tester with test force of either 500 grams and a test time of 15 seconds. The SEM photos were taken using a FEI XL30 low-vacuum and environmental scanning microscopy (ESEM).

### 3.3 Pit Generation

This thesis research focused on the pit-to-crack transition during corrosion fatigue test using ACPD technique. In nature, the pitting process is stochastic [178], which means that pits can occur randomly on the sample surface in the environment. In order to monitor a single crack initiation event during the fatigue test, it was decided to use specimens with a single pre-made pit. A single pit was generated on the polished specimen surface (down to 3  $\mu\text{m}$ ) before fatigue testing. In this way the exact location of the pit was known. Because of the associated the stress concentration, crack initiation most likely to initiate from the artificial pit. Potential drop measurement wires were then attached on both sides of the pit and its potential drop monitored during the corrosion fatigue test. In addition, by using a single pit the complexity of multi-pit interaction [179] was minimized.

There are several methods that could be used to produce a pit on a specimen. Conventional mechanical methods include spark erosion [180] and drilling [181]. The advantage of these mechanical methods is that the pit geometry can be easily controlled. However, these mechanical methods may leave residual stress/strain around the pit which would likely effect the pit-to-crack transition [182]. To avoid the residual stress strain and better simulate a real corrosion pit, various electrochemical methods have been applied by Ahn [7] and Turnbull et al. [183][184]. Ahn [7] painted the specimens with a flexible lacquer and then exposed one small area by penetrating the lacquer with the tip of a pin. After that, the specimen was immersed in 1M NaCl solution and a potential was applied to initiate pitting. Turnbull et al. [184][183] used a droplet technique where a needle was electrically contacted to a stainless steel surface through a droplet at the tip of the needle. A potential or current was applied between the steel and the needle. A single pit would form within the wetted area on the steel surface when an appropriate potential or current was applied.

In this research, a plastic microcapillary was used, in a modification of the method used by Turnbull, to generate the pit on the steel surface. A schematic of the pit generation system is shown in Figure 3-2. A photograph of the setup is shown in Figure 3-3. A plastic syringe with a tip of 500  $\mu\text{m}$  in diameter was filled with 1wt. % NaCl solution and its tip is attached to the sample surface. A power supply with controlled current was used to force corrosion and pitting to occur. The cathode of the power supply was connected to a tubular stainless steel needle inside the plastic tip and the anode was the steel specimen. When the power supply was on, a voltage drop was imposed between the specimen and the needle, which drove localized corrosion of the iron with the plastic tip. A circulation loop was also incorporated into the system, in which solution was injected from the tubular needle and flowed out of the outlet at the side of the syringe. The solution flow flushed out the corrosion products within the pit and helped to stabilize the corrosion current.

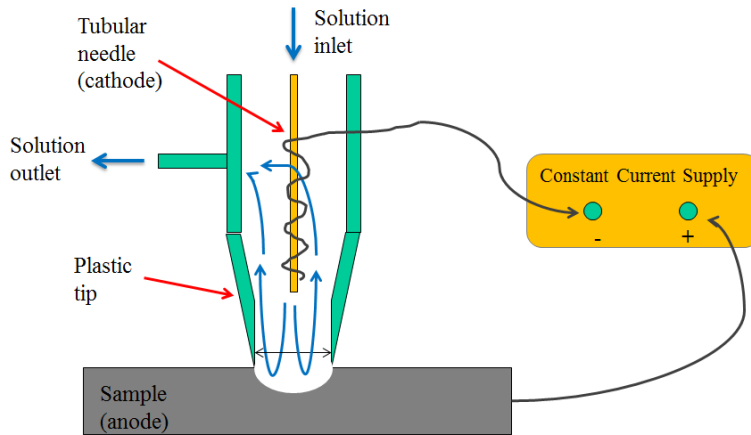


Figure 3-2: A schematic of the Pit Generation System

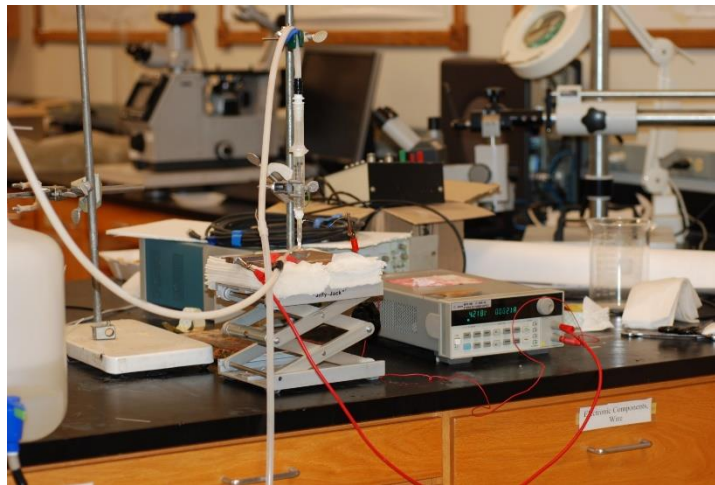


Figure 3-3: The actual pit generation system setup.

Using a current of 0.2 mA and a test duration of 100 minutes, a pit with approximately 500  $\mu\text{m}$  diameter (which was approximately the size of the plastic tip) and 150  $\mu\text{m}$  in depth (which was determined by the current and time used) could be consistently generated on the specimen surface. The geometry of one of the generated pits is shown in Figure 3-4. The pit has an approximately hemispherical shape with relatively smooth surface. The galvanostatic pitting method was used to produce controlled size pits with high repeatability. Variations of pit diameter and depth with different pits were within  $\pm 10\%$  of the designed values.

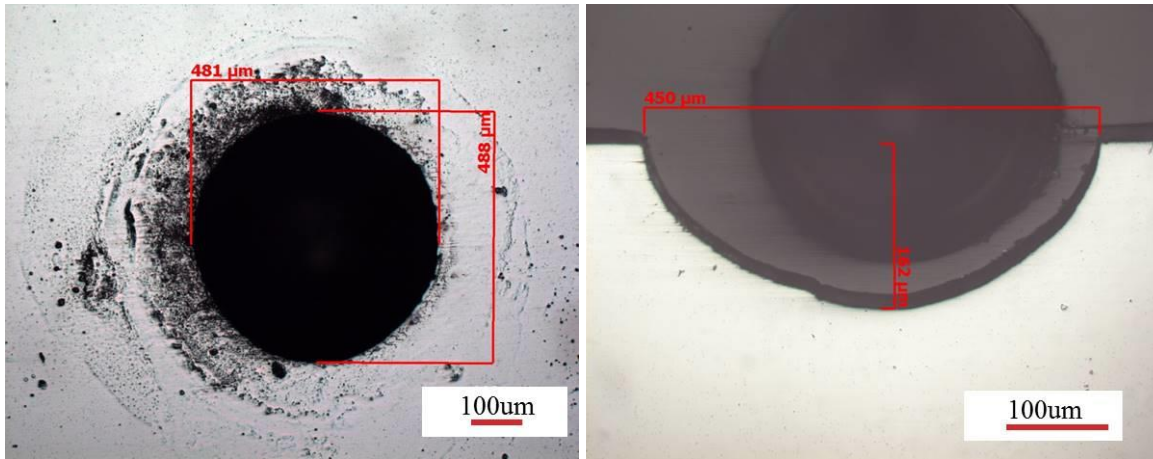


Figure 3-4: Geometry of the artificial pit. Left side looking down into the pit. Right side looking from the side after polishing.

### 3.4 Four-point Bending

In this research, cyclic loading in fatigue tests was applied through four-point bending following ASTM C1161-13 [185]. A schematic of the four-point bending geometry is shown in Figure 3-5. The technique uses four bearings to hold the specimen in the middle and load is applied on one side of the fixture. Three out of four bearings are free to roll and one bearing is fixed. Compared to the fatigue tests with uniaxial tension or compression [186], four-point bending has a simpler sample requirement. More importantly, with the four-point bending technique and the configuration the fatigue machine, the sample surface is perpendicular to the gravity force. In this case, the aggressive ions can be accumulated at the bottom of the pit on the surface as would occur in a field situation-which would be the most aggressive orientation. In the case of uniaxial fatigue, the sample surface is usually aligned parallel with gravity and the aggressive ions may not be able to concentrate at the bottom of the pit. Compared to three-point bending, four-point bending provides a uniform stress field between the inner supports. This means that even if the pre-made pit is not right at the center of the specimen, the stress will still be the same. While for three-point bending, the stress decreases from the midpoint towards the ends of the specimen. In this case, it may increase the uncertainty of the stress state around the pit.

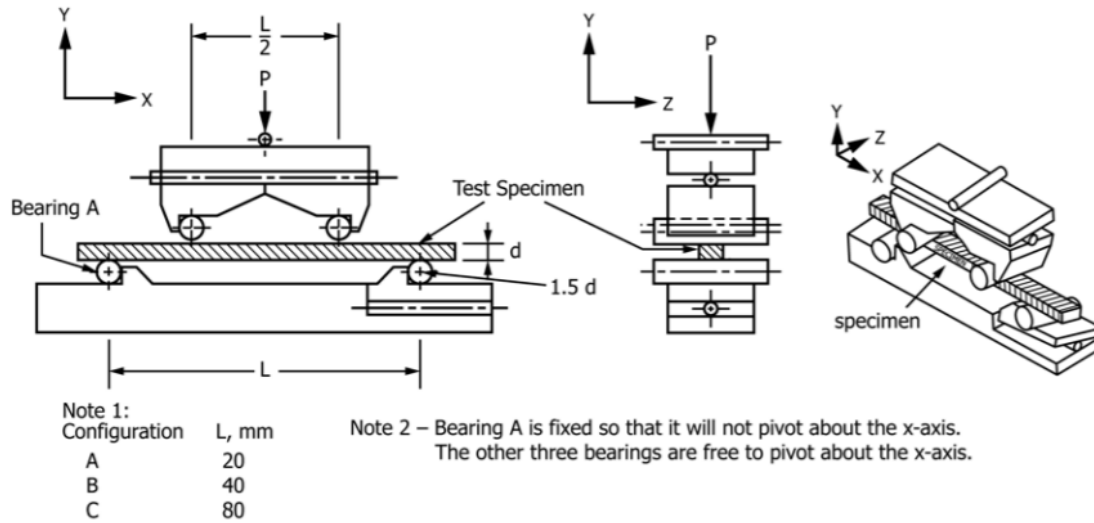


Figure 3-5: A schematic of four-point bending fixture [185].

In a four-point bending fixture, the surface stress is uniform between the two inner supports, but the tensile stress decreases from the surface in contact with the outer supports (the lower surface in Figure 3-5) towards the mid-plane of the specimen, and the stress becomes compressive when it gets past the mid-plane. The maximum tensile stress at the surface is given by:

$$\sigma = \frac{3 Pl}{4 bd^2} \quad (\text{Eq. 3-1})$$

where  $P$  is the total load on the fixture,  $l$  is the distance between two outer supports,  $b$  and  $d$  are the width and the thickness of the specimen respectively. The specific stress distribution helps to facilitate crack initiation at surface but complicates analysis as one moves away from the surface.

In the experiments, all the support pins used were made of aluminum oxide for the purpose of electrical isolation.

### 3.5 Specimen Preparation

Specimen were machined into a rectangular bar with 120.6 mm (4.75 inch) in length, 25.4 mm (1.00 inch) in width and 7.95 mm (0.313 inch) in thickness. Specimens were cut from the base metal of the pipe section. The length of the specimen was chosen to align with the longitudinal

direction of the pipe section. A schematic of how the specimens were cut from the pipe section is shown in Figure 3-6. The actual sample with a pre-made pit at the center is shown in Figure 3-7.

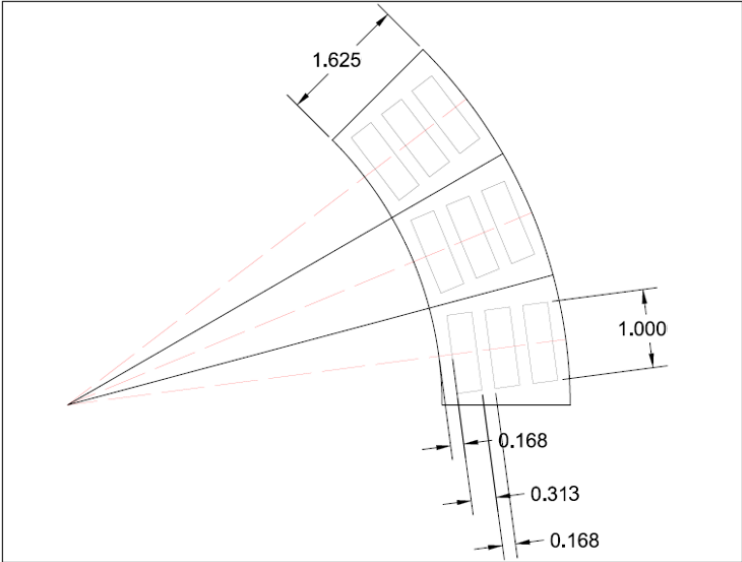


Figure 3-6: A schematic of cutting the specimen out of the original pipe section (unit: inch).

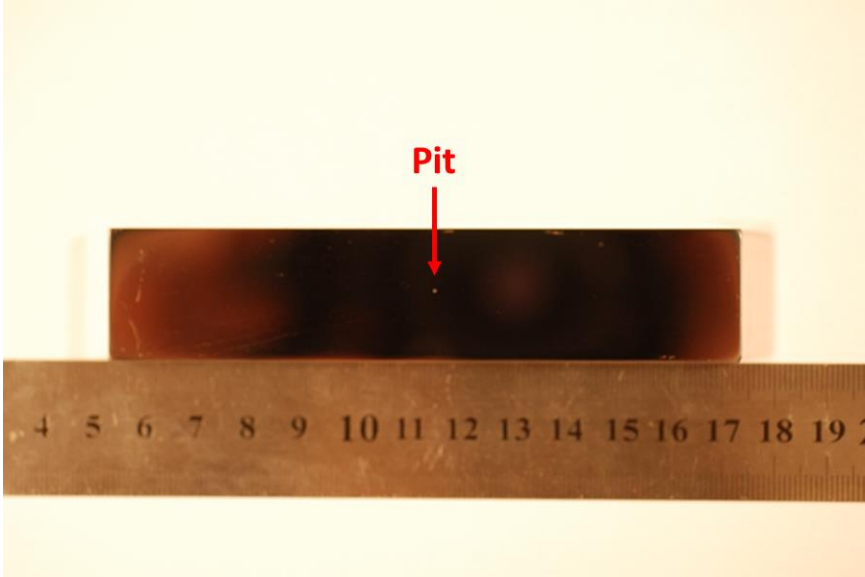


Figure 3-7: Actual pre-pit sample.

### 3.6 ACPD System

In order to monitor crack initiation and subsequent crack growth, the ACPD technique was

applied during the fatigue tests. A schematic of the circuit design of the ACPD system, which was developed as a part of this research, is shown in Figure 3-8. The lock-in amplifier used was a Model 7270 from Signal Recovery and the AC power supply was a Model 7224 from AE Techron. The lock-in amplifier served as both a function generator and a voltmeter. It supplied a small amplitude sinusoidal signal with a set frequency to the 7224 power amplifier. The amplifier amplified this signal to supply the current of the circuit. The voltage drop across the pit was measured by the lock-in amplifier while filtering out other frequencies which were different from the set frequency. A resistor with a fixed 10 ohm resistance and a voltmeter were used in order to detect the actual current through the sample. The voltage drop across the pit was normalized by this current value in order to minimize potential current fluctuation. The lock-in amplifier had a resolution of 0.1% to 0.01% depending on the amplitude of the signal. Note that both the pair of current wires and the pair of potential wires connected to the sample were tightly twisted in order to eliminate pick-up voltages caused by the magnetic field generated by the specimen [187] (See Figure 3-9).

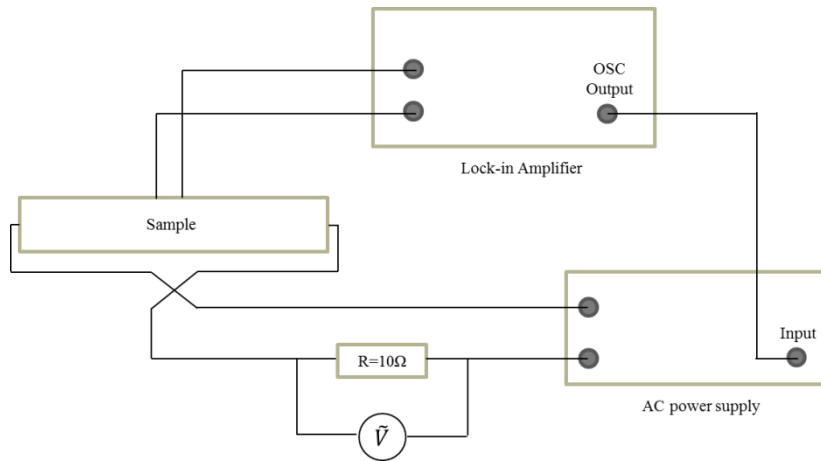


Figure 3-8: A schematic of the ACPD system circuit.

### 3.7 Integrated System for Fatigue Tests in Air and in Aerated NaCl Solution

Fatigue tests were performed in four different environments: (1) air at room temperature (RT), (2) aerated 1 wt.% NaCl at RT, (3) CO<sub>2</sub>-saturated 1 wt. %. NaCl solution at RT and, (4) CO<sub>2</sub>-saturated 1 wt.% NaCl solution at 120 °C. The first two types of tests were performed using a small

cell attached to the specimen. The overall system included the ACPD sub-system, a servo-hydraulic machine with four-point bend fixture installed and a data acquisition and loading control system (See Section 3.8.3).

Figure 3-9 shows how the potential drop wires spot-welded to the sample surface across the pit. The nickel wires were used. Teflon tubes were used to electrically isolate the wires from each other when they are twisted. The Teflon tubes also provided corrosion resistance for the wires when used in autoclave tests. Cables used to connect the electrical instruments were standard coaxial cables. As mentioned above, for tests in aerated NaCl solution, a plastic cell was placed on the top of the pit to contain the solution, as shown in Figure 3-10. A setup for the whole system is shown in Figure 3-11.

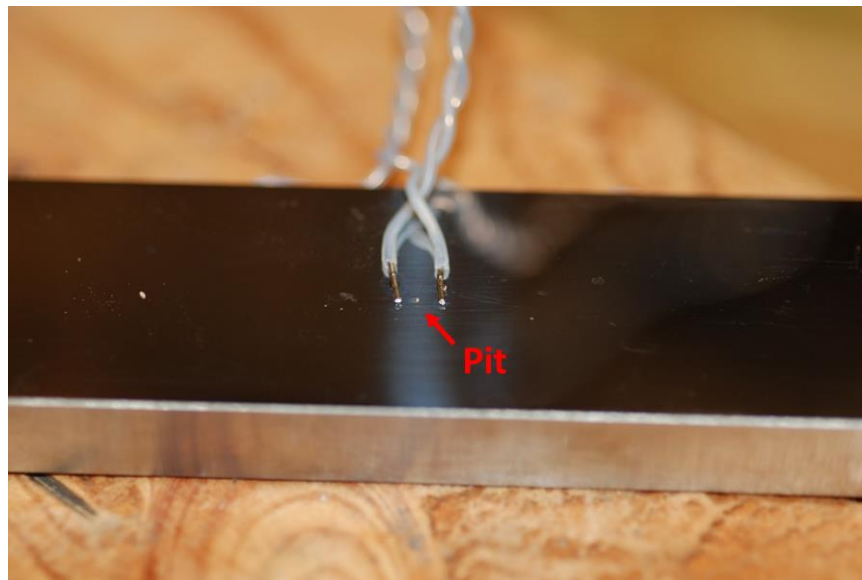


Figure 3-9: The spot-welded wires and the pit.

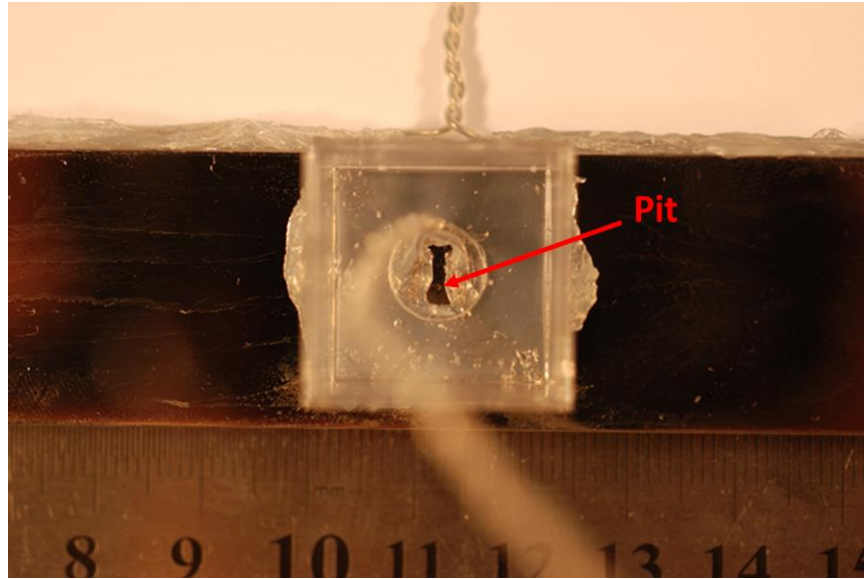


Figure 3-10: Plastic cell on top of the pit for addition of NaCl solution (top view).



Figure 3-11: System configuration for test in air and aerated NaCl solution at RT.

### 3.8 Integrated System for Fatigue Tests in CO<sub>2</sub>-saturated NaCl at RT and 120 °C

#### 3.8.1 Circulation System

In order to perform tests with desired water chemistry and at high temperature, an additional circulation system and temperature control system were added. The circulation system was built in order to provide the correct chemistry for the tests, i.e. CO<sub>2</sub>-saturated 1 wt.% NaCl with pH=6 (The pH was chosen to simulate the near-neutral pH environment in pipelines [38], saturation referred to the conditions of room temperature and 1 bar CO<sub>2</sub>).

A schematic of the chemistry control and circulation system is shown in Figure 3-12 and a photograph of the system is shown in Figure 3-13. The system consists of a makeup loop (on the left) and a test loop (on the right), with conductivity and pH meters installed in both loops to monitor the water chemistry. The makeup loop has a circulation pump and an ion exchange cartridge (Thermo Scientific Barnstead D0809) for purification of the water. The test loop has a circulation pump and a pressurization pump to provide the solution to the autoclave and pressurized it. The pressurization was needed in order to keep the system subcooled at 120 °C. Pressure meters were installed within the test loop to monitor the pressure. Gas cylinders with Argon or CO<sub>2</sub> were connected with both loops to provide the desired conditions.

Before a test, the makeup water column was first filled with deionized water. The water was further purified by circulating through the cartridge and with continuous purge of Argon gas to deaerate the system until the measured conductivity is lower than 80 nS/cm. After that 10 wt. % NaCl solution (made by mixing deionized water and analytical grade NaCl powder) was added into the deionized water until the water conductivity reached 17.6 mS/cm, which was the theoretical conductivity for 1% wt. NaCl solution [188].

After the conductivity stabilized at 17.6 mS/cm, Argon gas was switched to CO<sub>2</sub> gas at 1 bar. CO<sub>2</sub> gas was purged into the solution for about 30 minutes until the pH reached a saturation value (approximately 3.8). Thus when saturation occurs, there would be 1 bar CO<sub>2</sub> pressure above the surface. The corresponding CO<sub>2</sub> concentration dissolved in the NaCl solution would be 0.030 M [43]. The pH value was then adjusted to 6.0 by adding concentrated NaOH solution to the makeup water column. The pH usually took hours to stabilize because the slow reaction between dissolved CO<sub>2</sub> and NaOH.

After the chemistry reached the desired condition, the solution was pumped to the column in the test loop, from which the solution would be further pumped into the autoclave. In the 120 °C case, the autoclave would be pressurized to 4 to 6 bars by the pressurization pump and regulated by the back-pressure regulator in the test loop. After that the autoclave would be heated up to 120 °C by the heating tape which was wrapped around the autoclave. The autoclave was fabricated from alloy Hastelloy C-22 to minimize corrosion. A pH probe for high temperature was used to measure the pH in the autoclave as well as outside the autoclave. We first measured pH inside the autoclave. However, it was found that at high temperature, corrosion products deposited onto the pH probe and damaged the probe tip. The probe thus became useless after a few tests. For later

tests the pH probe was moved out of the autoclave and the pH was measured downstream of the autoclave. Another conductivity probe was used to detect the conductivity from the flow out of the autoclave during the test. CO<sub>2</sub> concentration inside the autoclave was assumed to be the same as the solution in the water column because of the continuous circulation. The flow rate of the test loop was approximately 20 mL/min. The volume of the test loop was estimated to be 4 L.

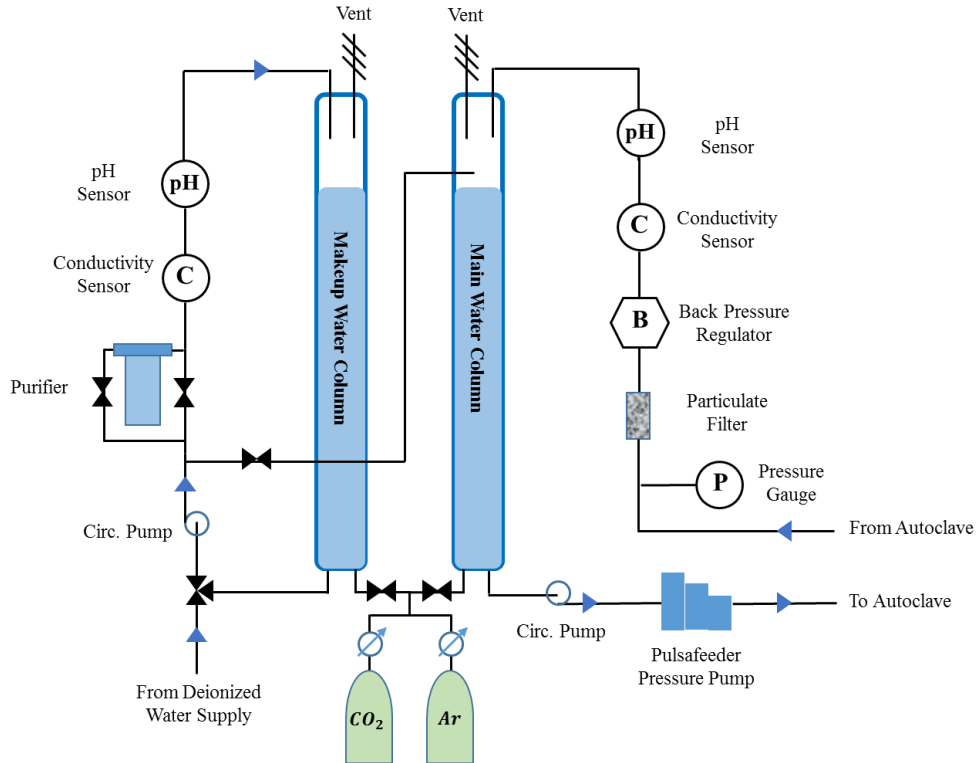


Figure 3-12: A schematic of the water board.

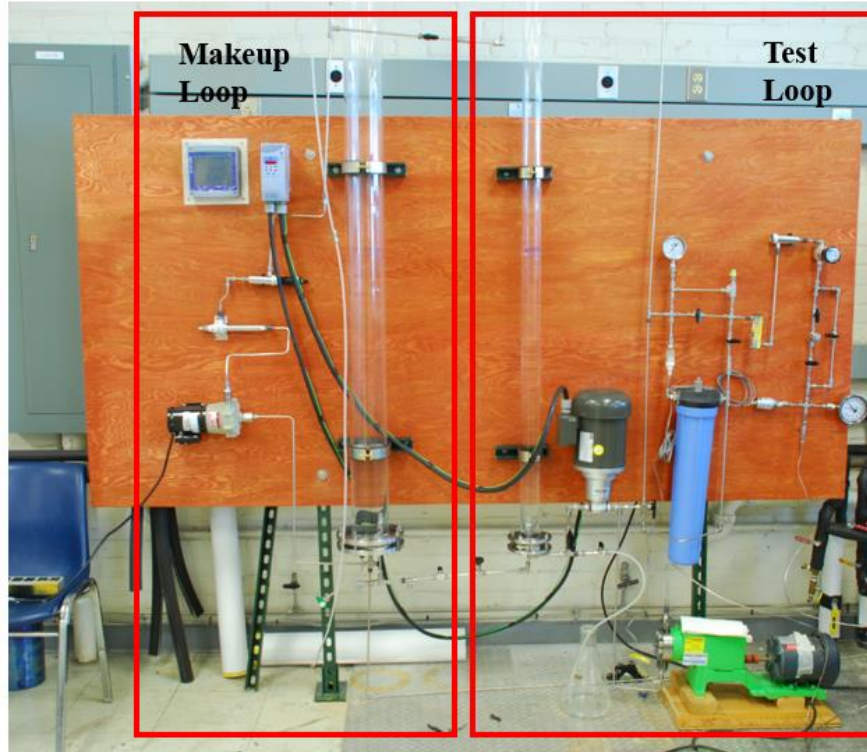


Figure 3-13: A photo of the actual setup of the water board.

### 3.8.2 Temperature and Pressure Control System

In order to maintain the temperature and pressure for fatigue tests at 120 °C, a temperature and pressure control system was built. The temperature and pressure control system consisted of an OMEGA Model CNi16D temperature controller, an OMEGA Model DP25-E process meter, a pair of thermocouples inside the autoclave and a back-pressure regulator. Figure 3-14 shows the electric circuit design of the system. There were two main loops of this design. One was the solid state relay (at the center of figure) driven by the pulse output of CNi16D which controlled the power of the heating tape which was wrapped around the autoclave. The CNi16D controller received the temperature from the thermocouple inside the autoclave used a simple on/off control to stabilize the temperature at the target value. The CNi16D controller turned on the heater when the temperature was lower than the set point and turned off the heater when the temperature was higher than the set point. The other main loop was the interlock chain of the CNi16D temperature controller and the DP25-E pressure meter. The interlock chain would shut down the heater automatically when the temperature was higher than a limit value (e.g. 130 °C) or the pressure deviated from a given range (e.g. 4 to 6 bars). The interlock chain greatly improved the safety of

the system for long term operation.

For tests at 120 °C, the temperature was maintained at  $120 \pm 1.5$  °C, and the pressure was maintained at 4 to 6 bar. For tests at room temperature, the autoclave was neither heated nor pressurized.

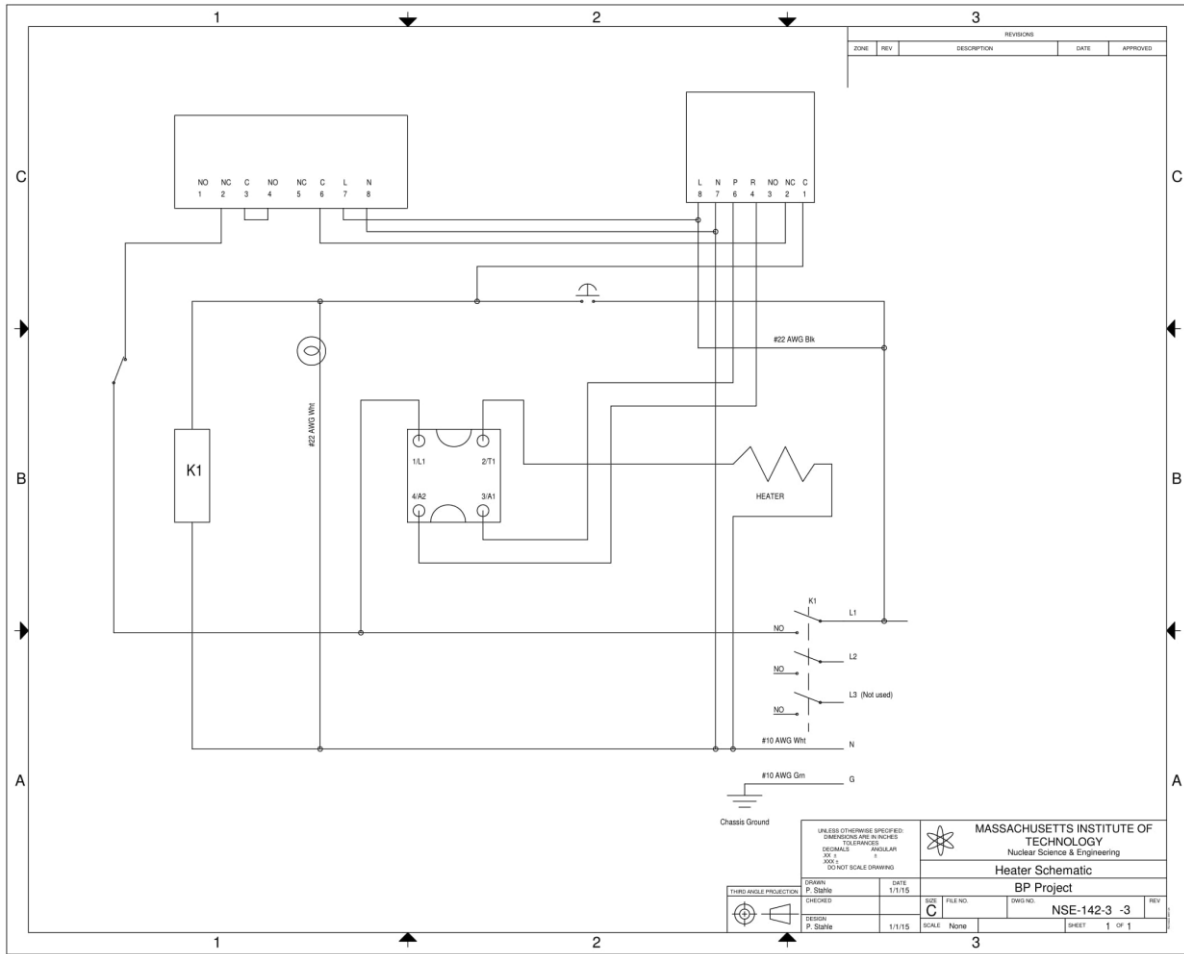


Figure 3-14: Circuit design of the temperature and pressure control system.

### 3.8.3 Data Acquisition and Loading Control System

A program was written using Visual Studio to record data obtained from the ACPD system and sensors, and to capture crack initiation. The user interface of the program is shown in Figure 3-15. The program allows users to setup the input parameters of the ACPD system including the

desired test frequencies (e.g. 1 kHz, 4 kHz, 16 kHz), the crack detection threshold (e.g. 0.5%), and the number of data points for baseline calculation. The program also allowed users to setup the loading condition, including the waveform of the loading, the mean load and the load amplitude. By coordinating the ACPD system and the loading system, this program was designed to capture crack initiation in the following way:

- (1) The program recorded the potential drop signal for one AC frequency and set the lock-in amplifier to the next input frequency and recorded the potential drop signal for the next AC frequency.
- (2) At the beginning of fatigue tests (or in the middle of the tests after the voltage signals stabilized), the program calculated the baseline value and standard deviation for each frequency using a specified number of data points (e.g.  $X=50$ ). The program kept monitoring the potential drop signals throughout the test.
- (3) When potential drop values for all frequencies exceeded a prescribed limit,  $r$  (e.g. 0.5%), of their corresponding baseline value for  $Y$  points in sequence, the program sent an order to the servohydraulic machine to stop the fatigue loading on the specimen. The specimen would be taken out from the autoclave for examination.

Here,  $X$ ,  $r$  and  $Y$  were values which were input by the user from the program interface, along with the desired frequency values. A schematic flow chart of how the control system work is in shown in Figure 3-16.

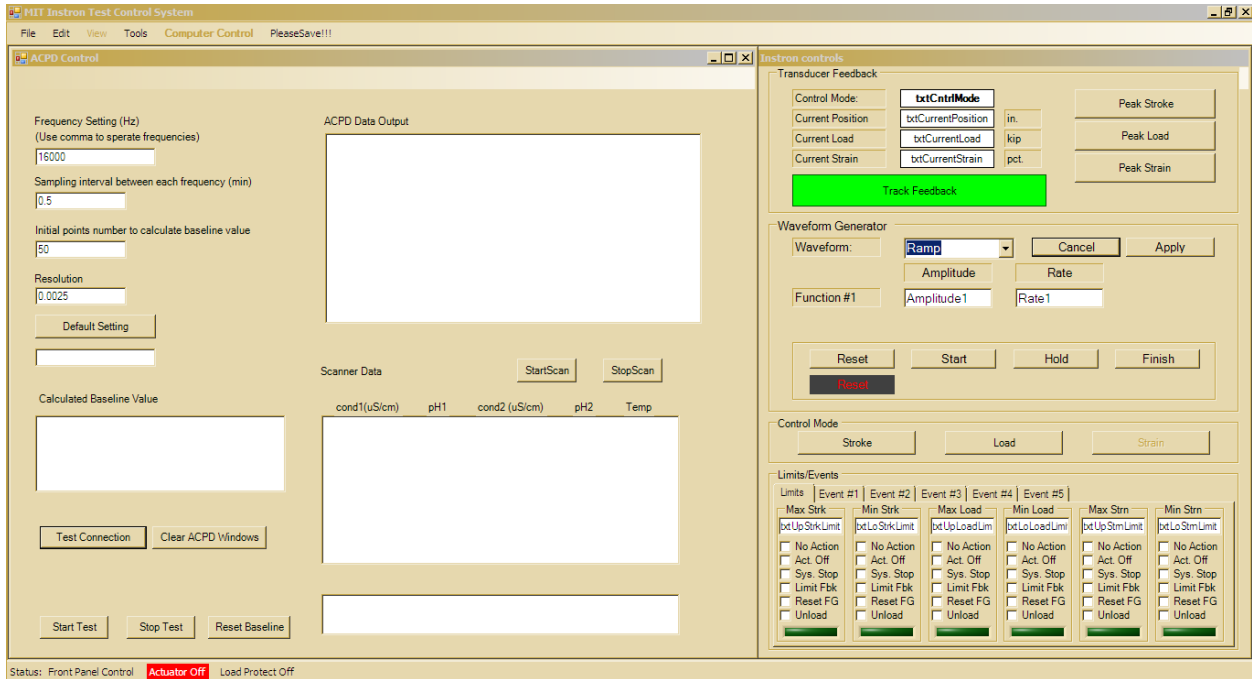


Figure 3-15: A screen shot of user interface of the data requisition and control program.

### ACPD Measurement System

### Fatigue Machine

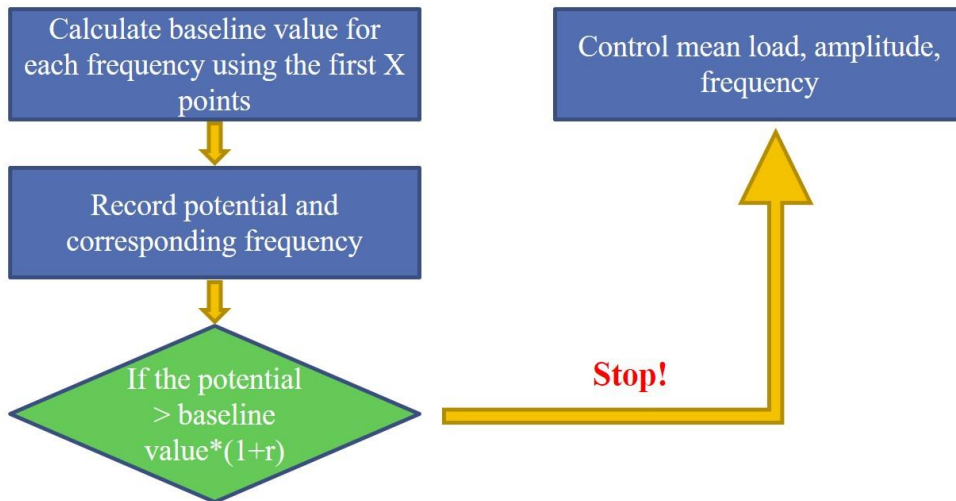


Figure 3-16: Flow chart showing how the ACPD system and the fatigue machine work together.

### 3.8.4 Autoclave Setup

An autoclave was built in order to contain the high pressure and high temperature environment. The autoclave was fabricated of Hastloy C22, which is an austenitic nickel-chromium-molybdenum-tungsten alloy and is corrosion resistant to NaCl solution [189]. The four-point

bending fixture, also fabricated from Hastelloy C-22 was designed and installed with the autoclave, along with a pH sensor and a pair of thermocouple. The setup of the autoclave is shown in Figure 3-17 and Figure 3-18.

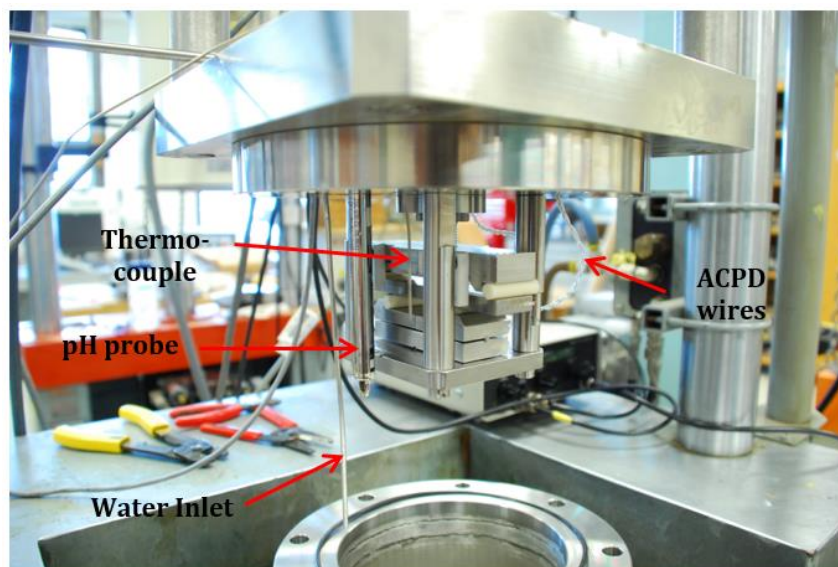


Figure 3-17: Inside of the autoclave



Figure 3-18: The cap of the autoclave.

## Chapter 4 Experimental Results

This chapter summarizes the experimental results in this research, including material characterization of the X65 steel, electrochemical tests and fatigue tests in different environments. It will also include some analysis and discussion of these results.

### 4.1 Material Characterization

#### 4.1.1 Microstructure and Vickers Hardness

The microstructure and hardness of the X65 piping material was analyzed for both the base metal and the weld. Figure 4-1 shows how the samples were sectioned from the original pipe and gives the direction of the surfaces which have been analyzed. Samples for microstructure observation of base metal were taken from different directions (transverse, longitudinal, circumferential directions, see Figure 4-1 for reference) and from different locations (outer, middle, inner surface) of the X65 pipe.

Microstructures of the base metal are shown in Figure 4-2 and Figure 4-3, and the microstructures of areas around the weld are shown in Figure 4-4. It was confirmed that the base metal structure of each direction on X65 piping was homogeneous and was mainly constituted by the polygonal and quasi-polygonal ferrite grains [190][191]. Average grain size of ferrite phase was approximately 5  $\mu\text{m}$ . In the case of the weld area, the heat affected zone was clearly observed next to the fusion line (Figure 4-4). The heat affected zone was constituted by mainly three regions (large grain region, small grain region and large grain region again) of different microstructures depending on their distance from the fusion line. The difference between microstructures in these three regions was caused by the history of heating on each region during the welding process. The width of heat affected zone was estimated approximately 2 mm starting from the fusion line.

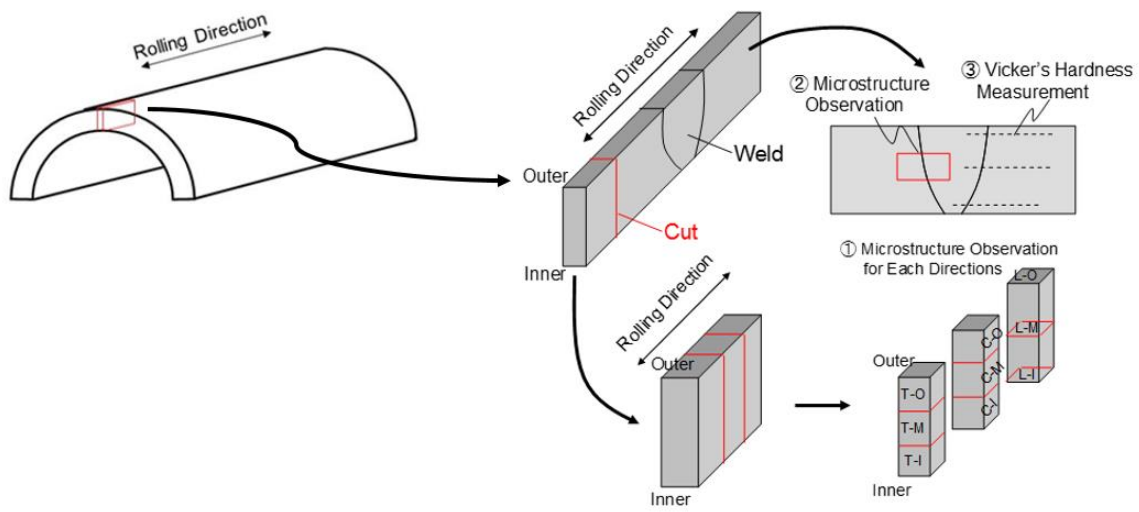
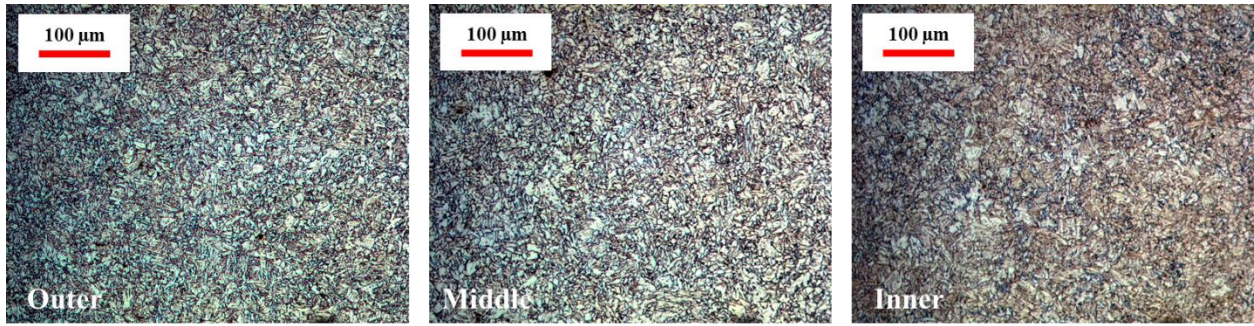
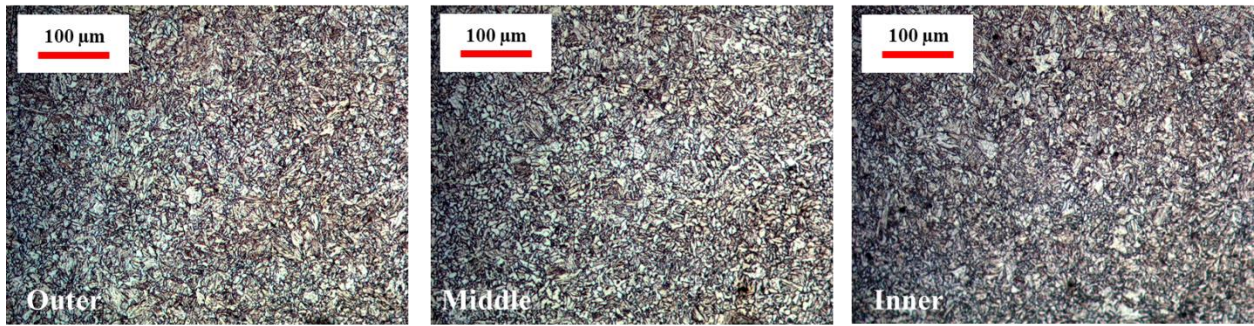


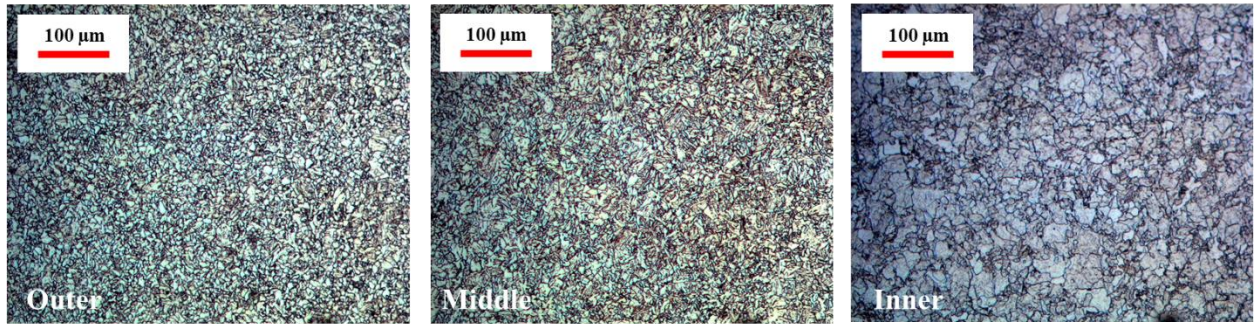
Figure 4-1: Diagram of sample sectioning for microstructural observation and Vickers hardness measurement.



(a) Transversal Direction of the Pipe



(b) Circumferential Direction of the Pipe



(c) Longitudinal Direction of the Pipe

Figure 4-2: Microstructures of the base metal of the X65 pipe at different locations.

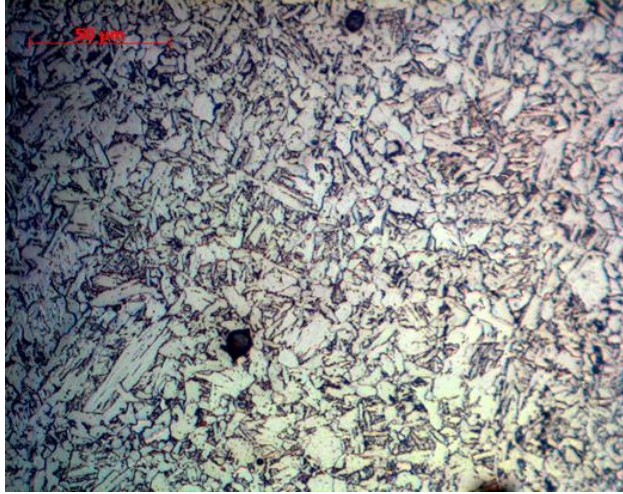
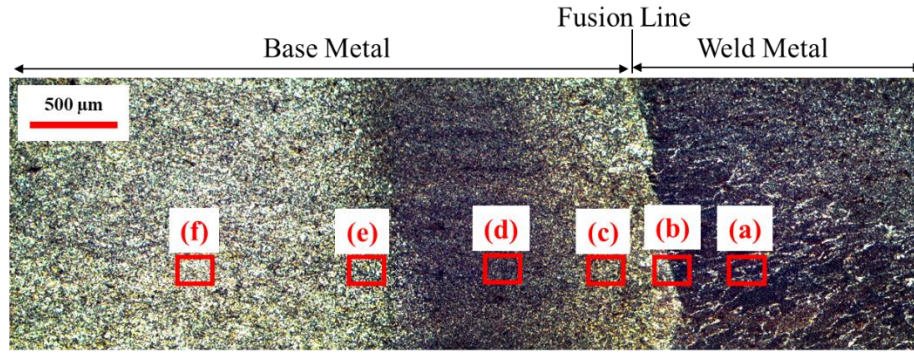


Figure 4-3: Microstructures of the base metal of the X65 pipe at higher magnification.



Microstructure around the Weld Metal

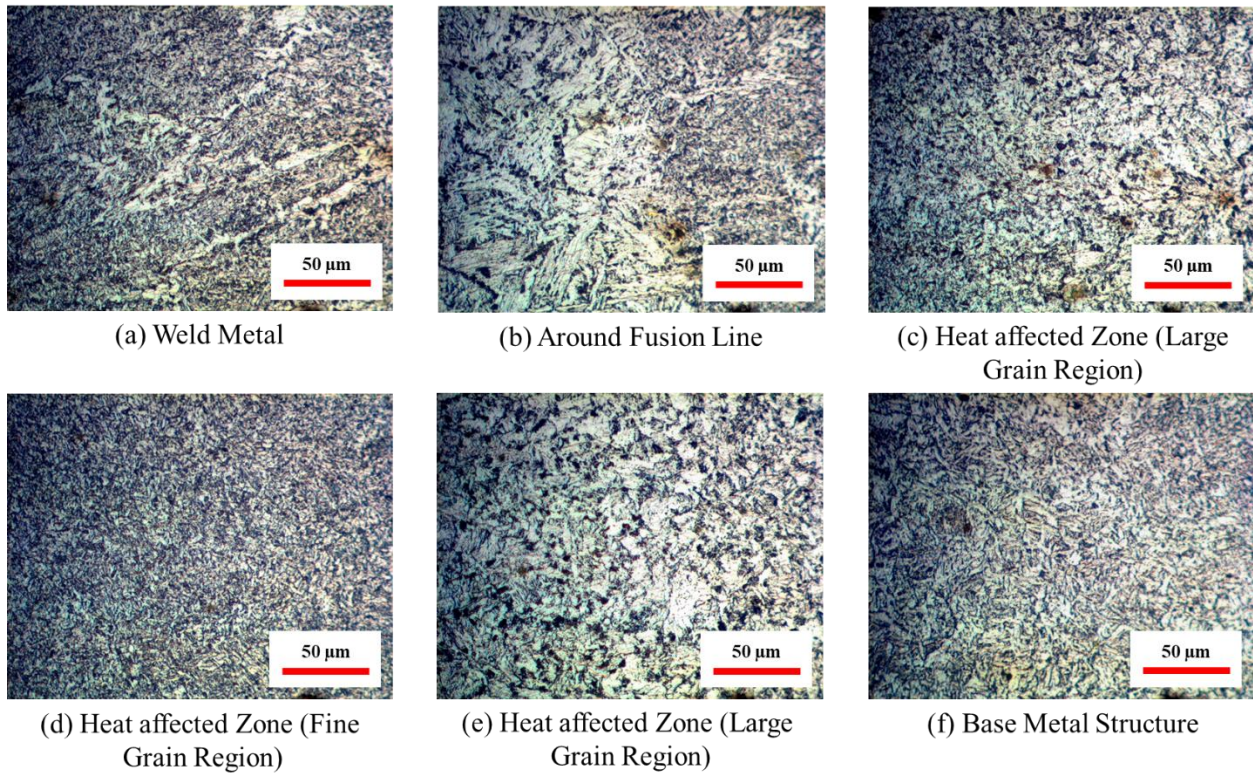


Figure 4-4: Microstructures of areas around the weld of the X65 pipe.

Results of Vickers hardness measurements are shown in Figure 4-5 to Figure 4-8. Hardness measurement was carried out according to the map that shown in Figure 4-5. The average Vickers hardness of the weld metal was approximately 250 Hv and the hardness on the fusion line of each specimens was around 260 Hv. Vickers hardness at the outer surface and the middle of the thickness decreased as the distance from the fusion line increased. The width of heat affected zone was estimated to be 2-2.5 mm. These results were in agreement with the results of microstructural observation around the weld. The Vickers hardness of the base metal at the outer surface and at the

middle is approximately 220 Hv, while the Vickers hardness of the base metal at the inner surface is approximately 240 Hv.

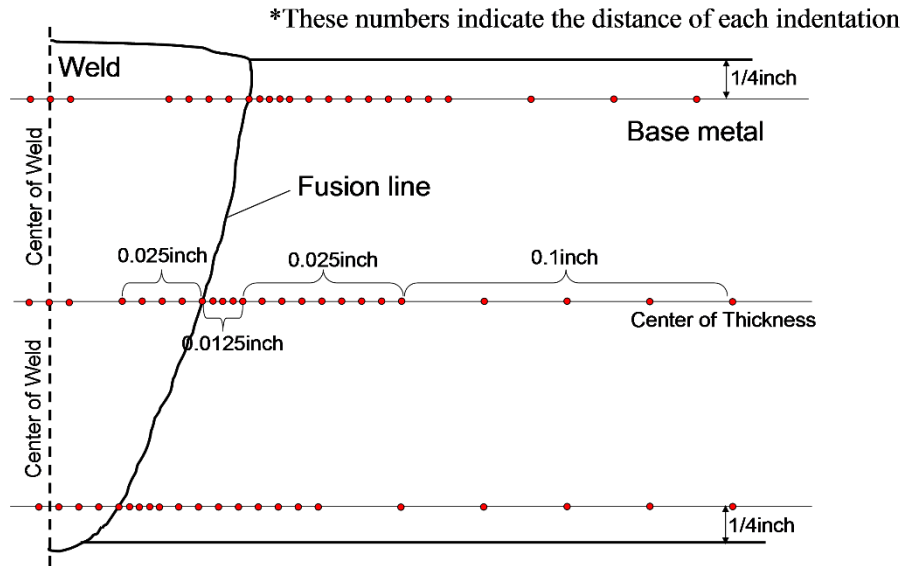


Figure 4-5: Schematic of Vickers hardness measurement map

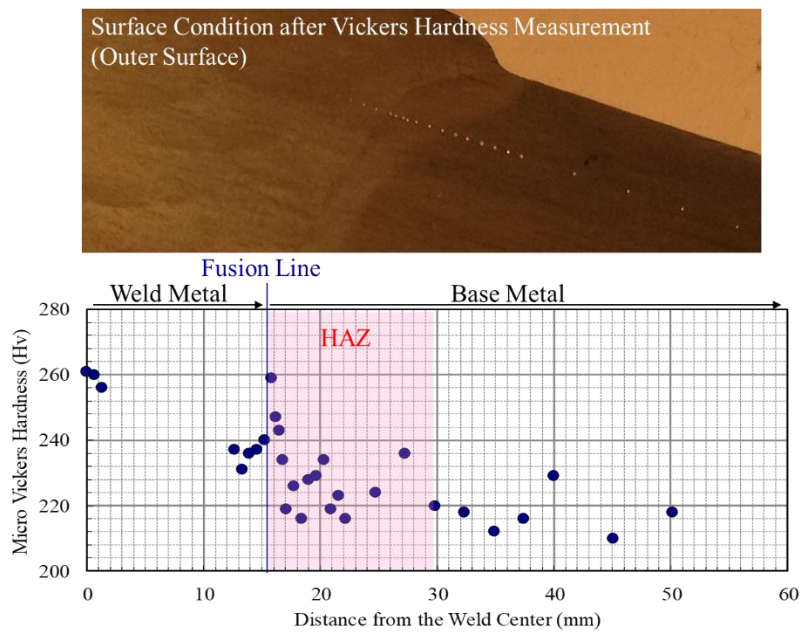


Figure 4-6: Hardness distribution around the weld (0.25 inch far from the outer surface)

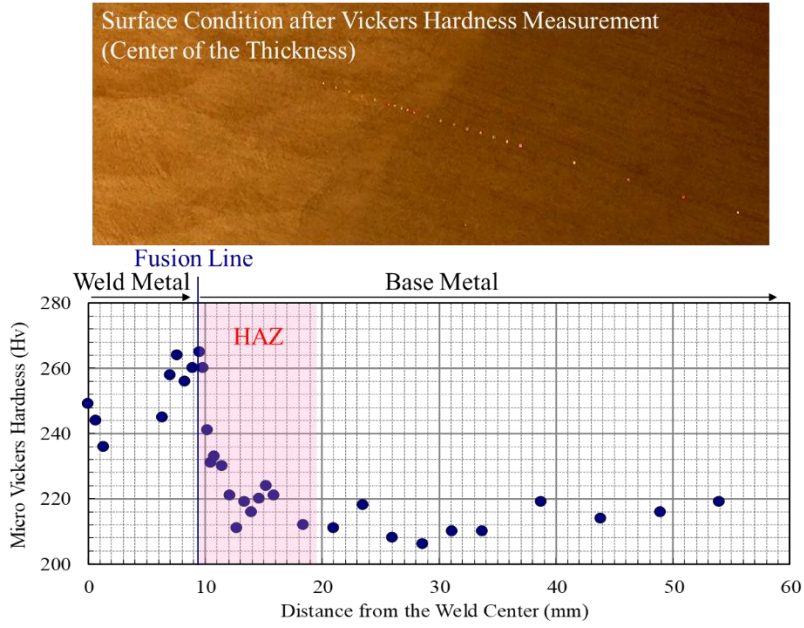


Figure 4-7: Hardness distribution around the weld (middle of the thickness)

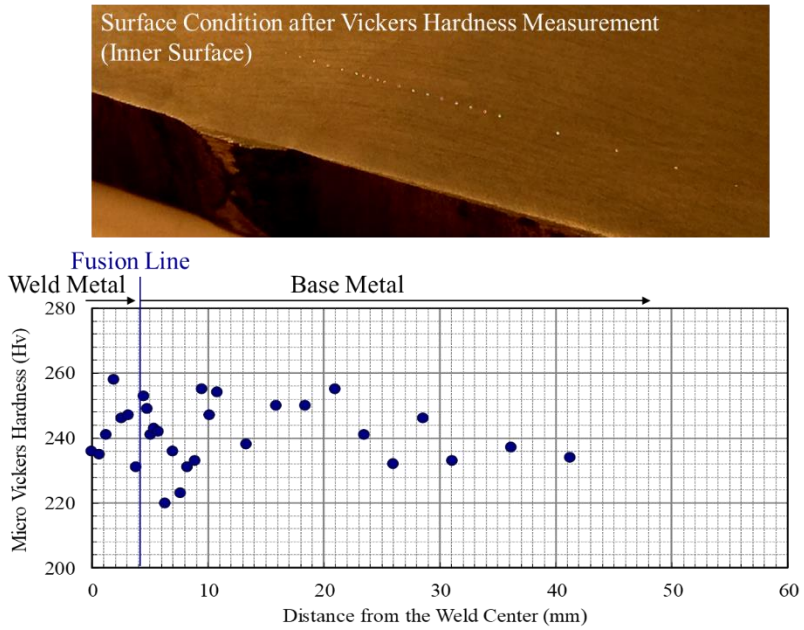


Figure 4-8: Hardness distribution around the weld (inner surface)

#### 4.1.2 Tensile Behavior

The deformation response of the X65 steel under monotonic loading was measured in air at room temperature at a nominal strain rate of  $6.7 \times 10^{-4}$  /s. A total of nine tests were carried out to obtain the average 0.2% yield strength. Figure 4-9 shows representative true and engineering tensile stress-strain curves for the steel. The material shows upper and lower yield points which is typical for steel with low carbon content [192]. The average 0.2% yield strength is  $521 \pm 16.3$  MPa.

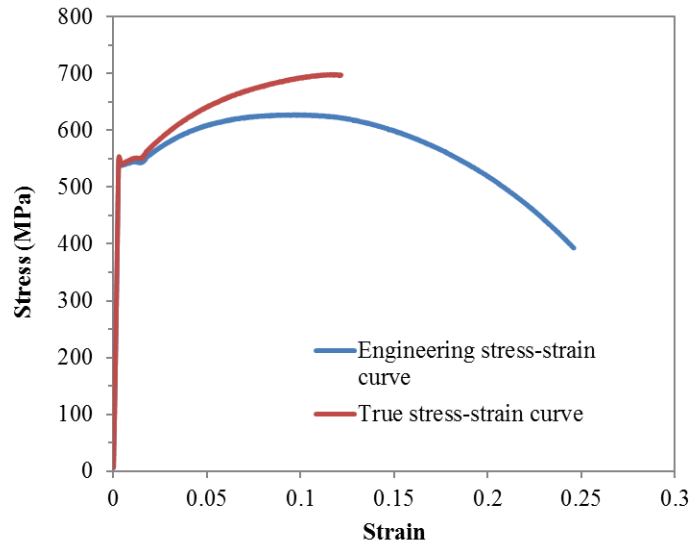


Figure 4-9: Tensile stress-strain curve for X65 steel at room temperature

## 4.2 Alternate Pit Generation Methods

In this research, two other electrochemical/corrosion methods were explored to make pits in the X65 steel specimens in a CO<sub>2</sub> environment. Note that the method finally settled on did not include a CO<sub>2</sub> environment. Although these two methods were not used to make actual pre-pit specimens for fatigue tests, some of description of the tests and their results are given in this section. These results shed some light on the electrochemical process of CO<sub>2</sub> corrosion of the steel, especially on the characteristics of the FeCO<sub>3</sub> corrosion layer which influenced the process at elevated temperature in the fatigue study.

### 4.2.1 Jiang et al. Method [193]

The first method was adopted from Jiang et al. [193], which basically includes three steps (1) Supersaturation: achieve a high concentration of Fe<sup>2+</sup> ion to cause supersaturation of FeCO<sub>3</sub>

(supersaturation factor (SS) >200). In this case, the  $\text{FeCO}_3$  particles which precipitate from the solution will deposit onto the specimen surface and form a compact  $\text{FeCO}_3$  layer. (2) Partial removal of the  $\text{FeCO}_3$  layer: After the formation of the surface layer, change the pH of the solution in order to decrease the SS to a very low level ( $\text{SS} < 0.4$ ), which will cause the dissolution of the layer. Because the dissolution rate is not uniform over the whole surface, some of the bare metal will be exposed to the solution earlier than the other, which forms a local anode. (3) Pit growth: Keep the SS in the grey zone ( $0.5 < \text{SS} < 1$ ) and let the bare metal part be corroded as it gradually becomes a pit because of galvanic corrosion. In this case, a galvanic couple forms between the bare metal (serves as anode) and the  $\text{FeCO}_3$ -covered surface (serves as cathode).

The method of Jiang et al. was applied and the actual procedure is described as follows:

- (1) Three sample “couples” were polished to 600 grit. The surface area for each sample was approximately  $1.5 \text{ cm}^2$ .
- (2) An electrochemical cell was filled with 0.7L 1% wt. NaCl solution and then heated to  $80^\circ\text{C}$ .  $\text{CO}_2$  gas was purged to the cell for 1 hour until the pH stabilized. The partial pressure of  $\text{CO}_2$  was 0.53 bar in this case. Deoxygenated NaOH was then added to cell to increase the pH to 6.4. Concentrated  $\text{FeCl}_2$  solution was added to the cell to achieve a supersaturation factor of approximately 300.
- (3) Stage I: The samples were immersed into the cell for 2 days for surface layer formation.  $\text{CO}_2$  gas was purged to the cell during the entire test.
- (4) Stage II: After two days, one coupon sample was taken out for surface characterization. The other two samples were switched to another cell with  $80^\circ\text{C}$ ,  $\text{CO}_2$ -deoxygenized, 1wt. % NaCl solution. The pH was adjusted to 5.0 by adding NaOH solution. No  $\text{FeCl}_2$  solution was added. In this case, the supersaturation factor would be very low (close to zero) and partial removal of the layer was expected.
- (5) Stage III: After 4 hours, the second coupon sample was taken out of the cell for surface characterization and the third sample was switched to a cell with  $80^\circ\text{C}$ ,  $\text{CO}_2$ -deoxygenized, 1 wt. % NaCl solution. The pH was adjusted to 6.0 and  $\text{FeCl}_2$  solution was added to achieve a supersaturation factor to 1. Under this condition, exposed bare metal is supposed to grow into a pit.
- (6) After 6.5 days for pit growth, the last sample was taken out for surface characterization.

The test cells are shown Figure 4-10. Two cells were used in order to eliminate the time to switch from one condition to the other. Figure 4-11 shows the sample surface after Stage I. As expected, because of the high saturation factor in the bulk solution in Stage I,  $\text{FeCO}_3$  precipitated and deposited on the sample surface. However, it was observed that under this condition, the corrosion layer did not completely cover the whole sample surface. Figure 4-12 shows some bare metal spots (bright areas) observed on the second sample after Stage II. Under the condition we used, the number of exposed bare metal spots was small.

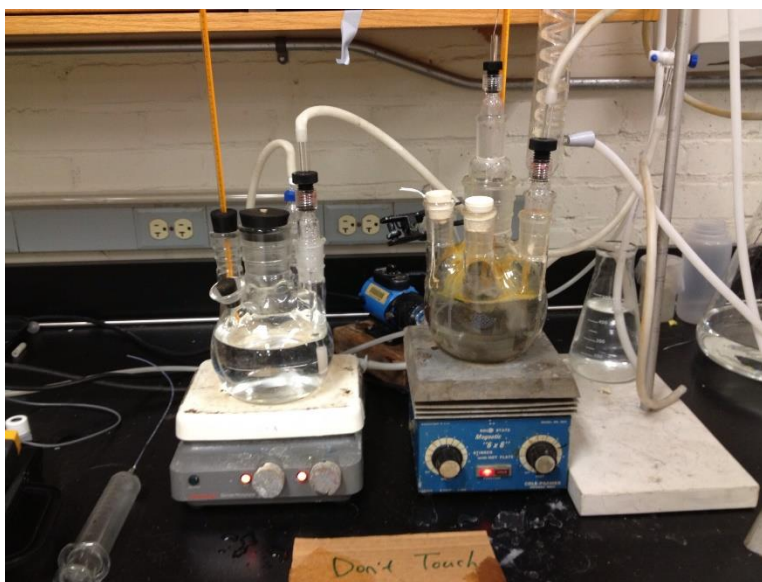


Figure 4-10: Setup of electrochemical cells.

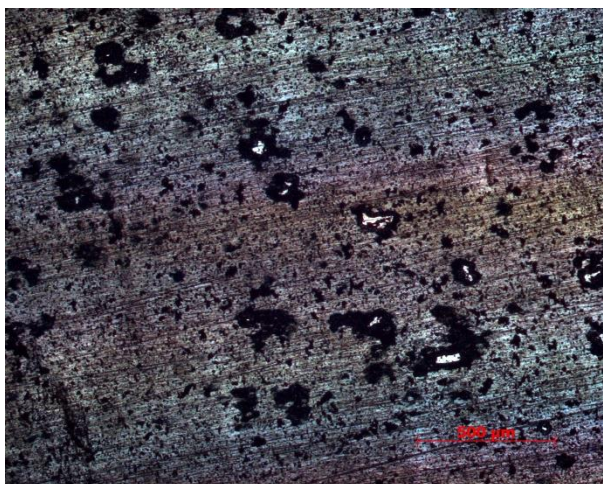


Figure 4-11: Surface morphology after stage 1.

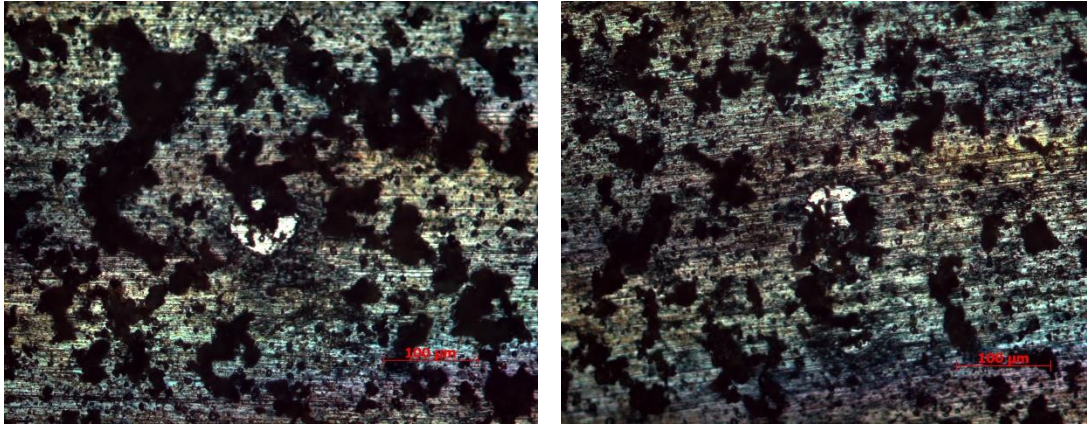


Figure 4-12: Some bare metal spots found after stage 2.

After Stage III, only one pit was found on the third sample surface, which is shown in Figure 4-13. It was suspected that the saturation level in Stage III was not low enough so some bare metal spots after Stage II were covered with the corrosion product. Although the bulk supersaturation factor was adjusted to 1, the supersaturation factor at the bare metal surface could be much higher because of the enhanced  $\text{Fe}^{2+}$  concentration due to corrosion. The areas with bare metal thus could be repassivated by forming a corrosion layer. As a result, only one pit could be observed after Stage III. In any case, this test still shows that it is possible to induce pitting on the steel surface by solely controlling the supersaturation factor of  $\text{FeCO}_3$ .

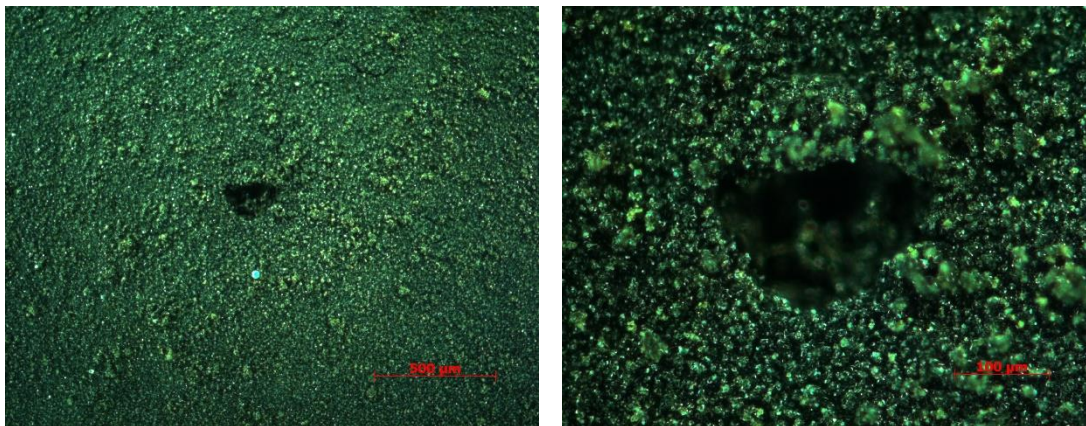


Figure 4-13: Pit found after stage 3.

#### 4.2.2 Anodic Polarization

The second method was to apply anodic polarization in an attempt to locally breach the corrosion layer locally to form pits, which was analogous to pitting in stainless steel. A coupon sample was immersed into 80°C, CO<sub>2</sub>-saturated 1% wt. NaCl solution. The corrosion rate of the sample was monitored using the linear polarization method during the test. At the beginning the supersaturation factor in the bulk was very low, but as corrosion continued, the concentration of Fe<sup>2+</sup> increased. At the surface of the sample, a high concentration of Fe<sup>2+</sup> could be achieved [194]. As a result, an FeCO<sub>3</sub> corrosion layer formed on the sample surface and the corrosion rate gradually decreased. When the measured corrosion rate was lower than 0.3 mm/year, which suggested that a protective corrosion layer was formed, a +200mV anodic potential was applied to the sample in order to breach the corrosion layer and initiate pitting. This scenario was similar to what happens to stainless steel when a potential higher than its pitting potential is applied.

Figure 4-14 shows the morphology of the naturally formed corrosion layer (without any external addition of Fe<sup>2+</sup> to the NaCl solution) after 12 hours. The corrosion layer exhibited a different characteristic from that deposited in the previous method as shown in Figure 4-11. The corrosion layer was like a “dry skin”, which had many cracks on the whole surface. This may be because when corrosion the layer started to grow, it started from different spots on the surface and formed many “islands” of corrosion product. When these “islands” grew and intersected each other, deep cracks were formed between them.

Figure 4-15 shows the change of the linear polarization resistance (LPR) and the corrosion rate (CR) versus immersion time. It can be seen that the natural layer initially formed was not protective, probably because of the existence of cracks. However, after approximately 30 hours, the corrosion rate of the sample decreased significantly. It was concluded that as the specimen corroded, the solution in the cell gradually reached saturation. FeCO<sub>3</sub> started to deposit on the surface and covered the cracks. The corrosion layer became protective and thus the corrosion rate decreased. A similar phenomenon has been observed by Palacios and Shadley [195], where they called the corrosion layer formed on the steel surface “the primary layer” and the layer formed by deposition “the secondary layer”.

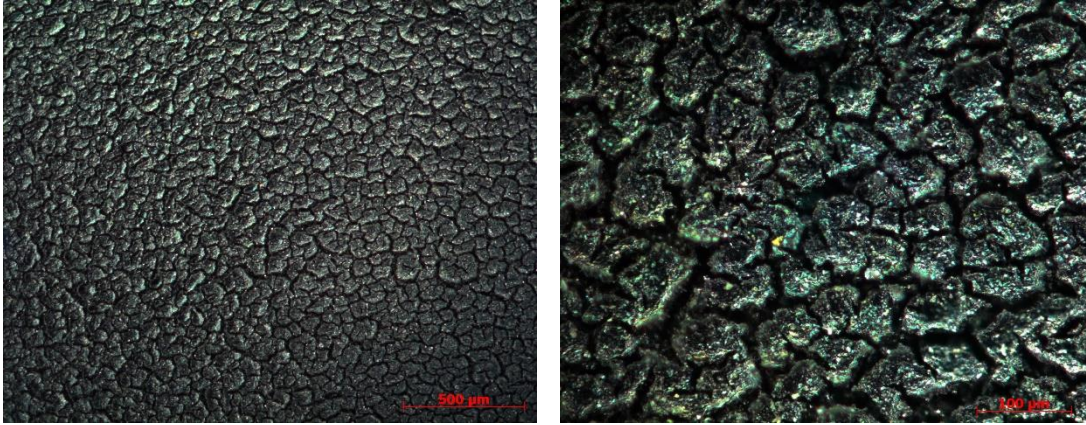


Figure 4-14: Photos of optical microscope showing the morphology of the naturally formed corrosion layer in CO<sub>2</sub>-saturated 1 wt.% NaCl solution at 80°C.

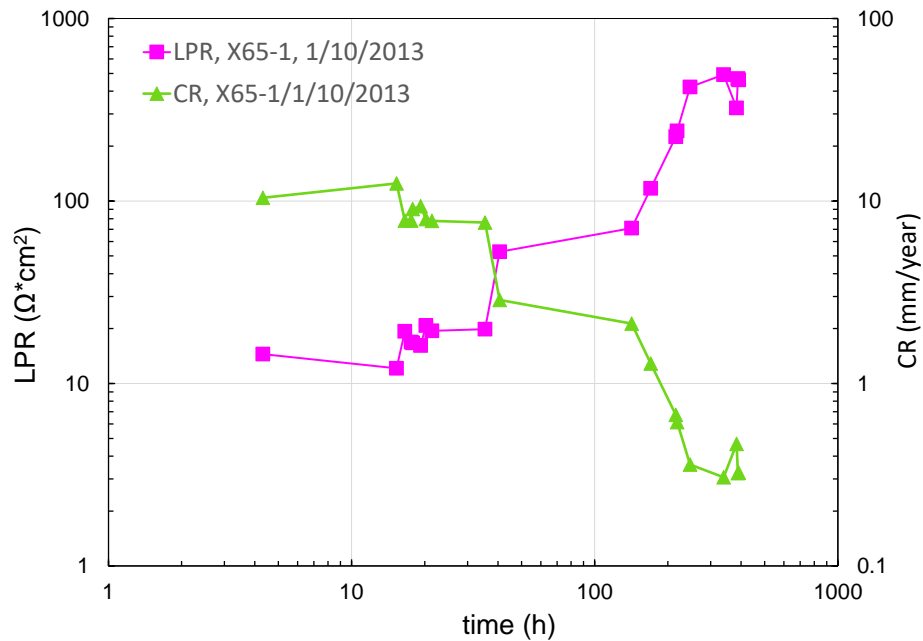


Figure 4-15: Change of LPR and CR versus immersion time. The corrosion rate decreased as the corrosion product layer formed.

When the CR is lower than 0.3 mm/year, an anodic potential was applied on the specimen in order to break down the corrosion layer. Different levels of anodic polarization have been applied, as shown in Figure 4-16. It was interesting to note that only when the anodic polarization was higher than a critical value would the corrosion current increase. This increase of corrosion current

may indicate that the corrosion layer was broken by the applied potential. As can be seen from Figure 4-16, this critical value under the test condition was about +200mV.

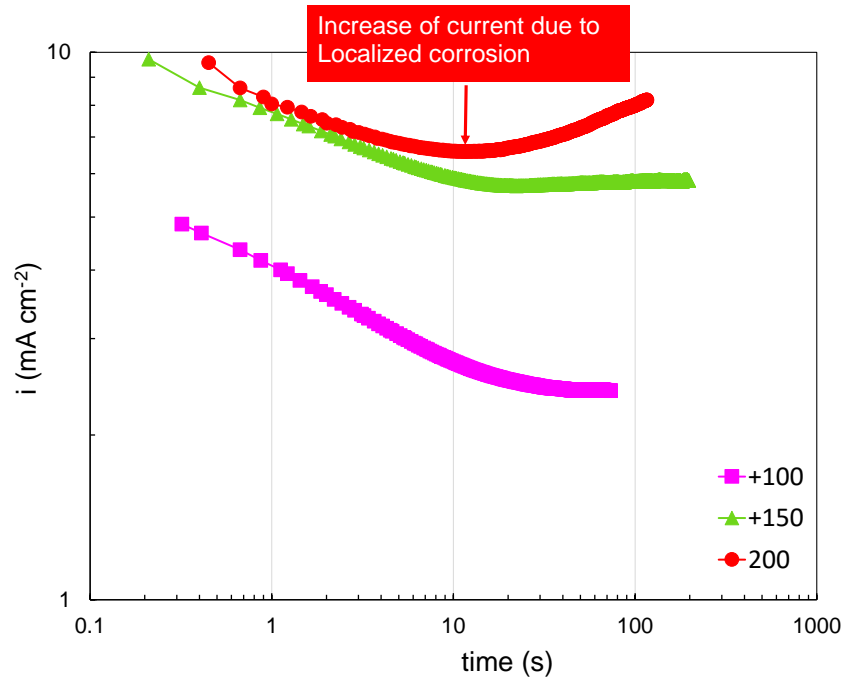


Figure 4-16: Potentiostat curves at different applied anodic potential levels. Increase of corrosion current was observed with a +200 mV applied anodic potential.

The results of surface characterization after the +180 mV and +200 mV applied anodic potentials is shown in Figure 4-17. The microscopic photos focus at the bottom of the pits to see whether the pits penetrate the corrosion layer(s). It can be seen that for +180 mV case, only the deposited layer breaks down but not the naturally formed layer, thus pitting cannot initiate. Unlike stainless steel whose oxide layer is only few nanometers thick, the FeCO<sub>3</sub> corrosion product layer can be as thick as 100~200μm depending on the total time and conditions of the test [196]. However, for +200 mV case, both layers break down and a pit has formed at the surface. These observations are consistent with the results of potentiostat curves.

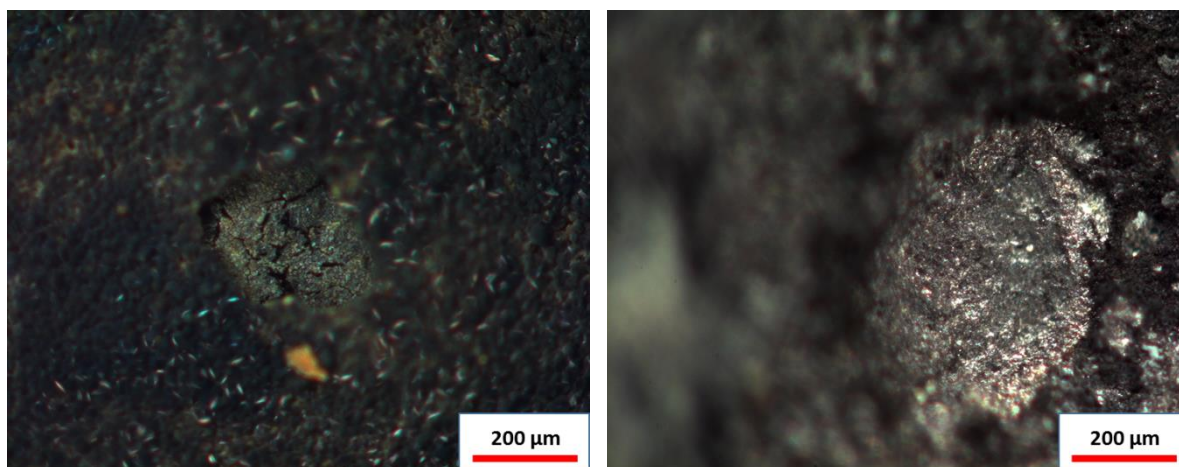


Figure 4-17: Surface condition after anodic polarization. Left: after +180 mV; Right: after +200 mV. A pit form at the bare metal surface was observed in the +200 mV case.

## 4.3 Fatigue Tests

### 4.3.1 Introduction of the Fatigue Tests

Most of the fatigue tests were performed using the same pit geometry, loading conditions and similar ACPD system setup. The pre-generated pits on the specimen had a diameter of  $500 \pm 50 \mu\text{m}$  and a depth of  $150 \pm 10 \mu\text{m}$ . The fatigue tests were conducted using four-point bending fixtures with maximum surface stress  $\sigma_{\text{max}}=413 \text{ MPa}$  (80% yield stress) and a stress ratio  $R=0.1$ . The loading frequency was 5 Hz. The AC current used was 0.5 or 1.0 ampere. The AC frequencies ranged from 250 Hz to 16 kHz, which corresponded to skin depths from 800  $\mu\text{m}$  to 100  $\mu\text{m}$ .

After testing specimens were sectioned, ground and polished to the approximate center of the pit in order to examine the pit/crack. Figure 4-18 illustrates how the original rectangular specimens were processed for crack observation or fractography.

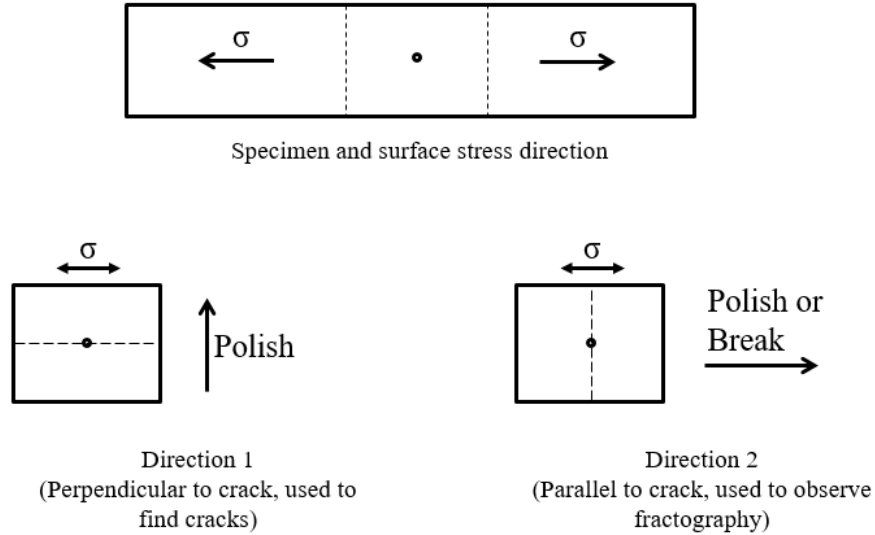


Figure 4-18: A schematic of sectioning the specimen.

#### 4.3.2 Fatigue Tests in Air at Room Temperature (RT)

Fatigue tests in air with pre-pitted specimens were performed with  $\sigma_{\max}=413$  MPa (80% yield stress), stress ratio  $R=0.1$  and load frequency  $f=5$  Hz. Up to  $1 \times 10^7$  cycles, no failure of the specimens was observed. One of the fatigue tests was stopped after  $1.7 \times 10^5$  fatigue cycles, and the specimen was sectioned and polished in Direction 1 to determine if there were any initiated crack. Figure 4-19 and Figure 4-20 show a small crack-like feature under optical microscope and scanning electron microscope (SEM). The dark area around the crack in the SEM photos was caused by the radiation of the electron beam. Notice the crack direction was perpendicular to the polishing direction so the small crack was unlikely to be an artifact caused by polishing. Closer examination of Figure 4-20 suggests that the path is along a grain boundary.

The observed crack size was approximately  $2 \mu\text{m}$ , which is less than the grain size. It is important to keep in mind that a crack initiated from a pit is necessarily a two-dimensional feature, and the photos here can only give a cross-sectional view of this feature. Small differences can be seen between the optical and the SEM photos, this is because the SEM images were taken after additional polishing of the sample using  $0.25$  and  $0.05 \mu\text{m}$  diamond suspensions. These differences imply that this crack feature is small not only in the direction perpendicular to the specimen surface, but also small in the direction perpendicular to the polishing/crack direction.

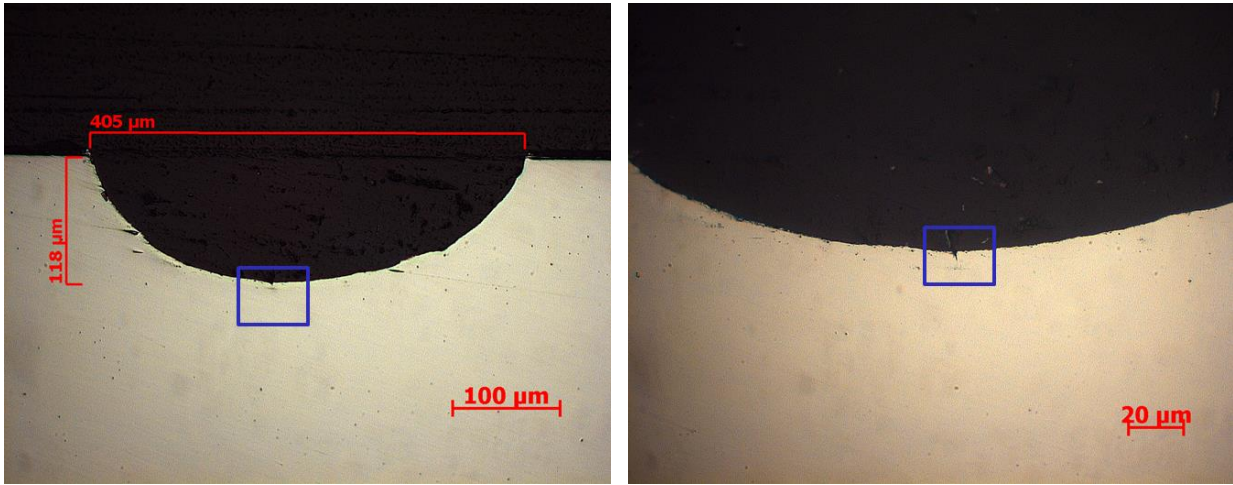


Figure 4-19: Photos of optical microscope showing small crack initiated in an air fatigue test. Left: 200x magnification; Right 500x magnification.

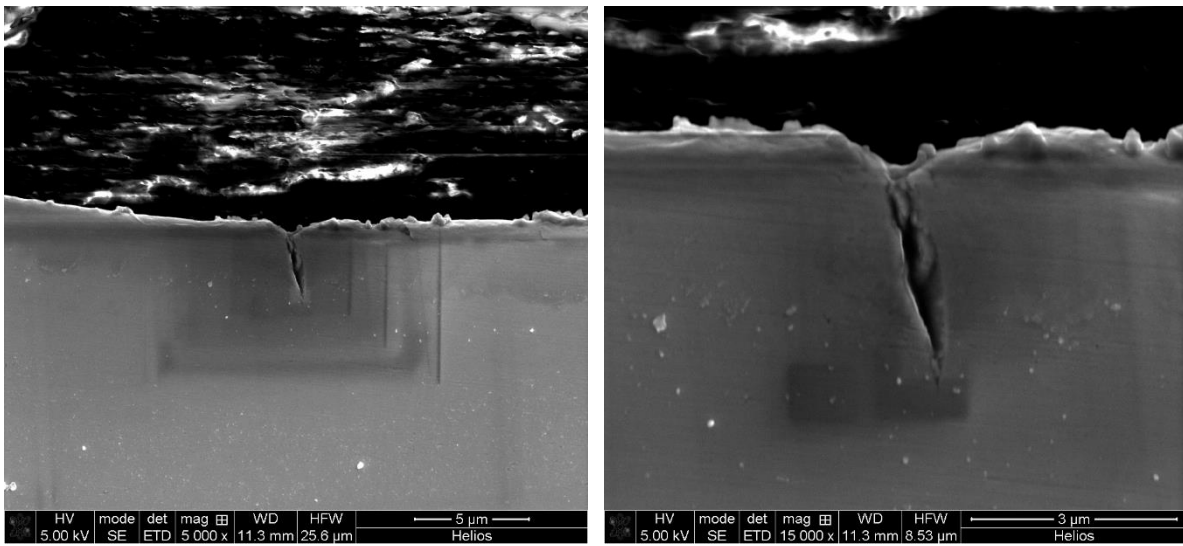


Figure 4-20: SEM images of pit cross section showing small crack initiated in an air fatigue test.

Another example of small cracks found after air fatigue testing is shown in Figure 4-21. This specimen was fatigued in air for  $1.5 \times 10^5$  cycles. Figure 4-21(a) shows the locations of the cracks found in the pit. One of the crack is observed at the bottom of the pit and the other one is observed near the pit mouth. The surface stress is along the vertical direction in Figure 4-21.

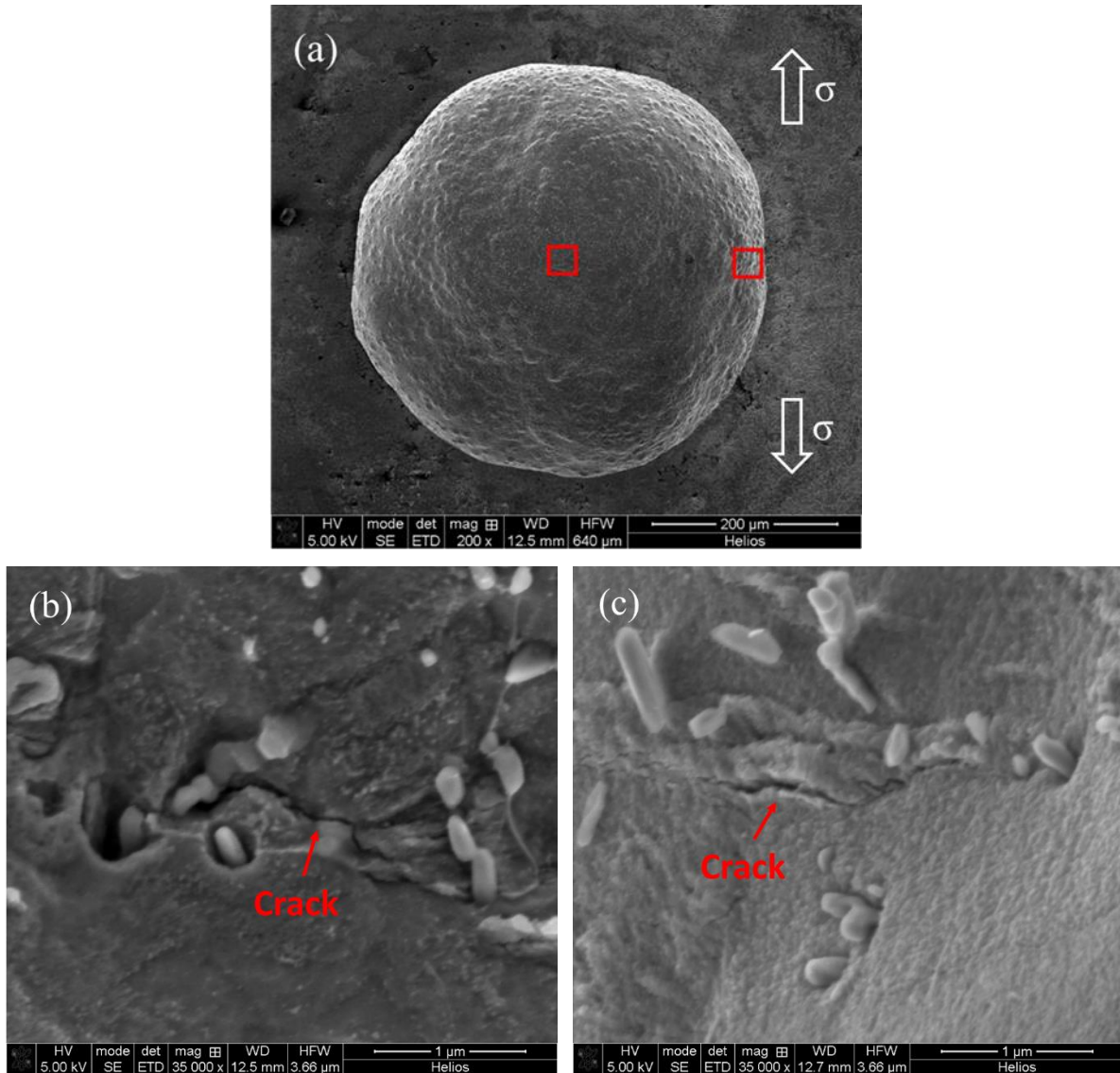


Figure 4-21: SEM images of top view of a pit showing small cracks initiated in an air fatigue test. (a) Locations of cracks with respect to the pit, the surface stress is along the vertical direction; (b) a small crack found at the bottom of the pit; (c) a small crack found at the near-mouth of the pit.

Based on these results it was concluded that for air fatigue tests under the loading conditions of the tests, small cracks (less than grain size) can initiate from pits but do not grow into long cracks. No failure of the specimens was observed up to  $1 \times 10^7$  cycles.

#### 4.3.3 Fatigue Tests in Aerated NaCl Solution at Room Temperature (RT)

Fatigue tests in aerated 1 wt. % NaCl solution at RT with pre-pitted specimens have been performed with  $\sigma_{\max}=413$  MPa (80% yield stress), stress ratio  $R=0.1$  and loading frequency  $f=5$  Hz. The ACPD system was used to record crack initiation and growth. Three frequencies were used in the tests, 250 Hz, 1000 Hz and 4000 Hz. The corresponding skin depths were estimated to be 800  $\mu\text{m}$ , 400  $\mu\text{m}$  and 200  $\mu\text{m}$  respectively.

Two sets of ACPD signals are shown in Figure 4-22, with a detection threshold of 1% and 0.25% respectively (the thresholds are indicated by the yellow dash lines). The x axis shows the number of the cycles and the y axis shows the relative change of the potentials compared to the averaged baseline value. The averaged baseline value was calculated using the first 50 data points either at the beginning of a test or at a specified time during a test but before any obvious deviation. In the first test, the baseline was recoded at the beginning of the test. In the second test, the baseline was recorded at  $1 \times 10^5$  cycles because the voltage signals were not stable before that. In both cases, the program was set to stop the fatigue loading when there were three data points in sequence for all frequencies that exceed the specified threshold. In the second test, only 1000 Hz and 4000 Hz frequencies were used, because it was found that these two frequencies were more sensitive than 250 Hz. In these two tests, the time constant of the lock-in amplifier was set to be 30 seconds (which mean the measured data point was averaged with signals within every 30 seconds). A data point was recorded every two minutes and then the lock-in amplifier was switched to the next frequency.

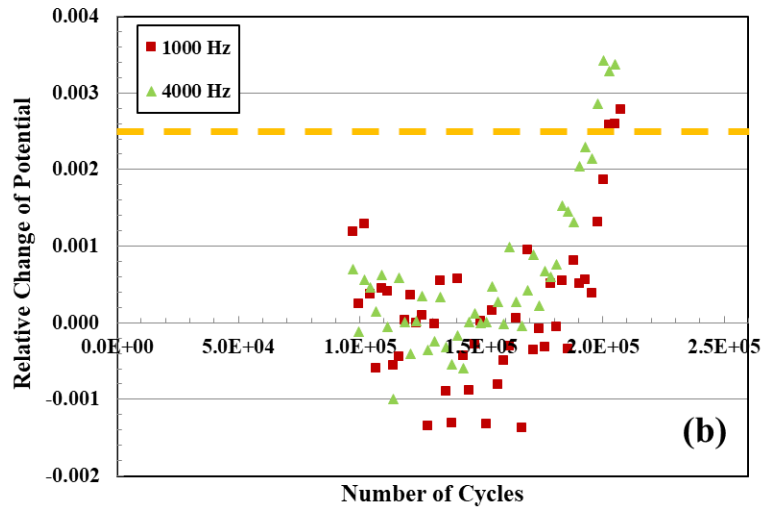
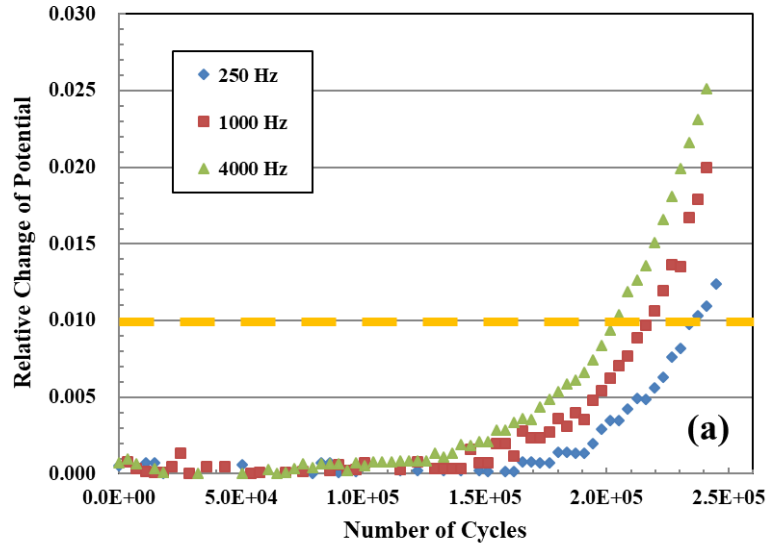


Figure 4-22: ACPD signals of two fatigue tests in areated NaCl solution using two detection thresholds. (a) 1%; (b) 0.25%.

After the fatigue tests were automatically stopped by the control program, samples were sectioned and polished for crack observation. Figure 4-23 shows the observed cracks corresponding to the ACPD data in Figure 4-22. In Figure 4-22 (a), a crack of 550  $\mu\text{m}$  in length was observed to initiate from the pit with the detection threshold of 1%, and in (b) a crack of 250  $\mu\text{m}$  in length was observed to initiate from the pit with the detection threshold of 0.25%. Both

cracks grow perpendicular to the direction of applied surface stress. From these results, it was estimated that the crack initiated from the pit after approximately  $1.5 \times 10^5$  cycles in aerated NaCl solution. The results show that the ACPD systems successfully captures the crack initiation and growth from the pits. Note that several smaller regions of localized degradation/corrosion are also present but with no initiated crack. These locations are likely crack “precursors” that could have served as locations for crack initiation. The morphology of these regions are unlike the regions observed in the air fatigue tests. However, it should also be noted that Figure 4-23 is a 2-dimensional look at a 3-dimensional process. Subsequent examinations showed that it is likely that multiple crack “precursors” developed with the possibility that more than one crack may have initiated but at a location not examined.

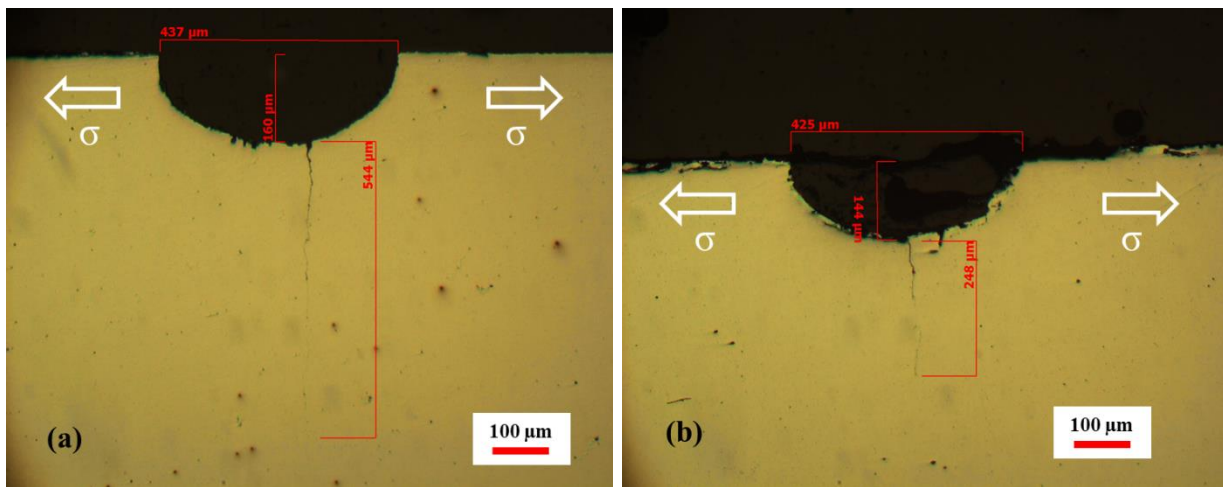


Figure 4-23: Crack initiation from pits. Left: 550  $\mu\text{m}$  crack corresponding to 1% detection threshold; Right: 250  $\mu\text{m}$  crack corresponding to 0.025% detection threshold.

#### 4.3.4 Fatigue Tests in CO<sub>2</sub>-saturated NaCl Solution at RT

Fatigue tests in CO<sub>2</sub>-saturated 1 wt. % NaCl solution at RT with pre-pitted specimens were performed with  $\sigma_{\text{max}}=413$  MPa (80% yield stress), stress ratio  $R=0.1$  and loading frequency  $f=5$  Hz. The saturation of CO<sub>2</sub> is referred to the condition of 1 bar CO<sub>2</sub> at RT which resulted in a dissolved CO<sub>2</sub> gas concentration of 0.030 M. The ACPD system was used to record the crack initiation and growth. Three frequencies were used in these tests, 1000 Hz, 4000 Hz and 16000 Hz. The corresponding skin depths were estimated to be 400  $\mu\text{m}$ , 200  $\mu\text{m}$  and 100  $\mu\text{m}$  respectively. To

obtain more data points, the time constant of the lock-in amplifier was set to be 5 seconds. Every 30 seconds, a data point was measured and the lock-in amplifier switched the next frequency.

The ACPD data and images of a pit after  $2.34 \times 10^5$  cycles in  $\text{CO}_2$ -saturated NaCl solution at RT are shown in Figure 4-24, Figure 4-25 and Figure 4-26. Figure 4-24 shows the ACPD signals measured during the test. The threshold value chosen was 1.5%. From the ACPD data, we can estimate that crack initiation from the pit occurred at approximately  $1.5 \times 10^5$  cycles. Figure 4-25 shows an SEM image of the top view of the pit after the test. The SEM image clearly shows that multiple cracks have initiated from the pit. The cracks were all perpendicular to the stress direction (which is along the vertical direction of the image). Figure 4-26 further shows three consecutive cross-sectional views of the pit. In accordance with the SEM image, multiple cracks were observed initiated from the pit. The largest size of the cracks was approximately  $100 \mu\text{m}$ . In this case, it was difficult for the ACPD signal to distinguish each crack, and the increase of ACPD signal can be considered to attribute to all initiated cracks.

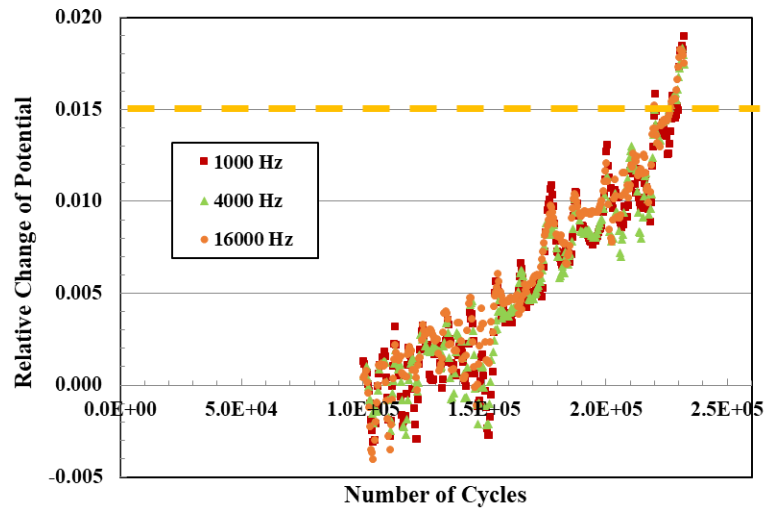


Figure 4-24: ACPD signals of a fatigue test in  $\text{CO}_2$ -saturated NaCl solution at RT.

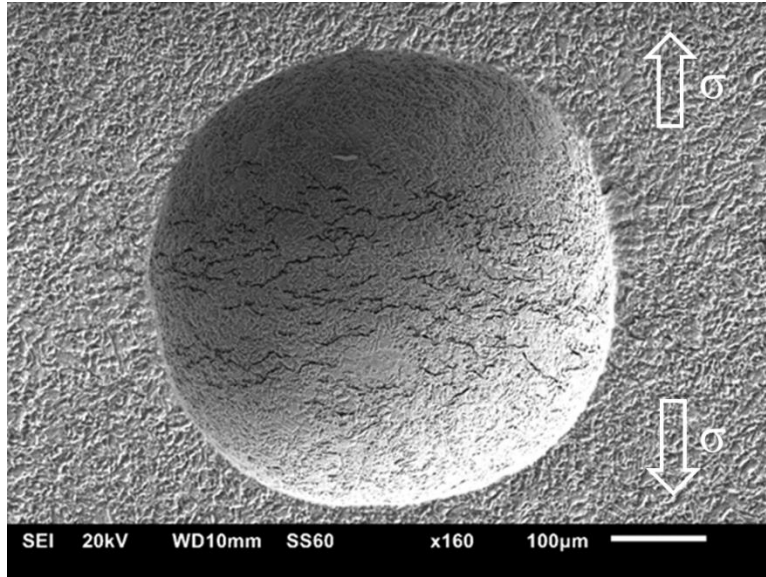
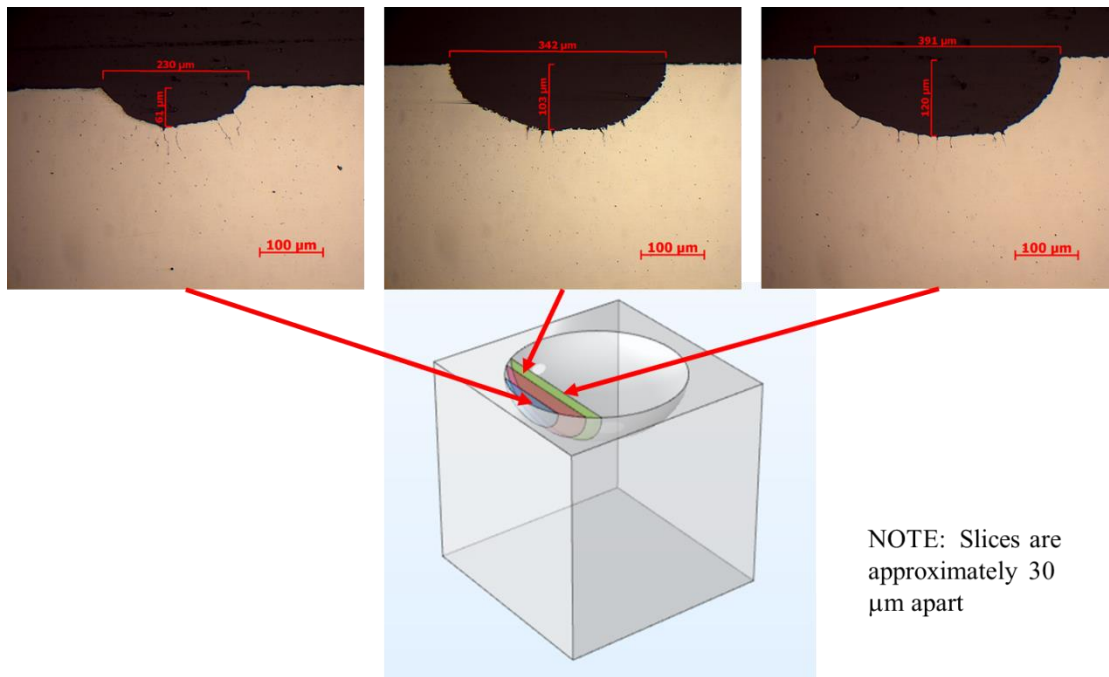


Figure 4-25: SEM image of a pit in CO<sub>2</sub>-saturated NaCl after  $2.34 \times 10^5$  cycles (top view). The surface stress is along the vertical direction.



NOTE: Slices are approximately 30 μm apart

Figure 4-26: Microscopic photos of three pit cross sections. The schematic shows the locations of the three cross sections.

The fracture surface of the crack was also examined for one of the sample tested in CO<sub>2</sub>-saturated NaCl solution at RT. In order to observe the fracture surface for this sample, the detection

level of ACPD was set to 5%. The ACPD signals for the test are shown in Figure 4-27. Crack initiation occurred after approximately at  $1.5 \times 10^5$  cycles, which is consistent with previous tests. Interestingly, it can be seen that the 16000 Hz signal was the most insensitive among the three, which seems to be contradictory to the theory [187] which predicts that higher frequency results in higher sensitivity for surface crack. However, by closer examination, we observe that when the crack was small (right after  $1.5 \times 10^5$  cycles), the 16000 Hz signal was more sensitive than the 4000 Hz and 1000 Hz signals, i.e. sensitivity (16000 Hz) > sensitivity (4000 Hz) > sensitivity (1000 Hz). This trend changed after approximately  $2.0 \times 10^5$  cycles, and became sensitivity (4000 Hz) > sensitivity (16000 Hz) > sensitivity (1000 Hz). After approximate  $2.4 \times 10^5$  cycles, sensitivity (4000 Hz) > sensitivity (1000 Hz) > sensitivity (16000 Hz). Finally, after approximately  $2.6 \times 10^5$  cycles, sensitivity (1000 Hz) > sensitivity (4000 Hz) > sensitivity (16000 Hz). One can see that as the crack grew larger, the lower frequencies became more sensitive. This may be explained by the combination effect of AC and DC potential drop [171]. ACPD picks up the length of the surface crack, while the DCPD picks up the reduction of the conductive cross section of the specimen. When the crack is small, the reduction of cross section is negligible, thus higher frequency is more sensitive to the crack growth. However, as the crack grows longer, the reduction of cross section is significant, and the DC effect become important. The DC effect favors low frequencies (or larger skin depths), the lower frequencies will become more sensitive for longer cracks. The transition of sensitivity is related to the size of the crack compared to the cross section of the specimen. For infinite cross section, as considered in [168][187], higher frequencies will be more sensitive to cracks. This reverse of sensitivity did not show up in the previous the ACPD signals in aerated NaCl solution tests because the cracks were not large enough.

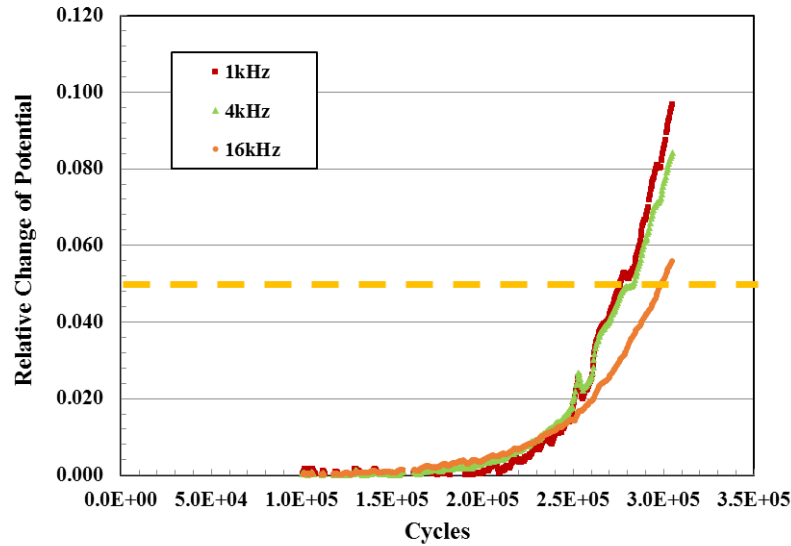


Figure 4-27: ACPD signals of a fatigue test in CO<sub>2</sub>-saturated NaCl solution at RT.

To observe the fracture surface, the specimen was further fatigued in air after removal from the autoclave in order to grow the crack and capture the initial crack without distortion. After the crack extended to almost the edge the specimen, the air fatigue test was terminated. The specimen was then placed in liquid nitrogen for about ten minutes. The specimen was then mechanically broken. The specimen snapped into two halves along the crack surface. The fracture surfaces related to environmental fatigue and later air fatigue could then be examined by optical and SEM. Figure 4-28 shows the fracture surface of the environmental fatigue. Figure 4-29 and Figure 4-30 show SEM images of the fracture surface at different magnifications. From these images, a series of radiating ridges from the edge of the pit can be clearly observed. The ridges start from different locations along the perimeter of the pit but not from a single point of the edge. It is concluded that the crack grew fairly uniformly from multiple initiation points around the edge of pit and did not likely to start from one very local point at the edge and extend to the whole pit perimeter.

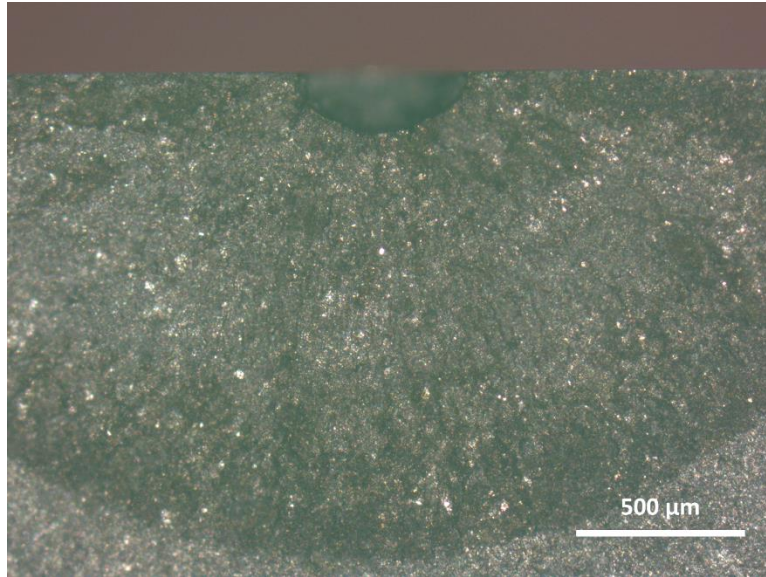


Figure 4-28: Optical microscope photo of the fracture surface of a sample tested test in CO<sub>2</sub>-saturated NaCl solution at RT. The brighter area at the bottom of the photo is fracture surface of faitigue in air.

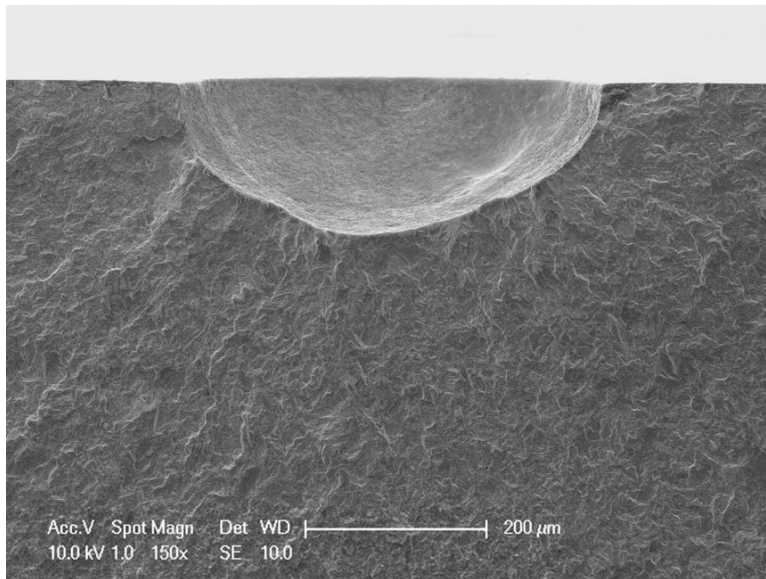


Figure 4-29: SEM image of the fracture surface of the same sample.

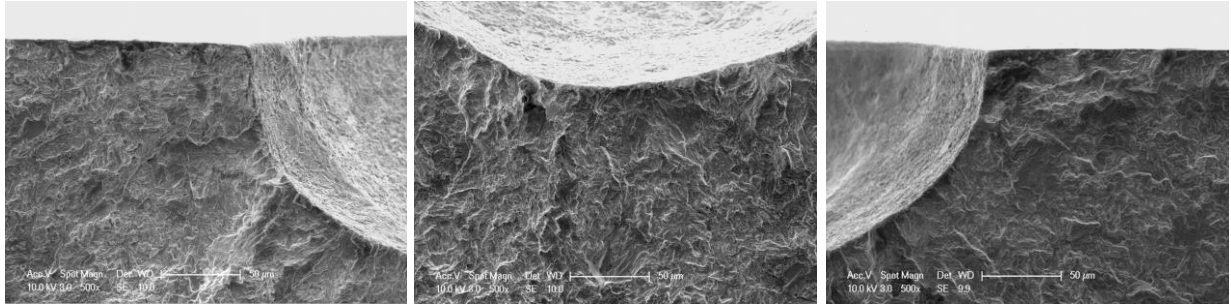


Figure 4-30: SEM images of the fracture surface at higher magnification.

#### 4.3.5 Fatigue Tests in CO<sub>2</sub>-saturated NaCl Solution at 120 °C

Fatigue tests in CO<sub>2</sub>-saturated NaCl solution at 120 °C with pre-pitted specimens were performed with  $\sigma_{\max}=413$  MPa (80% yield stress), stress ratio  $R=0.1$  and loading frequency  $f=5$  Hz. For exposures up to  $5 \times 10^6$  cycles, crack initiation was not detected by ACPDs. One of the fatigue tests was stopped after  $1.7 \times 10^5$  fatigue cycles, and the specimen was sectioned and polished in Direction 1 (See Figure 4-18) to determine if there were any initiated cracks.

Figure 4-31 and Figure 4-32 show optical microscope and SEM images around the pit perimeter. The SEM image was provided by GE Global Research staff using a Hitachi SU-70 SEM with 12 kV accelerating voltage. Multiple small crack or crack-like features are observed around the bottom of the pit. Notice that in the current cross section, the bottom of the pit was in tension while the mouths of the pit were in slight compression. The size of these small cracks were approximately 10  $\mu\text{m}$ , and were less than or comparable to the grain size. Excessive corrosion product can be observed on the surface of the pit, which was likely FeCO<sub>3</sub> considering the temperature and CO<sub>2</sub> concentration of the test [43].

It is concluded that for fatigue tests in CO<sub>2</sub>-saturated NaCl solution at 120 °C under the considered loading conditions, small cracks (at the level of grain size) can initiate from pits but do not grow into long cracks, which is similar to what we saw in air fatigue tests. No failure of the specimens were observed up to  $5 \times 10^6$  cycles.

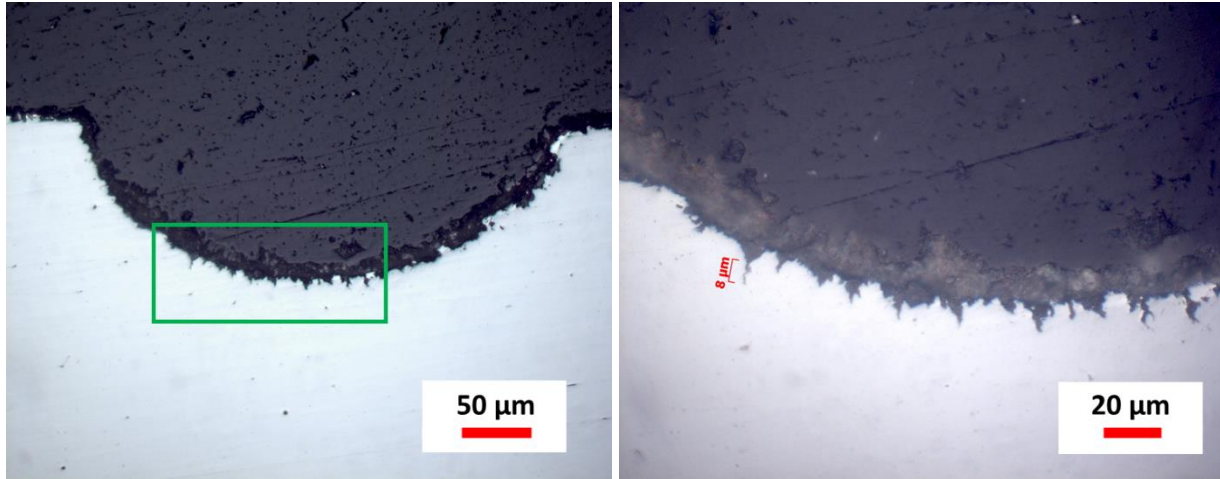


Figure 4-31: Optical microscope photos of the pit cross section after  $1.7 \times 10^5$  cycles in  $\text{CO}_2$ -saturated NaCl solution at  $120^\circ\text{C}$ . The figure on the right is a zoom-in view of the green box area on the left.

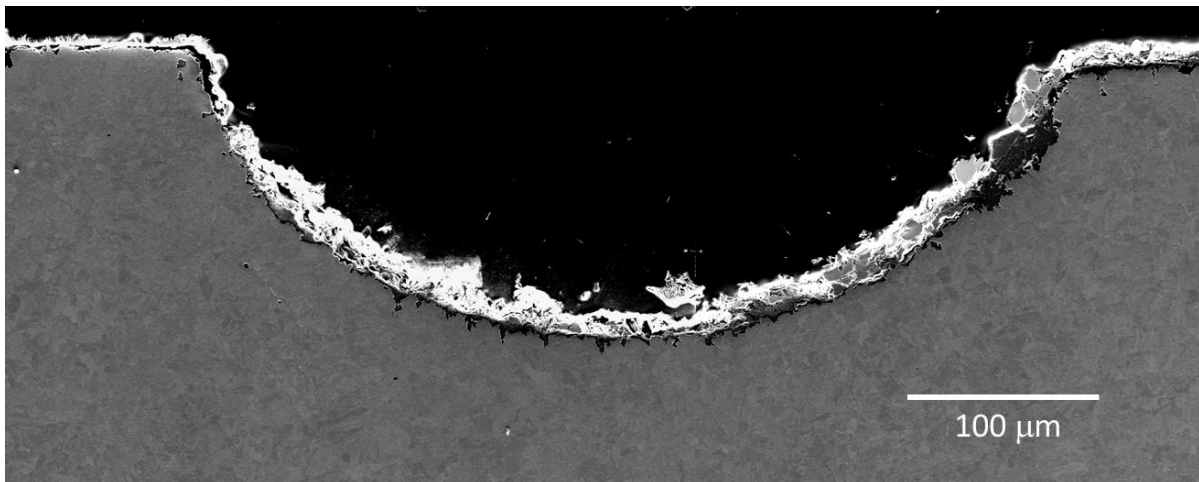


Figure 4-32: SEM image of the pit cross section after  $1.7 \times 10^5$  cycles in  $\text{CO}_2$ -saturated NaCl solution at  $120^\circ\text{C}$ .

#### 4.3.6 Summary of the fatigue tests in different environments

- (1) In all four environments considered, crack initiation was detected/observed after  $\sim 1.5 \times 10^5$  cycles, which indicates that the crack initiation process is mainly controlled by mechanical factors (e.g. pit geometry, loading conditions).
- (2) Subsequent crack growth was observed in aerated and  $\text{CO}_2$ -saturated NaCl solution at RT, but not in air or in  $\text{CO}_2$ -saturated NaCl solution at  $120^\circ\text{C}$ .

- (3) Non-propagating small cracks were observed in air fatigue and CO<sub>2</sub>-saturated NaCl solution at 120 °C. The size of these small cracks were comparable or smaller than the grain size of the X65 steel. Compared to air fatigue, multiple crack initiation sites were observed in the CO<sub>2</sub>-saturated NaCl solution at 120 °C, showing the effect of the corrosive environment.
- (4) Closer examination of the crack initiation in aerated NaCl solution shows that crack initiated from finer precursor at the perimeter of the pit (e.g. Figure 4-23), which may be a result of corrosion-fatigue interaction [94].
- (5) Examination of the fracture surface of the test in CO<sub>2</sub>-saturated NaCl solution at RT shows the crack initiated at multiple sites which linked up at an early stage and then grew uniformly from the edge of the pit.

A more detailed discussion of the crack initiation behavior and the comparison with other literature results will be made in Chapter 7.

#### **4.4 Conversion of ACPD Data to Crack Growth Rate**

While the ACPD system can capture crack initiation, as well as subsequent crack growth, it will be helpful if we can convert the ACPD signals into crack length and crack growth rate. However, the geometry (pit and crack) is complicated in our case, and as far as the author knows, there is no simple formula that can be used directly. In order to obtain the crack length and crack growth rate data, the COMSOL Multiphysics software was used to model/calibrate the change of potential drop versus crack depth.

To calculate the AC potential drop across the defect (pit/crack), it is important to account for the AC current distribution in the specimen and around the defect. However, full accuracy modeling of AC current can be quite complicated because of the mesh requirements within the small skin depth [197]. COMSOL offers an impedance boundary condition (IBC) which is suggested for high frequency applications [198]. This boundary condition assumes that all current flows at the surface of the conductor, so there is no need for any mesh within the conductor. This significantly simplified the meshing of the complex pit/crack geometry. However, using this boundary condition may result in some limitations which will be further discussed below.

A schematic of the COMSOL model setup is shown in Figure 4-33. The rectangle represents the steel specimen, with the wire connecting its two ends. The closed circuit along with the air (not shown in the figure) is simulated in order to insure the correct electromagnetic field around the specimen. A power source is implemented in the loop with fixed current output. The defect (pit or crack) is placed at the upper surface of the sample and the potential drop is calculated with a line integral of the electric field across the defect from one voltage probe to the other. In order to simplify the situation, we only consider one major crack at the pit. A zoom-in view of the pit and crack with mesh is also shown in Figure 4-33.

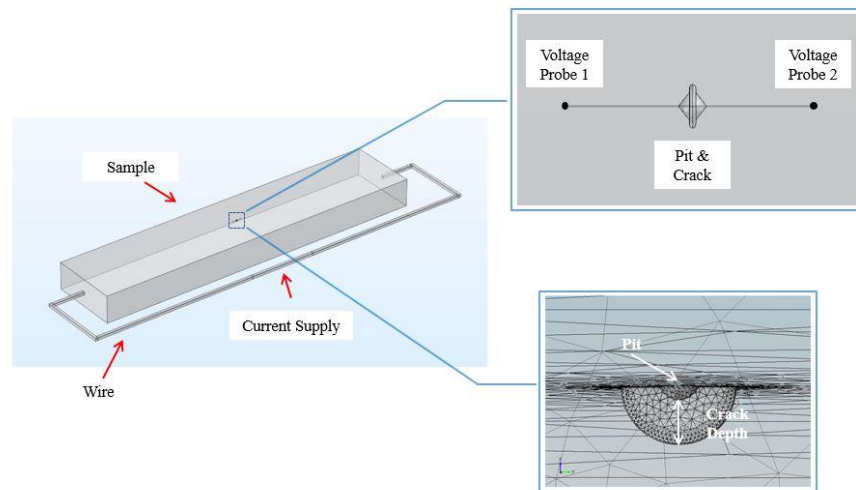


Figure 4-33: Model setup in COMSOL

As a benchmark simulation, we first calculated the potential drop across a hemispherical pit with different sizes (no crack). The results are shown in Figure 4-34. As predicted by Collins et al. [199], the potential drop remains unchanged as the pit depth increases. Although the path of the current for one voltage probe to another across the pit was longer compared to a flat surface/no-pit situation, the current density along the path decreased as the current spread and wrapped around the pit. The potential drop, which was the product of current path and current density, remained unchanged. Figure 4-34 also shows that the amplitude of the voltage approximately doubles as the frequency increases by four times. This is because as frequency increases, the skin depth and thus the effective cross section of the conductor decreases. According to the Ohm's law, the resistance between the two probes increases. For fixed current, the voltage drops between the two probes

thus increases. Because the skin depth is proportional to the inverse of square root of frequency (see (Eq. 2-28)), when the frequency increases by four times, the voltage drop doubles.

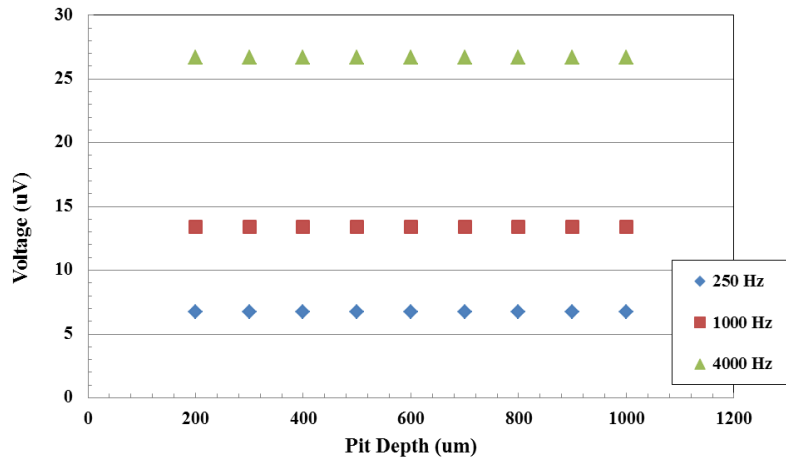


Figure 4-34: Change of ACPD signals with different sizes of pits.

The current simulation results show that the ACPD signals will not change when the pit grows as long as it remains hemispherical [199]. This is actually favorable in our case because our primary concern is to measure pit-to-crack transition. In the case where direct current is employed, both pit and crack growth will be detected. The combination of DC/ACPD is likely to allow the detection of pit growth followed by crack initiation. The use of the combined DC/ACPD technique is considered as future work.

Another benchmark test was done with 1-D cracks which go through the width of the specimen. The potential drop across the crack was calculated for different crack depths. The calculated change of voltage for different frequencies and different crack depths is shown in Figure 4-35.

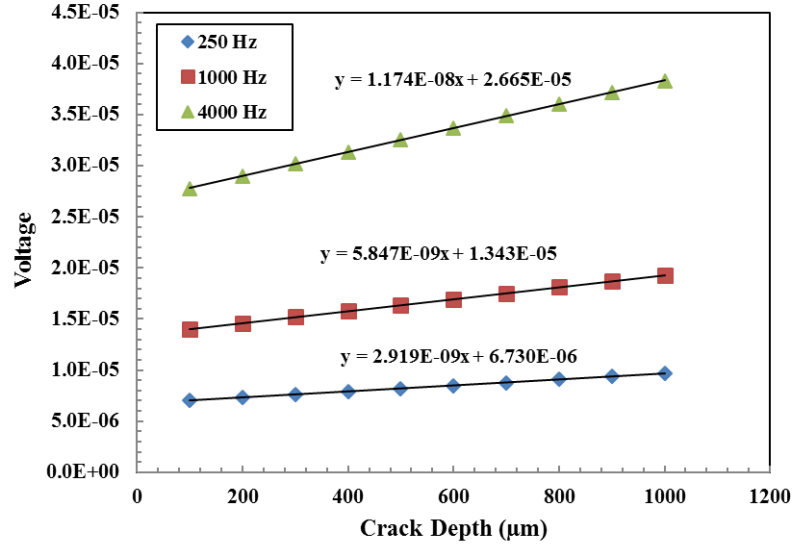


Figure 4-35: Change of ACPD signals with different sizes of 1D cracks.

To examine whether the model gives reasonable results, notice that for an ideal 1D crack [200]:

$$a = L \left( \frac{V}{V_0} - 1 \right) \quad (\text{Eq. 4-1})$$

where  $a$  is the crack depth,  $2L$  is spacing between the two voltage probes,  $V_0$  is the voltage with no crack, and  $V$  is the voltage with the crack. From (Eq. 4-1), we have:

$$V = \frac{V_0}{L} a + V_0 = p * a + q \quad (\text{Eq. 4-2})$$

which means that the voltage should change linear with the crack depth. Compare (Eq. 4-2) with the linear fitting in Figure 4-35, the fitting parameters,  $p$  and  $q$  should satisfy:

$$\frac{p}{q} = \frac{1}{L} = \frac{1}{2 \text{ mm}} = 5 \times 10^{-4} \mu\text{m}^{-1} \quad (\text{Eq. 4-3})$$

The calculated values of  $p/q$  of the simulation are given in Table 4-1.

	250 Hz	1000 Hz	4000 Hz
$p/q$ ( $\mu m^{-1}$ )	$4.34 \times 10^{-4}$	$4.35 \times 10^{-4}$	$4.41 \times 10^{-4}$

Table 4-1: Values of  $p/q$  for different frequencies

It may seem counterintuitive that the calculated  $p/q$  is smaller than  $5 \times 10^{-4}$ . The reason is that in the ideal case, the metal is assumed to be an infinite half plane while in our simulation the sample has a finite (and small) cross section. When the upper surface has a crack, its resistance goes up and thus more current goes through the sample from the other surfaces (i.e. bottom and the two sides). Thus the voltage drop on the top surface decreases which counteracts the increment caused by the crack, so the calculated  $p/q$  is less than 0.5. To examine whether this is the case, one can simply increase the sample size. For example, if we change the sample size to 50 cm\*10 cm\*10 cm, the new  $p/q$  for 4000 Hz increases to  $4.93 \times 10^{-4}$ , which is close to  $5 \times 10^{-4}$ .

The agreement between the theoretical predictions [199][200] and the model demonstrated that the current model worked properly. We then used this model to simulate the potential drop versus crack depth for the pit/crack scenario. The pit size used in the simulation was fixed at 450  $\mu m$  in diameter and 150  $\mu m$  in depth. The crack geometry used was semicircular. The crack depth was calculated from the bottom of the pit to the crack front instead of using the radius of the semicircle (see Figure 4-33 for reference). Potential drop was calculated for different crack depths with the same size of pit. The simulation results are shown in Figure 4-36. The trend of potential drop versus crack depth for each frequency was further fitted using a quadratic function (also shown in Figure 4-36).

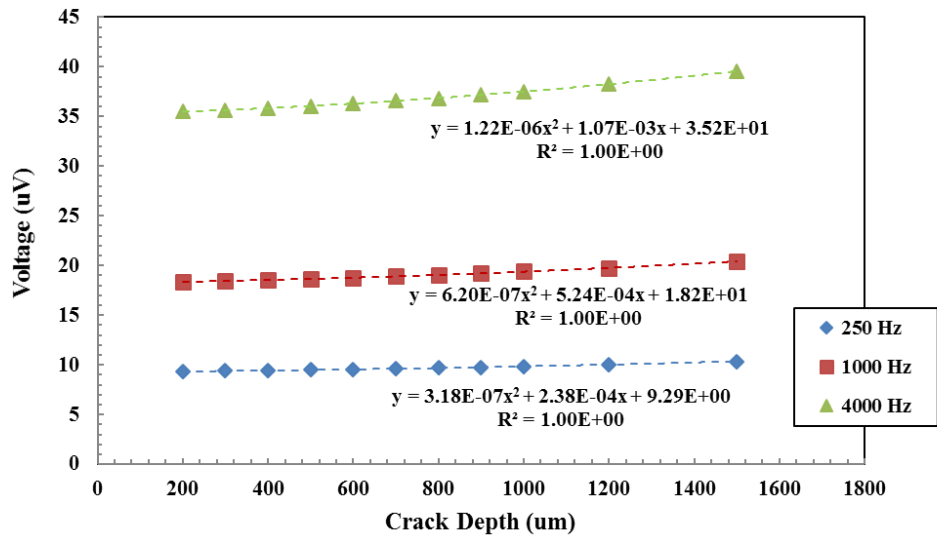


Figure 4-36: Calculated Potential drop versus crack depth for different frequencies. Quadratic functions are used to fit the curves.

Figure 4-36 shows that the voltage drop increases as the crack depth increases, and its trend can be well fitted using a quadratic function. We can use this function to convert the change of potential drop measured in the fatigue test in aerated NaCl solution (data in Figure 4-22 (a)) into an estimate of crack depth. The converted crack length versus number of cycles result is shown in Figure 4-37.

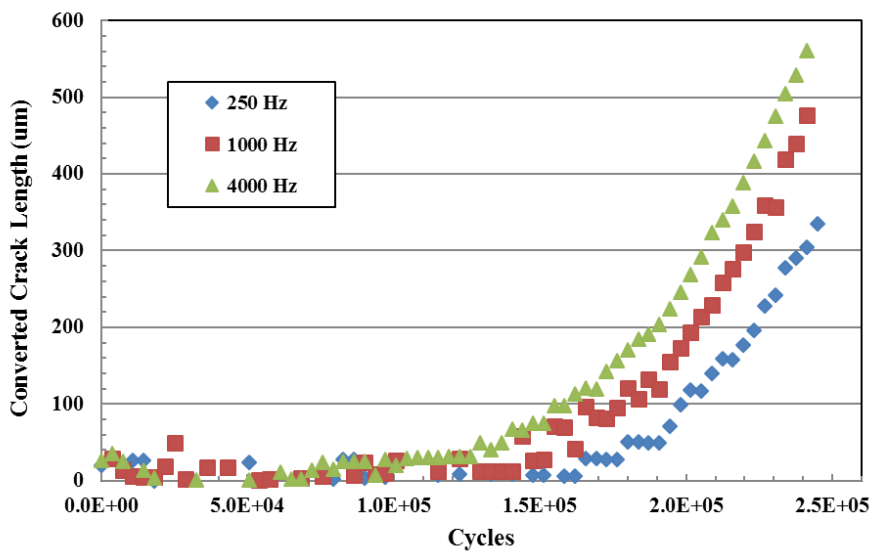


Figure 4-37: Converted crack length using the ACPD data shown in Figure 4-22 (a).

Note that the converted curves for crack depth vs. number of cycles for different frequencies do not completely converge to the same curve (they should because they are measuring the same crack). This is, at least in part, due to the simplified IBC method used in the COMSOL model, which assumes that current flows at the surface. This assumption is only accurate for high frequency (or small skin depth). The skin depths for the frequencies used in the analysis were 800, 400, and 200  $\mu\text{m}$  for 250, 1000, and 4000 Hz respectively. As the frequency decreases the IBC assumption breaks down due to the electric field penetrating deeper into the material and not flowing strictly at the surface of the pit and the crack. The converted crack depth for 4000 Hz at the end of the test is 561  $\mu\text{m}$ , which is very close to the actual observed value of 544  $\mu\text{m}$  in Figure 4-23 (a). We conclude from this analysis that the simplified IBC method is useful for small skin depths or long crack depths. From the current results, we suggest that the crack depth should be at least twice as the skin depth in order to use the quadratic function for converting the potential drop to crack depth.

After obtaining the crack length data, we can further estimate crack growth rate (CGR). An estimation of the crack growth rate can be made using the data in Figure 4-37. As mentioned above, the IBC method is only suitable for high frequencies so we will only use the 4000 Hz data. In order to obtain a relatively smooth curve, we used the following scheme, and averaged every five experimental data points to get an average crack length, and then differentiated every two consecutive average crack lengths to get a crack growth rate, i.e.

$$CGR|_{at\ crack\ depth=(x_i+x_{i+1}+x_{i+2}+x_{i+3}+x_{i+5})/5} = \frac{x_{i+6} - x_i}{5\Delta n} \quad (\text{Eq. 4-4})$$

where  $x_i$  is one crack depth data point,  $\Delta n$  is the number of cycles between two data points.

The converted (estimated) crack growth rate is shown in Figure 4-38. The crack growth rate is believed to be more accurate when the crack depth is relatively large. From Figure 4-38, we can estimate that when the crack depth is 500  $\mu\text{m}$ , the crack growth rate is approximately 0.008  $\mu\text{m}/\text{cycle}$  under our test condition.

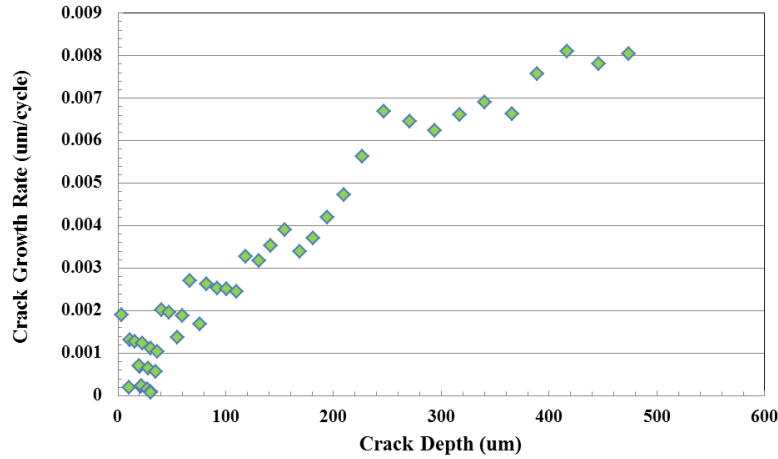


Figure 4-38: Calculated Crack growth rate using 4000 Hz data from Figure 4-37.

To compare the crack growth data with existing literature [201], we assume that the entire pit+crack geometry is a semi-penny shaped crack in which the new crack depth  $a$  equals the pit depth plus crack depth. We are then able to approximate the stress intensity factor using the formula from [202] for surface crack under bending, which is,

$$K_I = HS_b \sqrt{\pi \frac{a}{Q} F\left(\frac{a}{t}, \frac{a}{c}, \frac{c}{b}, \varphi\right)} \quad (\text{Eq. 4-5})$$

where  $a$  is the crack depth,  $c$  is the half-length of the crack,  $t$  is the sample thickness,  $b$  is the half-width of the sample,  $\varphi$  is the parametric angle of the crack eclipse,  $Q$  is a shape factor, and  $S_b$  is the maximum surface stress. Here we consider  $a/c = 1$  and  $\varphi = \pi/2$ . An illustration of the geometric parameters is shown in Figure 4-39. A more detailed presentation of (Eq. 4-5) can be found in [202] and in Appendix A of the thesis.

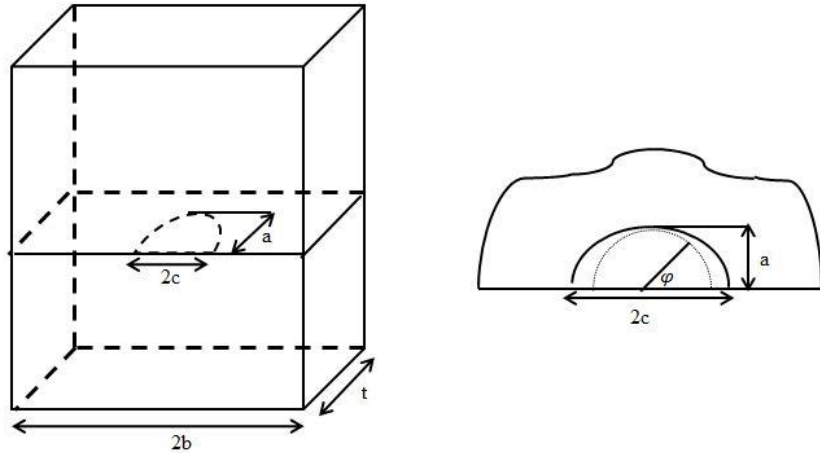


Figure 4-39: A schematic showing the geometric parameters used in (Eq. 4-5).

With a stress ratio  $R=0.1$ , and maximum surface stress level of 80% of the yield stress, the stress intensity factor can be calculated using (Eq. 4-5). We can then convert the crack length versus number of cycles estimates in Figure 4-38 into crack growth rate versus stress intensity factor estimates, which is shown in Figure 4-40. The data from Vosikovsky [201] in 3.5 wt.% percent NaCl solution at a loading frequency of 1 Hz is also shown in Figure 4-40. Although the NaCl concentration and loading frequency were not the same as in our experiment, Vosikovsky [201] showed that the crack growth rate was not sensitive to these parameters. Good consistency can be seen from Figure 4-40 when the crack is relatively large. The discrepancy at smaller crack depth (where  $\Delta K$  is small) is because when the initiated crack depth is small, the assumption of pit serving as pre-crack fails. The pit does not serve as effectively as a sharp crack, and this becomes significant when the initiated crack depth is small. From our results, the assumption of pit as partial crack works well when the initiated crack depth is larger than  $40 \mu\text{m}$  and  $\Delta K$  is larger than  $5.9 \text{ MPa}\sqrt{\text{m}}$ .

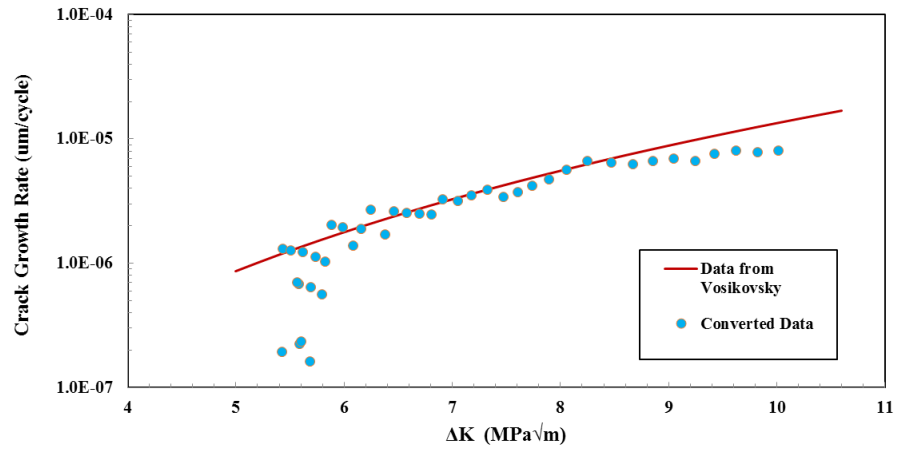


Figure 4-40: Converted crack growth data compared with data from Vosikovsky [201].

# Chapter 5 Simulation of Strain Accumulation around Pit during Fatigue Cycles

## 5.1 Introduction

For a smooth specimen, fatigued at a low stress/strain level (lower than the yield stress), plasticity occurs at a micro/sub-grain level [58]. However, when a pit is formed on the specimen surface, the stress around the pit can exceed the yield stress even if the normal stress far away from the pit is below yield [95]. As a result, significant plastic strain may accumulate around the pit which is considered to be the key for crack initiation [19].

This chapter introduces the mechanical model developed in this research to predict the strain accumulation around the pit during fatigue cycles. The current model uses a finite-strain framework with kinematic hardening. The material parameters in the model are calibrated with experimental data and then the model is used to simulate strain evolution around the pit.

## 5.2 Model Description

In order to simulate the strain evolution around the pit and predict the number of cycles of crack initiation, an isotropic finite strain model with kinematic hardening has been implemented. The model uses the finite strain framework proposed by Kröner [203]. Most of the constitutive equations used are adopted from the lecture notes of Course 2.073 by Professor Lallit Anand at MIT. A new kinematic hardening rule is proposed and implemented to simulate the kinematic hardening behavior of the investigated X65 steel.

We consider the dual decomposition of the deformation gradient  $\mathbf{F}$ :

$$\mathbf{F} = \mathbf{F}^e \mathbf{F}^p \quad (\text{Eq. 5-1})$$

where  $\mathbf{F}^e$  and  $\mathbf{F}^p$  are the elastic and plastic distortions, respectively. For metals, we consider that the plasticity is incompressible, thus the determinant of  $\mathbf{F}^p$  is one, i.e.,  $\det(\mathbf{F}^p) = 1$ .

The polar decomposition of the elastic distortion into the elastic rotation and the right elastic

stretch tensor gives:

$$\mathbf{F}^e = \mathbf{R}^e \mathbf{U}^e \quad (\text{Eq. 5-2})$$

where  $\mathbf{R}^e$  is the elastic rotation, and  $\mathbf{U}^e$  is the right elastic stretch.

And the spectral decomposition of the right elastic stretch tensor gives:

$$\mathbf{U}^e = \sum_{i=1}^3 \lambda_i^e \mathbf{r}_i^e \otimes \mathbf{r}_i^e \quad (\text{Eq. 5-3})$$

where  $\{\lambda_i^e\}$  and  $\{\mathbf{r}_i^e\}$  are the eigenvalues and eigenvectors of the right stretch tensor.

We define the logarithmic elastic strain tensor using the right elastic stretch tensor:

$$\mathbf{E}^e \equiv \ln(\mathbf{U}^e) = \sum_{i=1}^3 E_i^e \mathbf{r}_i^e \otimes \mathbf{r}_i^e \quad (\text{Eq. 5-4})$$

where  $E_i^e = \ln \lambda_i^e$ .

We start with a separable free energy function,

$$\psi = \psi^e + \psi^p \quad (\text{Eq. 5-5})$$

where  $\psi^e$  is an elastic energy, and  $\psi^p$  is an plastic energy associated with plastic flow. The elastic part of the free energy can be written using the logarithmic measure of finite strain in the following form:

$$\psi^e(\mathbf{E}^e) = G |\mathbf{E}_0^e|^2 + \frac{1}{2} \left( K - \frac{2}{3} G \right) (\text{tr} \mathbf{E}^e)^2 \quad (\text{Eq. 5-6})$$

where  $K > 0$  is the bulk modulus and  $G > 0$  is the shear modulus. The magnitude of a matrix  $\mathbf{A}$  is defined by  $|\mathbf{A}| = \sqrt{\mathbf{A}:\mathbf{A}} = \sqrt{A_{ij}A_{ij}}$ .

The corresponding elastic Mandel stress can be derived:

$$\mathbf{M}^e = \sum_{i=1}^3 \frac{\partial \psi^e(E_1^e, E_2^e, E_3^e)}{\partial E_i^e} \mathbf{r}_i^e \otimes \mathbf{r}_i^e = 2G\mathbf{E}_0^e + Ktr(\mathbf{E}^e)\mathbf{1} = \mathbb{C}\mathbf{E}^e \quad (\text{Eq. 5-7})$$

where  $\mathbb{C} = 2G\mathbf{II} + (K - \frac{2}{3}G)\mathbf{1} \otimes \mathbf{1}$  is a fourth order isotropic elastic tensor.  $\mathbf{II}$  denotes the fourth order symmetric identity tensor and  $\mathbf{1}$  denotes the second order symmetric identity tensor.

We adopt the following form for the plastic part of the free energy:

$$\psi^p = \frac{1}{2} \sum_{i=1}^M B_i |\mathbf{A}_i|^2 \quad (\text{Eq. 5-8})$$

The plastic energy is considered to be the sum of several components, as proposed by Chaboche et al. [204], Chaboche and Rousselier [205].  $B_i$  is the back-stress modulus of the  $i$  component with  $B_i \geq 0$  and  $\mathbf{A}_i$  is a dimensionless internal variable which is symmetric and deviatoric. Inspired by Kang et al. [206] and the observed ratcheting behavior in our experiments, we consider  $B_i$  as a function of the equivalent tensile plastic strain in our model, instead of a constant, i.e.

$$B_i = B_i(\bar{\epsilon}_p) \geq 0 \quad (\text{Eq. 5-9})$$

And for materials exhibit an increasing ratcheting rate:

$$\frac{dB_i}{d\bar{\epsilon}_p} < 0 \quad (\text{Eq. 5-10})$$

for at least one of the components. The definition of  $\bar{\epsilon}_p$  is given by (Eq. 5-21). The effect of introducing a non-constant  $B_i$  will be further illustrated in this section.

To capture the Bauschinger effect [207] of the carbon steel in reverse loading, we introduce the symmetric and deviatoric back-stress which acts to oppose the Mandel stress. The  $i$ th component of the back-stress can be derived from the partial derivative of the plastic free energy

with respect to  $\mathbf{A}_i$ :

$$\mathbf{S}_{back,i} = \frac{\partial \psi^p}{\partial \mathbf{A}_i} = B_i \mathbf{A}_i \quad (\text{Eq. 5-11})$$

$$\mathbf{S}_{back} = \sum_{i=1}^M \mathbf{S}_{back,i} \quad (\text{Eq. 5-12})$$

And the deviatoric effective stress driving the plastic flow is given by:

$$(\mathbf{M}_{eff}^e)_0 = \mathbf{M}_0^e - \mathbf{S}_{back} \quad (\text{Eq. 5-13})$$

The evolution equation of the plastic distortion is given by:

$$\mathbf{L}^p = \dot{\mathbf{F}}^p \mathbf{F}^{p-1} \quad (\text{Eq. 5-14})$$

where  $\mathbf{L}^p$  is the plastic velocity gradient.  $\mathbf{L}^p$  can be decomposed into its symmetric and skew parts:

$$\mathbf{L}^p = \mathbf{D}^p + \mathbf{W}^p \quad (\text{Eq. 5-15})$$

$\mathbf{D}^p$  and  $\mathbf{W}^p$  are called the plastic stretching and spin tensors. We assume that the plastic flow is irrotational [208], so  $\mathbf{W}^p = 0$ , which leads to:

$$\mathbf{D}^p = \dot{\mathbf{F}}^p \mathbf{F}^{p-1} \quad (\text{Eq. 5-16})$$

We further define the scalar value and the direction of the plastic stretching tensor:

$$d^p = |\mathbf{D}^p|, \mathbf{N}^p = \frac{\mathbf{D}^p}{|\mathbf{D}^p|} \quad (\text{Eq. 5-17})$$

We assume that the direction of the plastic flow,  $\mathbf{N}^p$  is codirectional to the deviatoric effective

Mandel stress, i.e.

$$\mathbf{N}^p = \frac{(\mathbf{M}_{eff}^e)_0}{|(\mathbf{M}_{eff}^e)_0|} \quad (\text{Eq. 5-18})$$

And define the equivalent effective tensile stress and the equivalent plastic tensile strain rate:

$$\bar{\sigma}_{eff} \equiv \sqrt{3/2} |(\mathbf{M}_{eff}^e)_0| \quad (\text{Eq. 5-19})$$

$$\dot{\epsilon}^p \equiv \sqrt{2/3} |\mathbf{D}^p| = \sqrt{2/3} d^p \quad (\text{Eq. 5-20})$$

The equivalent tensile strain is the integration of its rate:

$$\bar{\epsilon}_p(t) = \int_0^t \dot{\epsilon}^p dt \quad (\text{Eq. 5-21})$$

We assume the scalar flow stress is independent of the direction the flow, and a function of scalar flow rate and flow resistant of the material so that,

$$\bar{\sigma}_{eff} = Y(\dot{\epsilon}^p, S) \quad (\text{Eq. 5-22})$$

where  $S$  is the flow resistance of the material. We further specify a general power law function for the flow stress, which is

$$\bar{\sigma}_{eff} = S \left( \frac{\dot{\epsilon}^p}{\dot{\epsilon}_0} \right)^m \quad (\text{Eq. 5-23})$$

which gives the equivalent tensile plastic strain rate:

$$\dot{\bar{\epsilon}}^p = \dot{\epsilon}_0 \left( \frac{\bar{\sigma}_{eff}}{S} \right)^{1/m} \quad (\text{Eq. 5-24})$$

where  $\dot{\epsilon}_0$  is the reference plastic strain rate,  $m$  is the strain rate sensitivity parameter, and  $S$  is the isotropic deformation resistance. (Eq. 5-18) and (Eq. 5-22) are called the codirectionality hypotheses and strong isotropy hypotheses in [208].

We consider an evolution equation for the internal variable  $\mathbf{A}_i$  in the Armstrong-Frederick form [209]:

$$\dot{\mathbf{A}}_i = \mathbf{D}^p - \gamma_i \mathbf{A}_i \dot{\bar{\epsilon}}^p \quad (\text{Eq. 5-25})$$

And the corresponding the back-stress is given by:

$$\dot{\mathbf{S}}_{back,i} = \frac{d(B_i \mathbf{A}_i)}{dt} = B_i \dot{\mathbf{A}}_i + \mathbf{A}_i \frac{dB_i}{d\bar{\epsilon}_p} \dot{\bar{\epsilon}}^p \quad (\text{Eq. 5-26})$$

We propose a specific form of  $B_i$  which satisfies (Eq. 5-9) and (Eq. 5-10):

$$B_i(\bar{\epsilon}^p) = \frac{2}{3} c_i \exp(-m_{s,i} \bar{\epsilon}^p) \quad (\text{Eq. 5-27})$$

$\frac{2}{3} c_i$  is the value of the back-stress modulus when  $\bar{\epsilon}^p = 0$ . In addition, a damaging factor  $D(\bar{\epsilon}^p) = \exp(-m_s \bar{\epsilon}^p)$  acts on the modulus and lowers its value as  $\bar{\epsilon}^p$  increases, so the material will appear softer.

Given the form of  $B_i$ , we can calculate:

$$\frac{dB_i}{d\bar{\epsilon}_p} = -m_{s,i} \frac{2}{3} c_i \exp(-m_{s,i} \bar{\epsilon}^p) = -m_{s,i} B_i \quad (\text{Eq. 5-28})$$

Substitute (Eq. 5-25) (Eq. 5-28) into (Eq. 5-26), we can get:

$$\dot{\mathbf{S}}_{back,i} = B_i(\mathbf{D}^p - \gamma_i \mathbf{A}_i \dot{\bar{\epsilon}}^p) - \mathbf{A}_i m_{s,i} B_i \dot{\bar{\epsilon}}^p \quad (\text{Eq. 5-29})$$

which can be rearranged into:

$$\dot{\mathbf{S}}_{back,i} = \frac{2}{3} c_i \exp(-m_{s,i} \bar{\epsilon}^p) \mathbf{D}^p - (\gamma_i + m_{s,i}) \mathbf{S}_{back,i} \dot{\bar{\epsilon}}^p \quad (\text{Eq. 5-30})$$

Notice that if we take  $m_{s,i} = 0$ , which means no softening effect, and take  $\gamma_i + m_{s,i} = d_i$ , (Eq. 5-30) becomes:

$$\dot{\mathbf{S}}_{back,i} = \frac{2}{3} c_i \mathbf{D}^p - d_i \mathbf{S}_{back,i} \dot{\bar{\epsilon}}^p \quad (\text{Eq. 5-31})$$

which is an Armstrong-Frederick form of back-stress. The first term represents a direct hardening term, where  $c_i > 0$  is a backs-stress modulus. The second term is a dynamic recovery term with  $d_i > 0$ .

However, the original Armstrong-Frederick form of kinematic hardening usually overestimate the ratcheting strain [210]–[214]. To overcome this issue, Ohno and Wang proposed an evolution equation for the back-stress (Model B in [214]):

$$\dot{\mathbf{S}}_{back,i} = d_i \left( \frac{2}{3} r_i \mathbf{D}^p - \left( \frac{\bar{S}_{back,i}}{r_i} \right)^{m_{d,i}} \mathbf{S}_{back,i} \dot{\bar{\epsilon}}^p \right) \quad (\text{Eq. 5-32})$$

Here  $r_i = c_i/d_i$ , is the saturation level of the equivalent tensile back-stress  $\bar{S}_{back,i}$ . The additional factor  $\left( \frac{\bar{S}_{back,i}}{r_i} \right)^{m_{d,i}}$  compared to the original Armstrong-Frederick model suppresses the recovery term when the back stress is small and thus help lower the ratcheting strain rate [210]–[212].

We include the factor  $\left( \frac{\bar{S}_{back,i}}{r_i} \right)^{m_{d,i}}$  in the model developed in this research. To do that, we choose  $\gamma_i$  in (Eq. 5-30) to be a function of the equivalent tensile back stress,  $\bar{S}_{back,i}$  and take the following form:

$$\gamma_i = \hat{\gamma}_i(\bar{S}_{back,i}) = -m_{s,i} + \left(\frac{\bar{S}_{back,i}}{r_i}\right)^{m_{d,i}} \quad (\text{Eq. 5-33})$$

where  $\bar{S}_{back,i} = \sqrt{3/2} |(\mathbf{S}_{back,i})_0| = \sqrt{3/2} |\mathbf{S}_{back,i}|$ .

Substitute (Eq. 5-33) into (Eq. 5-30), and use  $r_i = c_i/d_i$ , we can get:

$$\dot{\mathbf{S}}_{back,i} = d_i \left( \frac{2}{3} r_i \exp(-m_{s,i} \bar{\epsilon}^p) \mathbf{D}^p - \left(\frac{\bar{S}_{back,i}}{r_i}\right)^{m_{d,i}} \mathbf{S}_{back,i} \dot{\bar{\epsilon}}^p \right) \quad (\text{Eq. 5-34})$$

(Eq. 5-34) is the final form of our back-stress evolution equation.

In our model, we consider two components of plastic energy and use a back-stress with two branches. We define a hard branch and a soft branch, depending on their back-stress modulus, i.e.

$$\psi^p = \frac{1}{2} B_h |\mathbf{A}_h|^2 + \frac{1}{2} B_s |\mathbf{A}_s|^2 \quad (\text{Eq. 5-35})$$

$$\dot{\mathbf{S}}_{back} = \dot{\mathbf{S}}_{back,h} + \dot{\mathbf{S}}_{back,s} \quad (\text{Eq. 5-36})$$

For simplicity, we only consider a softening in the hard branch, but not in the soft branch (i.e.  $m_{s,s} = 0$ ). The evolution rules of the two back-stress components are:

$$\dot{\mathbf{S}}_{back,h} = d_h \left( \frac{2}{3} r_h \exp(-m_{s,h} \bar{\epsilon}^p) \mathbf{D}^p - \left(\frac{\bar{S}_{back,h}}{r_h}\right)^{m_{d,h}} \mathbf{S}_{back,h} \dot{\bar{\epsilon}}^p \right) \quad (\text{Eq. 5-37})$$

$$\dot{\mathbf{S}}_{back,s} = d_s \left( \frac{2}{3} r_s \mathbf{D}^p - \left(\frac{\bar{S}_{back,s}}{r_s}\right)^{m_{d,s}} \mathbf{S}_{back,s} \dot{\bar{\epsilon}}^p \right) \quad (\text{Eq. 5-38})$$

Next, we consider the hardening rule of the isotropic deformation resistance. In observation of the shape of cyclic stress-strain curve in ratcheting tests, minimum expanding or shrinking of the yield surface was found, thus we choose a non-hardening model for the deformation resistance,

i.e.

$$S = S_0 \quad (\text{Eq. 5-39})$$

Finally, the Cauchy stress is given by:

$$\mathbf{T} = J^{-1} \mathbf{R}^e \mathbf{M}^e \mathbf{R}^{eT} \quad (\text{Eq. 5-40})$$

where for plastic incompressible metals,  $J \equiv \det \mathbf{F} = \det \mathbf{F}^e$ .

### 5.3 Summary of the constitutive equations

#### (1) Free energy

We consider a separable free energy:

$$\psi = \psi^e + \psi^p \quad (\text{Eq. 5-41})$$

With the finite strain framework,

$$\mathbf{F} = \mathbf{F}^e \mathbf{F}^p, \mathbf{F}^e = \mathbf{R}^e \mathbf{U}^e \quad (\text{Eq. 5-42})$$

and the elastic logarithmic strain measurement

$$\mathbf{U}^e = \sum_{i=1}^3 \lambda_i^e \mathbf{r}_i^e \otimes \mathbf{r}_i^e, \mathbf{E}^e \equiv \ln(\mathbf{U}^e) = \sum_{i=1}^3 E_i^e \mathbf{r}_i^e \otimes \mathbf{r}_i^e \quad (\text{Eq. 5-43})$$

We adopt the following form of the elastic free energy:

$$\psi^e(\mathbf{E}^e) = G |\mathbf{E}_0^e|^2 + \frac{1}{2} \left( K - \frac{2}{3} G \right) (\text{tr} \mathbf{E}^e)^2 \quad (\text{Eq. 5-44})$$

where  $K > 0$  is the bulk modulus and  $G > 0$  is the shear modulus.

We adopt the following form of the plastic free energy:

$$\psi^p(\mathbf{A}_h, \mathbf{A}_s) = \frac{1}{2} B_h |\mathbf{A}_h|^2 + \frac{1}{2} B_s |\mathbf{A}_s|^2 \quad (\text{Eq. 5-45})$$

where  $B_h, B_s > 0$  is the back-stress modulus of the hard and soft components of the plastic strain. And  $\mathbf{A}_h, \mathbf{A}_s$  are the internal variables associated with the hard and soft components. In our model, we consider  $B_h, B_s$  are functions of the equivalent tensile plastic strain,  $\bar{\epsilon}^p$ , with the following forms:

$$B_h = \hat{B}_h(\bar{\epsilon}^p) = \frac{2}{3} c_h \exp(-m_{s,h} \bar{\epsilon}^p) \quad (\text{Eq. 5-46})$$

$$B_s = \hat{B}_s(\bar{\epsilon}^p) = \frac{2}{3} c_s \exp(-m_{s,s} \bar{\epsilon}^p) \quad (\text{Eq. 5-47})$$

where  $\frac{2}{3} c_i$  is the value of the back-stress modulus when  $\bar{\epsilon}^p = 0$ .  $m_{s,h}, m_{s,s}$  are the softening parameters for the hard and soft component of the back stress.

(2) Cauchy stress. Mandel stresses. Back-stress. Effective stress.

Corresponding to the special free-energy functions, the Cauchy stress is given by:

$$\mathbf{T} = J^{-1} \mathbf{R}^e \mathbf{M}^e \mathbf{R}^{eT} \quad (\text{Eq. 5-48})$$

With the elastic Mandel stress:

$$\mathbf{M}^e = \sum_{i=1}^3 \frac{\partial \psi^e(E_1^e, E_2^e, E_3^e)}{\partial E_i^e} \mathbf{r}_i^e \otimes \mathbf{r}_i^e = 2G \mathbf{E}_0^e + K \text{tr}(\mathbf{E}^e) \mathbf{1} \quad (\text{Eq. 5-49})$$

The symmetric and deviatoric back-stress is given by:

$$\mathbf{S}_{back} = \sum_{i=1}^M \frac{\partial \psi^p}{\partial \mathbf{A}_i} = \mathbf{S}_{back,h} + \mathbf{S}_{back,s} = B_h \mathbf{A}_h + B_s \mathbf{A}_s \quad (\text{Eq. 5-50})$$

And the effective stress for driving the plastic stretching is:

$$(\mathbf{M}_{eff}^e)_0 = \mathbf{M}_0^e - \mathbf{S}_{back} \quad (\text{Eq. 5-51})$$

The corresponding equivalent effective tensile stress is

$$\bar{\sigma}_{eff} \equiv \sqrt{3/2} |(\mathbf{M}_{eff}^0)_0| \quad (\text{Eq. 5-52})$$

### (3) Flow rules

The evolution equations for  $\mathbf{F}^p$  are:

$$\mathbf{D}^p = \dot{\mathbf{F}}^p \mathbf{F}^{p-1} \quad (\text{Eq. 5-53})$$

$$\mathbf{D}^p = (3/2) \dot{\epsilon}^p \frac{(\mathbf{M}_{eff}^0)_0}{\bar{\sigma}_{eff}} \quad (\text{Eq. 5-54})$$

$$\dot{\epsilon}^p = \dot{\epsilon}_0 \left( \frac{\bar{\sigma}_{eff}}{S} \right)^{1/m} \quad (\text{Eq. 5-55})$$

where  $\dot{\epsilon}_0$  is the reference plastic strain rate,  $m$  is the strain rate sensitivity parameter, and  $S$  is the isotropic deformation resistance.

### (4) Evolution equations for the internal variable $\mathbf{A}_i$

$$\dot{\mathbf{A}}_i = \mathbf{D}^p - \gamma_i \mathbf{A}_i \dot{\epsilon}^p \quad (\text{Eq. 5-56})$$

where we consider the recovery coefficient  $\gamma_i$  is a function of the equivalent tensile back-stress and take the following form:

$$\gamma_i = \hat{\gamma}_i(\bar{S}_{back,i}) = -m_{s,i} + \left(\frac{\bar{S}_{back,i}}{r_i}\right)^{m_{d,i}} \quad (\text{Eq. 5-57})$$

and

$$\bar{S}_{back,i} = \sqrt{3/2} |\mathbf{S}_{back,i}| \quad (\text{Eq. 5-58})$$

(5) Evolution equations for the back-stress

$$\dot{\mathbf{S}}_{back,i} = \frac{d(B_i \mathbf{A}_i)}{dt} = B_i \dot{\mathbf{A}}_i + \mathbf{A}_i \frac{dB_i}{d\bar{\epsilon}^p} \dot{\bar{\epsilon}}^p \quad (\text{Eq. 5-59})$$

Use (Eq. 5-46),(Eq. 5-47),(Eq. 5-50),(Eq. 5-56),(Eq. 5-57), we can get:

$$\dot{\mathbf{S}}_{back,h} = d_h \left( \frac{2}{3} r_h \exp(-m_{s,h} \bar{\epsilon}^p) \mathbf{D}^p - \left(\frac{\bar{S}_{back,h}}{r_h}\right)^{m_{d,h}} \mathbf{S}_{back,h} \dot{\bar{\epsilon}}^p \right) \quad (\text{Eq. 5-60})$$

$$\dot{\mathbf{S}}_{back,s} = d_s \left( \frac{2}{3} r_s \mathbf{D}^p - \left(\frac{\bar{S}_{back,s}}{r_s}\right)^{m_{d,s}} \mathbf{S}_{back,s} \dot{\bar{\epsilon}}^p \right) \quad (\text{Eq. 5-61})$$

where  $r_h = c_h/d_h, r_s = c_s/d_s$  are the saturation values of the equivalent tensile back-stress (without softening),  $d_h, d_s > 0$  are the recovery coefficients,  $m_{d,h}, m_{d,s}$  are the ratcheting strain control parameter,  $m_{s,h}$  is the softening parameter for the hard component of the back stress (For simplicity, we take  $m_{s,s} = 0$  and take out the softening term in the soft component). And

$$\dot{\mathbf{S}}_{back} = \dot{\mathbf{S}}_{back,h} + \dot{\mathbf{S}}_{back,s} \quad (\text{Eq. 5-62})$$

(6) Evolution equation for the isotropic deformation resistance

We adopt a non-hardening isotropic deformation resistance:

$$S = S_0 \quad (\text{Eq. 5-63})$$

(Eq. 5-41) to (Eq. 5-63) summarizes all the constitutive equations used in this model. The material parameters used in this model are  $\{G, K, \dot{\epsilon}_0, m, r_h, r_s, d_h, d_s, m_{d,h}, m_{d,s}, m_{s,h}, S_0\}$ . A semi-implicit time integration procedure of the constitutive equations is given in Appendix B.

## 5.4 Calibration of the Material Parameters of the Model

A time-integration procedure has been implemented in the commercial finite element program Abaqus/Standard by writing a user material subroutine (UMAT). The UMAT and the associated algorithmic tangent of the UMAT is adopted from Weber and Anand [215], with revision for new features implemented in the current model. In this section, we present the calibration of the material parameters of our model and compare the simulation results with the experimental data. Some salient properties of our model are also discussed.

### 5.4.1 Material parameters used in the model

The material parameters are tuned to fit the experimental data of the tensile, symmetric strain cyclic and asymmetric stress cyclic tests, for smooth un-pitted specimens. The tensile test data was obtained from GE Global Research, and the strain and stress cyclic test data are obtained from the researchers who collaborated on this project from University of Manchester, UK. The values of material parameters are listed in Table 5-1.

$E$ (GPa)	$\nu$	$\dot{\epsilon}_0$	$m$	$r_h$ (MPa)	$r_s$ (MPa)
200	0.3	$1.33 \times 10^{-3}$	0.02	200	180
$d_h$	$d_s$	$m_{d,h}$	$m_{d,s}$	$m_{s,h}$	$S_0$ (MPa)

1000	20	6.0	2.0	0.45	325
------	----	-----	-----	------	-----

Table 5-1: Values of material parameters used in the model.

#### 5.4.2 Benchmark Simulation Results

For benchmark, the model was compared with the experimental data from tensile, symmetric strain cyclic and asymmetric stress cyclic tests.

The setup of the model is shown Figure 5-1. The model uses a cube consisting of  $7 \times 7 \times 7 = 343$  elements. Three of the cube surfaces are fixed in corresponding directions. One surface in z direction (referred to the active surface) is subjected to displacement or load boundary condition depending on the type of test. For tensile and strain-controlled cyclic tests, displacement boundary condition is used. For stress-controlled cyclic test, a load boundary condition is used. Engineering stress and engineering strain are calculated by:

$$\sigma_{eng} = \frac{Load}{Area}, \epsilon_{eng} = \frac{Displacement}{Length\ of\ the\ cube} \quad (\text{Eq. 5-64})$$

The (true) stress and (true) strain are calculated using the engineering stress and engineering strain:

$$\sigma = \sigma_{eng}(1 + \epsilon_{eng}), \epsilon = \ln(1 + \epsilon_{eng}) \quad (\text{Eq. 5-65})$$

The load in (Eq. 5-64) is taken from the active surface directly in the displacement boundary condition case, and it is derived from the reaction force of the opposite surface (the one fixed in z direction) in the load boundary condition case. The way that stress and strain are calculated in the simulation is analogous to the experiments.

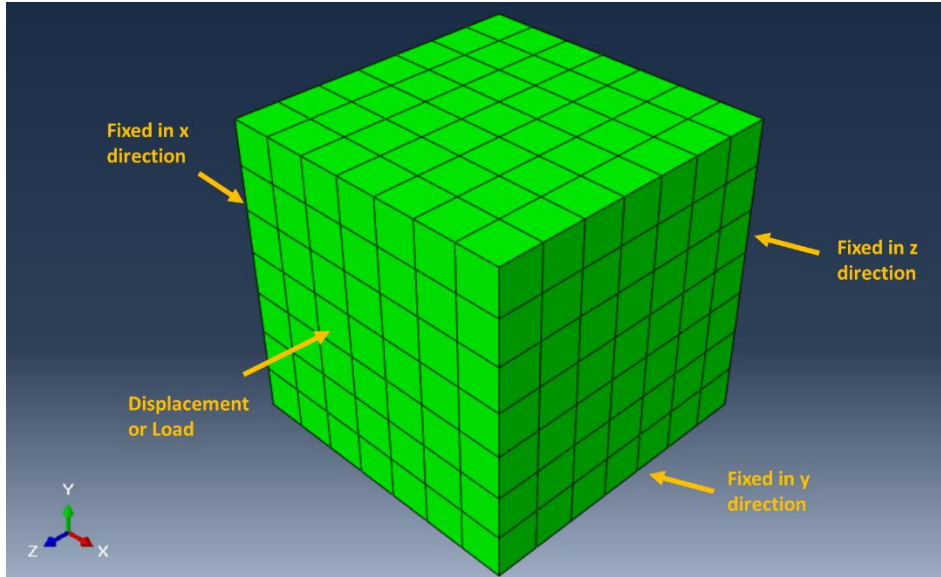


Figure 5-1: Model setup for benchmark tests.

Figure 5-2 shows the results of experiment and simulation of a uniaxial tensile test. As mentioned in Section 4.1.2, the X65 steel exhibits yield point phenomenon [192], which is not considered in the current model. As a result, discrepancies between the experimental data and the simulation can be observed near yield. To simulate the upper and lower yield points, one can refer to Xie et al. [216].

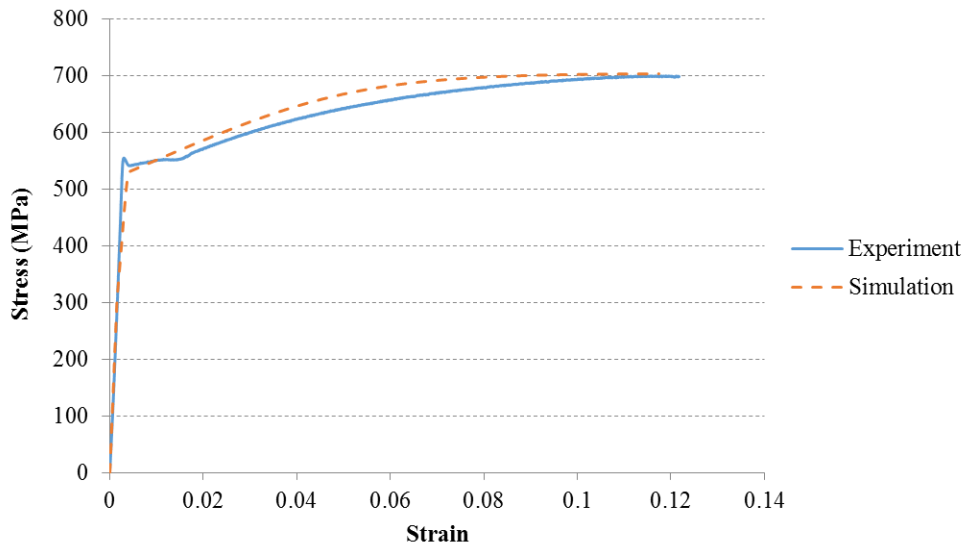


Figure 5-2: Results of experiment and simulation of uniaxial tensile test.

The current model uses a non-hardening isotropic resistance model. Thus the hardening part in Figure 5-2 is provided solely by kinematic hardening. Using the parameters showed in Table 5-1, the steel starts yielding at 325 MPa, and after that the hard component of the back stress dominates. The hard component causes the flow stress to increase until it saturates at  $r_h = 200 \text{ MPa}$ . When the flow stress reaches  $325+200=525 \text{ MPa}$  (which is approximately the apparent yield stress measured by the experiment), the hard component saturates and the soft component of the back stress takes control. The flow stress keeps increasing until the soft component saturates at  $r_h = 180 \text{ MPa}$ . The total flow stress reaches the ultimate level of  $325+200+180=705 \text{ MPa}$ .

Figure 5-3 and Figure 5-4 show the experiment and simulation results for the first 1 ¼ cycle of the symmetric strain cyclic test for 1% and 0.5% strain amplitude, respectively. The simulation results capture the shape of the strain cycles fairly well, but they are not as smooth as the experimental data. The simulation curves show “kinks” caused by the transition of two components of the back stresses which have very different moduli [213]. To make the simulation curve more smooth, one can use more components of back stress, as discussed by Chaboche [217]. However, this will induce more fitting parameters into the model. For simplicity, we only include two components of the back stress.

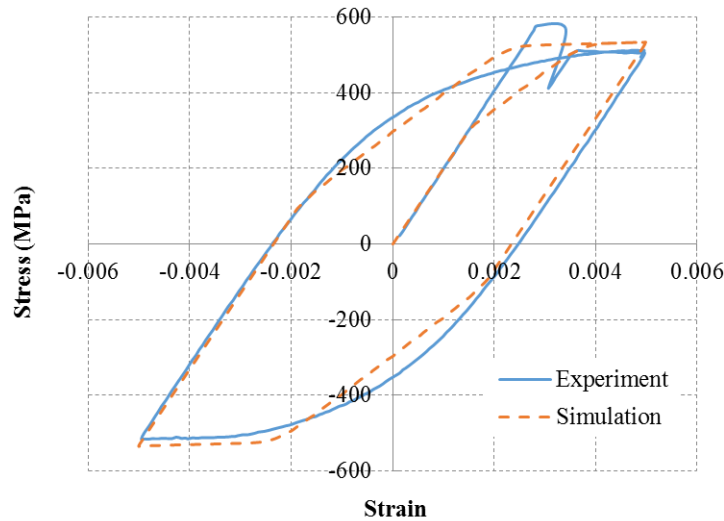


Figure 5-3: First 1 ¼ cycle of 1% systemic strain cyclic test.

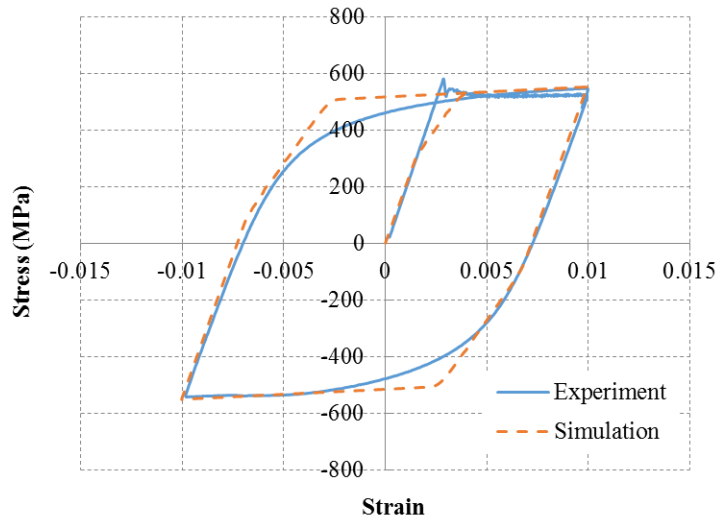


Figure 5-4: First 1/4 cycle of 0.5% systemic strain cyclic test.

From the cyclic strain experimental data, one can see that the upper and lower yield points effects only appear on the first cycle and the first yielding occurs at a higher level of stress. The “true” yield stress can be estimated, from a pure kinematic hardening point of view [217], using the flow stress at the end of the first 1/4 cycle ( $\approx 500$  MPa from the 0.5% strain data), and the flow stress of yielding in the subsequent reverse loading ( $\approx -150$  MPa from the 0.5% strain data). The difference of the two flow stresses divided by 2 gives the “true” yield stress of the material in the kinematic hardening model, which is 325 MPa. This explains why we use  $S_0 = 325$  MPa in our model, rather than 521 MPa as measured in the tensile test which is subject to the yield point phenomenon.

Figure 5-5 to Figure 5-7 show the results of the asymmetric stress-controlled cyclic test using a mean engineering stress of 100 MPa and a stress amplitude of 450 MPa. The waveform of the load is sinusoidal. Here we use the engineering stress-strain curve to show the results because the test is under engineering stress controlled condition. Figure 5-5 shows the engineering stress-strain curve of the experiment and the simulation of the first 200 cycles (The specimen failed after 273 cycles in the experiment). From these curves, we can see that the stress-strain loop continues to translate to the right which means that the strain level keep increasing during the cyclic test. This is a typical ratcheting scenario [218]. In addition, we can see that the gap between the stress-strain loops first decreases dramatically at the first few cycle, and then transitions to a stable value, and

begins to increase again after some cycles. All of these features are captured by the current model as shown in Figure 5-5.

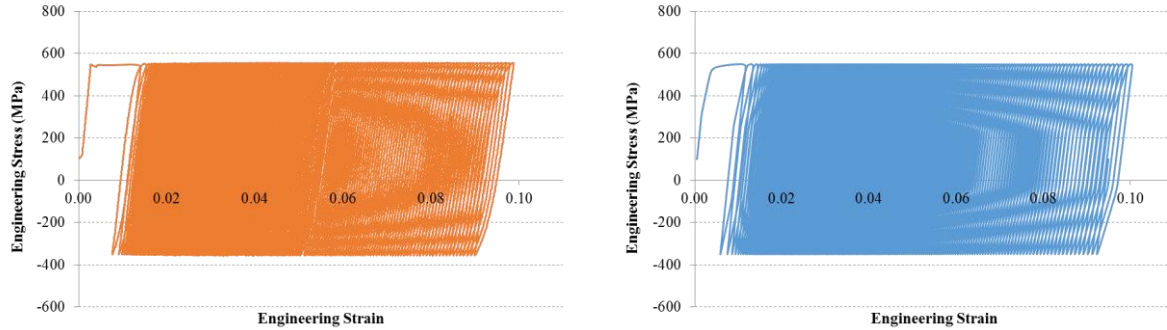


Figure 5-5: Engineering stress-strain curves of asymmetric stress cyclic test with mean stress = 100 MPa, stress amplitude = 450 MPa. Left: Experimental data; Right: Simulation.

Figure 5-6 shows the comparison between the experimental data and the simulation of selective cycles. We can see that the simulation calculates the strain level at different cycles reasonably well. More importantly, the simulation captures the shape change of the stress-strain loop. The stress-strain loop first narrows and then becomes wider at later cycles. This is mainly due to the softening of the plastic modulus and it is captured by the model using the softening model in the back stress modulus.

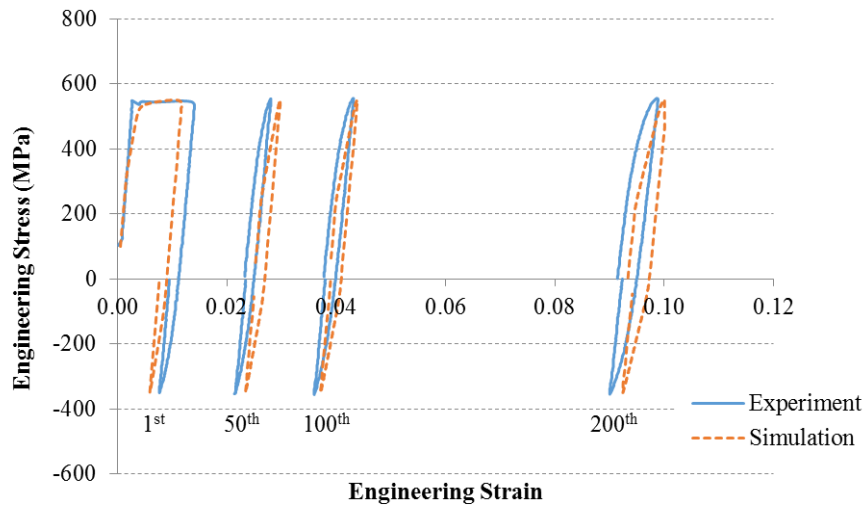


Figure 5-6: Comprision between experiment and simulation for seleted cycles (1<sup>st</sup>, 50<sup>th</sup>, 100<sup>th</sup>, 200<sup>th</sup> cycles).

Figure 5-7 shows the true strain versus the number of cycles. Here the true strain is calculated using the average of the maximum engineering strain and minimum engineering strain at each cycle, i.e.,

$$\epsilon = \frac{\ln(1 + \epsilon_{eng,max}) + \ln(1 + \epsilon_{eng,min})}{2} \quad (\text{Eq. 5-66})$$

The strain versus cycles curve shows three distinct stages in strain accumulation. These stages are: (1) Primary stage for first few cycles, where the strain increment for each cycle (ratcheting rate) is large but rapidly decreasing. (2) Secondary or “steady state” stage where ratcheting rate is almost constant. (3) Tertiary stage of large strain accumulation with increasing ratcheting rate. Features of all three stages are captured by the current model and the simulation result fits the experimental data very well.

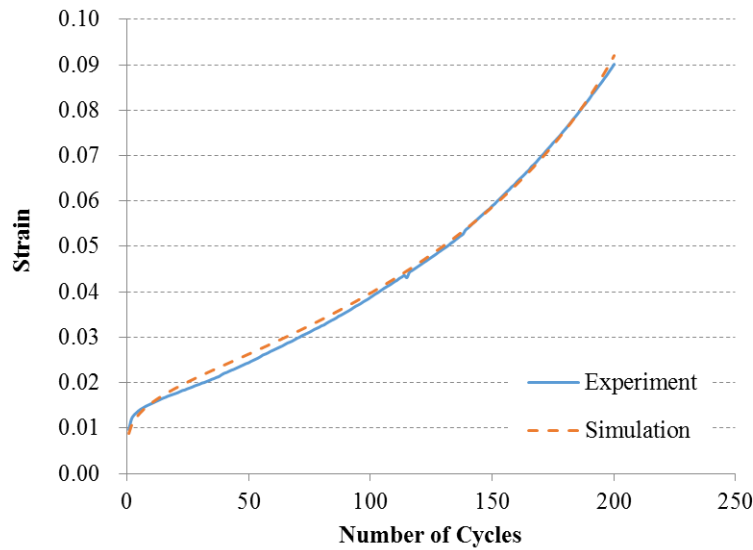


Figure 5-7: Strain versus number of cycles curve of experiment and simulation.

Figure 5-8 further shows the strain versus number of cycles curves of various loading conditions. We can see that the current model fits the experimental data reasonably well. Some experimental data are shifted with a fixed strain in Figure 5-8. This is because of the instability of

the yield point phenomenon, the strain level of first cycle is somewhat uncertain (examples shown in Figure 5-9). Thus some experimental data is shifted in the y direction to better compared to the simulation results.

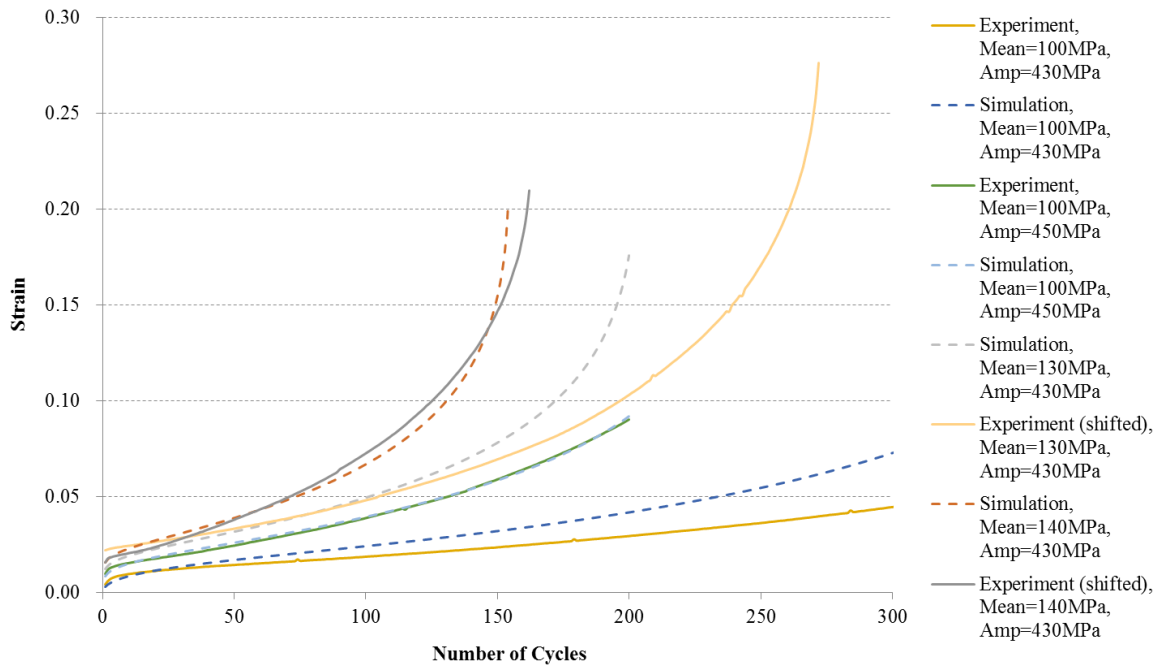


Figure 5-8: Simulation results and experimental data of various loading conditions

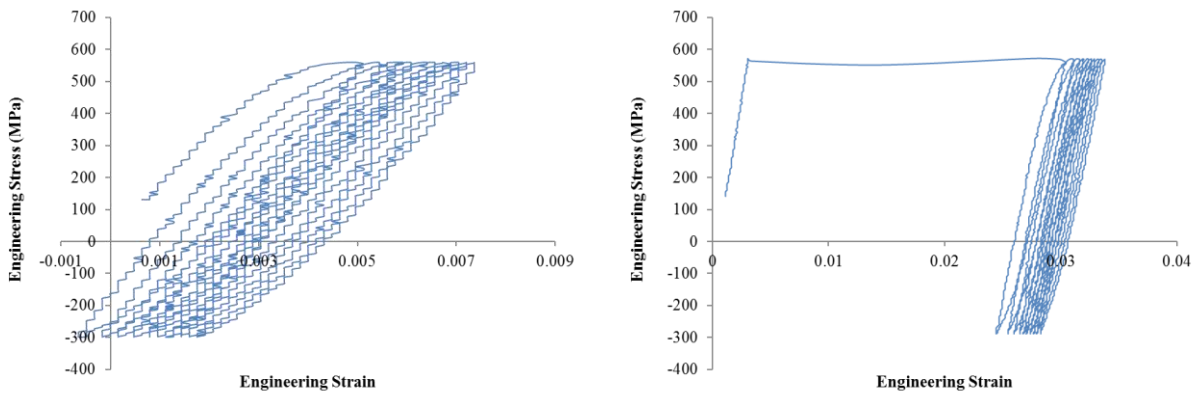


Figure 5-9: Instability of strain accumulation at the first cycle causing by the yield point phenomenon. Left: Mean stress of 130 MPa, stress amplitude of 430 MPa; Right: Mean stress of 140 MPa, stress amplitude of 430 MPa.

### 5.4.3 Discussion

From the benchmark tests, we can see the model developed in this work is able to reproduce the experimental results of the tensile, the strain-controlled cyclic and the asymmetric stress-controlled cyclic behavior with good agreement. Especially for the asymmetric stress-controlled cyclic tests, the current model captures both the initial cyclic hardening and the later softening of the X65 steel, and predicts the strain accumulation fairly accurately. This is mainly due to the evolution rule of the back stress used in the model, which is,

$$\dot{\mathbf{S}}_{back,i} = d_i \left( \frac{2}{3} r_i \exp(-m_{s,i} \bar{\epsilon}^p) \mathbf{D}^p - \left( \frac{\bar{S}_{back,i}}{r_i} \right)^{m_{d,i}} \mathbf{S}_{back,i} \dot{\bar{\epsilon}}^p \right) \quad (\text{Eq. 5-67})$$

The specific equation for the hard and soft branches considered in the model:

$$\dot{\mathbf{S}}_{back,h} = d_h \left( \frac{2}{3} r_h \exp(-m_{s,h} \bar{\epsilon}^p) \mathbf{D}^p - \left( \frac{\bar{S}_{back,h}}{r_h} \right)^{m_{d,h}} \mathbf{S}_{back,h} \dot{\bar{\epsilon}}^p \right) \quad (\text{Eq. 5-68})$$

$$\dot{\mathbf{S}}_{back,s} = d_s \left( \frac{2}{3} r_s \mathbf{D}^p - \left( \frac{\bar{S}_{back,s}}{r_s} \right)^{m_{d,s}} \mathbf{S}_{back,s} \dot{\bar{\epsilon}}^p \right) \quad (\text{Eq. 5-69})$$

Notice that if we take  $m_{s,i} = 0$  and  $m_{d,i} = 0$ , which means no softening of the back-stress modulus and no suppression of the recovery term of the back-stress, (Eq. 5-67) becomes:

$$\dot{\mathbf{S}}_{back,i} = d_i \left( \frac{2}{3} r_i \mathbf{D}^p - \mathbf{S}_{back,i} \dot{\bar{\epsilon}}^p \right) \quad (\text{Eq. 5-70})$$

And use  $c_i = r_i d_i$ , we get

$$\dot{\mathbf{S}}_{back,i} = \frac{2}{3} c_i \mathbf{D}^p - d_i \mathbf{S}_{back,i} \dot{\bar{\epsilon}}^p \quad (\text{Eq. 5-71})$$

(Eq. 5-71) is the original form of the Armstrong-Frederick kinematic hardening [209], in the finite-

strain framework.

Notice that if we take  $m_{s,i} = 0$ , which means no softening of the back-stress modulus (Eq. 5-67) becomes:

$$\dot{\mathbf{S}}_{back,i} = d_i \left( \frac{2}{3} r_i \mathbf{D}^p - \left( \frac{\bar{S}_{back,i}}{r_i} \right)^{m_{d,i}} \mathbf{S}_{back,i} \dot{\epsilon}^p \right) \quad (\text{Eq. 5-72})$$

(Eq. 5-72) is the model proposed by Ohno and Wang [214], in the finite-strain framework.

Comparison between the model developed in this work, the Armstrong-Frederick model (AF model), and the Ohno-Wang model is shown in Figure 5-10. It can be seen that the AF model overestimates the ratcheting rate, as discussed in [210]–[214]. The Ohno-Wang model, by introducing the additional factor  $\left( \frac{\bar{S}_{back,i}}{r_i} \right)^{m_{d,i}}$ , suppresses the recovery term in the original AF model, and is able to predict a lower ratcheting rate [214]. However, the Ohno-Wang model does not account for the softening characteristic of the X65 steel. The current model, by introducing the softening term to the AF model and the Ohno-Wang model, correctly represents the softening feature and the strain accumulation.

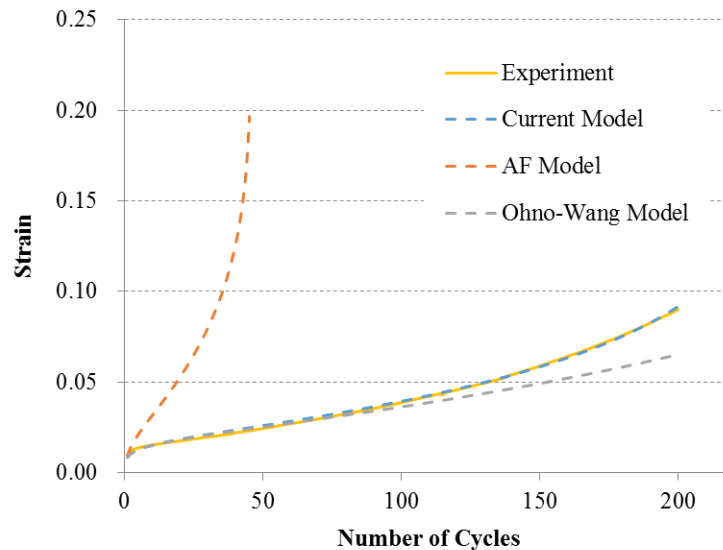


Figure 5-10: Comparison between the current model, AF model and Ohno-Wang model using the experimental data of mean stress of 100 MPa, stress amplitude of 450 MPa.

## 5.5 Application to Strain Accumulation around a Pit

After calibrating the material parameters in the model using the experimental data, we can now use this model to estimate strain accumulation around a pit during fatigue. Figure 5-11 shows the setup for the pit simulation. In order to reduce the computation time, only one-fourth of the pit is simulated and we only consider a small volume around the pit but not the whole specimen. The volume of the cube shown in Figure 5-11 is  $500\ \mu\text{m} \times 500\ \mu\text{m} \times 500\ \mu\text{m}$ . The pit has an oval shape, with the pit opening (diameter) of  $500\ \mu\text{m}$  and the pit depth of  $150\ \mu\text{m}$ . The element size at the pit surface is  $10\ \mu\text{m}$ . The stress distribution of the four-point bending is simplified and assumed to be uniform stress applied on the right surface (see Figure 5-11 for reference). In the actual situation, the stress is maximum at the top surface and decreases linear towards the neutral surface. The simulation volume only considers  $500\ \mu\text{m}$  from the top surface, and the actual stress at the base surface is 12% smaller than the top surface in the actual case. The approximation using a uniform stress is considered to be acceptable.

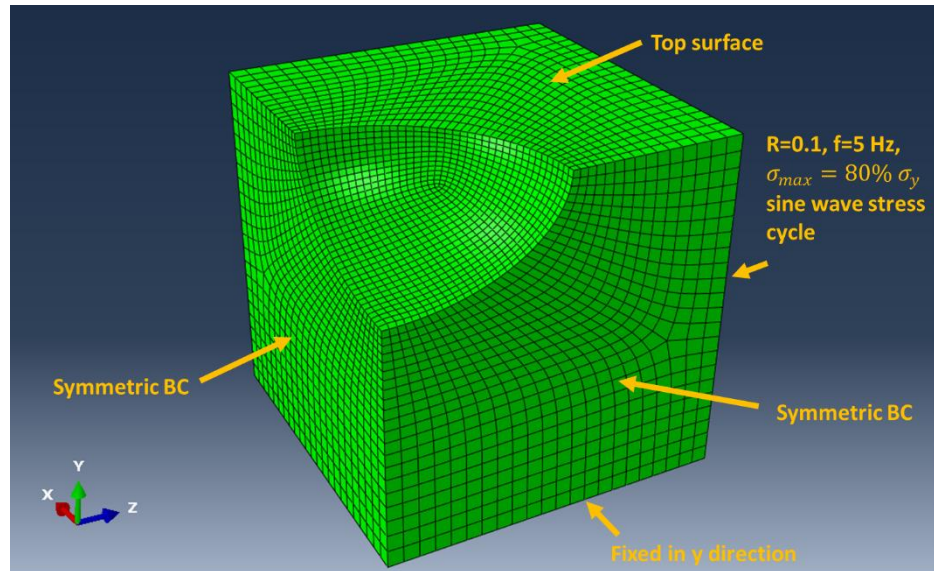


Figure 5-11: Model setup for the pit geometry.

In the benchmark tests, because the simulation volume is a cube under uniaxial loading, it is easy to define the strain/plastic strain using the load and displacement of the active surface ((Eq. 5-64) and (Eq. 5-65)) and compare the simulation results with the experimental data. With the pit

geometry, we cannot calculate the strain using (Eq. 5-64) and (Eq. 5-65). It is not for sure what quantity we should use in the model to compare to the plastic strain measured using electron backscatter diffraction (EBSD) as will be discussed in Chapter 6. Some research used the equivalent tensile plastic strain (Eq. 5-21) or equivalent plastic strain in Abaqus (PEEQ, [219]) to quantify the plastic damage (e.g. [220]–[222]). However, we believe that the equivalent tensile plastic strain may not be a good indicator of plastic strain in a fatigue situation. We propose to use the following plastic strain measurement  $\mathbf{E}^p$ :

$$\mathbf{E}^p = \ln \mathbf{V}^p = \ln \left( \sqrt{\mathbf{F}^p \mathbf{F}^{pT}} \right) \quad (\text{Eq. 5-73})$$

where  $\mathbf{F}^p$  is the plastic distortion in the model, and  $\mathbf{V}^p$  is the plastic left stretch tensor [223], and  $\mathbf{E}^p$  should be called the spatial plastic logarithmic strain measure of Hencky (refer to plastic strain tensor in the following text).

Figure 5-12 shows the comparison between true plastic strain, equivalent tensile plastic strain and  $\mathbf{E}_{33}^p$  in the simulation of the benchmark tensile test. Here the true plastic strain is obtained by subtracting the true elastic strain from the true axial strain calculated using (Eq. 5-65). The true plastic strain calculated in this way can be directly compared to the experimental data (because in the experiment, strain and plastic strain is also converted from displacement) and thus it is considered as a correct value. The equivalent tensile plastic strain is given by (Eq. 5-21).  $\mathbf{E}_{33}^p$  is the (3,3) component of the  $\mathbf{E}^p$  tensor defined by (Eq. 5-73). The (3,3) component is used because the load is applied in the z direction. One can see that the three quantities are equal in the tensile test, both the equivalent tensile plastic strain and  $\mathbf{E}_{33}^p$  gives the measured axial plastic strain in the experiment.

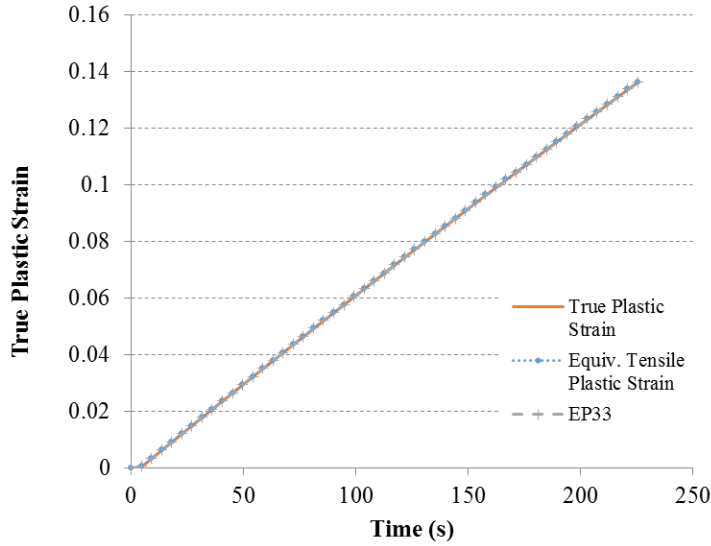


Figure 5-12: Comparison between true plastic strain, equivalent tensile plastic strain and  $E_{33}^p$  in a uniaxial tensile test.

Figure 5-13 shows the comparison between true plastic strain, equivalent tensile plastic strain and  $E_{33}^p$  in the simulation of the benchmark asymmetric stress cyclic test with mean stress of 100 MPa and stress amplitude of 450 MPa. Unlike the tensile test, the equivalent tensile plastic strain gives much higher value than the true plastic strain, while  $E_{33}^p$  still matches pretty well with the true plastic strain. This means that the equivalent tensile plastic strain may not be a good number to use to compare to the experimental measured plastic strain in a cyclic test. The reason that the equivalent tensile plastic strain overestimate the plastic strain level can be seen from the definition of equivalent tensile plastic strain rate:

$$\dot{\epsilon}^p \equiv \sqrt{2/3} |\mathbf{D}^p| = \sqrt{2/3} d^p \quad (\text{Eq. 5-74})$$

The equivalent tensile plastic strain rate takes the magnitude of the plastic stretching tensor  $\mathbf{D}^p$  (an absolute value  $> 0$ ) and the equivalent tensile plastic strain is the integration of its rate over time. In the monotonic loading case, the plasticity flows in one direction, the equivalent tensile plastic strain is consistent with the measured plastic strain. However, in the cyclic loading case, the plasticity can flow backward during the reversed loading stage and the material is partially recovered. At the microstructural level, this is caused by the partial dissolution of the dislocations

[224]–[226]. Although this feature (i.e. the Bauschinger effect) is captured by the kinematic hardening equations in the model, it makes the equivalent tensile plastic strain deviate from the macroscopic plastic strain measured in the experiments. As a result, we cannot use the equivalent tensile plastic strain to estimate the plastic strain level in the material. However, as we can see from Figure 5-13, the proposed plastic strain tensor  $\mathbf{E}^p$ , capture the measured plastic strain in both monotonic and cyclic tests, so we can use it as an indicator of the plastic strain level in the material.

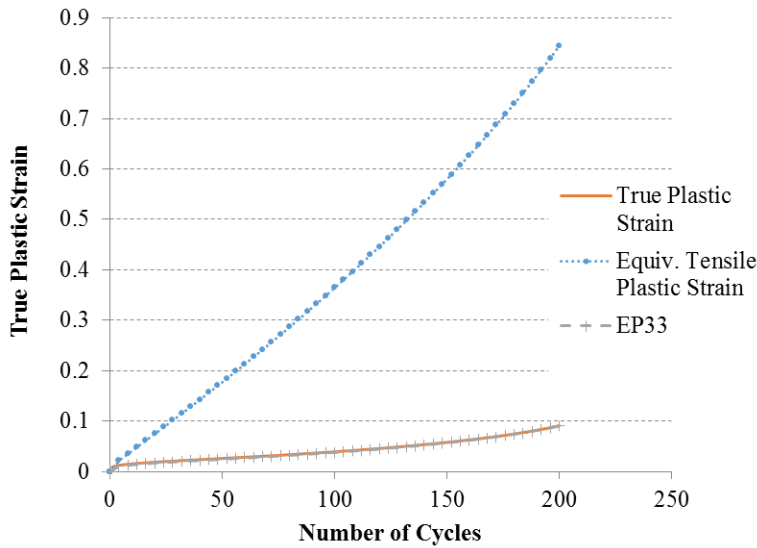


Figure 5-13: Comparison between true plastic strain, equivalent tensile plastic strain and  $\mathbf{E}_{33}^p$  in an asymmetric stress cyclic test with mean stress = 100 MPa, stress amplitude = 450 MPa.

Considering the elements around the pit is not subjected to an uniaxial stress, we consider the magnitude of the plastic strain tensor,  $\epsilon^p$ , instead of a component of  $\mathbf{E}^p$ . The equivalent tensile magnitude of the plastic strain tensor,  $\epsilon^p$ , is given by:

$$\epsilon^p = \sqrt{2/3} |\mathbf{E}^p| \quad (\text{Eq. 5-75})$$

We will call this quantify magnitude of the plastic strain or plastic strain in the following text.

Figure 5-14 shows the magnitude of the plastic strain around the pit after  $10^4$  fatigue cycles. We can see that the plastic strain is localized within a band at the center of the pit perpendicular to the external applied stress direction. The plastic strain is fairly uniform within this band, and its

maximum occurs at the location a bit lower than the mouth. The current simulation result is consistent with the result given by Turnbull [1] for a pit under static tensile loading.

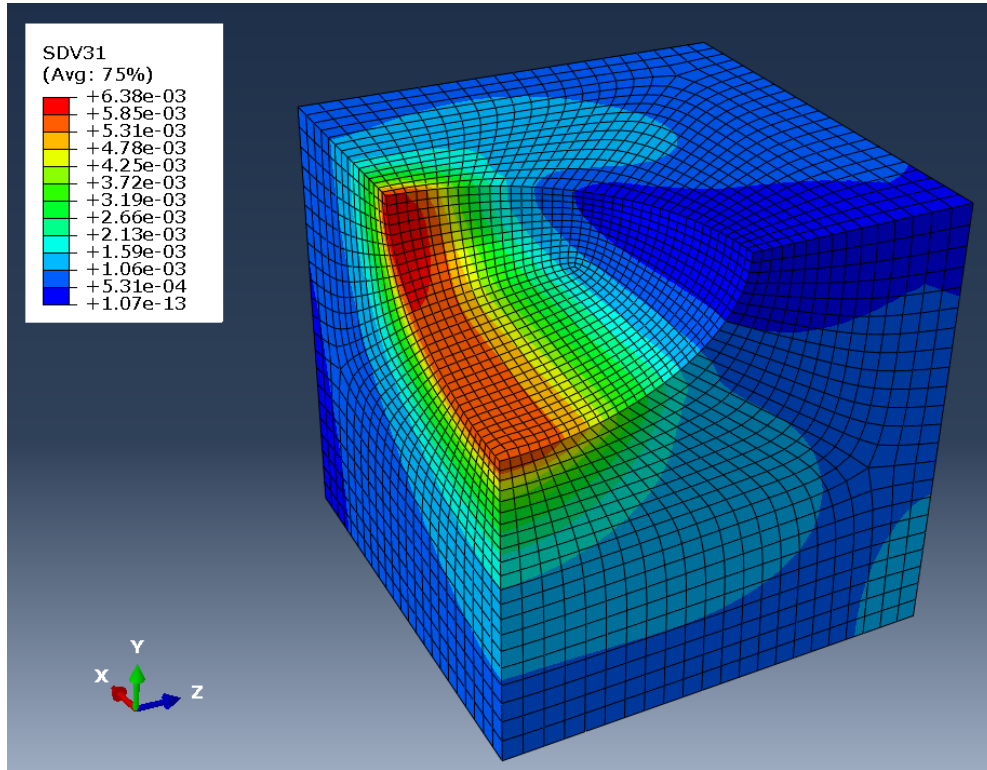


Figure 5-14: Magnitude of plastic strain around the pit after  $10^4$  cycles.

Although the maximum strain does not occur at the bottom, to compare to the current EBSD result (discussed in the next chapter), we extract the history of the magnitude of the plastic strain of the element at the bottom of the pit. The plastic strain magnitude versus number of cycles curve is given in Figure 5-15. We can see that the plastic strain increases dramatically at the first tens of cycles and then transitions to a stage of stable growth. A similar trend can be overserved from the experimental data (See Figure 5-8 for reference). Due to limited computation power, it is impossible to directly calculate the strain level to the number of cycles for crack initiation ( $\sim 1.5 \times 10^5$ ). By assuming that a stable strain growth rate is achieved after  $10^4$  cycles and maintained up the  $1.7 \times 10^5$  cycle (the number of cycles for the sample discussed in the next chapter), we can estimate the strain level at  $1.7 \times 10^5$  cycles by extrapolating the curve shown in Figure 5-15.

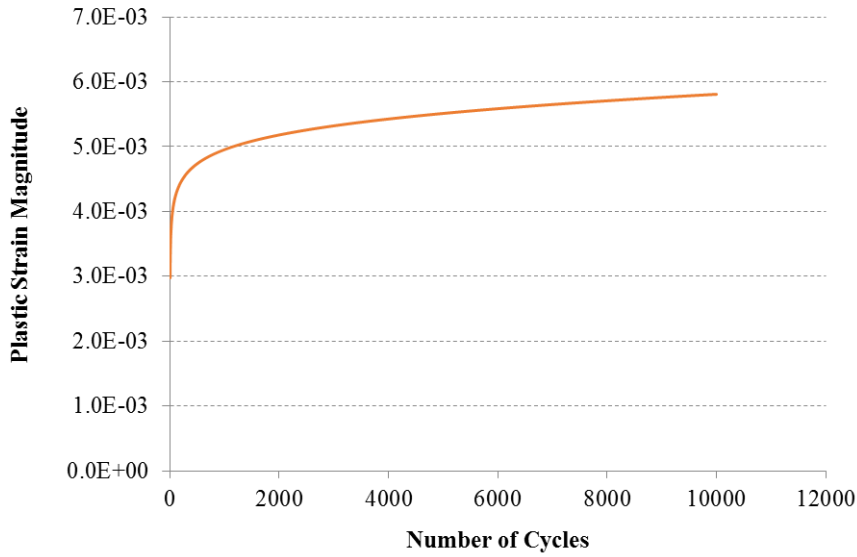


Figure 5-15: Plastic strain magnitude versus number of cycles curve of the element at the bottom of the pit.

To obtain the strain growth rate and to extrapolate the curve, we use the simulation results from 9000 to 10000 cycles, and fit the data with a linear curve. The result is shown in Figure 5-16. We can see that the plastic strain can be well fitted by a linear curve, from which we can estimate the strain ratcheting rate, which is  $4.83 \times 10^{-8}$  /cycle. The strain level at  $1.7 \times 10^5$  cycle can be estimated using this linear fit, which is approximately 1.35%.

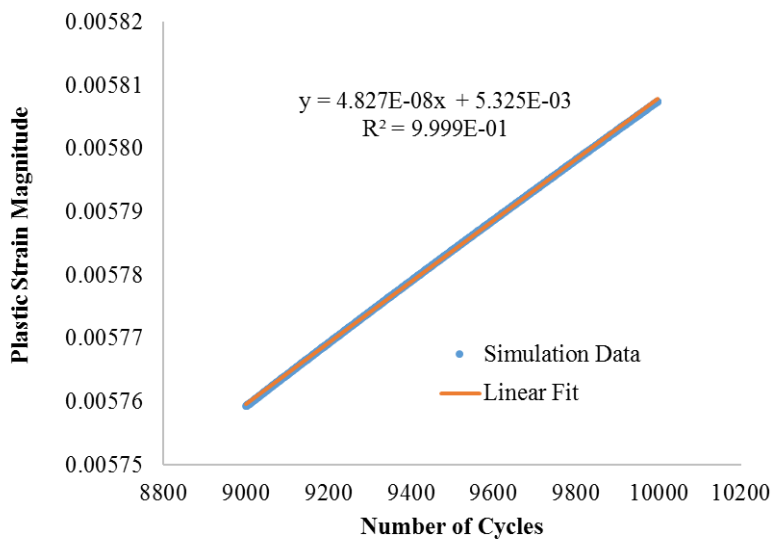


Figure 5-16: Linear fit of the plastic strain accumulation.

# Chapter 6 Plastic Strain Estimation using Electron Backscatter Diffraction (EBSD)

## 6.1 Introduction

Electron backscatter diffraction (EBSD) can be used to measure the collective effects of dislocations accumulated in the material under deformation and hence an approximate indicator of strain [227]. These dislocations can be divided into two categories: (1) geometrically necessary dislocations (GNDs) which give rise to curvature in the lattice and (2) statistically stored dislocations (SSDs) which do not result in lattice rotation [228]. The EBSD technique can be used to assess the plastic strain level in the material by (1) detecting the lattice imperfection caused by the GNDs and SSDs [229], [230] or (2) measuring the curvature in the lattice caused by the GNDs [231]–[236]. In this research, we will use the second method and estimate the plastic strain by measuring the misorientations in the lattice. Figure 6-1 illustrates schematically how an array of dislocations can generate sub-grains within a grain and how the EBSD detects the misorientation between these sub-grains.

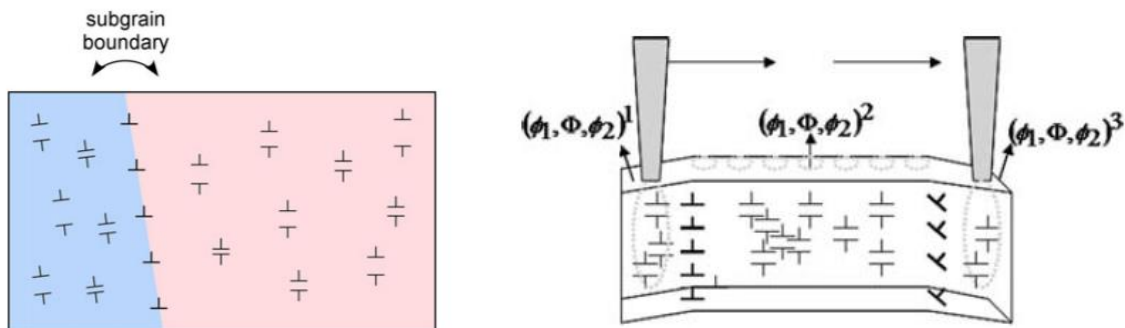


Figure 6-1: Left: Schematic of sub-grains generated by a dislocation wall [237]. Right: Schematic of change in orientation as the electron beam scan across the sample surface. Notice that the orientation only change when the beam crosses an array of dislocations with a net non-zero Burgers vector [227].

Under plastic deformation, the distortions in the crystal lattice are accommodated by the

formation of dislocations. Within the material, there are regions with dislocation density with a net Burger vector of zero (SSDs) and regions with dislocation density with nonzero Burgers vectors (GNDs). When the electron beam scans across the regions with GNDs in EBSD mode, a change in orientation (in the form of Euler angles) will be detected, as illustrated in Figure 6-1.

In order to assess the macroscopic plastic strain level through measurement of the microscopic misorientation in the crystal lattice., a proper average misorientation approach has to be applied. Here we use the average intragrain misorientation (AMIS) proposed by Sultiff [235] to average the microscopic misorientation. The microscopic misorientation is first calculated within each grain segment and then averaged over multiple grain segments to estimate the macroscopic plastic strain in that area.

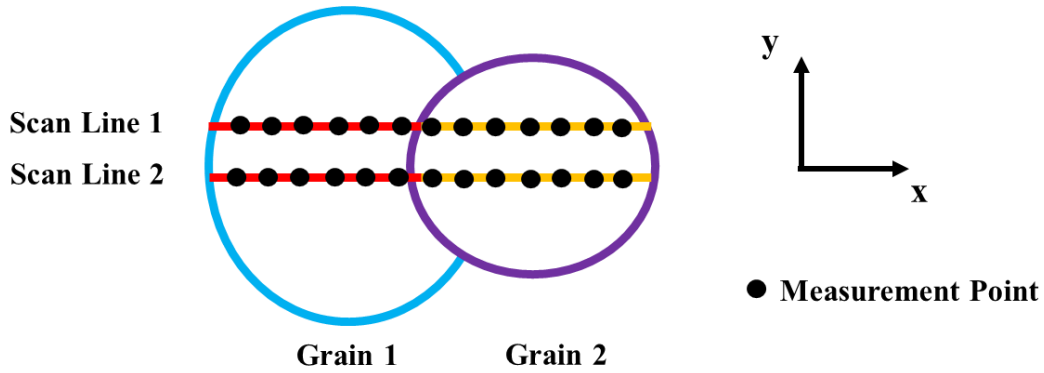


Figure 6-2: A schematic of the EBSD scan across grains.

Figure 6-2 shows a schematic of an EBSD scan across an area consisting of multiple grains. For each measurement point, the crystal orientation (three Euler angles) of this point is recorded. The AMIS value of a scan line across M grains is given by:

$$AMIS_{line} = \frac{\sum_{i=1}^M \left( \frac{\sum_{j=1}^{N_i-1} \sum_{k=j+1}^{N_i} \theta_{jk}}{N_i(N_i - 1)} \right)_{grain\ i}}{M} \quad (\text{Eq. 6-1})$$

where  $N_i$  is the number of measurement points within grain  $i$ , and  $\theta_{jk}$  is the scalar misorientation [227] between measurement point  $j$  and  $k$  within a grain. This formula first calculates the misorientation for every two points within a grain segment, and then averages over all grain

segments in the scan line. A critical value (e.g. 15°) is used identify grain boundaries. If the misorientation between two adjacent points on a scan line is larger than the critical value, the second point is considered to be within a new grain segment.

The AMIS value of an area is given by the average of AMIS line values in the area:

$$AMIS_{area} = \frac{\sum_i AMIS_{line,i}}{\text{number of scan lines}} \quad (\text{Eq. 6-2})$$

The  $AMIS_{area}$  is then used as an average misorientation value of this area and to correlate with the macroscopic strain.

## 6.2 Calibration Procedure and Results

To obtain the calibration curve between the plastic strain and the AMIS value of the X65 steel, specimens with different tensile plastic strain were made and their AMIS values measured. The selected plastic strain levels were 0%, 0.5%, 1%, 5%, 10%, 15%, 20%, 25%, and 30%. These measurements were performed at the GE-Global Research Center in Schenectady, NY. Figure 6-3 shows how the samples were sectioned from the original tensile specimen and mounted for EBSD measurement. Notice that both the transverse and longitudinal surfaces were characterized.

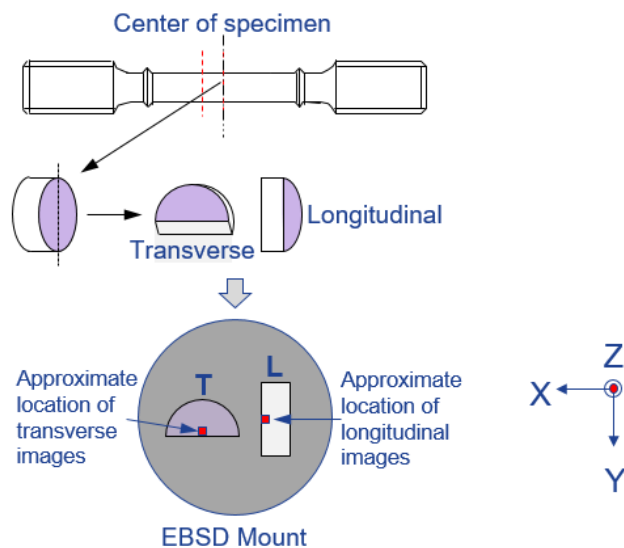
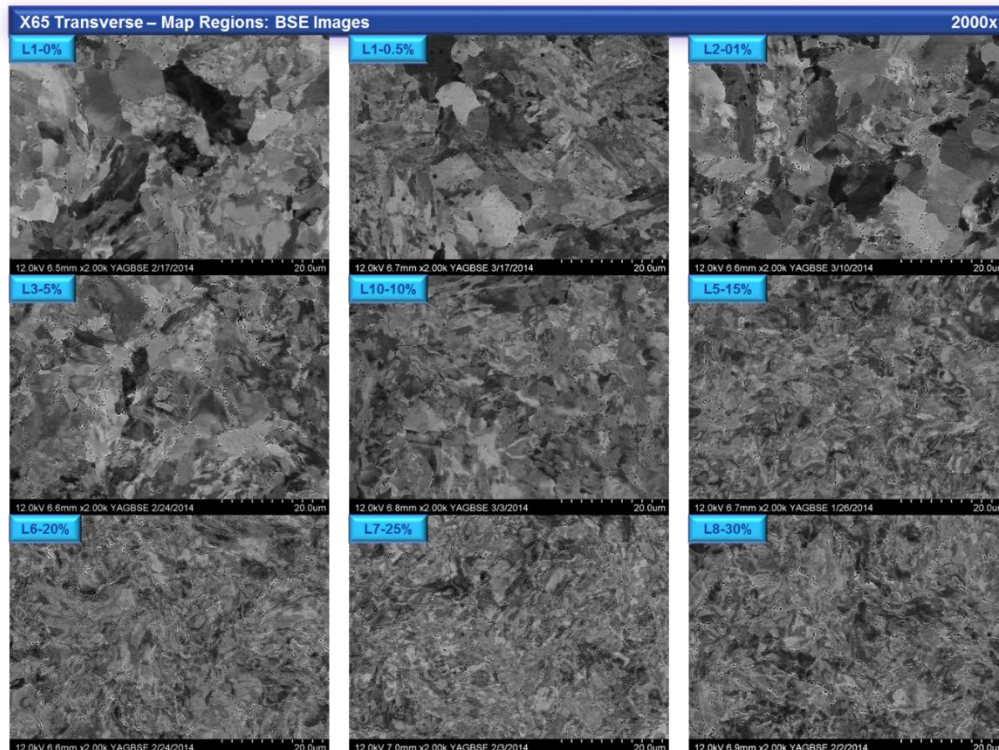


Figure 6-3: A schematic of EBSD sample preparation.

A Hitachi SU-70 SEM was used for surface characterization and EBSD measurement. The accelerating voltage used was 12 kV and the magnification used was 2000x. The scan area was approximately 64  $\mu\text{m}$  in the x direction and 44  $\mu\text{m}$  in the y direction. The scan steps for mapping was 0.05  $\mu\text{m}$  for both directions. For  $AMIS_{area}$  calculation, the spacing between scan lines was approximately 0.4  $\mu\text{m}$  and in total 110 scan lines were averaged in the area.

Figure 6-4 shows the backscattered electron (BSE) images for both transverse and longitudinal samples at different plastic strain levels. A backscattered electron is a primary electron that has been ejected from a solid by scattering through an angle greater than  $90^\circ$  [238]. The BSE signal shows Z-contrast due to differences in local atomic number and orientation contrast between grains in a polycrystalline specimen due to differences in electron penetration [238]. Thus BSE images can reveal grain/sub-grain information. Figure 6-4 shows that as the plastic strain level increases, the microstructure breaks into more small pieces because of the emergence of the sub-grain boundaries within the original grains.



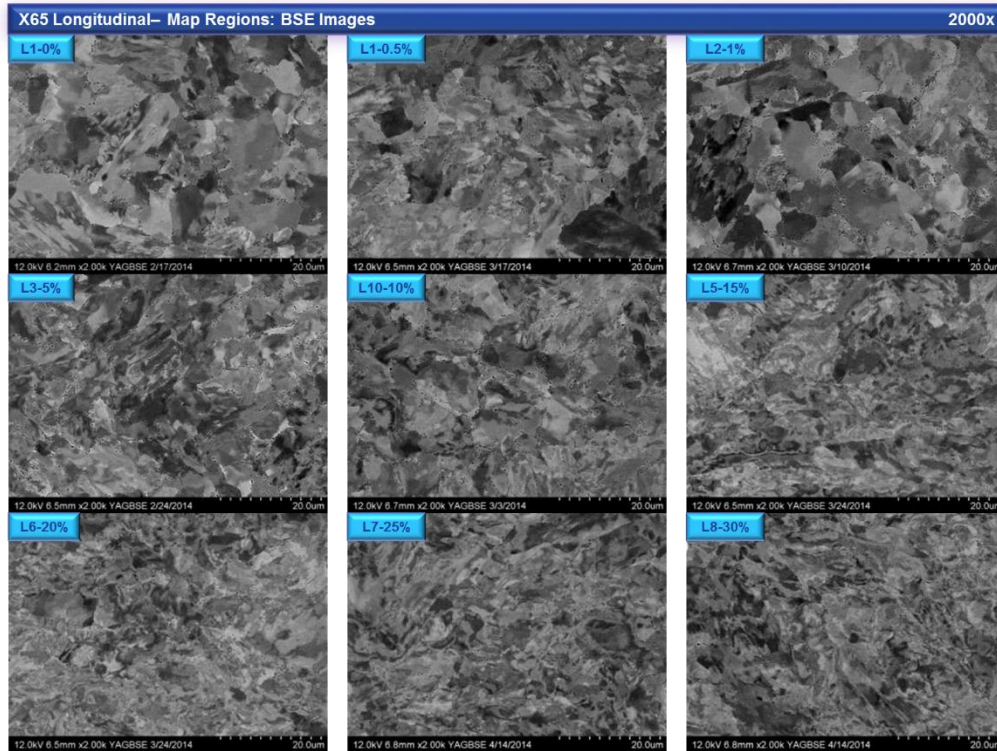


Figure 6-4: BSE images of transverse and longitudinal samples at different plastic strain levels.

Figure 6-5 shows the boundary maps for both transverse and longitudinal samples at different plastic strain levels. The boundary map is a basic EBSD measurement and is a direct visualization of misorientation. Boundaries in EBSD are determined as locations at which the scalar misorientation between adjacent pixels is greater than some critical value [227]. In Figure 6-5, high angle boundaries with misorientation larger than  $15^\circ$  are in blue, large angle boundaries with misorientation within  $3^\circ$  to  $15^\circ$  are in yellow and low angle boundaries with misorientation within  $1.5^\circ$  to  $3^\circ$  are in red. We can see that as the plastic strain increases, the density of low angle boundaries (red lines) increases, which represent the formation of dislocation walls and sub-grain boundaries. One thing to keep in mind is that the boundary map is calculated using the differential of orientation of two adjacent pixels, so the boundary map shows the local sources of misorientation, but not their net effect across the grain [227]. This also explains why the boundary maps can be noisy.

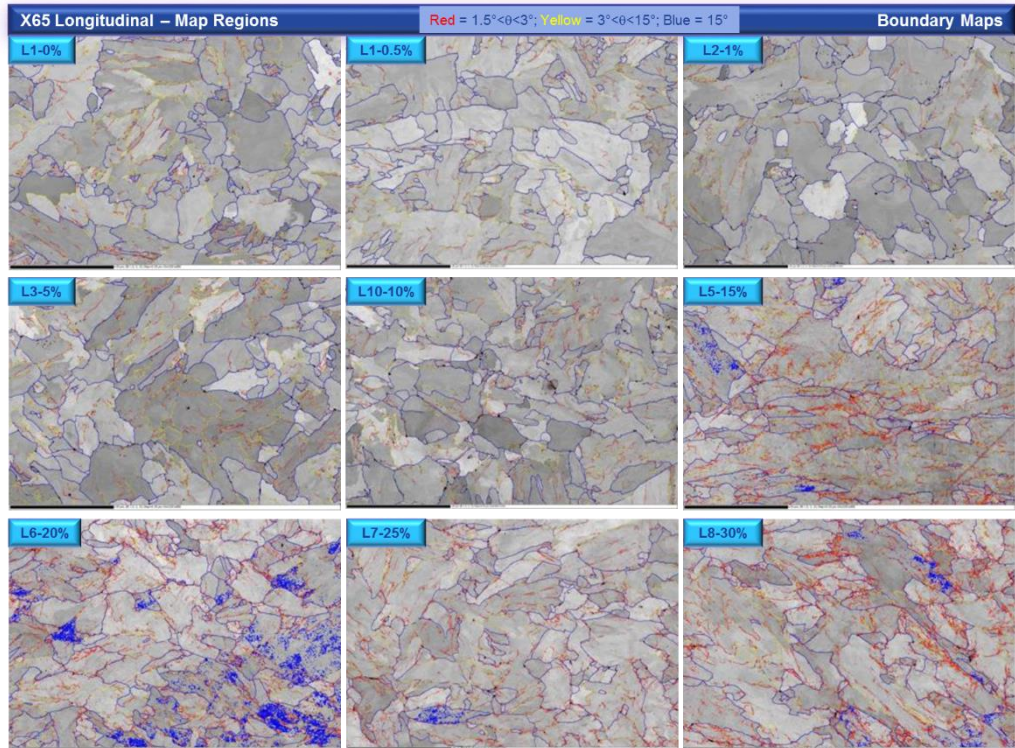
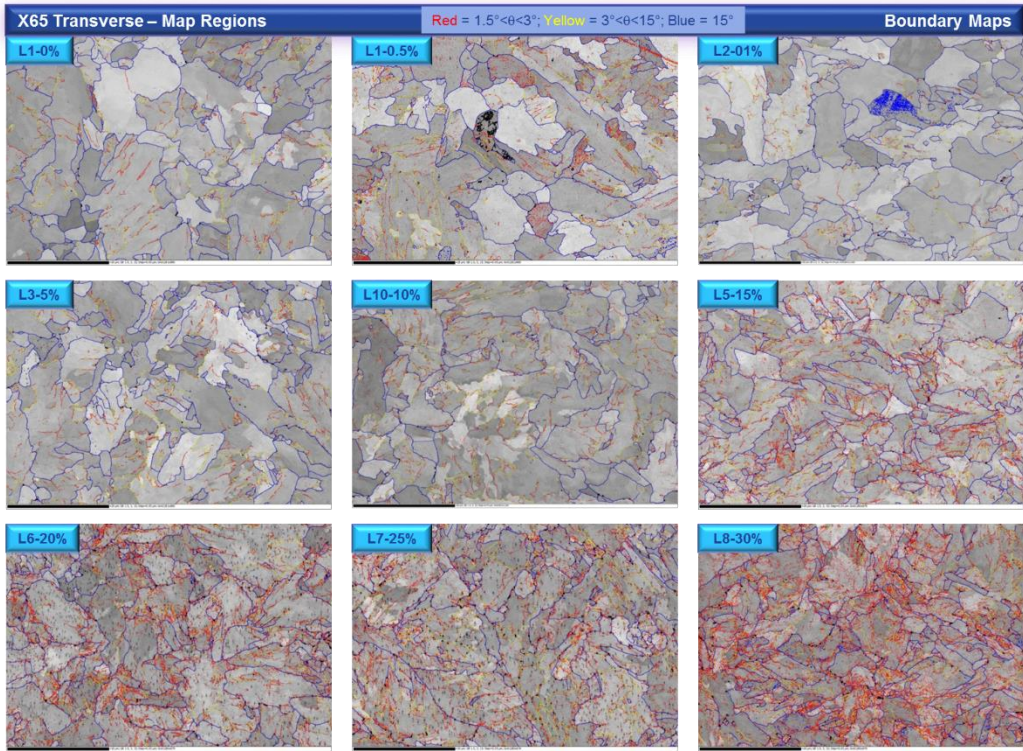


Figure 6-5: Boundary maps of transverse and longitudinal samples at different plastic strain levels (black line at bottom left corner in each figure is a scale bar of 20  $\mu\text{m}$ ). The density of low angle boundaries (red lines) increases with higher plastic strain levels.

Figure 6-6 shows the calibration curves for both transverse and longitudinal directions. The AMIS values in Figure 6-6 were calculated using (Eq. 6-1) and (Eq. 6-2), and were the average values over the scan area. This AMIS value calculated the misorientation in each grain segment, and then averaged over all grain segments in the scan area as illustrated in Section 6.1. We can see that the AMIS values of the transverse and longitudinal directions both increase linearly as the plastic strain increase. The AMIS values for the transverse and longitudinal directions are comparable, and both can be well fitted by linear equations. The linear relationship between the AMIS value and plastic strain was also reported by Sutliff [235], Young et al. [234], Lehockey [239]. The final calibration curve was obtained by averaging the data for the two directions, and is shown in Figure 6-7. It is noted that strain distribution in the material is inherently three dimensional while a single EBSD map only provide misorientations in one plane. It may be possible that with grain-based measures of misorientations as in one plane a grain may appear strained, whereas in another plane it may appear unstrained [240][241]. This is the reason for performing the calibration on two directions perpendicular to each other and averaging the AMIS data to get the final calibration curve.

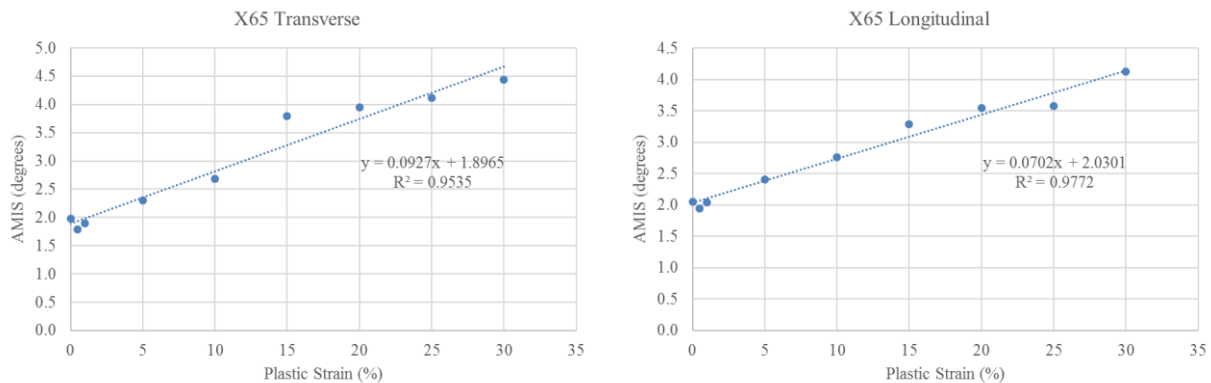


Figure 6-6: Calibration curves for both transverse and longitudinal directions.

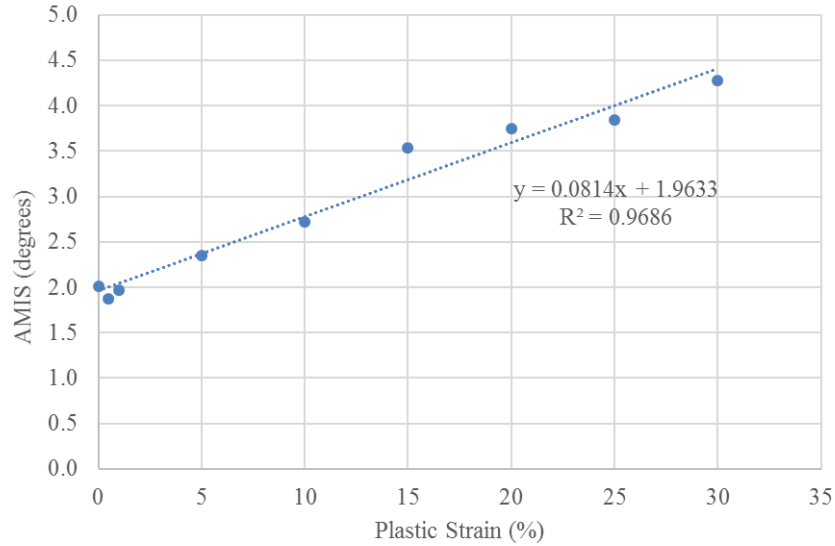


Figure 6-7: Averaged calibration curve for X65 steel.

### 6.3 Estimation of plastic strain level of the actual pit

After obtaining the calibration curve for the X65 steel, we can now use it to estimate the strain level at the actual pit after the fatigue test. Figure 6-8 shows a BSE image of the pit that has been analyzed. This pit was fatigued up to  $1.7 \times 10^5$  cycles in  $\text{CO}_2$ -saturated NaCl solution at  $120^\circ\text{C}$  (Same pit discussed in Section 4.3.5). A number of small cracks/crack-like features can be observed around the pit perimeter. As summarized in 4.3.6, we consider  $1.7 \times 10^5$  cycles is approximately the number of cycles for crack initiation under all four environments tested. Thus examining the strain level around the pit after  $1.7 \times 10^5$  cycles will give us an estimation of the strain level for crack initiation. However, it should be noted that the exact sequence of evolution of the morphology was not known. For example, the evolution of the crack/crack-like features is not known. We do not know when these features began to appear nor do we know the effect of this evolution on the rate of subsequent evolution. In general terms, we do know that the appearance of these features introduced an additional stress concentration which also may have, in turn, influenced the environmental interaction. In Figure 6-8, the sample is polished perpendicular to the cracks (Direction 1) in order to observe any potential crack. In this case, the tensile strain is localized at the bottom of pit, but not the mouths of the pit (See Figure 5-14 for reference). Thus it is useful to analyzed the strain level at the bottom of the pit. The area being analyzed is highlighted in a red box in Figure 6-8.

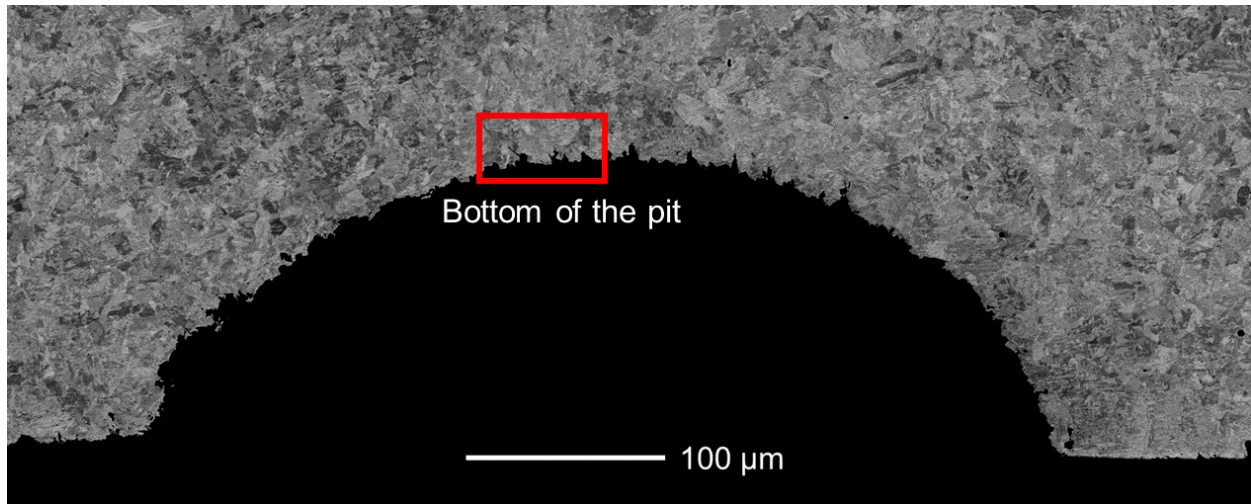


Figure 6-8: BSE image of the pit after  $1.7 \times 10^5$  cycles in  $\text{CO}_2$ -saturated NaCl solution at  $120^\circ\text{C}$ .

Figure 6-9 shows a zoom-in BSE image of the highlighted area shown in Figure 6-8 and the corresponding measured AMIS line values. The AMIS line values were calculated using (Eq. 6-1) and the number of grain segments used to calculate each AMIS line value is also given in Figure 6-9 (numbers at the y axis on the right side). The same BSE image of the scanned area is also given at the top left corner of the AMIS figure. The x axis of the plot, distance from the top line, is referred to the BSE image. The scan line of AMIS is closer to the surface of the pit as the distance from the top line increases. We can see that there is a slight increasing trend of the AMIS values as the distance increases, which means the strain is higher at the surface of the pit. A large peak is observed at around  $12\ \mu\text{m}$ , which may be due to ill statistics caused by low number of averaged grain segments.

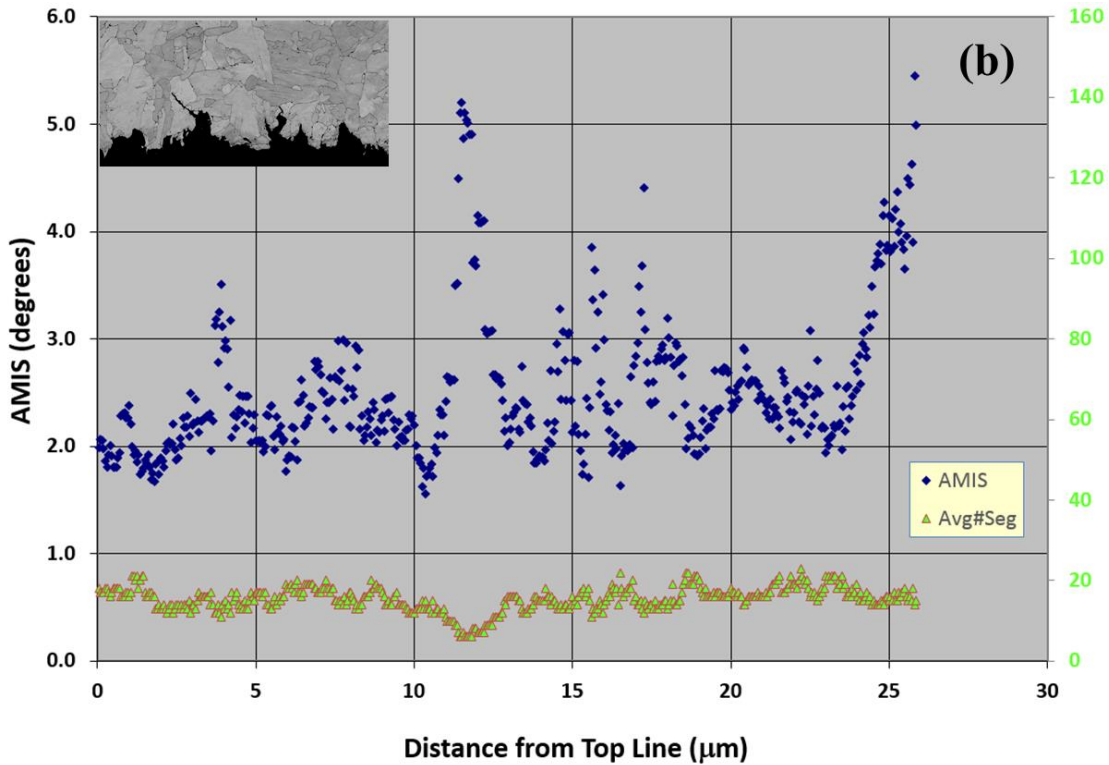
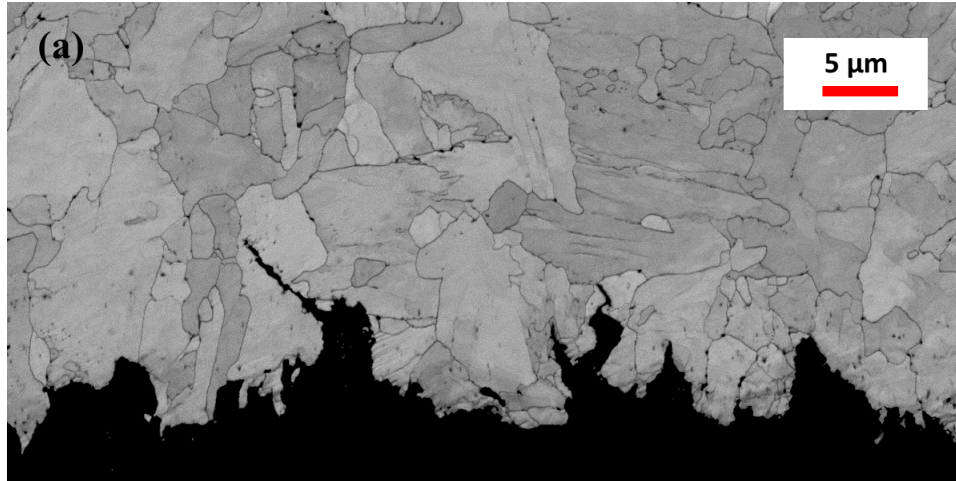


Figure 6-9: (a) A BSE image of the scanned area at the bottom of the pit; (b) AMIS line values measured in the scanned area.

The AMIS line values in Figure 6-9 are scattered. To obtain a better estimation of the strain level, it was helpful to average all the AMIS line values within every 5 μm from the top line to get the AMIS area values. The result is shown in Figure 6-10. We can see an increase in the average AMIS values as the distance increases (closer to the pit surface). It is worth noting that, the

scattering of the AMIS line values in may be physically true (rather than statistical noise), as the dislocation density on a microstructural level can be very localized [241].

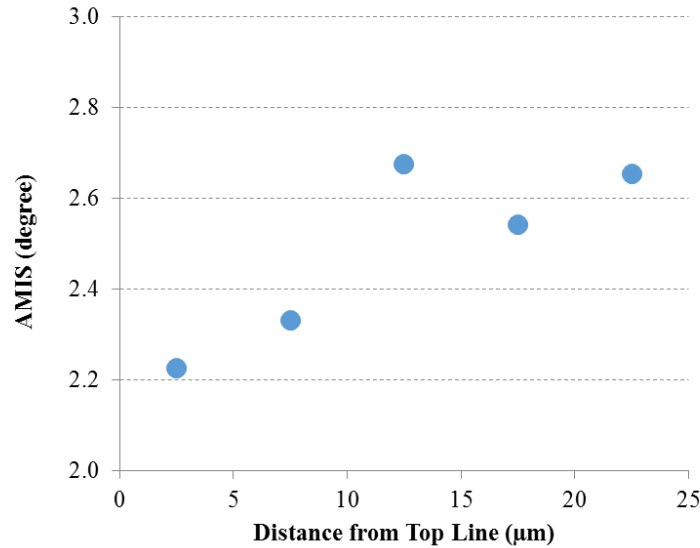


Figure 6-10: AMIS area values derived from Figure 6-9.

From the calibration curve obtained in Figure 6-7, we developed the following empirical correlation between AMIS and plastic strain (PS):

$$AMIS = 0.0814 * PS (\%) + 1.9633 \quad (\text{Eq. 6-3})$$

Using this correlation, we can convert the AMIS values to plastic strain. The converted values are shown in Figure 6-11. The converted plastic strain curve is on top of the BSE image of the scan area. Each plastic strain data point represents the average plastic strain in the area between the red dash lines. We can see that there is a clear increasing trend of the plastic strain toward the pit surface. At the surface, the plastic strain level is estimated to be approximated 8.5%. Considering the element size at the pit surface used in the simulation as 10 μm, it may be better to further average the two strain data points close to the surface, which yields approximately 7.8%. The figure also gives the minimum and maximum strain values (indicated by the orange bars with each data point) within each segment. Large scattering can be seen, in accordance with Figure 6-9. The simulation result we obtained in Section 5.5 predicts that after  $1.7 \times 10^5$  cycles, the plastic strain

level at the bottom of the pit is 1.35%, which is lower than the measured averaged value at the pit surface. The mismatch between the experimental results and simulation results will be discussed in Chapter 7.

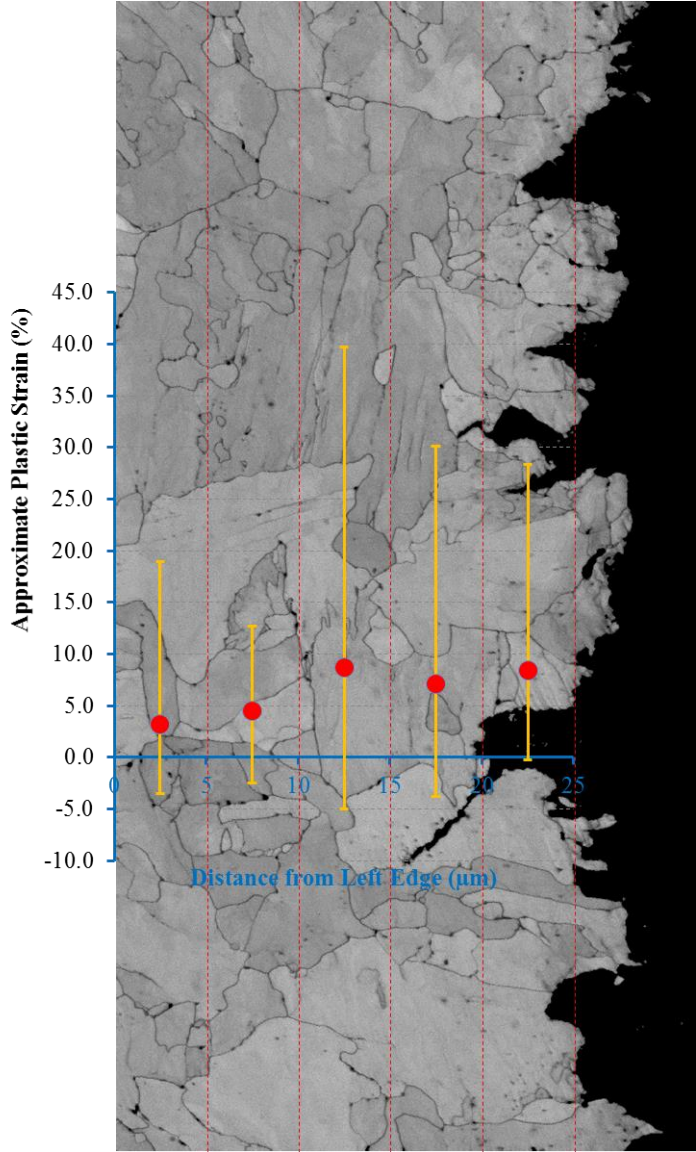


Figure 6-11: Converted plastic strain at the bottom of the pit.

# Chapter 7 Discussions, Conclusions and Future Work

## 7.1 Discussions

### 7.1.1 Pit-to-crack Transition Mechanism

Fatigue tests to detect crack initiation from pit have been performed in four different environments including (1) air at room temperature (RT); (2) aerated 1 wt.% NaCl solution at RT; (3) CO<sub>2</sub>-saturated 1 wt.% NaCl solution at RT; (4) CO<sub>2</sub>-saturated 1 wt.% NaCl solution at 120 °C. Pit geometry and loading conditions were the same for all tested environments. In environment (1) and (4), non-propagating fatigue cracks were observed after  $1.7 \times 10^5$  cycles by examining the cross-section of the pit under optical microscope and SEM. In environment (2) and (3), crack initiation was detected by ACPD. Crack initiation was estimated to occur after approximately  $1.5 \times 10^5$  cycles. Based on these experiment results, we concluded that the pit-to-crack transition was dominated by a combination of mechanical factors to provide necessary strain concentration and the presence of the aggressive environment to provide locally accelerated penetration via the production of crack “precursors” in cases where film formation was not adequately protective.

Plastic strain has been recognized as a key mechanical factor for pit-to-crack transition [1][242]. In this research, a model was developed to simulate the plastic strain evolution around the pit during stress controlled cyclic loading. The simulation results show that under the loading conditions applied in the experiments, plastic strain around the pit continues to increase with the number of cycles. Although the applied stress level far away from the pit is below yield stress, because of the stress concentration effect of the pit [243], the area around the pit is in effect in a ratcheting scenario. Notice that the crack initiation mechanism in this case may be not simply categorized into high cycle fatigue where plasticity occurs within only a few grains, or low cycle fatigue where plastic strain amplitude is typically fixed [58]. It may also be different from the “general” ratcheting phenomenon discussed in most literature where specimens are usually subjected to uniaxial loading condition and ratcheting occurs uniformly in the whole gauge section (e.g. [153][155]). To the best of the author’s knowledge, the damage mechanism of pit-to-crack transition under current investigation can be termed as “local ratcheting” [244]. The word “local” here is referred to the pit geometry, and should still be considered on the macroscopic scale. While

the model developed in this work has been shown to well characterize the local plastic strain evolution, as shown by comparison against data from the literature, the development of crack/crack-like precursors as a result of the corrosive environment introduces additional factors that will act to augment/enhance initiation. These precursors will add additional stress concentrations that are not accounted for and which, in the case where the film is not stable, constitute the effect of the corrosive environment. In all cases the fatigue loading conditions were below the literature fatigue limit (defined at  $10^7$  cycles) and likely below the endurance limit in air.

In summary, based on a combination of the experimental and simulation results, we propose that the underlying mechanical mechanism driving the pit-to-crack transition under the applied test conditions is local ratcheting. Plastic strain accumulates around the pit during fatigue cycles, and when it reaches a critical plastic strain level, which depends on the interaction with the environment, a crack initiates from the pit. Whether the crack then propagates depends on the interaction between the local strain and the environment which facilitates the introduction of crack precursors. Using the EBSD technique, the upper bound of the critical strain level for crack initiation of X65 steel was estimated to be approximately 8.5% at the bottom of a pit where small cracks were observed. Sinha and Ghosh [157] proposed that the critical strain level for crack initiation in ratcheting can be estimated using the true strain level where the peak true stress occurs from a monotonic tensile test. From the stress-strain curve shown in Figure 7-1, the peak stress occurs at the strain level of 11.7%. The corresponding plastic strain level is 11.4%. This is comparable to the plastic strain level (8.5%) measured using EBSD.

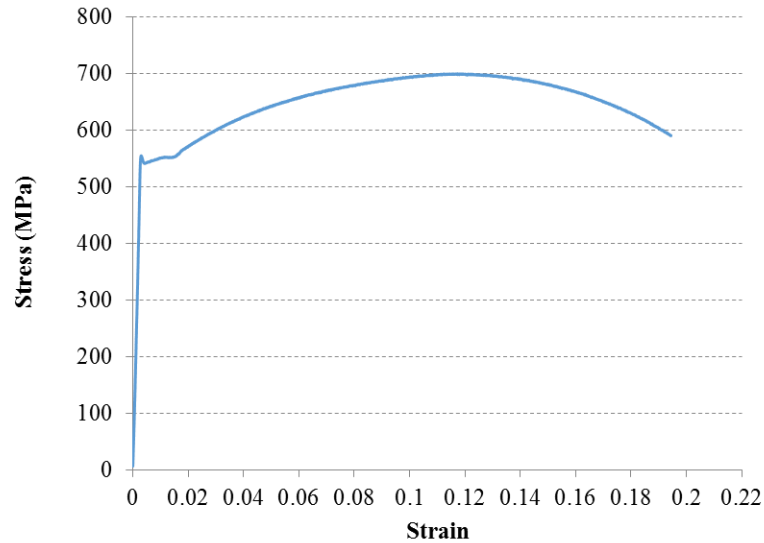


Figure 7-1: True stress- strain curve of a monotonic tensile test of the X65 steel.

The current simulation predicts that the strain level at  $1.7 \times 10^5$  cycles to be approximately 1.35%, which is lower than the measured level of 8.5% (or 7.8% on a 10  $\mu\text{m}$  average). Several reasons may account for this difference:

1. To predict the strain level at  $1.7 \times 10^5$  cycles, we extrapolated the plastic strain versus number of cycles curve assuming that the strain rate, which was obtained by fitting the simulation results from 9000 to 10000 cycles, remained constant towards  $1.7 \times 10^5$  cycles. However, this may not be accurate. As shown in Section 5.4.2, the X65 steel exhibits a three-stage ratcheting behavior where the strain rate first decreases, then becomes stable, and then increases. The plastic strain rate may increase after 10000 cycles, and lead to a higher level of plastic strain at  $1.7 \times 10^5$  cycles. Due to limited computational power, only  $10^4$  fatigue cycles could be analyzed in this thesis.
2. In the simulation, we assume the pit has a smooth surface. However, the artificially made pit is not perfectly smooth, as can be seen in Figure 4-21. Furthermore, in corrosion fatigue tests, the pit surface will suffer from corrosion and become more rough. In Figure 6-11, it can be seen that perimeter of the pit was ragged after the corrosion fatigue test in in  $\text{CO}_2$ -saturated NaCl solution at 120 °C, with some indents at the edge. These indents can serve as additional stress concentrators [245] and increase the strain level around the pit.
3. In Figure 6-11 we show the full range of the data used in the averaging process to arrive

at the “data” points. While there is considerable scatter on the data, the general trend is as identified. When comparing the simulation results with the observed scatter a better insight can be obtained.

### 7.1.2 Role of Corrosion in Pit-to-crack Transition

Although the current results suggest that the strain for crack initiation conditions are established by mechanical factors, significant effects of corrosion were observed based on the experimental results.

#### 7.1.2.1 Corrosion Effect on Crack Initiation

Figure 7-2 shows pit cross-sections after fatigue in air and in CO<sub>2</sub>-saturated NaCl solution at 120 °C after  $1.7 \times 10^5$  cycles. Small cracks/crack-like features were observed in both cases. However, only one crack initiation spot was found in the air fatigue case (highlighted with the green box), while multiple crack or crack like features were observed in the corrosion fatigue case. We can also see that the pit surface became rougher after corrosion fatigue compared to in air fatigue. Corrosion can result in enhanced surface roughness of the pit because of inhomogeneity in material [246][247]. The surface roughness may act as additional stress concentrator [248][249] and facilitate crack initiation via the production of crack precursors. In these two cases crack initiation (or propagation) did not occur. As mentioned above, in all cases the stress range for the test program was below the fatigue limit, defined at  $10^7$  cycles and likely below the endurance limit for the material. Iron-based alloys typically exhibit an endurance limit in air but not in a corrosive environment [250]. In a corrosive environment the interaction between the environment, material, and the formation and stability of any protective film becomes critical.

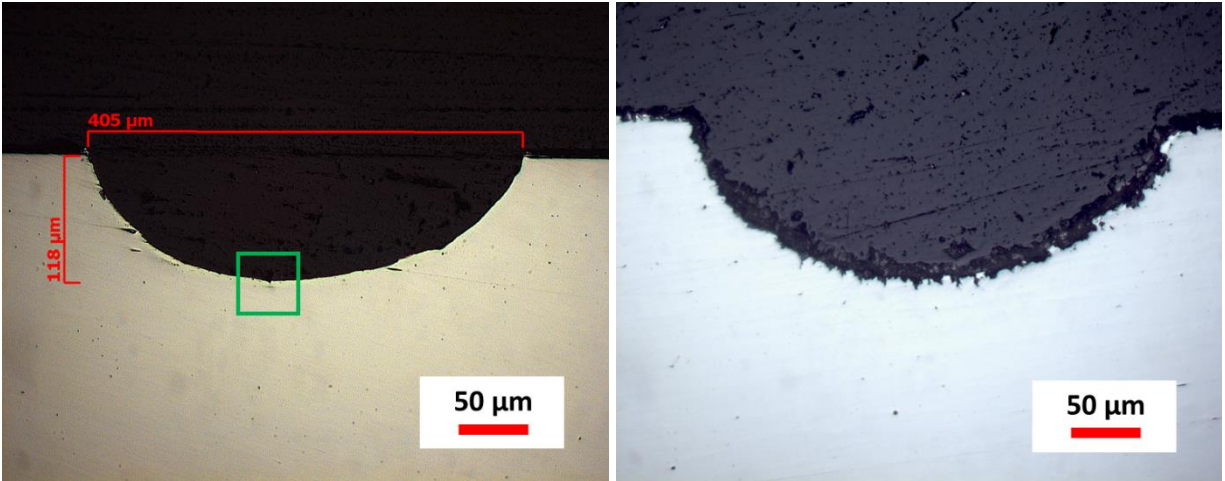


Figure 7-2: Comparison of crack initiation in air (left) and in CO<sub>2</sub>-saturated NaCl at 120 °C (right).

In the corrosion fatigue case, the interaction between strain and corrosion may promote the preferential corrosion and the resulting surface roughness. Xu and Cheng [251] have tested the corrosion rate of X100 steel specimens in a neutral pH bicarbonate solution at different plastic strain levels. They designed a flat specimen with gradually-increasing width from one end of the gauge section to the other, which allowed them to obtain a continuous plastic strain distribution on one sample. The Scanning Vibrating Electrode Technique (SVET) was applied to measure the local corrosion current along the sample surface with different plastic strain levels. Their result showed that the corrosion rate of X100 carbon steel was increased by the plastic strain. They further pointed out that a non-uniform distribution of plastic strain would cause different corrosion activities on the steel and initiate preferential localized corrosion.

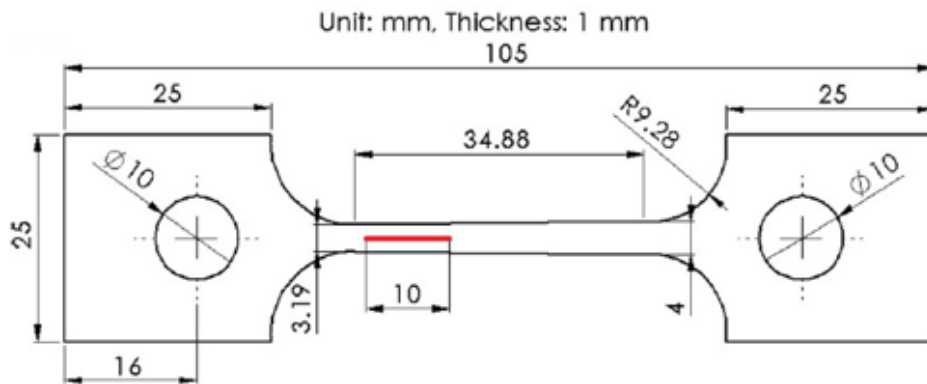


Figure 7-3: Specimen used in [251], the red line shows the scanning path for corrosion current measurement.

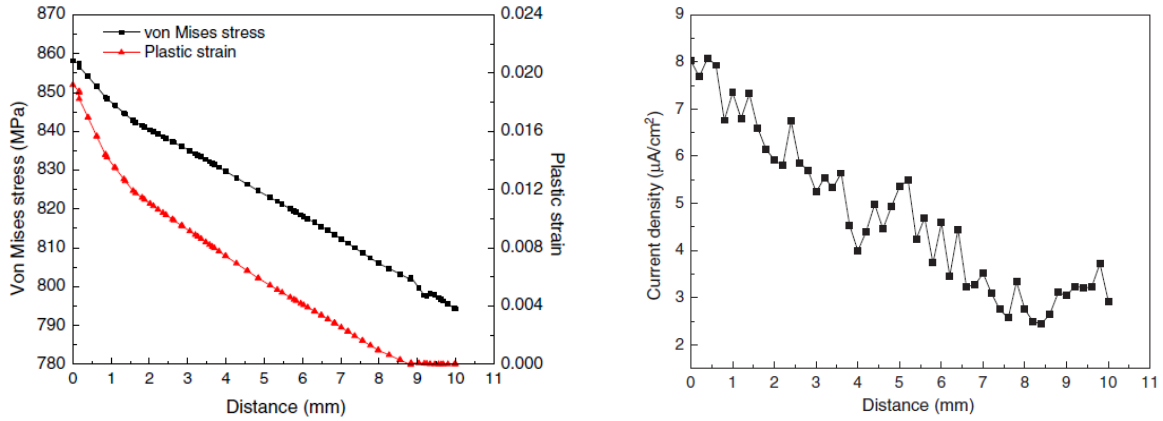


Figure 7-4: Left: Distribution of von Mises stress and plastic strain along the scanning path; Right: Measured corrosion current density [251]. A positive correlation between the plastic strain and the corrosion rate can be observed.

If the conclusion from the experiment by Xu and Cheng [251] is applicable on the grain level, some grains exhibit higher plastic strain than the adjacent grains and may be sites for preferential corrosion. The volume left by the preferentially corroded grains may serve as additional stress concentrators for crack initiation. This may result in enhanced surface roughness and facilitate multiple crack initiation, as what we see in Figure 7-2. Furthermore, in the corrosion fatigue test in aerated 1 wt.% NaCl solution, we observed crack initiation from precursors which exhibited granular feature (see Figure 7-5). This might be due the preferential corrosion on certain strained grains. However, from our experimental results, the additional stress concentration effect caused by the corrosion will be small. None-the-less, in cases where the film is not stable and active corrosion occurs, this is likely enough of an effect to facilitate initiation.

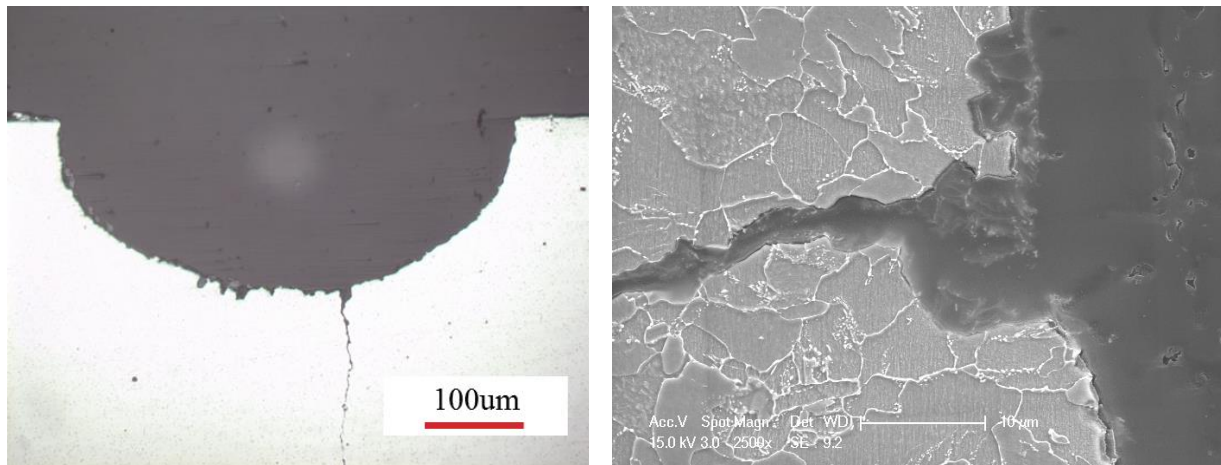


Figure 7-5: Left: Optical microscopic photo of crack initiation in aerated 1 wt.% NaCl solution; Right: SEM image of crack initiation site at higher magnification.

The effect of corrosion on corrosion fatigue, while obvious, can become confusing when discussing the actual initiation process. Ahn [7] defined crack initiation as when a surface crack initiates from the pit and reaches 20  $\mu\text{m}$  in length. With this definition, the initiation life in air and  $\text{CO}_2$ -saturated NaCl solution at 120  $^\circ\text{C}$  in our tests will be infinite since we did not observe “cracks” of this length. In our study, we considered initiation of small non-propagating as initiation. Fatoba [139] used a higher stress level and more aggressive environment (brine solution) than our study, which may have led to the differences in the observed crack initiation time. In summary, the conclusion that corrosion does not significantly affect crack initiation life only applies to some of the specific test conditions/environments used in this study, and may not be applicable in other environments and loading conditions.

#### 7.1.2.2 Corrosion Effect on Crack Propagation

Although small cracks were observed in all four testing environments, crack propagation was only detected in the aerated NaCl solution case, in the  $\text{CO}_2$ -saturated NaCl solution at RT, but not in air or in the  $\text{CO}_2$ -saturated NaCl solution at 120  $^\circ\text{C}$ . Non-propagating fatigue cracks have been observed in other studies (e.g. [252][253]). Small fatigue cracks can be arrested by microstructural barriers in the material when the applied stress is relatively low [254][255]. In the air fatigue case, the initiated crack may be arrested by microstructural barriers in the material and become a non-propagating crack. The non-propagation of cracks in air in our tests can be predicted using the

concept fatigue limit, as fatigue cracks will not initiate and grow below a defined fatigue limit (typically defined at  $10^7$ - $10^8$  cycles) [6]. In our tests, the nominal applied maximum stress is 80% yield stress with stress ratio  $R=0.1$ , so the stress amplitude is:

$$\sigma_a = \frac{\sigma_{max} - R * \sigma_{max}}{2} = 0.36 \sigma_y = 187 \text{ MPa} \quad (\text{Eq. 7-1})$$

Note that the yield stress of the material is 521 MPa, and the tensile strength is 700 MPa. In order to account for the stress concentration effect, the fatigue notch factor is applied. The fatigue notch factor for a similar pit geometry is estimated to be  $K_f = 1.1$  by Fatoba [139]. The elastic stress concentrator of the pit cannot be used here because of the plasticity effect associated with the pit [55]. The enhanced stress amplitude is:

$$K_f \sigma_a = 206 \text{ MPa} \quad (\text{Eq. 7-2})$$

The fatigue limit at  $10^7$  cycles of the X65 steel with  $R=0.1$  is estimated to be 225 MPa by Fatoba [139], which is higher than the current used stress amplitude. So the cracks are not able to grow in air under current loading conditions. We can also correct the stress amplitude using the Gerber relation [256] to account for the non-zero mean stress effect, which gives:

$$K_f \sigma_a = \sigma_a |_{\sigma_m=0} \left\{ 1 - \left( \frac{K_f \sigma_m}{\sigma_{UTS}} \right)^2 \right\} \quad (\text{Eq. 7-3})$$

where  $\sigma_m = \frac{\sigma_{max} + R * \sigma_{max}}{2} = 0.44 \sigma_y$ . We can solve the corresponding stress amplitude with zero mean stress:

$$\sigma_a |_{\sigma_m=0} = \frac{K_f \sigma_a}{1 - \left( \frac{K_f \sigma_m}{\sigma_{UTS}} \right)^2} = 236 \text{ MPa} \quad (\text{Eq. 7-4})$$

The fatigue limit of X65 steel with zero mean stress can be estimated using the data obtained by Fatoba and Akid [257]. In their paper, they fitted the coefficients of the Basquin relations for X65

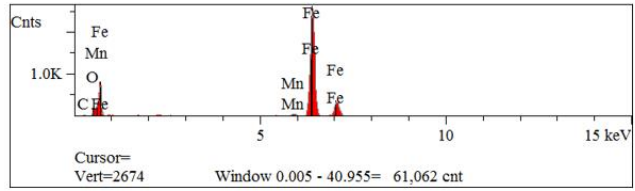
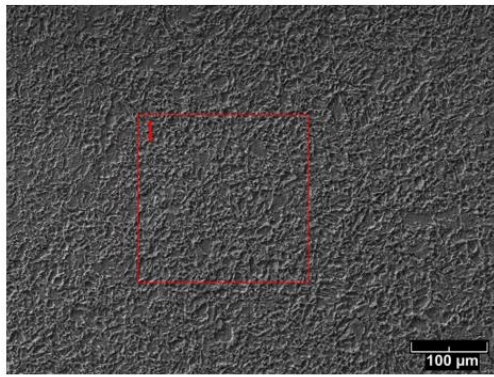
steel using their experiment data:

$$\sigma_a = \sigma_f' (2N_f)^b \quad (\text{Eq. 7-5})$$

where  $\sigma_f' = 801.8 \text{ MPa}$  and  $b = -0.068$ . Using  $N_f = 1 \times 10^7$  as the fatigue limit, the corresponding fatigue limit with zero mean stress is 255 MPa, which is higher than stress level given by (Eq. 7-4). These simple analyses are consistent with the air fatigue results as no failure was observed in the air fatigue case up to  $1 \times 10^7$  cycles. However, in the aerated NaCl solution at RT, microstructural barriers may be weakened or corroded by the environment [6]. This effect may couple with the slight increase in stress concentration resulting from the precursor. No fatigue limit was observed by Fatoba [139] down to stress amplitude of 150 MPa with  $R=0.1$  in brine solution. These effects help to explain the observed crack growth in the aerated NaCl solution at RT tests.

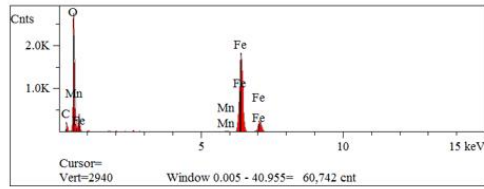
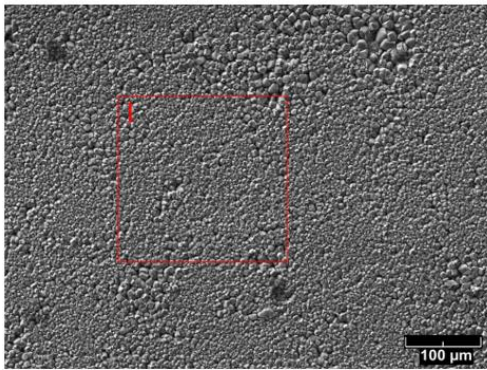
For the two other test environments with  $\text{CO}_2$ , although a corrosive environment is presented in both cases, crack growth was observed at the RT case but not the 120 °C case. This phenomenon can be explained by the formation of a protective corrosion product layer at high temperature. Nescic has shown that a protective  $\text{FeCO}_3$  corrosion product layer can only form at temperatures higher than 60 °C at near neutral pH in aqueous  $\text{CO}_2$ -containing environments [38]. Below 60 °C, the corrosion rate was high without the corrosion layer (See Figure 2-9). Although one would expect that the corrosion rate steadily increases with temperature, the rapid precipitation of the  $\text{FeCO}_3$  protective layer formation, decreases the corrosion rate at higher temperature.

Figure 7-6 and Figure 7-7 show the EDS analysis of two specimens tested in  $\text{CO}_2$ -saturated NaCl solution at RT and 120 °C, respectively. The EDS analysis shows that for the RT case, the surface was mainly F. While at the 120 °C, a higher level of O and C atoms were detected, which suggests the existence of iron carbonate and iron oxide. The morphology of the two surfaces were also different, as shown in Figure 7-8. The morphology of the  $\text{FeCO}_3$  layer observed is similar to those in literature [43][44].



Element	Line	Intensity (c/s)	Atomic %	Atomic Ratio	Conc	Units
C	Ka	44.16	7.3	0.68	1.8	wt.%
O	Ka	240.51	10.7	1.00	3.5	wt.%
Mn	Ka	143.79	1.5	0.14	1.7	wt.%
Fe	Ka	6,080.13	80.5	7.53	92.9	wt.%
			100.0		100.0	wt.%

Figure 7-6: EDS analysis of the surface of a specimen test in CO<sub>2</sub>-saturated NaCl solution at RT after 14 hours. Left: SEM image of the surface, red retangle highlights the analysis area; Right: EDS analysis result. The blue box highlights the atomic ratio of different elements. The result shows that the surface is mainly Fe.



Elt.	Line	Intensity (c/s)	Atomic %	Atomic Ratio	Conc	Units
C	Ka	164.03	13.9	0.23	6.4	wt.%
O	Ka	2,174.17	59.2	1.00	36.2	wt.%
Mn	Ka	46.56	0.3	0.01	0.7	wt.%
Fe	Ka	3,006.81	26.6	0.45	56.7	wt.%
			100.0		100.0	wt.%

Figure 7-7: EDS analysis of specimen surface after test in CO<sub>2</sub>-saturated NaCl solution at 120 °C after one weeks. Left: SEM image of the surface, red retangle highlights the analysis area; Right: EDS analysis result. The blue box highlights the atomic ratio of different elements. The result suggests that the surface is mainly covered by FeCO<sub>3</sub> and iron oxide.

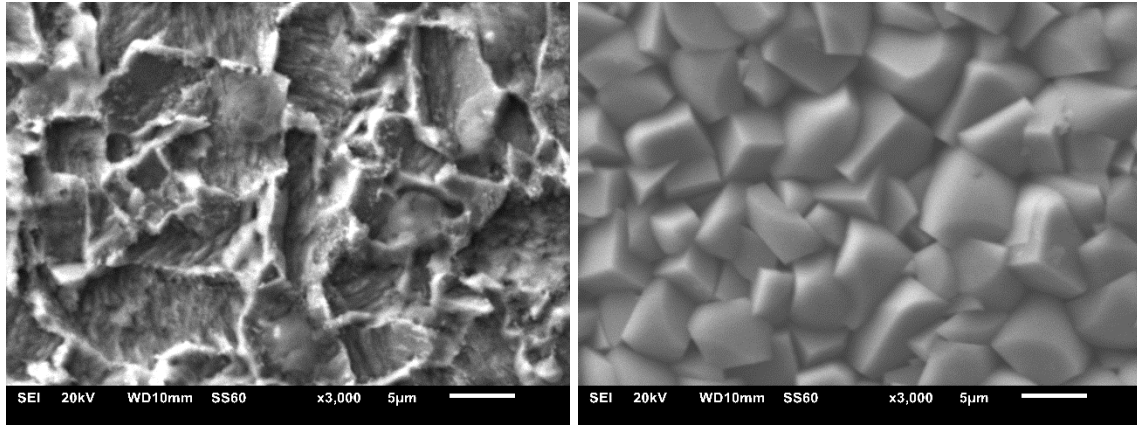


Figure 7-8: SEM images of specimens tested in at CO<sub>2</sub>-saturated NaCl solution at different temperatures. Left: specimen tested at RT, the surface is mainly corroded bare metal; Right: specimen tested at 120 °C, the surface is covered by FeCO<sub>3</sub> scales.

According to the literature and EDS analysis results, it is proposed that in our tests in CO<sub>2</sub>-saturated NaCl solution at RT, the crack is able to initiate and grow due to the environment, while at 120 °C small cracks are arrested by the microstructural barriers as the formation of a protective FeCO<sub>3</sub> layer stops the corrosion. Figure 7-9 shows the bottom of pit of the specimen fatigued in CO<sub>2</sub>-saturated NaCl solution at 120 °C. Possible crack arrestment at grain boundary can be observed (highlighted by the yellow arrows).

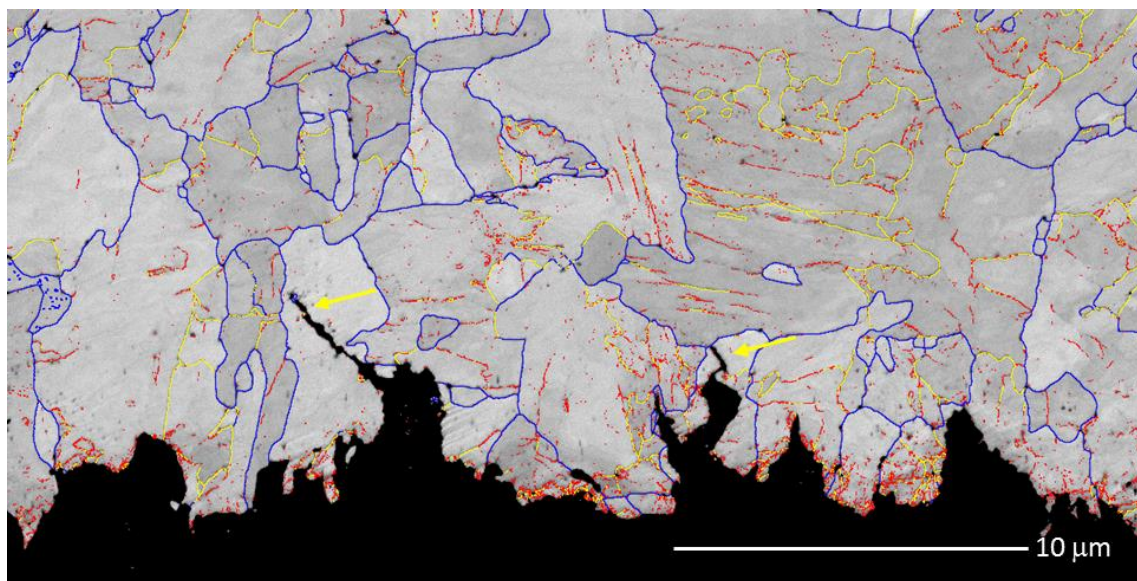


Figure 7-9: Possible crack arrestment at grain boundary observed from the specimen fatigued in CO<sub>2</sub>-saturated NaCl solution at 120 °C.

In summary, corrosion plays a significant role in facilitating the production of crack precursors. Accelerated corrosion is promoted by the presence of local strain concentrations produced by the mechanical action but the role of protective film formation is also a critical factor. Crack propagation is further facilitated by corrosion due to the surmounting of microstructural barriers that would normally prevent simple mechanical propagation. With the help of corrosion. Small cracks can overcome the microstructural barriers in the material and continue to grow into long cracks [6].

### 7.1.3 Resolution of the ACPD System

With a threshold of 0.25%, a crack of 250 μm can be detected using the developed ACPD system. The resolution of the current system is limited by the probe spacing. We used a probe spacing of 4 mm in our experiments. Using the analytical relation between the potential drop and crack length for 2D cracks developed by Dover et al. [168]:

$$\frac{\Delta V}{V_0} = \frac{2a}{3L} \cot\left(\frac{\xi}{3}\right) - 1 \quad (\text{Eq. 7-6})$$

where  $V_0$  is the potential drop without the crack and  $\Delta V$  is the increment of potential drop with the crack.  $2L$  is the spacing between the two voltage probes, and  $\xi = 2\cot^{-1}(L/a)$ , we can plot  $\Delta V/V_0$  versus crack length with different probe spacings. The result is shown in Figure 7-10. As the probe spacing decreases, the sensitivity of the potential drop system increases. For example, with a detection threshold of 0.1%, a crack of 35 μm can be detected with probe spacing ( $2L$ ) of 1 mm, while a crack of 75 μm can be detected with probe spacing of 2 mm, and a crack of 150 μm can be detected with probe spacing of 4 mm. These results are consistent with our experimental results in general.

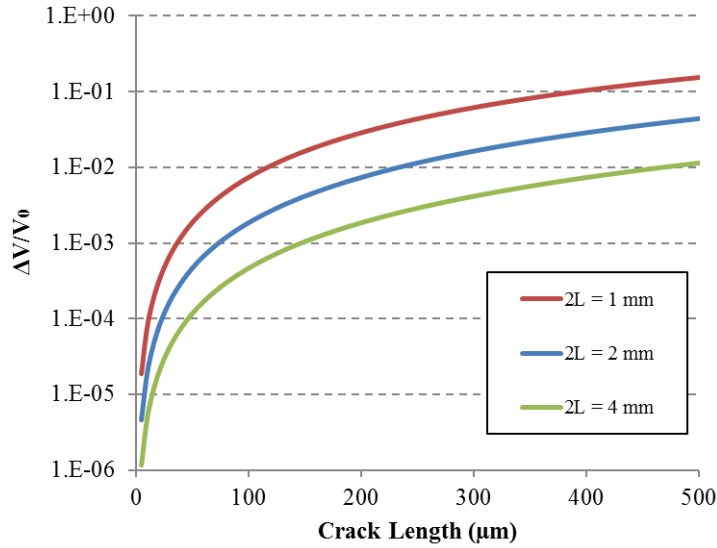


Figure 7-10: Change of potential drop versus crack length with different probe spacings.

The pit diameter used in this research was approximately 500  $\mu\text{m}$ , in theory we could have used a probe spacing of 1 mm to achieve better resolution. However, because the uncertainties associated with spot welding the probes, in practice it was very difficult to shrink the probe spacing without potentially damaging the pit. Other methods may be used to attach the electrical wire to the sample to achieve a smaller probe spacing, such as microscopic spot welding [167].

## 7.2 Conclusions

The pit-to-crack transition behavior of the X65 steel under fatigue and corrosion fatigue has been investigated. The following conclusions may be drawn:

- Crack initiation was observed using optical microscopy and SEM, or detected by the ACPD system, after  $\sim 1.5 \times 10^5$  cycles in all four tested environments, including in air, in aerated NaCl solution at RT, in  $\text{CO}_2$ -saturated NaCl solution at RT and in  $\text{CO}_2$ -saturated NaCl solution at 120 °C. The loading condition was the same in all four environments, with peak stress of 80% yield stress, stress ratio of 0.1 and loading frequency of 5 Hz. It is concluded that crack initiation process is dominated by a combination of mechanical factors (e.g. pit geometry, loading conditions) in tested environments facilitated by the environment.
- Crack propagation was observed in aerated and  $\text{CO}_2$ -saturated NaCl solution at RT, but not in air or in  $\text{CO}_2$ -saturated NaCl solution at 120 °C.

- Non-propagating small cracks were observed in air fatigue and CO<sub>2</sub>-saturated NaCl solution at 120 °C. The size of these small cracks were comparable to the grain size of the X65 steel. Compared to air fatigue, multiple crack initiation sites were observed in the CO<sub>2</sub>-saturated NaCl solution at 120 °C.
- Closer examination of crack initiation in aerated NaCl solution showed that crack initiated from finer precursors at the perimeter of the pit, which is likely a result of corrosion-fatigue interaction.
- An isotropic finite strain model with kinematic hardening was developed in this study. The model shows good agreement with the experimental data, i.e. monotonic tensile, symmetric strain cyclic and asymmetric stress cyclic test data. The model simulates the local ratcheting phenomenon around the pit, and could be used predict the accumulated plastic strain level during fatigue cycles.
- The critical plastic strain level for crack initiation of X65 steel was estimated using the EBSD technique. The critical plastic strain was measured to be approximately 8.5%. The measured critical value compares with the prediction from the model.

### 7.3 Major Contributions

- Precursors to crack initiation in X65 steel have been identified and characterized using a combination of experimentally generated pits and cracks, combined with local strain measurements that were then used to develop a model for the process.
- The Critical plastic strain level for crack initiation in the X65 steel was determined using the EBSD technique. The application of EBSD techniques for a ferritic material represents the first such application.
- An isotropic finite strain model with kinematic hardening was develop and implemented. The model accounts for softening characteristics of the X65 steel in ratcheting. The model can be used to calculate the plastic strain level around a pit. Given the critical plastic strain level, the model can predict the number of cycles to pit-to-crack transition in a ratcheting scenario.
- A system was developed and used to detect pit-to-crack transition. The system includes (1)

a pit-generation sub-system which can generate a pre-pit on the sample surface with controlled dimensions. (2) a circulation and autoclave sub-system which can provide the desired water chemistry with high temperature and pressure, and also the desired loading condition. (3) An ACPD sub-system which can measure the potential drop across the pit and detect the pit-to-crack transition and subsequent crack growth. (4) A computer control program which allows the user to setup the loading condition and ACPD test parameters. It also monitors the water chemical and records the potential drop data. When the potential drop exceeds a prescribed limit, the program can automatically stop the fatigue loading in order to capture the small crack initiated from the pit. The developed system can be used to study pit-to-crack transition phenomenon in general, for various materials with different pit geometries in different environments and different loading conditions. It should be noted that the use of ACPD for this process represents the first such application. The system was used to detect the pit-to-crack transition.

## 7.4 Future Work

- The combination of the use of ACPD techniques to capture crack initiation in combination with EBSD techniques to characterize the local strain represents the first such application to a ferritic material. The complications associated with performing this analysis included:
  - Optimization of the ACPD system to achieve appropriate sensitivity.
  - Achieving the appropriate surface preparation to achieve meaningful strain measurements.

With further development of both the ACPD system and EBSD techniques, it is expected that improved performance can be achieved.

- The EBSD-Strain calibration was based on tensile strains from monotonic tensile tests. The AMIS analysis only measures the effect of dislocation on distortion of the lattice by GNDs. In this work the focus was on cyclic loading. While we expect that the behavior of AMIS as a function of strain will be similar in general, further work is necessary to evaluate the effect of fatigue on AMIS.
- More experiments need to be done with different pit geometries, loading conditions and environments, which would yield more insights to the underlying physics of the pit-to-

crack transition. At low stress levels or with shallow pits, ratcheting may not occur around the pit, high cycle or low cycle fatigue mechanisms may dominate. With more corrosive environment or under cathodic protection condition, the environment may affect crack initiation more profoundly. Due to most time spent on developing the system, the current experimental data is limited. More experimental data will be helpful to further understanding the pit-to-crack transition phenomenon. However, with the developments in this thesis research the “door” has now been opened for additional progress.

- The application of in-situ techniques to characterize the pit-to-crack transition, e.g. synchrotron X-ray tomography, in-situ SEM should be considered. With high resolution in-situ techniques, the crack initiation could be captured more accurately and the microstructural effect on the pit-to-crack transition could be further explored.
- The connection between the evolution of local plastic strain and the material-environment interface should be more thoroughly explored. The work in this thesis provides the stepping off point for this. One possibility is the application of a crystal plasticity finite element approach to further investigate the strain distribution at the microstructural level. A crystal plasticity model could be used in combination with the current isotropic model. The crystal plasticity model can be applied to simulate a small area of interest while the other part of the geometry is simulated using the isotropic model. If a dislocation-based crystal plasticity model is used, it is possible to directly compare the simulation result of dislocation densities to the EBSD measurement without using any empirical correlation.

## References

- [1] A. Turnbull, D. A. Horner, and B. J. Connolly, “Challenges in modelling the evolution of stress corrosion cracks from pits,” *Eng. Fract. Mech.*, vol. 76, no. 5, pp. 633–640, 2009.
- [2] D. P. Baxter, S. J. Maddox, and R. J. Pargeter, “Corrosion Fatigue Behaviour of Welded Risers and Pipelines,” in *Volume 4: Materials Technology; Ocean Engineering*, 2007, pp. 117–124.
- [3] S. Papavinasam, A. Doiron, and R. W. Revie, “Model to predict internal pitting corrosion of oil and gas pipelines,” in *Corrosion*, 2010, vol. 66, no. 3, pp. 0350061–03500611.
- [4] S. Nešić, “Key issues related to modelling of internal corrosion of oil and gas pipelines—A review,” *Corros. Sci.*, vol. 49, no. 12, pp. 4308–4338, 2007.
- [5] A. Turnbull, “Corrosion pitting and environmentally assisted small crack growth,” *Proc. Math. Phys. Eng. Sci.*, vol. 470, no. 2169, p. 20140254, 2014.
- [6] R. Akid, I. M. Dmytrakh, and J. Gonzalez-Sanchez, “FATIGUE DAMAGE ACCUMULATION: ASPECTS OF ENVIRONMENTAL INTERACTION,” *Mater. Sci.*, vol. 42, no. 1, 2006.
- [7] S.-H. Ahn, F. V. Lawrence, and M. M. Metzger, “Corrosion Fatigue of an HSLA Steel,” *Fatigue Fract. Eng. Mater. Struct.*, vol. 15, no. 7, pp. 625–642, Jul. 1992.
- [8] B. Y. Fang, R. L. Eadie, W. X. Chen, and M. Elboudjaini, “Pit to crack transition in X-52 pipeline steel in near neutral pH environment Part 1 – formation of blunt cracks from pits under cyclic loading,” *Corros. Eng. Sci. Technol.*, vol. 45, no. 4, pp. 302–312, 2010.
- [9] A. Turnbull and S. Zhou, “Pit to crack transition in stress corrosion cracking of a steam turbine disc steel,” *Corros. Sci.*, vol. 46, no. 5, pp. 1239–1264, 2004.
- [10] K. Jones and D. W. Hoepfner, “Pit-to-crack transition in pre-corroded 7075-T6 aluminum alloy under cyclic loading,” *Corros. Sci.*, vol. 47, pp. 2185–2198, 2005.
- [11] M. Goto and H. Nisitani, “CRACK INITIATION AND PROPAGATION BEHAVIOUR OF A HEAT-TREATED CARBON STEEL IN CORROSION FATIGUE,” *Fatigue Fract. Eng. Mater. Struct.*, vol. 15, no. 4, pp. 353–363, Apr. 1992.
- [12] M. Nakajima and K. Tokaji, “FATIGUE LIFE DISTRIBUTION AND GROWTH OF CORROSION PITS IN A MEDIUM CARBON STEEL IN 3%NaCl SOLUTION,”

- Fatigue Fract. Eng. Mater. Struct.*, vol. 18, no. 3, pp. 345–351, Mar. 1995.
- [13] A. Turnbull, L. N. McCartney, and S. Zhou, “A model to predict the evolution of pitting corrosion and the pit-to-crack transition incorporating statistically distributed input parameters,” in *Environment-Induced Cracking of Materials*, 2008, pp. 19–45.
- [14] R. Wei, “Material Aging and Reliability of Engineered Systems,” in *Environmentally Assisted Cracking: Predictive Methods for Risk Assessment and Evaluation of Materials, Equipment, and Structures*. ASTM International, 100 Barr Harbor Drive, PO Box C700, West Conshohocken, PA 19428-2959: ASTM International, 2000.
- [15] A. Turnbull, L. McCartney, and S. Zhou, “Modelling of the evolution of stress corrosion cracks from corrosion pits,” *Scr. Mater.*, vol. 54, no. 4, pp. 575–578, 2006.
- [16] B. M. Schönbauer, A. Perlega, U. P. Karr, D. Gandy, and S. E. Stanzl-Tschegg, “Pit-to-crack transition under cyclic loading in 12% Cr steam turbine blade steel,” *Int. J. Fatigue*, vol. 76, pp. 19–32, 2015.
- [17] G. S. Chen, K.-C. Wan, M. Gao, R. P. Wei, and T. H. Flournoy, “Transition from pitting to fatigue crack growth—modeling of corrosion fatigue crack nucleation in a 2024-T3 aluminum alloy,” *Mater. Sci. Eng. A*, vol. 219, no. 1–2, pp. 126–132, Nov. 1996.
- [18] Y. Kondo, “Prediction method of corrosion fatigue crack initiation life based on corrosion pit growth mechanism,” *Trans. Japan Soc. Mech. Engrs*, vol. 53, no. 495, pp. 1983–1987, 1987.
- [19] A. Turnbull, L. Wright, and L. Crocker, “New insight into the pit-to-crack transition from finite element analysis of the stress and strain distribution around a corrosion pit,” *Corros. Sci.*, vol. 52, no. 4, pp. 1492–1498, 2010.
- [20] D. Jones, *Principles and prevention of corrosion*. 1992.
- [21] J. Koch, G. Varney, J. Thompson, N. Moghissi, O. Gould, M. Payer, ““International Measures of Prevention, Application, and Economics of Corrosion Technologies Study.” NACE International IMPACT Report,” 2016.
- [22] M. B. Kermani and A. Morshed, “Carbon Dioxide Corrosion in Oil and Gas Production—A Compendium,” *CORROSION*, vol. 59, no. 8, pp. 659–683, Aug. 2003.
- [23] R. E. Melchers, “Principles of Marine Corrosion,” in *Springer Handbook of Ocean Engineering*, 2016, pp. 111–126.
- [24] R. Staehle, “Anatomy of proactivity,” *Corros. Rev.*, vol. 28, no. 5, p. 197, 2010.

- [25] R. E. Melchers, “Recent Progress in the Modeling of Corrosion of Structural Steel Immersed in Seawaters,” *J. Infrastruct. Syst.*, vol. 12, no. 3, pp. 154–162, Sep. 2006.
- [26] R. E. Melchers, “Modeling of Marine Immersion Corrosion for Mild and Low-Alloy Steels—Part 2: Uncertainty Estimation,” *CORROSION*, vol. 59, no. 4, pp. 335–344, Apr. 2003.
- [27] R. E. Melchers, “Modeling of Marine Immersion Corrosion for Mild and Low-Alloy Steels—Part 1: Phenomenological Model,” *CORROSION*, vol. 59, no. 4, pp. 319–334, Apr. 2003.
- [28] R. E. Melchers, “Effect on marine immersion corrosion of carbon content of low alloy steels,” *Corros. Sci.*, vol. 45, no. 11, pp. 2609–2625, 2003.
- [29] R. E. Melchers, “Probabilistic Model for Marine Corrosion of Steel for Structural Reliability Assessment,” *J. Struct. Eng.*, vol. 129, no. 11, pp. 1484–1493, Nov. 2003.
- [30] R. E. Melchers and R. Jeffrey, “Early corrosion of mild steel in seawater,” *Corros. Sci.*, vol. 47, no. 7, pp. 1678–1693, 2005.
- [31] U. S. R.M. Cornell, *The Iron Oxides: Structure, Properties, Reactions, Occurrences and Uses. Second, Completely Revised and Extended Edition ed. 2003*. Weinheim: WILEY-VCH Verlag GmbH, 2003.
- [32] K. E. García, A. L. Morales, C. A. Barrero, and J. M. Greneche, “New contributions to the understanding of rust layer formation in steels exposed to a total immersion test,” *Corros. Sci.*, vol. 48, no. 9, pp. 2813–2830, 2006.
- [33] Y. Ma, Y. Li, and F. Wang, “The effect of  $\beta$ -FeOOH on the corrosion behavior of low carbon steel exposed in tropic marine environment,” *Mater. Chem. Phys.*, vol. 112, no. 3, pp. 844–852, 2008.
- [34] T. Nishimura, “Electrochemical behavior of rust formed on carbon steel in a wet/dry environment containing chloride ions,” *Corrosion*, vol. 56, no. 9, pp. 935–941, Sep. 2000.
- [35] Y. Zou, J. Wang, and Y. Y. Zheng, “Electrochemical techniques for determining corrosion rate of rusted steel in seawater,” *Corros. Sci.*, vol. 53, no. 1, pp. 208–216, 2011.
- [36] L. H. G. Chaves, “The role of green rust in the environment: a review,” *Rev. Bras. Eng. Agrícola e Ambient.*, vol. 9, no. 2, pp. 284–288, Jun. 2005.
- [37] J. Han, B. N. Brown, and S. Nešić, “Investigation of the galvanic mechanism for localized carbon dioxide corrosion propagation using the artificial pit technique,” in *Corrosion*,

- 2010, vol. 66, no. 9, pp. 0950031–09500312.
- [38] S. Nešić, “Carbon Dioxide Corrosion of Mild Steel,” in *Uhlig’s Corrosion Handbook*, Hoboken, NJ, USA: John Wiley & Sons, Inc., 2011, pp. 229–245.
- [39] S. Nešić, J. Postlethwaite, and S. Olsen, “An Electrochemical Model for Prediction of Corrosion of Mild Steel in Aqueous Carbon Dioxide Solutions,” *Corros.*, vol. 52, no. 4, pp. 280–294, Apr. 1996.
- [40] W. Sun, S. Netic, and R. C. Woollam, “The effect of temperature and ionic strength on iron carbonate ( $\text{FeCO}_3$ ) solubility limit,” *Corros. Sci.*, vol. 51, no. 6, pp. 1273–1276, 2009.
- [41] W. Sun and S. Nešić, “Kinetics of corrosion layer formation: Part 1 - Iron carbonate layers in carbon dioxide corrosion,” *Corrosion*, vol. 64, no. 4, pp. 334–346, Apr. 2008.
- [42] T. Tanupabrunsun, D. Young, B. Brown, and S. Nešić, “Construction and Verification of Pourbaix Diagrams for  $\text{CO}_2$  Corrosion of Mild Steel Valid up to  $250^\circ\text{C}$ ,” *Corros. NACE Expo*, pp. C2012-1418, 2012.
- [43] T. Tanupabrunsun, B. Brown, and S. Netic, “Effect of pH on  $\text{CO}_2$  Corrosion of Mild Steel at Elevated Temperatures,” *Nace Expo*, no. 2348, pp. 1–11, 2013.
- [44] X. Jiang, S. Netic, B. Kinsella, B. Brown, and D. Young, “Electrochemical investigation of the role of  $\text{Cl}^-$  on localized carbon dioxide corrosion behavior of mild steel,” *Corrosion*, vol. 69, no. 1, pp. 15–24, 2013.
- [45] J. Han, Y. Yang, B. Brown, and S. Netic, “Electrochemical investigation of localized  $\text{CO}_2$  corrosion on mild steel,” *Corros. Pap.*, 2007.
- [46] R. Nyborg, “Initiation and growth of mesa corrosion attack during  $\text{CO}_2$  corrosion of carbon steel,” in *Corrosion 1998*, 2007, no. 48, p. 11.
- [47] A. Dugstad, “Mechanism of Protective Film Formation During  $\text{CO}_2$  Corrosion of Carbon Steel,” *Corros. NACE Int.*, no. 31, 1998.
- [48] G. Schmitt, T. Gudde, and E. Strobel-Effertz, “Fracture mechanical properties of  $\text{CO}_2$  corrosion product scales and their relation to localized corrosion,” *Corrosion*, no. 9, pp. 1–21, 1996.
- [49] J. L. Crolet, N. Thevenot, and S. Netic, “Role of Conductive Corrosion Products in the Protectiveness of Corrosion Layers,” *CORROSION*, vol. 54, no. 3, pp. 194–203, Mar. 1998.

- [50] F. Farelas, M. Galicia, B. Brown, S. Netic, and H. Castaneda, "Evolution of dissolution processes at the interface of carbon steel corroding in a CO<sub>2</sub> environment studied by EIS," *Corros. Sci.*, vol. 52, no. 2, pp. 509–517, 2010.
- [51] K. Videm and J. Kvarekval, "Surface effects on the electrochemistry of iron and carbon steel electrodes in aqueous CO<sub>2</sub> solutions," in *Corrosion 1996*, 1996, p. Paper no. 1.
- [52] M. Ueda and A. Ikeda, "Effect of steel microstructure and Cr content in steel on CO<sub>2</sub> corrosion," *Corros. 1996*, no. 13, p. 16, 1996.
- [53] A. Dugstad, H. Hemmer, and M. Seiersten, "Effect of steel microstructure on corrosion rate and protective iron carbonate film formation," *Corrosion*, vol. 57, no. 4, pp. 369–378, 2001.
- [54] T. Li, Y. Yang, K. Gao, and M. Lu, "Mechanism of protective film formation during CO<sub>2</sub> corrosion of X65 pipeline steel," *J. Univ. Sci. Technol. Beijing Miner. Metall. Mater. (Eng Ed)*, vol. 15, no. 6, pp. 702–706, 2008.
- [55] S. Suresh, *Fatigue of Materials*. Cambridge University Press, 1998.
- [56] A. Wöhler, "Versuche über die Festigkeit der Eisenbahnwagenachsen," *Zeitschrift für Bauwes.*, vol. 10, pp. 160–161, 1860.
- [57] O. H. Basquin, "The exponential law of endurance tests," *Proc. Am. Soc. Test. Mater.*, vol. 10, pp. 625–630, 1910.
- [58] P. P. Milella, *Fatigue and corrosion in metals*. Springer Science & Business Media, 2013.
- [59] J. A. Ewing and J. C. W. Humfrey, "The Fracture of Metals under Repeated Alternations of Stress," *Philos. Trans. R. Soc. A*, vol. 200, no. 321–330, pp. 241–250, 1903.
- [60] S. S. Manson, "Behavior of materials under conditions of thermal stress," *Heat Transf. Symp. Univ. Michigan Eng. Res. Inst.*, 1953.
- [61] L. F. Coffin, "A study of the effects of cyclic thermal stresses on a ductile metal," *Trans. AIME*, vol. 76, pp. 931–950, 1954.
- [62] R. Akid, "Corrosion fatigue," in *Shreir's Corrosion*, 2010, pp. 928–953.
- [63] C. Rodopoulos, "Fatigue Damage Map as a Virtual Tool for Fatigue Damage Tolerance," in *Virtual Testing and Predictive Modeling*, Springer US, 2009.
- [64] R. O. Ritchie, F. A. McClintock, H. Nayeb-Hashemi, and M. A. Ritter, "Mode III fatigue crack propagation in low alloy steel," *Metall. Trans. A*, vol. 13, no. 1, pp. 101–110, Jan. 1982.

- [65] H. Mughrabi, "Microstructural mechanisms of cyclic deformation, fatigue crack initiation and early crack growth," *Philos. Trans. R. Soc. A*, vol. 373, no. 2038, p. 20140132, 2015.
- [66] M. D. Sangid, "The physics of fatigue crack initiation," *Int. J. Fatigue*, vol. 57, pp. 58–72, 2013.
- [67] J. Man, K. Obrtlík, and J. Polák, "Extrusions and intrusions in fatigued metals. Part 1. State of the art and history†," *Philos. Mag.*, vol. 89, no. 16, pp. 1295–1336, Jun. 2009.
- [68] H. Mughrabi, F. Ackermann, and K. Herz, "Persistent slipbands in fatigued face-centered and body-centered cubic metals," *Fatigue Mech.*, 1979.
- [69] H. Mughrabi, "Cyclic slip irreversibilities and the evolution of fatigue damage," *Metall. Mater. Trans. B Process Metall. Mater. Process. Sci.*, vol. 40, no. 4, pp. 431–453, Aug. 2009.
- [70] P. Lukáš and L. Kunz, "Role of persistent slip bands in fatigue," *Philos. Mag.*, vol. 84, no. 3–5, pp. 317–330, Jan. 2004.
- [71] N. Thompson and N. Wadsworth, "Metal fatigue," *Adv. Phys.*, vol. 7, no. 25, pp. 72–169, 1958.
- [72] S. N. S. K. R. Pascual and S. Basinski, "LOW AMPLITUDE FATIGUE OF GQPPER SINGLE CRYSTALS-1. THE ROLE OF THE SURFACE IN FATIGUE FAILURE," *Acta Metall.*, vol. 31, pp. 591–602, 1982.
- [73] Z. S. Basinski and S. J. Basinski, "Fundamental aspects of low amplitude cyclic deformation in face-centred cubic crystals," *Prog. Mater. Sci.*, vol. 36, no. C, pp. 89–148, Jan. 1992.
- [74] Z. S. Basinski and S. J. Basinski, "Copper single crystal PSB morphology between 4.2 and 350 K," *Acta Metall.*, vol. 37, no. 12, pp. 3263–3273, Dec. 1989.
- [75] A. Hunsche and P. Neumann, "Quantitative measurement of persistent slip band profiles and crack initiation," *Acta Metall.*, vol. 34, no. 2, pp. 207–217, Feb. 1986.
- [76] M. Bao-Tong and C. Laird, "Overview of fatigue behavior in copper single crystals-I. Surface morphology and stage I crack initiation sites for tests at constant strain amplitude," *Acta Metall.*, vol. 37, no. 2, pp. 325–336, 1989.
- [77] K. Differt, U. Esmann, and H. Mughrabi, "A model of extrusions and intrusions in fatigued metals II. Surface roughening by random irreversible slip," *Philos. Mag. A*, vol. 54, no. 2, pp. 237–258, Aug. 1986.

- [78] U. Essmann, U. Gösele, and H. Mughrabi, "A model of extrusions and intrusions in fatigued metals I. Point-defect production and the growth of extrusions," *Philos. Mag. A*, vol. 44, no. 2, pp. 405–426, Aug. 1981.
- [79] J. Polák, "On the role of point defects in fatigue crack initiation," *Mater. Sci. Eng.*, vol. 92, no. C, pp. 71–80, Aug. 1987.
- [80] J. Polák and M. Sauzay, "Growth of extrusions in localized cyclic plastic straining," *Mater. Sci. Eng. A*, vol. 500, no. 1–2, pp. 122–129, 2009.
- [81] E. Repetto and M. Ortiz, "A micromechanical model of cyclic deformation and fatigue-crack nucleation in f.c.c. single crystals," *Acta Mater.*, vol. 45, no. 6, pp. 2577–2595, Jun. 1997.
- [82] K. Tanaka and T. Mura, "A Dislocation Model for Fatigue Crack Initiation," *J. Appl. Mech.*, vol. 48, no. 1, pp. 97–103, 1981.
- [83] G. Venkataraman, Y. W. Chung, and T. Mura, "Application of minimum energy formalism in a multiple slip band model for fatigue-II. Crack nucleation and derivation of a generalised Coffin-Manson law," *Acta Metall. Mater.*, vol. 39, no. 11, pp. 2631–2638, Nov. 1991.
- [84] A. Seeger, "The temperature dependence of the critical shear stress and of work-hardening of metal crystals," *Philos. Mag. Ser. 7*, vol. 45, no. 366, pp. 771–773, 1954.
- [85] U. F. Kocks, A. S. Argon, and M. F. Ashby, "Thermodynamics and Kinetics of Slip," *Prog. Mater. Sci.*, vol. 19, no. 1968, pp. 171–229, 1975.
- [86] H. Mughrabi, K. Herz, and X. Stark, "Cyclic deformation and fatigue behaviour of alpha-iron mono-and polycrystals," *Int. J. Fract.*, vol. 17, no. 2, pp. 193–220, Apr. 1981.
- [87] C. Sommer, H. Mughrabi, and D. Lochner, "Influence of temperature and carbon content on the cyclic deformation and fatigue behaviour of  $\alpha$ -iron. Part I. Cyclic deformation and stress-behaviour," *Acta Mater.*, vol. 46, no. 5, pp. 1527–1536, 1998.
- [88] D. Caillard, "An in situ study of hardening and softening of iron by carbon interstitials," *Acta Mater.*, vol. 59, no. 12, pp. 4974–4989, 2011.
- [89] D. Caillard, "Kinetics of dislocations in pure Fe. Part II. In situ straining experiments at low temperature," *Acta Mater.*, vol. 58, no. 9, pp. 3504–3515, 2010.
- [90] C. Sommer, H. Mughrabi, and D. Lochner, "Influence of temperature and carbon content on the cyclic deformation and fatigue behaviour of  $\alpha$ -iron. Part II: Crack initiation and

- fatigue life,” *Acta Mater.*, vol. 46, no. 5, pp. 1537–1546, 1998.
- [91] A. Turnbull, “Environment–Assisted Fatigue in Liquid Environments,” in *Comprehensive Structural Integrity*, vol. 6, Ian Milne R. Ritchie B.L. Karihaloo, Ed. Elsevier, 2003, pp. 163–210.
- [92] C. Patel, “The influence of sulphate, chloride and nitrate anions on the cyclic strain-enhanced dissolution behaviour of mild steel,” *Corros. Sci.*, vol. 21, no. 2, pp. 145–158, Jan. 1981.
- [93] R. Akid, “The effect of solution pH on the initiation and growth of short fatigue cracks,” *ECF8, Torino 1990*, 2013.
- [94] R. Akid, I. M. Dmytrakh, and J. Gonzalez-Sanchez, “Fatigue damage accumulation: the role of corrosion on the early stages of crack development,” *Corros. Eng. Sci. Technol.*, vol. 41, no. 4, pp. 328–335, Dec. 2006.
- [95] M. Cerit, K. Genel, and S. Eksi, “Numerical investigation on stress concentration of corrosion pit,” *Eng. Fail. Anal.*, vol. 16, no. 7, pp. 2467–2472, 2009.
- [96] S. Zhou and A. Turnbull, “Influence of pitting on the fatigue life of a turbine blade steel,” *Fatigue Fract. Eng. Mater. Struct.*, vol. 22, no. 12, pp. 1083–1093, Dec. 1999.
- [97] M. H. El Haddad, T. H. Topper, and K. N. Smith, “Prediction of non propagating cracks,” *Eng. Fract. Mech.*, vol. 11, no. 3, pp. 573–584, Jan. 1979.
- [98] H. Kitagawa and S. Takahashi, “Applicability of fracture mechanics to very small cracks or the cracks in the early stage,” *Proc 2nd Int. Conf. on Mech. Behavior of Materials*. pp. 627–631, 1976.
- [99] Y. Wang, J. D. Atkison, R. Akid, and R. N. Parkins, “Crack Interactions, Coalescence and Mixed Mode Fracture Mechanics,” *Fatigue Fract. Eng. Mater. Struct.*, vol. 19, pp. 427–439, 1996.
- [100] Duquette D.J. and Uhlig H.H., “Critical reaction rate for corrosion fatigue of 0.18% carbon steel and the effect of pH,” *ASM Trans. Am. Soc. Met.*, vol. 62, no. 4, pp. 839–845, 1969.
- [101] R. Akid and K. J. Miller, “SHORT FATIGUE CRACK GROWTH BEHAVIOUR OF A LOW CARBON STEEL UNDER CORROSION FATIGUE CONDITIONS,” *Fatigue & Fract. Eng. Mater. & Struct.*, vol. 14, no. 6, pp. 637–649, Jun. 1991.
- [102] S. Suresh and R. O. Ritchie, “Propagation of short fatigue cracks,” *Int. Met. Rev.*, vol. 29,

- no. 1, pp. 445–475, 1984.
- [103] R. Akid, “the Influence of Environment Upon the Accumulation of Damage Under Corrosion Fatigue Conditions,” *Fatigue Fract. Eng. Mater. Struct.*, vol. 19, no. 2–3, pp. 277–285, Feb. 1996.
- [104] K. J. Miller, “Materials science perspective of metal fatigue resistance,” *Mater. Sci. Technol.*, vol. 9, no. 6, pp. 453–462, 1993.
- [105] R. P. Gangloff, “CRITICALITY OF CRACK SIZE IN AQUEOUS CORROSION FATIGUE,” *Res mechanica letters*, vol. 1, no. 7, pp. 299–306, 1981.
- [106] R. P. Gangloff, “Crack size effects on the chemical driving force for aqueous corrosion fatigue,” *Metall. Trans. A*, vol. 16, no. 5, pp. 953–969, May 1985.
- [107] A. Turnbull and D. H. Ferriss, “Mathematical modelling of the electrochemistry in corrosion fatigue cracks in structural steel cathodically protected in sea water,” *Corros. Sci.*, vol. 26, no. 8, pp. 601–628, Jan. 1986.
- [108] A. Turnbull and D. H. Ferriss, “Mathematical modelling of the electrochemistry in corrosion fatigue cracks in steel corroding in marine environments,” *Corros. Sci.*, vol. 27, no. 12, pp. 1323–1350, Jan. 1987.
- [109] D. Berechid, D. Larouche, J. Bailon, and J. Dickson, “Corrosion-fatigue propagation of short cracks in a structural steel tested in synthetic seawater,” *High. Educ. Press. Fatigue '99 Proc. Seventh Int. Fatigue Congr.*, vol. 4, 1999.
- [110] N. E. Dowling, “Crack Growth During Low-Cycle Fatigue of Smooth Axial Specimens,” in *ASTM STP 637*, 1977, pp. 97–121.
- [111] K. Tanaka and R. P. Wei, “Growth of short fatigue cracks in HY130 steel in 3.5% NaCl solution,” *Eng. Fract. Mech.*, vol. 21, no. 2, pp. 293–305, Jan. 1985.
- [112] Y. Nakai, K. Tanakai, and R. P. Wei, “Short-crack growth in corrosion fatigue for a high strength steel,” *Eng. Fract. Mech.*, vol. 24, no. 3, pp. 433–444, Jan. 1986.
- [113] M. Nakajima, M. Akita, K. Tokaji, and T. Shimizu, “Fatigue crack initiation and early growth behavior of a ferritic stainless steel in laboratory air and in 3% NaCl aqueous solution,” *JSME Int. J. ...*, vol. 46, no. 4, pp. 575–581, 2003.
- [114] L. A. James, “Surface-crack aspect ratio development during corrosion-fatigue crack growth in low-alloy steels,” *Nucl. Eng. Des.*, vol. 172, no. 1–2, pp. 61–71, Jul. 1997.
- [115] S. Suresh, G. F. Zamiski, and D. R. O. Ritchie, “Oxide-Induced Crack Closure: An

- Explanation for Near-Threshold Corrosion Fatigue Crack Growth Behavior,” *Metall. Trans. A*, vol. 12, no. 8, pp. 1435–1443, Aug. 1981.
- [116] R. O. Ritchie and S. Suresh, “Some considerations on fatigue crack closure at near-threshold stress intensities due to fracture surface morphology,” *Metall. Trans. A*, vol. 13, no. 5, pp. 937–940, May 1982.
- [117] A. K. Vasudeven, K. Sadananda, and N. Louat, “A review of crack closure, fatigue crack threshold and related phenomena,” *Materials Science and Engineering A*, vol. 188, no. 1–2, pp. 1–22, Nov-1994.
- [118] J. Schijve, “Fatigue crack closure: observations and technical significance,” *Mech. fatigue crack closure, ASTM STP 982*, pp. 5–34, 1988.
- [119] F. P. Ford, “Quantitative Prediction of Environmentally Assisted Cracking,” *Corros.*, vol. 52, no. 5, pp. 375–395, 1996.
- [120] T. Magnin, “Environment sensitive fracture mechanisms,” *Solid State Phenom.*, vol. 35, pp. 319–334, 1993.
- [121] S. Lynch, “Hydrogen embrittlement phenomena and mechanisms,” *Corrosion Reviews*, vol. 30, no. 3–4, pp. 105–123, 01-Jan-2012.
- [122] I. M. Robertson, “The effect of hydrogen on dislocation dynamics,” *Eng. Fract. Mech.*, vol. 68, no. 6, pp. 671–692, 2001.
- [123] M. Elboudjaini, R. Y.-Z. Wang, M. T. Shehata, R. N. Parkins, and W. Revie, “Stress Corrosion Crack Initiation Processes: Pitting and Microcrack Coalescence,” *Corros. 2000*, no. 379, 2000.
- [124] B. Fang, R. L. Eadie, M. Elboudjaini, and W. Chen, “Transition from Pits to Cracks in Pipeline Steel in Near-Neutral pH Solution,” in *ICF12*, 2009, pp. 1–11.
- [125] A. Turnbull, “The environmentally small/short crack growth effect: Current understanding,” *Corrosion Reviews*, vol. 30, no. 1–2, pp. 1–17, 2012.
- [126] R. Ebara, “Corrosion fatigue crack initiation in 12% chromium stainless steel,” *Mater. Sci. Eng. A*, vol. 468–470, no. SPEC. ISS., pp. 109–113, 2007.
- [127] E. Dolley, B. Lee, and R. Wei, “The effect of pitting corrosion on fatigue life,” *Fatigue Fract. ...*, vol. 62, no. 4–5, pp. 425–444, 2000.
- [128] S. Rokhlin, J. Kim, H. Nagy, and B. Zoofan, “Effect of pitting corrosion on fatigue crack initiation and fatigue life,” *Engineering Fracture Mechanics*, vol. 62, no. 4–5, pp. 425–

- 444, 1999.
- [129] J. Congleton, R. Olieh, and R. Parkins, “Corrosion-fatigue crack nucleation in 1·5Mn–0·5Si steel,” *Met. Technol.*, vol. 9 (1), pp. 94–103, 1982.
- [130] A. Boukerrou and R. Cottis, “Crack Initiation in the Corrosion Fatigue of Structural Steels in Salt Solutions.pdf,” *Corros. Sci.*, vol. 35 (1-4), pp. 577–585, 1993.
- [131] R. Ebara, “Corrosion fatigue crack initiation in 12% chromium stainless steel,” *Mater. Sci. Eng. A*, vol. 468–470, no. SPEC. ISS., pp. 109–113, 2007.
- [132] Y. Wang and R. Akid, “Role of nonmetallic inclusions in fatigue, pitting and corrosion fatigue,” *Corros. Sci.*, vol. 52, No. 2, pp. 92–102, 1996.
- [133] B. M. Schönbauer, S. E. Stanzl-Tschegg, A. Perlega, R. N. Salzman, N. F. Rieger, S. Zhou, A. Turnbull, and D. Gandy, “Fatigue life estimation of pitted 12% Cr steam turbine blade steel in different environments and at different stress ratios,” *Int. J. Fatigue*, vol. 65, pp. 33–43, 2014.
- [134] A. Turnbull, “Corrosion pitting and environmentally assisted small crack growth,” *Proc. Math. Phys. Eng. Sci.*, vol. 470, no. 2169, p. 20140254, 2014.
- [135] R. Akid, “The role of stress-assisted localised corrosion in the development of short fatigue cracks,” in *Effects of the environment on the initiation of crack growth, ASTM STP 1298*, 1997, pp. 3–17.
- [136] S. Ishihara, T. Goshima, A. J. Mcevely, S. Sunada, and S. Nomata, “Corrosion-Pit-Growth Behaviour During the Corrosion Fatigue Process in Aluminum,” *ICF10, Honolulu, Hawaii - 2001*, no. 1, 2001.
- [137] A. Turnbull, L. N. McCartney, and S. Zhou, “A model to predict the evolution of pitting corrosion and the pit-to-crack transition incorporating statistically distributed input parameters,” in *Environment-Induced Cracking of Materials*, vol. 48, no. 8, 2008, pp. 19–45.
- [138] G. S. Chen, K.-C. Wan, M. Gao, R. P. Wei, and T. H. Flournoy, “Transition from pitting to fatigue crack growth—modeling of corrosion fatigue crack nucleation in a 2024-T3 aluminum alloy,” *Mater. Sci. Eng. A*, vol. 219, no. 1–2, pp. 126–132, Nov. 1996.
- [139] O. Fatoba, “Experimental and modelling studies of corrosion fatigue damage in a linepipe steel,” University of Manchester, 2016.
- [140] J. A. Gonzalez-Sanchez, “Corrosion fatigue initiation in stainless steels : the scanning

- reference electrode technique,” Sheffield Hallam University, 2002.
- [141] D. G. Harlow and R. P. Wei, “A probability model for the growth of corrosion pits in aluminum alloys induced by constituent particles,” *Eng. Fract. Mech.*, vol. 59, no. 3, pp. 305–325, Feb. 1998.
- [142] J. D. Carroll, W. Abuzaid, J. Lambros, and H. Sehitoglu, “High resolution digital image correlation measurements of strain accumulation in fatigue crack growth,” *Int. J. Fatigue*, vol. 57, pp. 140–150, 2013.
- [143] T. Hassan and S. Kyriakides, “Ratcheting in cyclic plasticity, part I: Uniaxial behavior,” *Int. J. Plast.*, vol. 8, no. 1, pp. 91–116, Jan. 1992.
- [144] A. Kapoor, “A RE-EVALUATION OF THE LIFE TO RUPTURE OF DUCTILE METALS BY CYCLIC PLASTIC STRAIN,” *Fatigue Fract. Eng. Mater. Struct.*, vol. 17, no. 2, pp. 201–219, Feb. 1994.
- [145] K. Dutta, S. Sivaprasad, S. Tarafder, and K. K. Ray, “Influence of asymmetric cyclic loading on substructure formation and ratcheting fatigue behaviour of AISI 304LN stainless steel,” *Mater. Sci. Eng. A*, vol. 527, no. 29–30, pp. 7571–7579, 2010.
- [146] G. Chen, S. C. Shan, X. Chen, and H. Yuan, “Ratcheting and fatigue properties of the high-nitrogen steel X13CrMnMoN18-14-3 under cyclic loading,” *Comput. Mater. Sci.*, vol. 46, no. 3, pp. 572–578, 2009.
- [147] Y. Wang, D. Yu, G. Chen, and X. Chen, “Effects of pre-strain on uniaxial ratcheting and fatigue failure of Z2CN18.10 austenitic stainless steel,” *International Journal of Fatigue*, vol. 52, pp. 106–113, 2013.
- [148] G. Kang, Q. Gao, and X. Yang, “Uniaxial cyclic ratcheting and plastic flow properties of SS304 stainless steel at room and elevated temperatures,” *Mech. Mater.*, vol. 34, no. 3, pp. 145–159, 2002.
- [149] X. Yang, “Low cycle fatigue and cyclic stress ratcheting failure behavior of carbon steel 45 under uniaxial cyclic loading,” *Int. J. Fatigue*, vol. 27, no. 9, pp. 1124–1132, 2005.
- [150] C. L. Pun, Q. Kan, P. J. Mutton, G. Kang, and W. Yan, “Ratcheting behaviour of high strength rail steels under bi-axial compression-torsion loadings: Experiment and simulation,” *Int. J. Fatigue*, vol. 66, pp. 138–154, 2014.
- [151] S. K. Paul, S. Sivaprasad, S. Dhar, and S. Tarafder, “Ratcheting and low cycle fatigue behavior of SA333 steel and their life prediction,” *J. Nucl. Mater.*, vol. 401, no. 1–3, pp.

- 17–24, 2011.
- [152] K. Dutta and K. K. Ray, “Ratcheting strain in interstitial free steel,” *Mater. Sci. Eng. A*, vol. 575, pp. 127–135, 2013.
- [153] G. Kang and Y. Liu, “Uniaxial ratcheting and low-cycle fatigue failure of the steel with cyclic stabilizing or softening feature,” *Mater. Sci. Eng. A*, vol. 472, no. 1–2, pp. 258–268, 2008.
- [154] Y. Liu, G. Kang, and Q. Gao, “Stress-based fatigue failure models for uniaxial ratcheting-fatigue interaction,” *Int. J. Fatigue*, vol. 30, no. 6, pp. 1065–1073, 2008.
- [155] G. Z. Kang, Y. G. Li, J. Zhang, Y. F. Sun, and Q. Gao, “Uniaxial ratcheting and failure behaviors of two steels,” *Theor. Appl. Fract. Mech.*, vol. 43, no. 2, pp. 199–209, 2005.
- [156] G. Kang, Y. Liu, and Z. Li, “Experimental study on ratcheting-fatigue interaction of SS304 stainless steel in uniaxial cyclic stressing,” *Mater. Sci. Eng. A*, vol. 435–436, pp. 396–404, 2006.
- [157] S. Sinha and S. Ghosh, “Modeling cyclic ratcheting based fatigue life of HSLA steels using crystal plasticity FEM simulations and experiments,” *Int. J. Fatigue*, vol. 28, no. 12, pp. 1690–1704, 2006.
- [158] J. W. Ringsberg, “Life prediction of rolling contact fatigue crack initiation,” *Int. J. Fatigue*, vol. 23, no. 7, pp. 575–586, 2001.
- [159] N. Merah, “Detecting and Measuring Flaws Using Electric Potential Techniques,” *J. Qual. Maint. Eng.*, vol. 9, no. 2, pp. 160–175, 2003.
- [160] S. Ritter, D. A. Horner, and R.-W. Bosch, “Corrosion monitoring techniques for detection of crack initiation under simulated light water reactor conditions,” *Corros. Eng. Sci. Technol.*, vol. 47, no. 4, pp. 251–264, Jun. 2012.
- [161] S. Reaz Ahmed, M. Saka, and F. Takeo, “DC Potential-Drop Technique for the Evaluation of 3-D Back-Wall Cracks in Steel Structures,” *Key Eng. Mater.*, vol. 321–323, pp. 434–440, 2006.
- [162] N. Bowler, “Four-point potential drop measurements for materials characterization,” *Meas. Sci. Technol.*, vol. 22, no. 1, p. 12001, Jan. 2010.
- [163] D. Petersen, G. Belloni, E. Gariboldi, A. Lo Conte, M. Tono, and P. Speranzoso, “On the Experimental Calibration of a Potential Drop System for Crack Length Measurements in a Compact Tension Specimen,” *J. Test. Eval.*, vol. 30, no. 6, p. 11149, 2002.

- [164] D. Petersen, R. Link, R. Yee, and S. Lambert, "A Reversing Direct Current Potential Drop System for Detecting and Sizing Fatigue Cracks along Weld Toes," *J. Test. Eval.*, vol. 23, no. 4, p. 254, 1995.
- [165] M. Sakane and M. Ohnami, "Electrical Potential Drop and Notch Opening Displacement Methods for Detecting High Temperature Low Cycle Fatigue Cracks of Circumferential Notched Specimens," *J. Eng. Mater. Technol.*, vol. 110, no. 3, p. 247, 1988.
- [166] M. Andersson, C. Persson, and S. Melin, "Experimental and numerical investigation of crack closure measurements with electrical potential drop technique," *Int. J. Fatigue*, vol. 28, no. 9, pp. 1059–1068, 2006.
- [167] A. Turnbull, S. Zhou, N. McCormick, and M. Lukaszewicz, "An approach to measurement of environmentally assisted small crack growth," *Corros. 2013*, 2013.
- [168] W. Dover, F. Charlesworth, K. Taylor, R. Collins, and D. Michael, "The Use of A-C Field Measurements to Determine the Shape and Size of a Crack in a Metal," in *Eddy-Current Characterization of Materials and Structures*, 100 Barr Harbor Drive, PO Box C700, West Conshohocken, PA 19428-2959: ASTM International, 1981, pp. 401-401–27.
- [169] W. D. Dover and C. C. Monahan, "THE MEASUREMENT OF SURFACE BREAKING CRACKS BY THE ELECTRICAL SYSTEMS ACPD/ACFM," *Fatigue Fract. Eng. Mater. Struct.*, vol. 17, no. 12, pp. 1485–1492, Dec. 1994.
- [170] P. K. Singh, K. K. Vaze, V. Bhasin, H. S. Kushwaha, P. Gandhi, and D. S. Ramachandra Murthy, "Crack initiation and growth behaviour of circumferentially cracked pipes under cyclic and monotonic loading," *Int. J. Press. Vessel. Pip.*, vol. 80, no. 9, pp. 629–640, 2003.
- [171] I. S. Hwang, "A multi-frequency AC potential drop technique for the detection of small cracks," *Meas. Sci. Technol.*, vol. 3, no. 1, pp. 62–74, Jan. 1999.
- [172] Y. Dai, N. Marchand, and M. Hongoh, "Fatigue Crack Growth Measurements in TMF Testing of Titanium Alloys Using an ACPD Technique," in *Special Applications and Advanced Techniques for Crack Size Determination*, 100 Barr Harbor Drive, PO Box C700, West Conshohocken, PA 19428-2959: ASTM International, 1995, pp. 17-17–16.
- [173] R. P. Gangloff, D. C. Slavik, R. S. Piascik, and R. H. Van Stone, "Direct current electrical potential measurement of the growth of small cracks," in *Small-Crack Test Methods*, 1992, pp. 116–168.

- [174] G. Sposito, P. Cawley, and P. B. Nagy, “Potential drop mapping for the monitoring of corrosion or erosion,” *NDT E Int.*, vol. 43, no. 5, pp. 394–402, 2010.
- [175] G. Wilkowski and W. Maxey, “Review and applications of the electric potential method for measuring crack growth in specimens, flawed pipes, and pressure vessels,” *Fract. Mech. Fourteenth Symp.*, pp. 266–294, 1983.
- [176] R. Collins, D. Mirshekar-Syahkal, and D. H. Michael, “Surface Current Distributions Around Surface Flaws in Metals,” *Proc. R. Soc. London A Math. Phys. Eng. Sci.*, vol. 393, no. 1804, 1984.
- [177] R. Collins, D. H. Michael, D. Mirshekar-Syahkal, and H. G. Pinsent, “Surface electromagnetic fields around surface flaws in metals,” *J. Nondestruct. Eval.*, vol. 5, no. 2, pp. 81–93, Jun. 1985.
- [178] and R. O. C. Gabrielli, F. Huet, M. Keddam, “A review of the probabilistic aspects of localized corrosion,” *Corrosion*, vol. 4, no. 46, p. 266–278., Apr. 1990.
- [179] T. T. Lunt, J. R. Scully, V. Brusamarello, A. S. Mikhailov, and J. L. Hudson, “Spatial Interactions among Localized Corrosion Sites,” *J. Electrochem. Soc.*, vol. 149, no. 5, p. B163, 2002.
- [180] S. I. Rokhlin, J.-Y. Kim, H. Nagy, and B. Zoofan, “Effect of pitting corrosion on fatigue crack initiation and fatigue life,” *Engineering Fracture Mechanics*, vol. 62, no. 4–5, pp. 425–444, 1999.
- [181] G. S. Chen, K.-C. Wan, M. Gao, R. P. Wei, and T. H. Flournoy, “Transition from pitting to fatigue crack growth—modeling of corrosion fatigue crack nucleation in a 2024-T3 aluminum alloy,” *Mater. Sci. Eng. A*, vol. 219, no. 1–2, pp. 126–132, Nov. 1996.
- [182] K. S. Al-Rubaie, M. A. Del Grande, D. N. Travessa, and K. R. Cardoso, “Effect of pre-strain on the fatigue life of 7050-T7451 aluminium alloy,” *Mater. Sci. Eng. A*, vol. 464, no. 1–2, pp. 141–150, 2007.
- [183] B. M. Schönbauer, S. E. Stanzi-Tschegg, A. Perlega, R. N. Salzman, N. F. Rieger, S. Zhou, A. Turnbull, and D. Gandy, “Fatigue life estimation of pitted 12% Cr steam turbine blade steel in different environments and at different stress ratios,” *Int. J. Fatigue*, vol. 65, pp. 33–43, 2014.
- [184] S. Zhou and A. Turnbull, “Development of pre-pitting procedure for turbine disc steel,” *Br. Corros. J.*, vol. 35, no. 2, pp. 120–124, Feb. 2000.

- [185] ASTM, “ASTM C1161-13 Standard Test Method for Flexural Strength of Advanced Ceramics at Ambient Temperature,” pp. 1–19, 2013.
- [186] ASTM, “ASTM E466 Standard Practice for Conducting Force Controlled Constant Amplitude Axial Fatigue Tests of Metallic Materials,” vol. 3, pp. 4–8, 2002.
- [187] D. Mirshekar-Syahkal, “Probe characterization in ac field measurements of surface crack depth,” *J. Nondestruct. Eval.*, vol. 3, no. 1, pp. 9–17, Mar. 1982.
- [188] E. L. Lewis, “The Practical Salinity Scale 1978 and Its Antecedents,” *IEEE J. Ocean. Eng.*, vol. 5, no. 1, pp. 3–8, Jan. 1980.
- [189] K. V. Rybalka, L. A. Beketaeva, and A. D. Davydov, “Effect of self-passivation on the electrochemical and corrosion behaviour of alloy C-22 in NaCl solutions,” *Corros. Sci.*, vol. 54, no. 1, pp. 161–166, 2012.
- [190] G. Advanced KRAUSS and S. W. Thompson, “Review Ferritic carbon M icrostructures in Steels Oontinuously Cooled Low-and Ultralow,” *ISIJ Int.*, vol. 35, no. 8, pp. 937–945.
- [191] E. El-Danaf, M. Baig, A. Almajid, W. Alshalfan, M. Al-Mojil, and S. Al-Shahrani, “Mechanical, microstructure and texture characterization of API X65 steel,” *Mater. Des.*, vol. 47, pp. 529–538, 2013.
- [192] A. H. Cottrell and B. A. Bilby, “Dislocation Theory of Yielding and Strain Ageing of Iron,” *Proc. Phys. Soc. Sect. A*, vol. 62, no. 1, p. 49, Jan. 1949.
- [193] X. Jiang, S. Nesic, and B. Kinsella, “Electrochemical investigation of the role of Cl- on localized CO<sub>2</sub> corrosion of mild steel,” in *17th International Corrosion Congress, Las Vegas, NACE*, 2008.
- [194] M. Nordsveen, S. Nešić, R. Nyborg, and A. Stangeland, “A Mechanistic Model for Carbon Dioxide Corrosion of Mild Steel in the Presence of Protective Iron Carbonate Films—Part 1: Theory and Verification,” *CORROSION*, vol. 59, no. 5, pp. 443–456, May 2003.
- [195] C. A. Palacios and J. R. Shadley, “Characteristics of Corrosion Scales on Steels in a CO<sub>2</sub>-Saturated NaCl Brine,” *CORROSION*, vol. 47, no. 2, pp. 122–127, Feb. 1991.
- [196] K. Gao, F. Yu, X. Pang, G. Zhang, L. Qiao, W. Chu, and M. Lu, “Mechanical properties of CO<sub>2</sub> corrosion product scales and their relationship to corrosion rates,” *Corros. Sci.*, vol. 50, no. 10, pp. 2796–2803, 2008.
- [197] G. Sposito, P. Cawley, and P. B. Nagy, “An approximate model for three-dimensional

- alternating current potential drop analyses using a commercial finite element code,” *NDT E Int.*, vol. 43, no. 2, pp. 134–140, 2010.
- [198] G. L. Nicholson, A. G. Kostyrychev, X. J. Hao, and C. L. Davis, “Modelling and experimental measurements of idealised and light-moderate RCF cracks in rails using an ACFM sensor,” *NDT E Int.*, vol. 44, no. 5, pp. 427–437, 2011.
- [199] R. Collins, D. Mirshekar-Syahkal, and D. H. Michael, “Surface Current Distributions Around Surface Flaws in Metals,” *Proc. R. Soc. A Math. Phys. Eng. Sci.*, vol. 393, no. 1804, pp. 159–170, 1984.
- [200] H. Saguy and D. Rittel, “Flaw detection in metals by the ACPD technique: Theory and experiments,” *NDT E Int.*, vol. 40, no. 7, pp. 505–509, 2007.
- [201] O. Vosikovskiy, “Fatigue-Crack Growth in an X-65 Line-Pipe Steel at Low Cyclic Frequencies in Aqueous Environments,” *J. Eng. Mater. Technol.*, vol. 97, no. 4, p. 298, 1975.
- [202] J. C. Newman and I. S. Raju, “An empirical stress-intensity factor equation for the surface crack,” *Eng. Fract. Mech.*, vol. 15, no. 1–2, pp. 185–192, Jan. 1981.
- [203] E. Kröner, “Allgemeine Kontinuumstheorie der Versetzungen und Eigenspannungen,” *Arch. Ration. Mech. Anal.*, vol. 4, no. 1, pp. 273–334, Jan. 1959.
- [204] T. Jaeger, B. A. Boley, International Association for Structural Mechanics in Reactor Technology., and Commission of the European Communities., *Transactions of the 5th International Conference on Structural Mechanics in Reactor Technology, International Congress Center Berlin, Berlin, Germany, 13-17 August 1979*. North-Holland Pub. Co. for the Commission of the European Communities, 1979.
- [205] J. L. Chaboche and G. Rousselier, “On the Plastic and Viscoplastic Constitutive Equations, part I and II,” *ASME J. Press. Vessel Technol.*, vol. 105, no. I, pp. 153–164, 1983.
- [206] G. Kang, Y. Liu, J. Ding, and Q. Gao, “Uniaxial ratcheting and fatigue failure of tempered 42CrMo steel: Damage evolution and damage-coupled visco-plastic constitutive model,” *Int. J. Plast.*, vol. 25, no. 5, pp. 838–860, May 2009.
- [207] J. Bauschinger, “Über die Veränderung der Elastizitätsgrenze und die Festigkeit des Eisens und Stahl durch Strecken und Quetschen, durch Erwärmen und Abkühlen und durch oftmal wiederholte Beanspruchung,” *Mitth. aus dem Mech. Lab. der kgl. Tech.*

- Hochschule München*, vol. 13, pp. 1–116, 1886.
- [208] D. L. Henann and L. Anand, “A large deformation theory for rate-dependent elastic–plastic materials with combined isotropic and kinematic hardening,” *Int. J. Plast.*, vol. 25, no. 10, pp. 1833–1878, Oct. 2009.
- [209] C. O. Frederick and P. J. Armstrong, “A mathematical representation of the multiaxial Bauschinger effect,” *Mater. High Temp.*, vol. 24, no. 1, pp. 1–26, 2007.
- [210] N. Ohno, “Recent Topics in Constitutive Modeling of cyclic plasticity and viscoplasticity,” *Appl. Mech. Rev.*, vol. 43, no. 1978, pp. 283–295, 1990.
- [211] N. Ohno, “Recent progress in constitutive modeling for ratchetting,” *Mater. Sci. Res. Int.*, vol. 3, no. 1, pp. 1–9, 1997.
- [212] G. KANG, “Ratchetting: Recent progresses in phenomenon observation, constitutive modeling and application,” *Int. J. Fatigue*, vol. 30, no. 8, pp. 1448–1472, Aug. 2008.
- [213] N. Ohno and J. D. Wang, “Kinematic hardening rules with critical state of dynamic recovery, part I: formulation and basic features for ratchetting behavior,” *Int. J. Plast.*, vol. 9, no. 3, pp. 375–390, 1993.
- [214] N. Ohno and J. Wang, “Kinematic hardening rules for simulation of ratchetting behavior,” *Eur. J. Mech. A. Solids*, vol. 13, no. 4, pp. 519–531, 1994.
- [215] G. Weber and L. Anand, “Finite deformation constitutive equations and a time integration procedure for isotropic, hyperelastic-viscoplastic solids,” *Comput. Methods Appl. Mech. Eng.*, vol. 79, no. 2, pp. 173–202, 1990.
- [216] C. L. Xie, S. Ghosh, and M. Groeber, “Modeling cyclic deformation of HSLA steels using crystal plasticity,” *J. Eng. Mater. Technol. Asme*, vol. 126, no. 4, pp. 339–352, 2004.
- [217] J. L. Chaboche, “A review of some plasticity and viscoplasticity constitutive theories,” *Int. J. Plast.*, vol. 24, no. 10, pp. 1642–1693, Oct. 2008.
- [218] T. Hassan and S. Kyriakides, “Ratcheting in cyclic plasticity, part I: Uniaxial behavior,” *Int. J. Plast.*, vol. 8, no. 1, pp. 91–116, Jan. 1992.
- [219] Hibbett, Karlsson, and Sorensen, “ABAQUS/standard: User’s Manual,” vol. 1, 1998.
- [220] S. K. Paul and A. Kumar, “Micromechanics based modeling to predict flow behavior and plastic strain localization of dual phase steels,” *Comput. Mater. Sci.*, vol. 63, pp. 66–74, 2012.
- [221] L. Anand, O. Aslan, and S. A. Chester, “A large-deformation gradient theory for elastic-

- plastic materials: Strain softening and regularization of shear bands,” *Int. J. Plast.*, vol. 30–31, pp. 116–143, 2012.
- [222] X. Sun, K. S. Choi, W. N. Liu, and M. A. Khaleel, “Predicting failure modes and ductility of dual phase steels using plastic strain localization,” *Int. J. Plast.*, vol. 25, no. 10, pp. 1888–1909, 2009.
- [223] L. Anand, “A large deformation poroplasticity theory for microporous polymeric materials,” *J. Mech. Phys. Solids*, vol. 98, pp. 126–155, 2017.
- [224] T. Hasegawa, T. Yakou, and S. Karashima, “Deformation Behavior and Dislocation-Structures Upon Stress Reversal in Polycrystalline Aluminum,” *Mater. Sci. Eng.*, vol. 20, no. 3, pp. 267–276, 1975.
- [225] E. V. Nesterova, B. Bacroix, and C. Teodosiu, “Microstructure and texture evolution under strain-path changes in low-carbon interstitial-free steel,” *Metall. Mater. Trans. A*, vol. 32, no. October, pp. 2527–2538, Oct. 2001.
- [226] G. Vincze, E. F. Rauch, J. J. Gracio, F. Barlat, and A. B. Lopes, “A comparison of the mechanical behaviour of an AA1050 and a low carbon steel deformed upon strain reversal,” *Acta Mater.*, vol. 53, no. 4, pp. 1005–1013, 2005.
- [227] L. N. Brewer, D. P. Field, and C. C. Merriman, “Mapping and assessing plastic deformation using EBSD,” in *Electron Backscatter Diffraction in Materials Science*, Boston, MA: Springer US, 2009, pp. 251–262.
- [228] M. F. Ashby, “The deformation of plastically non-homogeneous materials,” *Philos. Mag.*, vol. 21, no. 170, pp. 399–424, Feb. 1970.
- [229] D. J. Prior, S. I. Wright, B. L. Adams, and D. J. Dingley, “Orientation Contrast Imaging of Microstructures in Rocks Using Forescatter Detectors in the Scanning Electron Microscope,” *Mineral. Mag.*, vol. 60, no. 403, pp. 859–869, 1996.
- [230] A. J. Wilkinson and D. J. Dingley, “Quantitative deformation studies using electron back scatter patterns,” *Acta Metall. Mater.*, vol. 39, no. 12, pp. 3047–3055, Dec. 1991.
- [231] S. I. Wright, “Quantification of recrystallized fraction from orientation imaging scans,” in *National Research Council of Canada, Proceedings of the Twelfth International Conference on Textures of Materials(ICOTOM-12).*, 1999, vol. 1, pp. 104–109.
- [232] L. N. Brewer, M. a Othon, L. M. Young, and T. M. Angeliu, “Misorientation mapping for visualization of plastic deformation via electron back-scattered diffraction,” *Microsc.*

- Microanal.*, vol. 12, no. 1, pp. 85–91, 2006.
- [233] L. Brewer, M. Othon, Y. Gao, B. T. Hazel, W. H. Buttrill, and Z. Zhong, “Comparison of diffraction methods for measurement of surface damage in superalloys,” *J. Mater. Res.*, vol. 21, no. 7, pp. 1775–1781, 2006.
- [234] G. A. Young, N. Lewis, C. K. Battige, R. A. Somers, M. A. Penik, L. Brewer, and M. Othon, “Quantification of residual plastic strains in Ni-Cr-Mn-Nb GTAW welds via electron backscatter diffraction,” in *TRENDS IN WELDING RESEARCH, PROCEEDINGS*, 2003, pp. 912–917.
- [235] J. A. Sutcliffe, “An investigation of plastic strain in copper by automated-EBSP,” *Microsc. Microanal.*, vol. 5, no. 2, pp. 236–237, 1999.
- [236] T. M. Angeliu, P. L. Andresen, E. Hall, J. A. Sutliff, S. Sitzman, and R. M. Horn, “Intergranular Stress Corrosion Cracking of Unsensitized Stainless Steels in BWR Environments,” in *Ninth International Symposium on Environmental Degradation of Materials in Nuclear Power Systems-Water Reactors*, Hoboken, NJ, USA: John Wiley & Sons, Inc., 2013, pp. 311–318.
- [237] S. I. Wright, M. M. Nowell, and D. P. Field, “A review of strain analysis using electron backscatter diffraction,” *Microscopy and microanalysis : the official journal of Microscopy Society of America, Microbeam Analysis Society, Microscopical Society of Canada*, vol. 17, no. 3. Springer US, pp. 316–329, 22-May-2011.
- [238] R.F. Egerton, *Physical Principles of Electron Microscopy*. New York: Springer, 2005.
- [239] E. Lehockey, Y. Lin, and O. Lepik, “Mapping residual plastic strain in materials using electron backscatter diffraction,” in *Electron backscatter diffraction in materials science*, 2000, pp. 247–265.
- [240] M. D. Uchic, M. Groeber, R. Wheeler IV, F. Scheltens, and D. M. Dimiduk, “Augmenting the 3D Characterization Capability of the Dual Beam FIB-SEM,” *Microsc. Microanal.*, vol. 10, no. S02, pp. 1136–1137, 2004.
- [241] A. J. Wilkinson, T. B. Britton, J. Jiang, and P. S. Karamched, “A review of advances and challenges in EBSD strain mapping,” *IOP Conf. Ser. Mater. Sci. Eng.*, vol. 55, no. 1, p. 12020, Mar. 2014.
- [242] A. Turnbull, L. Wright, and L. Crocker, “New insight into the pit-to-crack transition from finite element analysis of the stress and strain distribution around a corrosion pit,” *Corros.*

- Sci.*, vol. 52, no. 4, pp. 1492–1498, 2010.
- [243] M. Cerit, K. Genel, and S. Eksi, “Numerical investigation on stress concentration of corrosion pit,” *Eng. Fail. Anal.*, vol. 16, no. 7, pp. 2467–2472, 2009.
- [244] J. Rudolph, A. Götz, and R. Hilpert, “LOCAL RATCHETING BY ELASTIC-PLASTIC FEA - CRITERIA AND CODE BASED APPROACHES,” *ASME 2011 Press. Vessel. Pip. Conf. Vol. 1*, pp. 1–11, 2011.
- [245] A. Turnbull, K. Mingard, J. D. Lord, B. Roebuck, D. R. Tice, K. J. Mottershead, N. D. Fairweather, and A. K. Bradbury, “Sensitivity of stress corrosion cracking of stainless steel to surface machining and grinding procedure,” *Corros. Sci.*, vol. 53, no. 10, pp. 3398–3415, Oct. 2011.
- [246] W. Li and D. Y. Li, “Influence of surface morphology on corrosion and electronic behavior,” *Acta Mater.*, vol. 54, no. 2, pp. 445–452, 2006.
- [247] Y. Tan, “Understanding the effects of electrode inhomogeneity and electrochemical heterogeneity on pitting corrosion initiation on bare electrode surfaces,” *Corros. Sci.*, vol. 53, no. 5, pp. 1845–1864, 2011.
- [248] D. Arola and C. L. Williams, “Estimating the fatigue stress concentration factor of machined surfaces,” *Int. J. Fatigue*, vol. 24, no. 9, pp. 923–930, 2002.
- [249] H. Gao, “Stress concentration at slightly undulating surfaces,” *J. Mech. Phys. Solids*, vol. 39, no. 4, pp. 443–458, 1991.
- [250] R. Akid and K. J. Miller, “The Application of Microstructural Fracture Mechanics to Various Metal Surface States,” *Proc. R. Soc. London A*, vol. 452, no. 1949, pp. 1411–1432, 1996.
- [251] L. Y. Xu and Y. F. Cheng, “Corrosion of X100 pipeline steel under plastic strain in a neutral pH bicarbonate solution,” *Corros. Sci.*, vol. 64, pp. 145–152, 2012.
- [252] K. Tanaka and Y. Nakai, “PROPAGATION AND NON-PROPAGATION OF SHORT FATIGUE CRACKS AT A SHARP NOTCH,” *Fatigue Fract. Eng. Mater. Struct.*, vol. 6, no. 4, pp. 315–327, Jan. 1983.
- [253] K. J. Miller, “THE BEHAVIOUR OF SHORT FATIGUE CRACKS AND THEIR INITIATION PART II-A GENERAL SUMMARY,” *Fatigue Fract. Eng. Mater. Struct.*, vol. 10, no. 2, pp. 93–113, Feb. 1987.
- [254] K. J. Miller, “Materials science perspective of metal fatigue resistance,” *Mater. Sci.*

- Technol.*, vol. 9, no. 6, pp. 453–462, Jun. 1993.
- [255] S. Suresh and R. O. Ritchie, “Propagation of short fatigue cracks,” *Int. Met. Rev.*, vol. 29, no. 1, pp. 445–475, Jan. 1984.
- [256] H. Gerber, “Bestimmung der zulässigen spannungen in eisen-constructionen,” *Z. Bayer Arch. Ing.*, vol. 6, no. 6, pp. 101–110, 1874.
- [257] O. Fatoba and R. Akid, “Low cycle fatigue behaviour of API 5L X65 pipeline steel at room temperature,” in *Procedia Engineering*, 2014, vol. 74, pp. 279–286.

## Appendix A: Stress Intensity Factor of an Elliptical Crack

In Section 4.4, we calculated the stress intensity factor of the penny-shaped crack. The detailed equations used to calculate the stress intensity factor adopted from [202] are shown below.

$a$  depth of surface crack

$b$  half-width of cracked plate

$c$  half-length of surface crack

$F$  stress-intensity boundary correction factor

$h$  half-length of cracked plate

$K_I$  mode I stress intensity factor

$M$  applied bending moment

$Q$  shape factor for elliptical crack

$S_b$  remote bending stress on outer fiber

$t$  plate thickness

$\varphi$  parametric angle of the ellipse

The stress intensity factor for bending load is

$$K_I = HS_b \sqrt{\pi \frac{a}{Q}} F\left(\frac{a}{t}, \frac{a}{c}, \frac{c}{b}, \varphi\right) \quad (\text{A-1})$$

for  $0 < a/c \leq 1, 0 \leq a/t < 1, c/b < 0.5$  and  $0 \leq \varphi \leq \pi$ .

The shape factor  $Q$  can be approximated as

$$Q = 1 + 1.464 \left(\frac{a}{c}\right)^{1.65} \quad (\text{A-2})$$

The functions F was taken to be

$$F = \left[ M_1 + M_2 \left( \frac{a}{c} \right)^2 + M_3 \left( \frac{a}{c} \right)^4 \right] f_\varphi g f_w \quad (\text{A-3})$$

where

$$M_1 = 1.13 - 0.09 \left( \frac{a}{c} \right) \quad (\text{A-4})$$

$$M_2 = -0.54 + \frac{0.89}{0.2 + (a/c)} \quad (\text{A-5})$$

$$M_3 = 0.5 - \frac{1.0}{0.65 + (a/c)} + 14 \left( 1.0 - \frac{a}{c} \right)^{24} \quad (\text{A-6})$$

$$g = 1 + \left[ 0.1 + 0.35 \left( \frac{a}{c} \right)^2 \right] (1 - \sin\varphi)^2 \quad (\text{A-7})$$

The angular function from the embedded elliptical-crack solution  $f_\varphi$  is

$$f_\varphi = \left[ \left( \frac{a}{c} \right)^2 \cos^2\varphi + \sin^2\varphi \right]^{1/4} \quad (\text{A-8})$$

The finite-width correction  $f_w$  is

$$f_w = \left[ \sec \left( \frac{\pi c}{2b} \sqrt{\frac{a}{t}} \right) \right]^{1/2} \quad (\text{A-9})$$

The function H has the form

$$H = H_1 + (H_2 - H_1)\sin^p \varphi \quad (\text{A-10})$$

where

$$p = 0.2 + \frac{a}{c} + 0.6 \frac{a}{t} \quad (\text{A-11})$$

$$H_1 = 1 - 0.34 \frac{a}{t} - 0.11 \frac{a}{c} \left( \frac{a}{t} \right) \quad (\text{A-12})$$

$$H_2 = 1 + G_1 \left( \frac{a}{t} \right) + G_2 \left( \frac{a}{t} \right)^2 \quad (\text{A-13})$$

In the equation for  $H_2$

$$G_1 = -1.22 - 0.12 \frac{a}{c} \quad (\text{A-14})$$

$$G_2 = 0.55 - 1.05 \left( \frac{a}{c} \right)^{0.75} + 0.47 \left( \frac{a}{c} \right)^{1.5} \quad (\text{A-15})$$

## Appendix B: Time Integration Procedure of the Finite Element Model

A semi-implicit time integration procedure of the finite element model is described in this appendix.

At time  $t$ , we are given  $\mathbf{F}(t)$  and the list of variables  $\{\mathbf{F}^p(t), \mathbf{T}(t), \mathbf{S}_{back}(t)\}$ . And we are also given an estimation of deformation gradient  $\mathbf{F}(\tau)$  at time  $\tau = t + \Delta t$ .

The goal of this time integration procedure is to calculate variables  $\{\mathbf{F}^p(\tau), \mathbf{T}(\tau), \mathbf{S}_{back}(\tau)\}$  at time  $\tau$ .

From

$$\dot{\mathbf{F}}^p = \mathbf{D}^p \mathbf{F}^p = \frac{d\mathbf{F}^p}{dt} \quad (\text{B-1})$$

Integration the equation above on both sides and we can get:

$$\mathbf{F}^p(\tau) = \exp(\Delta t \mathbf{D}^p(\tau)) \mathbf{F}^p(t) \quad (\text{B-2})$$

$$\mathbf{F}^{p-1}(\tau) = \mathbf{F}^{p-1}(t) \exp(-\Delta t \mathbf{D}^p(\tau)) \quad (\text{B-3})$$

We can obtain the trail of elastic distortion by freezing the plastic flow at time  $\tau$ :

$$\mathbf{F}_{tr}^e = \mathbf{F}(\tau) \mathbf{F}^{p-1}(t) \quad (\text{B-4})$$

The exact elastic distortion and its relation with its trial is

$$\begin{aligned} \mathbf{F}^e(\tau) &= \mathbf{F}(\tau) \mathbf{F}^{p-1}(\tau) = \mathbf{F}(\tau) \mathbf{F}^{p-1}(t) \exp(-\Delta t \mathbf{D}^p(\tau)) \\ &= \mathbf{F}_{tr}^e \exp(-\Delta t \mathbf{D}^p(\tau)) \end{aligned} \quad (\text{B-5})$$

Polar decomposition on both sides gives:

$$\mathbf{R}^e(\tau)\mathbf{U}^e(\tau) = \mathbf{R}_{tr}^e\mathbf{U}_{tr}^e \exp(-\Delta t\mathbf{D}^p(\tau)) \quad (\text{B-6})$$

We can equation the rotation part and stretch part, respectively,

$$\mathbf{R}^e(\tau) = \mathbf{R}_{tr}^e \quad (\text{B-7})$$

$$\mathbf{U}^e(\tau) = \mathbf{U}_{tr}^e \exp(-\Delta t\mathbf{D}^p(\tau)) \quad (\text{B-8})$$

Take logarithmic on both sides of the stretch equation, we get,

$$\mathbf{E}^e(\tau) = \mathbf{E}_{tr}^e - \Delta t\mathbf{D}^p(\tau) \quad (\text{B-9})$$

where  $\mathbf{E}_{tr}^e \equiv \ln\mathbf{U}_{tr}^e$  is the “trial elastic strain”.

Multiply the elastic tensor on both sides, and we can get:

$$\mathbf{M}^e(\tau) = \mathbf{M}_{tr}^e - \mathbb{C}(\Delta t\mathbf{D}^p(\tau)) \quad (\text{B-10})$$

where  $\mathbf{M}_{tr}^e \equiv \mathbb{C}\mathbf{E}_{tr}^e$  is the “trial Mandel stress”.

Subtract the back stress  $\mathbf{S}_{back}(\tau)$  on the left hand sides, and  $\mathbf{S}_{back}(t)$  from the right hand side.

Noticed that

$$\mathbf{S}_{back}(t) = \mathbf{S}_{back,tr} \quad (\text{B-11})$$

because the trial values are estimated with plastic flow frozen.

We can get:

$$\mathbf{M}_{eff}^e(\tau) = \mathbf{M}_{eff,tr}^e - \mathbb{C}(\Delta t \mathbf{D}^p(\tau)) \quad (\text{B-12})$$

where  $\mathbf{M}_{eff}^e(\tau) \equiv \mathbf{M}^e(\tau) - \mathbf{S}_{back}(\tau)$ ,  $\mathbf{M}_{eff,tr}^e \equiv \mathbf{M}_{tr}^e - \mathbf{S}_{back,tr}$

Take the deviatoric part of the equation above, and use the definition of the elastic tensor, we can get:

$$\left(\mathbf{M}_{eff}^e(\tau)\right)_0 = \left(\mathbf{M}_{eff,tr}^e\right)_0 - 2G(\Delta t \mathbf{D}^p(\tau)) \quad (\text{B-13})$$

And we know the following relations:

$$\mathbf{D}^p = \sqrt{3/2} \dot{\epsilon}^p \mathbf{N}^p, \quad \mathbf{N}^p = \frac{(\mathbf{M}_{eff}^e)_0}{\left|(\mathbf{M}_{eff}^e)_0\right|} = \frac{\sqrt{3/2}(\mathbf{M}_{eff}^e)_0}{\bar{\sigma}_{eff}} \quad (\text{B-14})$$

so we can get

$$\left(\sqrt{2/3} \bar{\sigma}_{eff}(\tau) + \sqrt{6} G \Delta t \dot{\epsilon}^p(\tau)\right) \mathbf{N}^p = \left(\mathbf{M}_{eff,tr}^e\right)_0 \quad (\text{B-15})$$

Define

$$\mathbf{N}_{eff,tr}^p = \frac{(\mathbf{M}_{eff,tr}^e)_0}{\sqrt{2/3} \bar{\sigma}_{eff,tr}}, \quad \bar{\sigma}_{eff,tr} = \sqrt{3/2} \left|(\mathbf{M}_{eff,tr}^e)_0\right| \quad (\text{B-16})$$

so we can write

$$\left(\sqrt{2/3}\bar{\sigma}_{eff}(\tau) + \sqrt{6}G\Delta t\dot{\epsilon}^p(\tau)\right)\mathbf{N}^p = \sqrt{2/3}\bar{\sigma}_{eff,tr}\mathbf{N}_{eff,tr}^p \quad (\text{B-17})$$

We can immediately see that

$$\bar{\sigma}_{eff}(\tau) + 3G\Delta t\dot{\epsilon}^p(\tau) = \bar{\sigma}_{eff,tr} \quad (\text{B-18})$$

$$\mathbf{N}^p = \mathbf{N}_{eff,tr}^p \quad (\text{B-19})$$

thus the direction of the plastic flow is determined by the trial direction of the plastic flow.

Notice that  $\bar{\sigma}_{eff}(\tau)$  can be expressed using  $\dot{\epsilon}^p(\tau)$  and the isotropic resistance  $S$ ,

$$\bar{\sigma}_{eff}(\tau) = Y(\dot{\epsilon}^p(\tau), S) \quad (\text{B-20})$$

We arrive the single equation contains the only unknown  $\dot{\epsilon}^p(\tau)$ :

$$Y(\dot{\epsilon}^p(\tau), S) + 3G\Delta t\dot{\epsilon}^p(\tau) = \bar{\sigma}_{eff,tr} \quad (\text{B-21})$$

We can solve  $\dot{\epsilon}^p(\tau)$  from this equation. And then update  $\mathbf{D}^p(\tau)$ ,  $\mathbf{F}^p(\tau)$ , and  $\mathbf{M}^e(\tau)$  by

$$\mathbf{D}^p(\tau) = \sqrt{3/2}\dot{\epsilon}^p(\tau)\mathbf{N}_{eff,tr}^p \quad (\text{B-22})$$

$$\mathbf{F}^p(\tau) = \exp(\Delta t\mathbf{D}^p(\tau))\mathbf{F}^p(t) \quad (\text{B-23})$$

$$\mathbf{M}^e(\tau) = \mathbf{M}_{tr}^e - \mathbb{C}(\Delta t\mathbf{D}^p(\tau)) = \mathbf{M}_{tr}^e - 2G(\Delta t\mathbf{D}^p(\tau)) \quad (\text{B-24})$$

We know that

$$\dot{\mathbf{S}}_{back,s} = d_s \left( r_s \mathbf{D}^p - \left( \frac{\bar{S}_{back,s}}{r_s} \right)^{m_{d,s}} \mathbf{S}_{back,s} \dot{\bar{\epsilon}}^p \right) \quad (\text{B-25})$$

$$\dot{\mathbf{S}}_{back,h} = d_h \left( r_h \mathbf{D}^p \exp(-m_{s,h} \bar{\epsilon}^p) - \left( \frac{\bar{S}_{back,h}}{r_h} \right)^{m_{d,h}} \mathbf{S}_{back,h} \dot{\bar{\epsilon}}^p \right) \quad (\text{B-26})$$

Integrate the equation gives:

$$\begin{aligned} \mathbf{S}_{back,s}(\tau) &= \mathbf{S}_{back,s}(t) + d_s r_s \Delta t \mathbf{D}^p(\tau) \\ &\quad - d_s \Delta t \left( \frac{\bar{S}_{back,s}(t)}{r_s} \right)^{m_{d,s}} \mathbf{S}_{back,s}(\tau) \dot{\bar{\epsilon}}^p(\tau) \end{aligned} \quad (\text{B-27})$$

$$\mathbf{S}_{back,s}(\tau) = \frac{\mathbf{S}_{back,s}(t) + d_s r_s \Delta t \mathbf{D}^p(\tau)}{1 + d_s \Delta t \left( \frac{\bar{S}_{back,s}(t)}{r_s} \right)^{m_{d,s}} \dot{\bar{\epsilon}}^p(\tau)} \quad (\text{B-28})$$

$$\begin{aligned} \mathbf{S}_{back,h}(\tau) &= \mathbf{S}_{back,h}(t) + d_h r_h \Delta t \mathbf{D}^p(\tau) \exp(-m_{s,h} \bar{\epsilon}^p) \\ &\quad - d_h \Delta t \left( \frac{\bar{S}_{back,h}(t)}{r_h} \right)^{m_{d,h}} \mathbf{S}_{back,h}(\tau) \dot{\bar{\epsilon}}^p(\tau) \end{aligned} \quad (\text{B-29})$$

$$\mathbf{S}_{back,h}(\tau) = \frac{\mathbf{S}_{back,h}(t) + d_h r_h \Delta t \mathbf{D}^p(\tau) \exp(-m_{s,h} \bar{\epsilon}^p)}{1 + d_h \Delta t \left( \frac{\bar{S}_{back,h}(t)}{r_h} \right)^{m_{d,h}} \dot{\bar{\epsilon}}^p(\tau)} \quad (\text{B-30})$$

$$\mathbf{S}_{back}(\tau) = \mathbf{S}_{back,s}(\tau) + \mathbf{S}_{back,h}(\tau) \quad (\text{B-31})$$

Finally, the Cauchy stress:

$$\mathbf{F}^e(\tau) = \mathbf{F}(\tau) \mathbf{F}^{p-1}(\tau) = \mathbf{R}^e(\tau) \mathbf{U}^e(\tau) \quad (\text{B-32})$$

$$J(\tau) = \det \mathbf{F}^e(\tau) \quad (\text{B-33})$$

$$\mathbf{T} = J(\tau)^{-1} \mathbf{R}^e(\tau) \mathbf{M}^e(\tau) \mathbf{R}^{eT}(\tau) \quad (\text{B-34})$$

### **Summary of the Time-Integration Procedure**

- Given:  $\{\mathbf{F}^p(t), \mathbf{T}(t), \mathbf{S}_{back}(t)\}$ , as well as  $\mathbf{F}(t)$  and  $\mathbf{F}(\tau)$  at time  $t$ .
- Calculate:  $\{\mathbf{F}^p(\tau), \mathbf{T}(\tau), \mathbf{S}_{back}(\tau)\}$  at time  $\tau = t + \Delta t$ .

Step 1. Calculate the trail elastic distortion

$$\mathbf{F}_{tr}^e = \mathbf{F}(\tau) \mathbf{F}^{p-1}(t) \quad (\text{B-35})$$

Step 2. Perform the polar decomposition of  $\mathbf{F}_{tr}^e$

$$\mathbf{F}_{tr}^e = \mathbf{R}_{tr}^e \mathbf{U}_{tr}^e \quad (\text{B-36})$$

Step 3. Calculate the logarithmic trial elastic strain

$$\mathbf{E}_{tr}^e = \ln \mathbf{U}_{tr}^e \quad (\text{B-37})$$

Step 4. Calculate the trial Mandel stress and the trial effective Mandel stress

$$\mathbf{M}_{tr}^e = \mathbb{C} \mathbf{E}_{tr}^e \quad (\text{B-38})$$

$$\mathbf{M}_{eff,tr}^e \equiv \mathbf{M}_{tr}^e - \mathbf{S}_{back}(t) \quad (\text{B-39})$$

Step 5. Calculate the deviatoric part of the trial effective Mandel stress, the trial equivalent tensile stress, and the trial direction of plastic flow

$$(\mathbf{M}_{eff,tr}^e)_0 = \mathbf{M}_{eff,tr}^e - \frac{1}{3}tr(\mathbf{M}_{eff,tr}^e)\mathbf{1} \quad (\text{B-40})$$

$$\bar{\sigma}_{eff,tr} = \sqrt{3/2} |(\mathbf{M}_{eff,tr}^e)_0| \quad (\text{B-41})$$

$$\mathbf{N}_{tr}^p = \frac{(\mathbf{M}_{eff,tr}^e)_0}{\sqrt{2/3}\bar{\sigma}_{eff,tr}} \quad (\text{B-42})$$

Step 6. Calculate the scalar plastic flow rate  $\dot{\epsilon}^p(\tau)$

$$Y(\dot{\epsilon}^p(\tau), S) + 3G\Delta t\dot{\epsilon}^p(\tau) = \bar{\sigma}_{eff,tr} \quad (\text{B-43})$$

Step 7. Update the plastic stretching tensor

$$\mathbf{D}^p(\tau) = \sqrt{3/2}\dot{\epsilon}^p(\tau)\mathbf{N}_{tr}^p \quad (\text{B-44})$$

Step 8. Update the plastic distortion

$$\mathbf{F}^p(\tau) = \exp(\Delta t\mathbf{D}^p(\tau))\mathbf{F}^p(t) \quad (\text{B-45})$$

Step 9. Update the Mandel stress

$$\mathbf{M}^e(\tau) = \mathbf{M}_{tr}^e - 2G(\Delta t\mathbf{D}^p(\tau)) \quad (\text{B-46})$$

Step 10. Update the back-stress

$$\mathbf{S}_{back,s}(\tau) = \frac{\mathbf{S}_{back,s}(t) + d_s r_s \Delta t \mathbf{D}^p(\tau)}{1 + d_s \Delta t \left( \frac{\bar{S}_{back,s}(t)}{r_s} \right)^{m_{d,s}} \dot{\bar{\epsilon}}^p(\tau)} \quad (\text{B-47})$$

$$\mathbf{S}_{back,h}(\tau) = \frac{\mathbf{S}_{back,h}(t) + d_h r_h \Delta t \mathbf{D}^p(\tau) \exp(-m_{s,h} \bar{\epsilon}^p)}{1 + d_h \Delta t \left( \frac{\bar{S}_{back,h}(t)}{r_h} \right)^{m_{d,h}} \dot{\bar{\epsilon}}^p(\tau)} \quad (\text{B-48})$$

$$\mathbf{S}_{back}(\tau) = \mathbf{S}_{back,s}(\tau) + \mathbf{S}_{back,h}(\tau) \quad (\text{B-49})$$

Step 11. Update the elastic distortion

$$\mathbf{F}^e(\tau) = \mathbf{F}(\tau) \mathbf{F}^{p-1}(\tau) \quad (\text{B-50})$$

Step 12. Perform the polar decomposition

$$\mathbf{F}^e(\tau) = \mathbf{R}^e(\tau) \mathbf{U}^e(\tau) \quad (\text{B-51})$$

Step 13. Update the Cauchy stress

$$J(\tau) = \det \mathbf{F}^e(\tau) \quad (\text{B-52})$$

$$\mathbf{T}(\tau) = J(\tau)^{-1} \mathbf{R}^e(\tau) \mathbf{M}^e(\tau) \mathbf{R}^{eT}(\tau) \quad (\text{B-53})$$